LEABHARLANN CHOLÁISTE NA TRÍONÓIDE, BAILE ÁTHA CLIATH | TRINITY COLLEGE LIBRARY DUBLIN
Ollscoil Átha Cliath | The University of Dublin

Terms and Conditions of Use of Digitised Theses from Trinity College Library Dublin

Copyright statement

All material supplied by Trinity College Library is protected by copyright (under the Copyright and Related Rights Act, 2000 as amended) and other relevant Intellectual Property Rights. By accessing and using a Digitised Thesis from Trinity College Library you acknowledge that all Intellectual Property Rights in any Works supplied are the sole and exclusive property of the copyright and/or other IPR holder. Specific copyright holders may not be explicitly identified. Use of materials from other sources within a thesis should not be construed as a claim over them.

A non-exclusive, non-transferable licence is hereby granted to those using or reproducing, in whole or in part, the material for valid purposes, providing the copyright owners are acknowledged using the normal conventions. Where specific permission to use material is required, this is identified and such permission must be sought from the copyright holder or agency cited.

Liability statement

By using a Digitised Thesis, I accept that Trinity College Dublin bears no legal responsibility for the accuracy, legality or comprehensiveness of materials contained within the thesis, and that Trinity College Dublin accepts no liability for indirect, consequential, or incidental, damages or losses arising from use of the thesis for whatever reason. Information located in a thesis may be subject to specific use constraints, details of which may not be explicitly described. It is the responsibility of potential and actual users to be aware of such constraints and to abide by them. By making use of material from a digitised thesis, you accept these copyright and disclaimer provisions. Where it is brought to the attention of Trinity College Library that there may be a breach of copyright or other restraint, it is the policy to withdraw or take down access to a thesis while the issue is being resolved.

Access Agreement

By using a Digitised Thesis from Trinity College Library you are bound by the following Terms & Conditions. Please read them carefully.

I have read and I understand the following statement: All material supplied via a Digitised Thesis from Trinity College Library is protected by copyright and other intellectual property rights, and duplication or sale of all or part of any of a thesis is not permitted, except that material may be duplicated by you for your research use or for educational purposes in electronic or print form providing the copyright owners are acknowledged using the normal conventions. You must obtain permission for any other use. Electronic or print copies may not be offered, whether for sale or otherwise to anyone. This copy has been supplied on the understanding that it is copyright material and that no quotation from the thesis may be published without proper acknowledgement.

Surface studies of magnetite (100)

A thesis submitted to the University of Dublin, Trinity College,
in application for the degree of Doctor in Philosophy
by

Ciarán Seoighe

Physics Department
Trinity College Dublin

January 2000

Declaration

This thesis is submitted by the undersigned for the degree of Doctor in Philosophy at the University of Dublin.
It has not been submitted as an exercise for a degree at any other university.

Apart from the advice, assistance and joint effort mentioned in the acknowledgements and in the text, this thesis is entirely my own work.
I agree that the library may lend or copy this thesis freely on request.

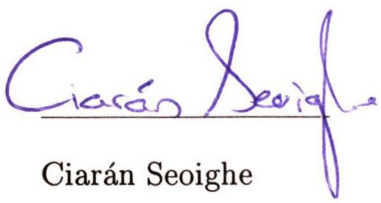

Ciarán Seoighe
October 1999

Acknowledgements

"If I have seen further it is by standing on the shoulders of Giants"

Sir. Isaac Newton

Over the four years of this thesis work Dr. I.V. Shvets has been an exemplary supervisor. We have spent many hours together discussing ideas to explain the myriad of weird and wonderful effects we have seen on magnetite. Igor's enthusiasm, dedication and the tremendous effort he puts into supervising, funding and looking after the welfare of his students is gratefully appreciated by all of us.

The instrumentation when I arrived was a *fait accompli* courtesy of Dr. A. Quinn. Aidan was always ready with advice and criticism and did a lot to improve this thesis. Thanks also to Dr. C. Durkan for all his wry comments in my formative years and to J. Naumann for starting the magnetite work. My mentor in the field of "dodgy" UHV techniques was Dr. J. Osing. Jürgen was always willing to discuss the problems I encountered because it made him happy he wasn't working with magnetite! S. Murphy has been a source of inspiration to me since he arrived because he has the ability to create something from nothing; STM tips, a preparation chamber and noise. I am repaying all G. Mariotto's help and hilarity over the past two years with the dubious pleasure of having to take over magnetite. Thanks to the lab ghosts (people whose circadian rhythms are independent of the sun) - originally F. Daly and now R. Kantor, S. Makarov and D. Kashanin. These men developed such intimate relationships with the lab computers that, together with the man who has everything, A. Gademann, they could fix just about any computer-related difficulties. A quick thanks to L. Seravalli for demonstrating that no matter how bad things are someone else can still be more miserable! To the recent recruits, V. Williams, W. Signac and D. MacMathuna, I wish all the best in their work. It has been great fun working with such a diverse bunch of people. But God, I hate foreigners. They take our jobs, our women....! The various members

of group D were always willing to lend a hand, especially R. Borges, A. Barry, J. O'Sullivan, P. Smith, T. Ní Mhíocain and countless others. Thanks to you all!

Within the physics department exists a body of people without whom this thesis would never have seen the light of day. The department staff have always been quick to help with any questions, in particular, Prof. I.T. McGovern, Prof. J.M.D. Coey and Dr. C. Beitia. D. Grouse is responsible for some wonderfully creative machining and for a particularly vindictive rumour... T. Burke has saved hosts of postgrads from ungodly administrative headaches and we're all grateful for this. J. Kelly processed all our photographs and still found time to invent "Seogy-bear"! The assistance of the departmental technicians, C. Smith, K. Concannon, J. Egan, P. Flanagan, J. McCauley and J. Kavanagh was gratefully appreciated. And a word of thanks to the secretaries, H. Hacket, N. Wynn, M. Duffy, E. Kavanagh and S. Murphy for all your work and especially Liz Gray for looking after our group so well.

Outside the lab there have been so many people involved in making the last four years such fun. As my mentor in life Judith (and the sisters of Murphy) has been invaluable. The coffee "harem" of Alison, Edwina, Naomi and Rowena were stalwarts for the cause. Thanks to the many sports/*Physoc*/pharmacy people and friends including, Andrew, Brian, Chrystelle, Colin, Maeve, Mary, Richard, Rosario, Simon, Suzanne, Vivienne and everyone else (you know who you are). I am grateful to Sophie for dragging me from the lab regularly to learn French, salsa and about real cuisine.

Finally my heartfelt thanks to my family. They are the backbone on which so much is based. Thanks Michael, Charlotte, Cathal, Deirdre, Anna, Bride and especially David (a.k.a Dots) for your unfailing support and patience.

The reasonable man persists in adapting himself to the world. The unreasonable man persists in adapting the world to himself. Therefore all progress depends on the unreasonable man.

George Bernard Shaw

Abstract

The (100) surface of magnetite (Fe_3O_4) has been studied using scanning tunneling microscopy (STM) in ultra high vacuum (UHV) with a view to establishing a test surface for spin polarised STM experiments. Two structured surface arrangements were found. The first was found to form after annealing in UHV at 970 ± 15 K for about 4 hours. This consists of cubic terraces with edges aligned along [110]. The terraces are separated by 2.0 ± 0.2 Å in the z-direction. This is twice the interplanar distance for magnetite (100) and implies that the observed terraces consist of a combination of octahedral and tetrahedral planes. However, this surface state is only metastable. Further annealing for a total of approximately 22 hours causes the surface to transform into another state. This state consists of rows running along [110] directions which rotate by 90° every 2.0 ± 0.3 Å in the z-direction. They have a width of 18 to 42 Å and are found to become generally narrower with increasing anneal time. The corrugation perpendicular to the direction of the rows is approximately 2.0 Å leading us to invoke the term nanoterrace to describe this structure. Once formed it persists until removed by mechanical polishing.

Atomic resolution images of both types of surface structure were obtained. Though it is difficult to distinguish between the Fe^{3+} and Fe^{2+} states in magnetite using the STM, we nonetheless present models which describe the atomic positions seen. They are justified on the basis of electron counting and charge balancing considerations.

Further experiments into the effect of iron deposition on the formation of the nanoterraces were begun. It would appear that depending on the amount of iron deposited and the pre-deposition anneal temperatures used on the

sample, the formation of nanoterraces may be assisted or hindered.

In the process of investigating iron growth on magnetite we found an unusual luminescent film to form on the surface after iron deposition and subsequent annealing to 970 ± 15 K in UHV. These films are easily removed by mechanical polishing. Amazingly the film was found to form again on the surface after polishing when the sample was annealed in UHV at 970 ± 15 K! This is without the deposition of any additional iron. Apparently the deposited film causes a cascade effect deep into the crystal which acts as a memory of the film.

Some preliminary results are presented on the effects due to an external magnetic field. Due to instrumental considerations the maximum field that can be applied at present is approximately 60 mT. Magnetostriction is the most striking feature seen in the STM due to the applied field. However, when a magnetic field of 60 mT was applied along the [110] direction some of the nanoterraces took on an unusual appearance that was not present when the magnetic field was switched off. The most likely explanation for this is that spin polarised tunneling may be responsible for the effect though the results are not conclusive due to instrumental limitations.

Publications

C. Seoighe, J. Naumann and I.V. Shvets. *"Studies of surface structures on single crystalline magnetite (100)" Surf. Sci.* **440**(1-2);116 (1999).

C. Seoighe and I.V. Shvets *"The formation of nanoterraces structures on the surface of magnetite (100)" Prob Mic. Lett.* Accepted for publication.

C. Seoighe and I.V. Shvets *"Memory of a deposited thin film deep within a crystal"* Submitted to *Nature.*

C. Seoighe and I.V. Shvets *"A model of the atomic structure of nanoterraces surface reconstructions on magnetite (100)"* Submitted to *Surf. Sci. Lett.*

I.V. Shvets, C. Seoighe, G. Mariotto, C. Beitia, and J.F. McGilp *"Effect of deposited thin film on bulk magnetite (100)"* In preparation for *Science.*

C. Seoighe, G. Mariotto and I.V. Shvets *"Surface stabilisation through electron balancing on magnetite (100)"* In preparation for *Phys. Rev. B.*

List of abbreviations

1D - one dimensional

2D - two dimensional

3D - three dimensional

AES - Auger electron spectroscopy

CMA - cylindrical mirror analyser

e-beam - electron beam

FIM - field ion microscopy(e)

GMR - giant magneto resistance

HOPG - highly orientated pyrolytic graphite

LDOS - local density of states

LEED - low energy electron diffraction

LTSTM - low temperature scanning tunneling microscopy(e)

MBE - molecular beam epitaxy

ML - monolayer

OD - outer diameter

PES - photoemission spectroscopy

PZT - lead zirconium titanate

RFA - retarding field analyser

RT - room temperature

RHEED - reflection high energy electron diffraction

RTSTM - room temperature scanning tunneling microscopy(e)

SPM - scanning probe microscopy(e)

SPSTM - spin polarised scanning tunneling microscopy(e)

SRO - short range order

STM - scanning tunneling microscopy(e)

STS - scanning tunneling spectroscopy

TiSTM - titanium scanning tunneling microscope

TSP - titanium sublimation pump

UHV - ultra high vacuum

XRD - x-ray diffraction

List of Figures

1.1 Stoner d band model of a ferromagnet 7

1.2 Potential diagram for two ferromagnets with insulating barrier 9

2.1 The vacuum system (plan view) 18

2.2 STM with electromagnet 20

2.3 Piezo arrangement used in the titanium STM walker 24

2.4 Walker spring arrangement 25

2.5 The scanner assembly arrangement for the titanium STM . . . 27

2.6 Large scale images of HOPG using the TiSTM 28

2.7 Atomic scale images of HOPG using the TiSTM 29

2.8 Resistive heater 32

2.9 Resistance V temperature curve for artificial magnetite 34

2.10 Hand-polishing apparatus 36

2.11 Loop technique for tip etching 40

3.1 Magnetite unit cell 47

3.2 Mizoguchi's patterns of magnetite 53

3.3 Surface unit cell of magnetite 58

3.4 Tasker's three ionic categories 61

3.5 The $\left(\sqrt{2} \times \sqrt{2}\right)$R45^o structure of magnetite by Kim 67

4.1 STM image of diamond particles on the magnetite surface . . 73

4.2 LEED image of structured magnetite surface 75
4.3 STM image of cubic terrace structures on magnetite 76
4.4 Large STM image of cubic terrace structures 77
4.5 Zoom in to area with saw-tooth edges 79
4.6 STM image of chemo-mechanically prepared magnetite 81
4.7 LEED image of reconstructed magnetite (100) surface 82
4.8 LEED image of regularly reconstructed magnetite surface . . . 83
4.9 STM of reconstructions on natural crystal 85
4.10 STM images of the formation of reconstructions 87
4.11 STM image of the onset of reconstructions 88
4.12 Atomic scale image of the onset of reconstructions 89
4.13 Larger image of the onset of reconstructions 90
4.14 Histograms of the reconstructions 91
4.15 STM images of reconstructions 92
4.16 STM images of reconstructions 93
4.17 STM of the range of reconstruction separations 94
4.18 A line profile of the corrugation along a nanoterrace 95
4.19 Atomic resolution image of magnetite (100) surface 98
4.20 Atomic resolution image of nanoterraces 99
4.21 STM of magnetite annealed in oxygen 106
4.22 STM of magnetite annealed in oxygen 107
4.23 STM of ion etched magnetite 108
4.24 STM of clusters from ion etching 109
4.25 Zoom-in of clusters from ion etching 110
4.26 STM using Fe/W tip 112
4.27 Anomalous surface structure 114

5.1 STM image of an atomic scale 11.8 × 11.8 Å structure 118

5.2 Atomically resolved square terrace 119
5.3 Software zoom in to tip change area 121
5.4 2D and 3D projections of atomic resolution 123
5.5 Line profiles of the A-lines and B-lines in fig. 5.4 124
5.6 STM image of fish-scale type structures 125
5.7 Effect of double tip on atomic resolution 127
5.8 A model of the atomic positions seen in fig. 5.4 130
5.9 Schematics of the octahedral and tetrahedral positions 133
5.10 Atomic resolution image of the nanoterraces 136
5.11 Atomic resolution images of the nanoterraces 137
5.12 Two atomically resolved images of the nanoterraces 138
5.13 Resolution of individual atoms 140
5.14 A high resolution image of nanoterraces 141
5.15 STM zoom-in image of the middle terrace seen in fig. 5.13 . . 142
5.16 A model of the atomic resolution image of fig. 5.15 145
5.17 A model of the formation of nanoterraces 146
5.18 STM image exhibiting atomic contrast reversal 151
5.19 Atomic orbitals at a tip end 152

6.1 STM image of wide rows due lapping machine 159
6.2 Onset of terraces after iron deposition 160
6.3 Cubic terraces after iron deposition 161
6.4 Square terraces even after 120 hours annealing 162
6.5 Formation of nanoterraces after iron deposition and annealing 164
6.6 Result of HV pulsing for tip conditioning 165
6.7 Coloured film 169
6.8 Coloured samples compared to normal magnetite. 170
6.9 SEM picture of the iron film on magnetite 172

6.10 Model 1 of the formation of coloured film 174
6.11 Model 2 of the formation of coloured film 176

7.1 Comparative STM images with and with out magnetic field . . 184
7.2 Magnetostriction in STM using iron tip on magnetite 185
7.3 Graph of magnetostriction in STM with non-magnetic tip . . . 186
7.4 STM of "low-density" nanoterraces 189
7.5 Line profiles of "low-density" nanoterraces 190
7.6 A close up of the "low-density" nanoterraces 191
7.7 Atomic resolution in 60 mT magnetic field 192

A.1 TiSTM full view 205
A.2 TiSTM head stage 206
A.3 TiSTM head 207

B.1 Schematic of LEED set-up 209
B.2 Example LEED image for calculations 211

C.1 A balanced unit cell of nanoterrace 214

List of Tables

3.1 Properties of iron oxides 45

6.1 Iron film deposition parameters 168
6.2 EDX of iron film on magnetite 173

7.1 Magnetostriction 186

Contents

1 Introduction **1**

1.1 Overview 1

1.2 Barrier tunneling 3

1.2.1 Scanning tunneling microscope 3

1.2.2 Spin polarised scanning tunneling microscope 6

1.2.3 Experimental results so far 11

1.2.4 Experimental difficulties 13

1.3 Conclusion 14

2 Experiment **15**

2.1 Overview 15

2.2 The vacuum system 17

2.2.1 The preparation chamber 17

2.2.2 The STM chamber 17

2.3 Equipment 19

2.3.1 Room temperature STM 19

2.3.2 Titanium STM 21

2.3.3 LEED/Auger 30

2.3.4 Resistive heater 31

2.4 Sample preparation 33

2.4.1 Polishing 35
2.4.2 UHV preparation 37
2.5 Tip preparation 37

3 Magnetite **42**
3.1 Historical background 42
3.2 Crystal structure 44
3.3 Verwey transition 48
3.3.1 Models 48
3.3.2 Nonstoichiometry 53
3.4 Bonding in magnetite 54
3.5 Electron counting and surface autocompensation 55
3.5.1 Electron counting on magnetite (100) 56
3.5.2 Charge balancing 60
3.5.3 Tapered termination theory 63
3.6 Surface characterisation work on magnetite 64
3.6.1 Fe_3O_4 (100) 65
3.6.2 Fe_3O_4 (110) 66
3.6.3 Fe_3O_4 (111) 68
3.7 Conclusion 69

4 Terrace-scale structures on magnetite **71**
4.1 Introduction 71
4.2 Results 72
4.2.1 Cubic terrace structures 72
4.2.2 Nanoterraces 80
4.2.3 Atomic resolution 97
4.3 Analysis 97

4.4 Conclusions 103
4.5 Other surface structures 104
4.6 A brief note about tip conditioning 113

5 Atomic scale structures **116**
5.1 Introduction 116
5.2 Metastable state 117
5.2.1 Results 117
5.2.2 Analysis 126
5.3 Nanoterraces 134
5.3.1 Results 134
5.3.2 Analysis 140
5.4 Contrast reversal 150
5.5 Conclusions 151

6 Iron growth experiments **155**
6.1 Introduction 155
6.2 Iron growth 156
6.2.1 Results 157
6.2.2 Analysis 163
6.3 Iron film induced transformation in the bulk 167
6.3.1 Results 167
6.3.2 Analysis 173
6.4 Conclusions 177

7 STM experiments with magnetic field **179**
7.1 Introduction 179
7.2 Magnetic investigations 180
7.2.1 Results 180

7.2.2 Analyses 193
7.3 Conclusions 196

8 Conclusions and further work **198**
8.1 Conclusions 198
8.2 Further work 202

A TiSTM Photos **204**

B LEED calculations **208**
B.1 Equations 208
B.2 Example 210

C Electron counting **213**

Chapter 1

Introduction

Science may be described as the art of systematic oversimplification.

Sir Karl Popper (1982)

1.1 Overview

The invention of the scanning tunneling microscope (STM) in the early eighties [1] opened up several new avenues of research in the field of surface science. For the first time since the advent of field ion microscopy (FIM) a new real space imaging technique of the atoms on the surface of a material was introduced. In conjunction with other techniques such as Auger spectroscopy and low energy electron diffraction (LEED) the STM proved to be a powerful tool for surface investigations. In the years following the inception of the STM an array of related techniques appeared. These included atomic force microscopy, scanning tunneling spectroscopy and magnetic force microscopy. Scanning probe techniques became standard practice for investigating a surface. To understand the importance of the STM one has merely to look at the number of companies now producing scanning tunneling microscopes

commercially. However, as with every field of scientific research the aim is to push the instrument to its limit and beyond. The STM was designed to image atoms. Now the intention is to take this further and image electronic spin.

In recent years attention has focused on the spin of electrons and the potential for further advances in electronic device miniaturisation. The driving force in the electronics industry is for smaller and smaller devices. It stands to reason that any new advance that could conceivably produce switches or transistors orders of magnitude smaller than at present will be researched extensively. And so it is with the polarisation of the electron spin.

Polarised electrons can be produced by a variety of means including, Mott scattering of electrons by nuclei, exchange scattering of electrons by polarised atoms, high energy electron-electron scattering, photon-electron (Compton) scattering, photo-ionisation of atoms, rf discharges (Penning ionisations), photo-, field-, or secondary electron emission from magnetic materials and spin-flip due to synchrotron radiation in high energy accelerators. In the case of magnetic materials spin polarised photoemission is used to provide information on the electronic structure [2]. Indeed, magnetite has been investigated on numerous occasions by spin polarised photoemission amongst others [3–5]. Mott scattering [6, 7] is used to measure the degree of polarisation in this and many other techniques. Spin polarisation has also been observed by tunneling, giant magnetoresistance (GMR) and optical pumping means. Essentially these systems consist of three consecutive layers; magnetic, non-magnetic and magnetic again. However, in the case of tunneling the non-magnetic layer is in fact a tunneling barrier. This is known as a tunnel junction. One interesting variation is the combination of a scanning tunneling microscope and a system for optical pumping as used by Alvarado

et al. [8]. In this thesis we are interested in direct spin dependent tunneling with a STM so we will not dwell on the other techniques.

The existence of a spin dependent tunnel current was first demonstrated in 1971 by Tedrow and Meservey [9]. They used a layered ferromagnet-oxide-superconductor tunnel junction. Later, in 1975, Julliere [10] showed that spin-dependent tunneling could also be found in planar ferromagnet-insulator-ferromagnet tunnel junctions. By 1990 Wiesendanger *et al.* [11] had demonstrated spin polarised tunneling using a STM. This involved using a Cr (001) surface and a CrO_2 tip. Since then many attempts have been made to reproduce these findings though with little success. Other avenues have been investigated with two of the most promising being the surface of magnetite (Fe_3O_4) [12] and iron films deposited on transition metal surfaces [13,14]. In this thesis we have focused on the (100) surface of magnetite as a possible test surface for spin polarised STM (SPSTM).

The theoretical background to SPSTM has been well documented and we will develop this in the next section. We will begin with the quantum mechanical interpretation of STM and continue from there to SPSTM.

1.2 Barrier tunneling

1.2.1 Scanning tunneling microscope

It is only in the light of a quantum mechanical interpretation that the working of a STM can be understood. Classically speaking an object cannot cross a barrier if the energy available to the object is less than that required to overcome the barrier. On the quantum scale this is not the case. In essence this is the principle of STM. Quantum mechanically an electron has a non-zero probability of tunneling through a potential barrier which in classical

mechanics would be impenetrable. The electron can be described as a wave-function $\psi(x)$ which satisfies the 1-D Schrödinger equation

$$-\frac{\hbar^2}{2m}\frac{d^2}{dx^2}\psi(x) + U(x)\psi(x) = E\psi(x) \tag{1.1}$$

In the classically forbidden region i.e. where $E < U$ there exists a solution to 1.1 of the form

$$\psi(x) = \psi(0)e^{-\kappa z} \tag{1.2}$$

where

$$\kappa = \frac{\sqrt{2m(U-E)}}{\hbar} \tag{1.3}$$

is the decay constant. In the case of STM the potential barrier is related to the work function (ϕ) of the tip/sample combination. For this example the work functions of the tip and sample are taken, for simplicity, to be approximately equal. A more in-depth discussion on the effect the tip has on the potential barrier can be found in [15]. In STM ϕ is usually referred to as the barrier height as it reflects the local chemical nature of the surface. We can simplify the problem greatly by assuming the work functions of the tip and sample to be similar. Following the approach of Chen [16] we set the vacuum energy level as reference such that now the Fermi level (the upper limit of occupied states in a metal) E_F, is equivalent to -ϕ. At this point an electron may tunnel from the tip to the sample or vice versa. Applying a bias voltage (to either tip or sample) creates a net tunnel current in one direction from the states lying between $E_F - eV$ and E_F. The tunnel current is proportional to the number of states on the sample surface in the energy range eV

$$I \propto \sum_{E_n=E_F-eV}^{E_F} |\psi_n(0)|^2 e^{-2\kappa w} \tag{1.4}$$

where w is the height of the tip above the sample surface. If V is sufficiently small that the number of electronic states doesn't vary considerably within it

then 1.4 can be written in terms of the local density of states (LDOS) at the Fermi level. At a certain position x and energy E the LDOS of the sample, $\rho(x, E)$, is defined as

$$\rho_s(x, E) \equiv \frac{1}{\epsilon} \sum_{E_n=E-\epsilon}^{E} \mid \psi_n(x) \mid^2 \tag{1.5}$$

where ϵ is small. It is now possible to write the tunnel current in terms of the LDOS at the sample surface (i.e. $x = 0$) as follows

$$I \propto V\rho_s(0, E)e^{-2\kappa w} \tag{1.6}$$

As we have seen the image generated by the STM over a flat surface is a contour plot of the LDOS of the sample surface at the Fermi level. Therefore scanning a tip over a surface as in STM one sees an image of the LDOS which is generally regarded as being the surface "topography". However, the image obtained does not necessarily reflect only the positions of the atoms on the surface but also other electronic contributions. The contribution of the tip to the tunnel current is as important as that of the sample. The commonly accepted approach is to treat the tip and sample as having overlapping wavefunctions as done by Bardeen [17] for a metal-insulator-metal tunnel junction. In this case we can deal with the tip and sample separately rather than as a coupled system. By solving each of the two subsystems for the stationary Schrödinger equation and calculating the rate of electron transfer from one electrode to the other using time-dependent perturbation theory, Bardeen showed that the tunneling matrix element is determined by a surface integral on some separation surface which is between the two electrodes, $z = z_0$.

$$M = \frac{\hbar}{2m} \int_{z=z_0} (\chi^* \frac{\partial \psi}{\partial z} - \psi \frac{\partial \chi^*}{\partial z}) dS \tag{1.7}$$

where ψ and χ are the wavefunctions of the two electrodes. The probability of an electron tunneling from sample state, ψ, to tip state χ is given by Fermi's Golden Rule

$$P = \frac{2\pi}{\hbar} \mid M \mid^2 \delta(E_\psi - E_\chi) \tag{1.8}$$

where δ implies that only elastic tunneling is permitted, i.e. the energy of the tunneling electrons is conserved. As before we now calculate the tunneling current by summing over all relevant states and assuming the electron occupancies in each electrode follow the Fermi distribution. Working in the limit of low temperature and low bias we get

$$I = \frac{4\pi e}{\hbar} \int_0^{eV} \rho_S(E_F - eV + \epsilon)\rho_T(E_F + \epsilon) \mid M \mid^2 d\epsilon \tag{1.9}$$

where ρ_s and ρ_T are the LDOS of the sample and tip respectively. Thus we see that a STM image is a convolution of the tip and sample LDOS.

1.2.2 Spin polarised scanning tunneling microscope

To see how this works we must examine the Stoner model for the d band of a ferromagnet (fig. 1.1). The exchange energy shifts the relative positions of the spin up and spin down parts of the density of states at the Fermi level. It can be deduced that this difference in the density of states at the Fermi level for the different spins will lead to an asymmetry in the current-voltage (I-V) characteristics of the junction. This was seen by Tedrow and Meservey in an Al-Al_2O_3-Ni tunnel junction arrangement [9]. The Al is superconducting at low temperatures and the discovery that Zeeman splitting of a superconducting thin film leads to two BCS-type density-of-states curves split by $\pm\mu H$ in the presence of a strong magnetic field, H (where μ is the electron magnetic moment) led to the belief that this junction arrangement would lead to an

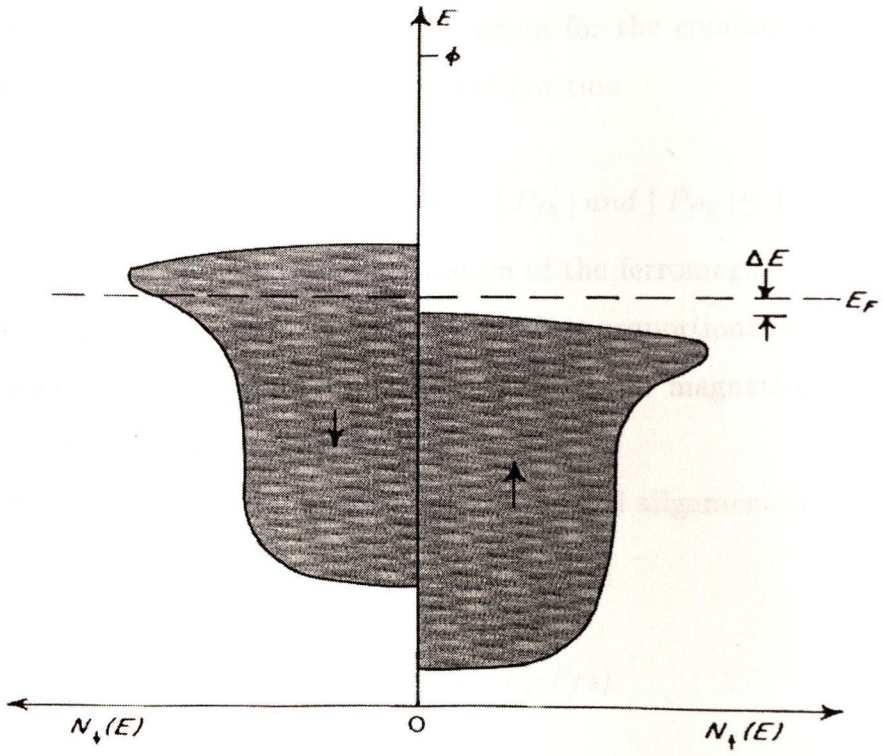

Figure 1.1: Stoner d band model of a ferromagnet. The majority spins are in a filled band slightly below the Fermi level.

asymmetry in the observed tunnel current. This was confirmed experimentally. A similar result was also observed by Julliere [10] and Maekawa [18] though in this case the arrangement was a planar ferromagnet-insulator-ferromagnet tunnel junction. To explain these results Slonczewski [19, 20] examined the theoretical case of a tunnel junction with two ferromagnetic electrodes. Using the free-electron model in the limit of small bias voltage, Slonczewski derived the following expression for the conductance σ of the ferromagnet-insulator-ferromagnet tunnel junction

$$\sigma = \sigma_{fbf'}(1 + P_{fb}P_{f'b}cos\theta) \quad | P_{fb} | \; and \; | P_{f'b} | \leq 1 \tag{1.10}$$

where P_{fb} is the effective spin polarisation of the ferromagnet-barrier interface and $\sigma_{fbf'}$ is the mean conductance which is proportional to $exp(-2kx)$. The angle θ is the angle between the directions of magnetisation of each ferromagnetic electrode (fig. 1.2)

For the special cases of parallel and antiparallel alignment of the internal fields (i.e. $\theta = 0$) we get

$$\sigma_{\uparrow\uparrow} = \sigma_{fbf'}(1 + P_{fb}P_{f'b}) \tag{1.11}$$

$$\sigma_{\uparrow\downarrow} = \sigma_{fbf'}(1 - P_{fb}P_{f'b}) \tag{1.12}$$

Putting these together and defining $P_{fbf'}$ as the effective polarisation for the whole tunnel junction we get

$$\frac{\sigma_{\uparrow\uparrow} - \sigma_{\uparrow\downarrow}}{\sigma_{\uparrow\uparrow} + \sigma_{\uparrow\downarrow}} = P_{fb}P_{f'b} \equiv P_{fbf'} \tag{1.13}$$

Prior to this we had been considering the tunnel current as dependent on the tip-sample distance, x, the local barrier height, ϕ, and the applied bias voltage U, i.e.

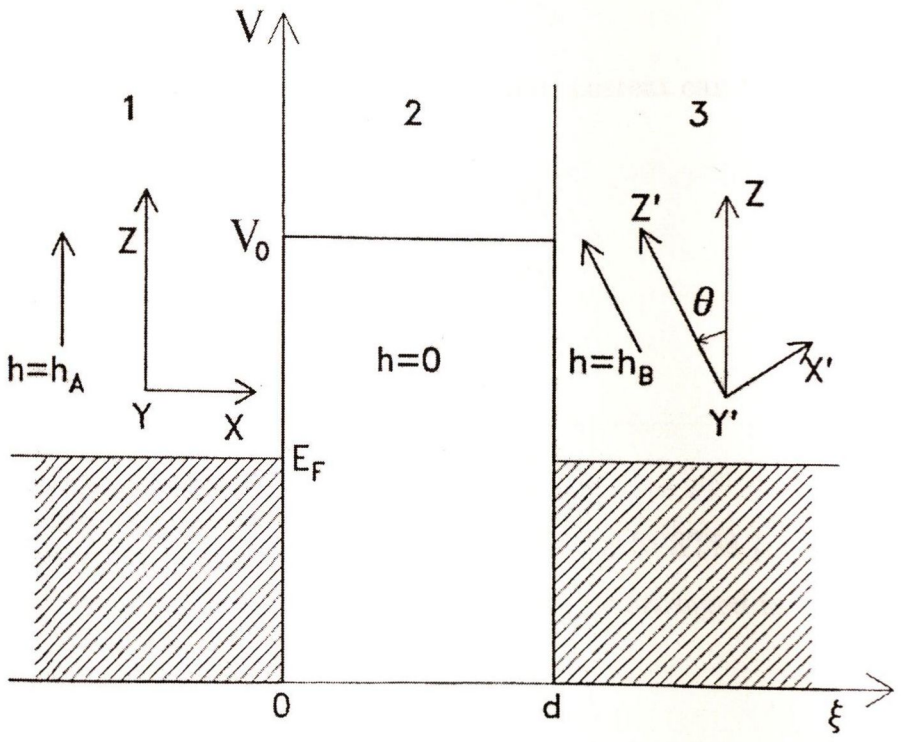

Figure 1.2: Schematic potential diagram for two metallic ferromagnets separated by an insulating barrier. The directions of magnetisation h_A and h_B form an angle θ.

$$I = I(x, \phi, U) \tag{1.14}$$

Now, however, we must add another term for the spin dependence of the tunnel current if magnetic electrodes are involved

$$I = I(x, \phi, U, \uparrow) \tag{1.15}$$

The effect of the polarisation on the tunnel current can be represented as

$$I_{\uparrow\uparrow} = I_0(1 + P) \tag{1.16}$$

$$I_{\uparrow\downarrow} = I_0(1 - P) \tag{1.17}$$

Rearranging 1.16 and 1.17 we get

$$P = \frac{I_{\uparrow\uparrow} - I_{\uparrow\downarrow}}{I_{\uparrow\uparrow} + I_{\uparrow\downarrow}} \tag{1.18}$$

In constant current mode the only variables for SPSTM (i.e. total height change, Δs and the local barrier height, ϕ) can be arranged in the form [15]

$$P = \frac{exp(A\sqrt{\phi}\Delta s) - 1}{exp(A\sqrt{\phi}\Delta s) + 1} \tag{1.19}$$

with A = 1.025 $eV^{-1/2}Å^{-1}$.

The results of Slonczewski's calculations were developed further in a paper by Minakov and Shvets [21]. They showed theoretically that a magnetic tip can be used to determine the spin directions of surface magnetic ions with atomic resolution. Furthermore they speculated that an antiferromagnetic tip could also be used and might even be superior to ferromagnetic tips in that they would not influence the studied surface through magnetostatic interactions. Three main predictions for experimental results came from this paper.

1) If there are filled, high-energy s band electronic states (which are non-magnetic) then most of the tunneling will be from these with a consequent reduction in the polarisation. 2) If the tunneling current from a magnetic ion is significantly less than that from a non-magnetic ion then the corrugation will be almost independent of the angle between the tip magnetisation direction and the spin direction of the magnetic species and 3) the atoms at the end of the tip must be ordered ferromagnetically or antiferromagnetically and there must be a sufficient number of atomic layers to scatter the tunneled electrons at the tip end. Minakov and Shvets also predicted that a chromium STM tip could be used as a candidate for SPSTM.

1.2.3 Experimental results so far

To date a number of articles have been published claiming spin polarisation with a scanning tunneling microscope. Excluding the methods involving optical pumping of III-V semiconductors there are two main approaches taken to achieving SPSTM. One is to use the intrinsic properties of certain tip and sample materials and the other is to use an external magnetic field to create identifiable oscillations in the tunnel current.

No external magnetic field

This approach utilises the unique magnetic properties of certain materials. Two of the most interesting results published so far have been obtained using a CrO_2 tip on the Cr(100) surface [11, 22] and using an iron tip on the Fe_3O_4 (100) surface [12]. However, neither experiment has been reproduced successfully to date. The former experiment was based on the assumed antiferromagnetic arrangement of the terraces on the Cr(100) surface which is far from being reliably proven. The terraces of this surface are thought to be

alternately magnetised when separated by monatomic steps. It was claimed that when using a magnetic tip the terrace steps alternated periodically in height thus indicating a degree of spin polarisation. The terraces steps on Cr(100) are separated by 1.4 Å. The terraces seen by Wiesendanger *et al.* were seen to alternate between 1.2 Å and 1.6 Å when a CrO_2 tip was used.

In the latter experiment the results of scanning the (100) surface of magnetite with a tungsten tip were compared with those resulting from scanning with an iron tip. A 12 Å periodicity was noted when using the iron tip which could not be detected with the non-magnetic tungsten tip. By comparing this with contemporary models of the surface Wiesendanger *et al.* associated the extra corrugation with the periodic arrangement of Fe^{2+} and Fe^{3+} ions on the surface. These ions have different spin configurations and hence might be expected to yield different values of the tunnel current with a magnetic tip. We will return to this result in chapters 5 and 7.

External magnetic field

The magnetisation of a sample could be modulated by the application of an external ac magnetic field. This could result in alternating parallel and antiparallel alignment of the tip and sample magnetisation directions. An advantage to this approach is that a lock-in amplifier could be used to improve the signal-to-noise ratio. Initial experiments using an external magnetic field have been performed by Johnson and Clarke [23] and values obtained for the local effective polarisation.

More recently, however, two further approaches to demonstrating SP-STM have been published. Bode *et al.* [24] have demonstrated SPSTM on Gd(0001) thin films using ferromagnetic probe tips in a low temperature STM. By tunneling into the exchange split surface state of Gd(0001) Bode

et al. demonstrated an asymmetry in the differential tunneling conductivity at bias voltages corresponding to the energetic positions of the two spin contributions of the exchange split surfaces in an external magnetic field. Magnetic contrast was obtained from this spectroscopic data. However, this method is limited by long data acquisition times and the need for surfaces with an exchange split surface state.

The second approach to SPSTM was recently published by Wulfhekel and Kirschner [25]. In this experiment the tip magnetisation is periodically changed and a lock-in amplifier used to detect the resulting change in tunnel current. The frequency of oscillation of the tip is much greater than the response time of the STM controller feedback. With this arrangement it was possible to simultaneously obtain and distinguish between the topographic and spin-dependent components of the tunnel current. Magnetic domain structures were imaged on polycrystalline Ni and Co(0001) surfaces. However, the minimum lateral resolution, which can only be determined by domain wall widths, is so far limited to some tens of nm.

1.2.4 Experimental difficulties

There are a number of fundamental difficulties with SPSTM experiments on bulk single crystals. The first of these is the magnetostriction of the sample when an external magnetic field is applied. This results in two main complications. Firstly, there is considerable movement of the surface under the tip (on the atomic scale) thereby making it impossible to directly observe the effect of turning on and off a relatively strong (50 mT) magnetic field on the local atomic structure. Secondly, due to the movement of the sample the magnetic field can only be changed slowly otherwise the tip will not be able to withdraw quickly enough and there would be a tip-crash.

Another experimental complication is the tip end. There is no way to know the exact tip geometry at the end in the present set-up. Therefore there is no knowledge of the magnetic orientation of the tip. Ferromagnetic tips such as iron or iron deposited on tungsten, would result in an extra tip-sample interaction due to the magnetostatic field. Antiferromagnetic probes are therefore preferred because, unlike using ferromagnetic probes, the surface is not influenced by the magnetostatic field [21].

1.3 Conclusion

In conclusion it would appear that there are a significant number of theoretical arguments for the use of magnetic probes in STM to investigate magnetic structure on the atomic scale. However, the experimental results to date are not fully comprehensive.

In this work we are following on from previous experiments by Wiesendanger *et al.* [12] on the possibility of using magnetite (100) as a test surface for spin polarised experiments. The crystallographic structure of magnetite will be developed further below but in brief it seems that at both the atomic and the terrace scales magnetite is a good candidate for spin polarised effects. On the atomic scale the two iron valences (2+ and 3+) were imaged by Shvets *et al.* [26] with atomic contrast using an iron tip. However, even in this case there was no clear atomic resolution, only some corrugations along atomic rows separated by $\sim$ 12 Å. The second potentially interesting feature for spin polarised experiments is the alternating arrangement of tetrahedral and octahedral iron planes in the [100] direction. It is conceivable that the experiments of Wiesendanger *et al.* on chromium could be repeated for the case of magnetite.

Chapter 2

Experiment

"I hear...I forget; I see...I remember; I do...I understand"

Confucius, c. 500 BC

2.1 Overview

The main thrust of the results presented here comes from STM experiments which were performed at room temperature in ultra high vacuum (UHV). These data are supported by LEED results and Auger electron spectroscopy (AES). In order to study a surface on the atomic scale it is necessary to first clean the surface and then to maintain this cleanliness for extended periods - long enough to perform the experiments. A number of different approaches are available for preparing clean surfaces including argon sputtering, in-situ cleaving of the sample, oxidation and subsequent electron-beam heating. However, by far the most common method is annealing. Vacuum is necessary in order to maintain a clean sample surface long enough to perform STM experiments. For example, at 1000 mbar one monolayer of nitrogen will be deposited on the surface in a matter of nanoseconds. At a pressure of

10^{-11} mbar this can take up to 60 hours.

Although extremely efficient at maintaining a clean surface the use of vacuum presents a host of challenges to the user. There are very strict conditions to be complied with. The range of materials one can use for apparatus within the vacuum system is restricted. All samples and materials placed in the vacuum must be free of grease or other non-UHV compatible contaminants. Ideally "dirty" processes such as sample preparation should be kept separate from "clean" ones like STM experiments. As a result the apparatus tends to be an arrangement of interconnecting vacuum chambers each dedicated to a different process. This is the vacuum system.

The vacuum is maintained by a series of pumps. From atmosphere a roughing pump backing a turbomolecular pump is used. Once the pressure has dropped to the order of $\sim 10^{-6}$ mbar the ion pumps can be used. These pumps are used to maintain a pressure of the order of $\sim 10^{-10}$ mbar. This pressure can be reduced further by use of a titanium sublimation pump encased in a cryoshroud. The cryoshroud is cooled using liquid nitrogen. Using this pump a pressure in the low 10^{-10} to mid 10^{-11} mbar can be achieved. For further details on the operating principles of these pumps see [27]. After being up at atmosphere the system is baked. This increases the rate of water desorption from the chamber walls so one can achieve UHV in a much shorter time. Baking is done using either heater tapes (in the case of the preparation chamber) or a bake-out tent with internal heaters (in the case of the room temperature STM chamber).

2.2 The vacuum system

The vacuum system used in these experiments was designed and built by Dr. I. V. Shvets, Dr. A. J. Quinn, Dr. J. Osing and S. Murphy. It consists of three interconnected chambers - a preparation chamber for tip and sample preparation, a room temperature STM chamber and a low temperature STM chamber (fig. 2.1). Each chamber can be valved off and brought up to atmosphere independent of the others. A fast entry lock is connected to the preparation chamber to facilitate tip and sample entry into the vacuum system. A tip or sample can be transferred from any one chamber to any other by means of a series of wobble-sticks and magnetic drives.

2.2.1 The preparation chamber

This chamber is dedicated to the more "dirty" processes of tip and sample preparation. Sample preparation is usually a combination of heating, film evaporation and/or argon ion sputtering. Tip preparation is usually limited to argon ion sputtering. The chamber is equipped with an electron-beam heater, a resistive heater, an argon ion gun, electron-beam evaporators (for deposition of Fe films) and precision leak valves for gas inlet. A quartz crystal monitor is used to monitor film growth. An upgrade of this chamber has recently been installed which also contains a cylindrical mirror analyser Auger system. The base pressure of this chamber is in the low 10^{-10} mbar range after baking.

2.2.2 The STM chamber

This chamber is dedicated to STM and LEED/Auger experiments. As well as an STM and a LEED/Auger system the chamber is also fitted with an

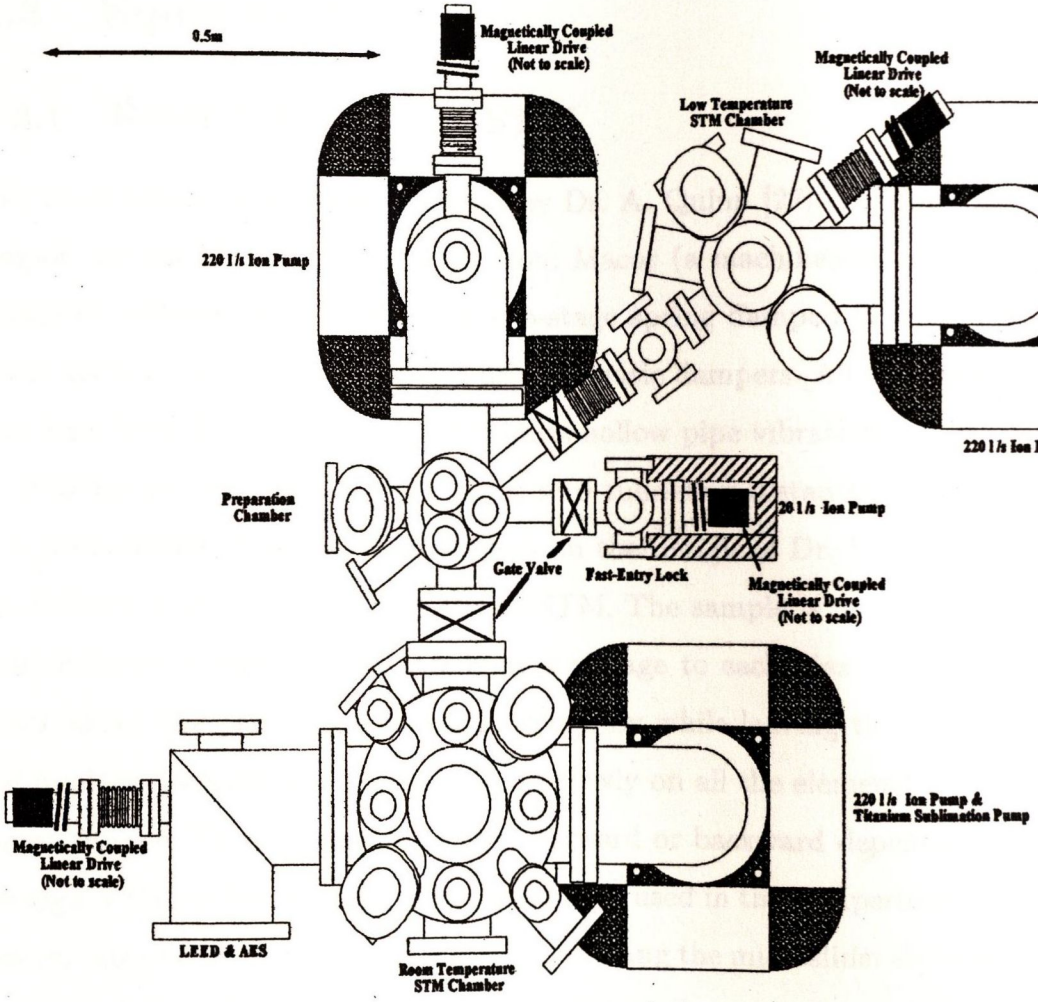

Figure 2.1: The vacuum system (plan view)

electromagnet and a tip and sample storage carousel. Tip and sample exchange is carried out using a pair of wobble-sticks. The pressure after baking is normally in the mid 10^{-11} mbar region.

2.3 Equipment

2.3.1 Room temperature STM

The room temperature STM was built by Dr. A. Quinn [27]. The base and support for the STM head are made from Macor (a machineable ceramic). Vibration isolation is by means of a two-stage spring damped system. The entire vacuum system can be floated on pneumatic dampers. All the support bars have been filled with sand to minimise hollow pipe vibrations.

The tip and sample can be brought into tunneling distances by means of a piezo-walker. A six-leg walker based on the design of Dr. S. H. Pan of the University of Basel is used in the RTSTM. The sample is mounted on a quasi-cylindrical sapphire rod. Applying a voltage to each piezo element in series causes the piezo elements to shear rapidly while leaving the sapphire rod in place. Relaxing the applied voltage slowly on all the elements at once moves the rod. The rod can move either forward or backward depending on the sign of the applied voltage. Three units were used in these experiments to control this movement with the most effective being the microslider electronic control unit from Omicron [28]. Further details on the operation and physics of the piezo-walker can be found in [29].

The STM uses a piezo tube scanner with outer electrodes quartered into; Z-X, Z-Y, Z+X and Z+Y. A voltage is applied to each quadrant by the STM controller in order to provide the required X, Y and Z movement of the scanner. The unit has a lateral dynamic range of $\pm$20600 Å and a vertical

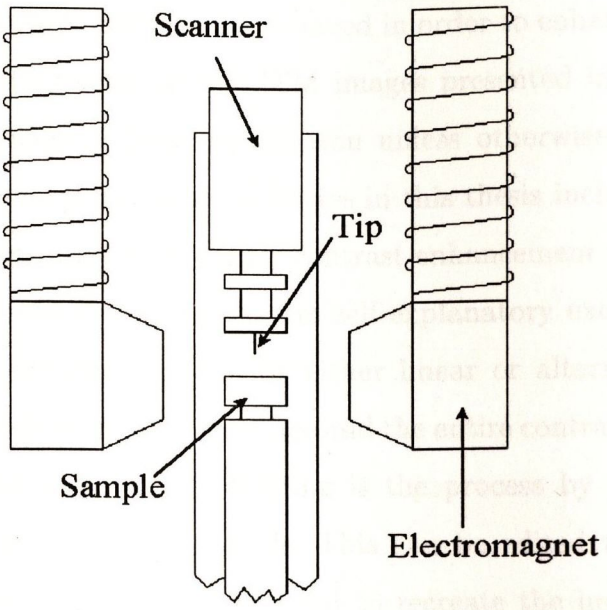

Figure 2.2: A schematic of the electromagnet around the STM

range of ±13000 Å. The former was calibrated on HOPG and the latter using monatomic steps on Cu (100). A commercial unit from WA Technology (TOPSII) is used to control the STM.

An in-plane electromagnet was designed and built by J. Naumann (fig. 2.2). It is made from Permanorm 5000 [30], Kapton-insulated copper wire and Kapton foil. A series of three internal thermocouples can be used to measure the temperature in the magnet. Although it is possible to cool the system using water or liquid nitrogen this would cause too much vibration during scanning and so could not be used. A field of 90 mT could be generated, parallel to the sample surface, without excessive heating ($\sim$ 35°C).

Data analysis was by means of the TOPSII software, an image processing package written by J. Naumann and A. Quinn and a commercially available package from NTMDT, Russia [31]. The most commonly used facility in image processing is plane subtraction. This is the means by which a global

slope on the sample or drift can be removed in order to enhance the contrast on the scale of the image (in the STM images presented in this thesis the only processing done is plane subtraction unless otherwise stated). Other features used in the preparation of images in this thesis include, smoothing, 3-dimensional presentation, zooming, contrast enhancement, fourier filtering and line normalisation. All of these are self-explanatory except for the last three. Contrast enhancement can be either linear or alternatively specific windows may be chosen within an image and the entire contrast range applied over this reduced area. Fourier filtering is the process by which a fourier transformation of the image is made. This can be edited to remove noise and then an inverse transformation used to recreate the image. Care must be taken when using this process not to invalidate the data by excessive filtering. Line normalisation is a means to view the full contrast range on each individual line in a scan. This can be particularly useful if there is, for example, a very high point in the scan which offsets the image contrast and makes it difficult to view other features of the scan. However, this must be offset against the information lost in the slow scan direction.

2.3.2 Titanium STM

The titanium scanning tunneling microscope (see photos in appendix A) was designed by Dr. I. V. Shvets and C. Kempf and modified and built by the author. The basic design is similar to the STM currently in use and described by Quinn [27] in detail. However, there are some very important modifications. The STM is designed to accommodate a microwave cavity which will be positioned around the tip-sample junction. This cavity will be used for future electron spin resonance experiments. An STM with a microwave cavity, though with different capabilities, has been built by Cohen and Wolf [32]. In

fact microwave induced effects on scanning tunneling techniques have been studied [33–36] in recent years with some success so far. In our case the cavity is suspended on two titanium rods (on either side of the STM scanner) and can be lifted up above the tip to facilitate tip and sample transfer *in situ.* Experiments with the cavity have not yet commenced. For these experiments a strong magnetic field is required. This is supplied by a Halbach-cylinder-type permanent magnet suspended above the STM on a linear drive system such that it can be lowered around the STM junction and removed for tip and sample transfer. The fields generated by the magnet can be as high as 270 mT.

Because of the magnetic fields involved care had to be taken in the production of this microscope that none of the components used were magnetic. As a result the previously used piezo scanners with nickel electrodes were replaced in this STM by scanners with non-magnetic silver electrodes. It is no longer possible to use stainless steel springs for vibration isolation. We found that after machining the steel became somewhat magnetic and therefore unsuitable for our applications. In place of stainless steel we used copper-beryllium springs made by Bywell Springs Ltd. [37]. The manufacture of these springs involves a complicated process of annealing in plaster in order to temper the springs so that they can withstand the bakeouts necessary for UHV work. The screws used on the STM head were made of aluminium (for M3 size) and of titanium (for M2 size). The washers are made from copper. The electrical wires used are kapton-coated copper wires of 0.15 mm diameter from California Fine Wires [38]. These are passed through Macor spacers on the spring support rings and down to UHV electrical feedthroughs from Caburn MDC [39].

Fine approach mechanism

As the distances involved in STM between the tip and sample are of the order of a few angstroms an automated fine approach mechanism is required. This is usually accomplished using a piezo walker.

The fine approach mechanism used for the TiSTM is based on the same six-leg piezo walker system as the RTSTM. The sample is mounted in a special holder on top of a cylindrical sapphire rod. This is the first main modification. Previously a quasi-cylindrical rod was used. Recent experiments by us [29] indicate that shearing all the piezos at once is a more efficient process for sample movement than sequential shearing. Furthermore, we originally used Macor pads on top of the piezos as contacts with the sapphire rod. These were found to wear down quickly and we now use alumina pads. The shearing piezos are no longer glued to one another. Instead a copper-beryllium foil is placed between each piezo element (fig. 2.3). This is helps to prevent any unwanted rotation of the sapphire rod during the small withdraw and approach sequences that occur in normal scanning sessions. Furthermore, by gluing to the protruding foil tabs instead of between the piezos the stack can be kept level. If such a rotation were to occur it would not be possible to reliably return to the required area. We have found that even when walking forward or backward at rates of up to 4 kHz over a distance of several centimetres there is very little rotation of the rod.

In the design of this walker it was thought that rotational motion might also be beneficial. Hence a second series of piezo elements was glued to the first with the shearing direction at right angles to them. Due to various mechanical restrictions (including the sample bias wire and the sample holder clamps) the rotation available is only of the order of 30-40 degrees in both the clockwise and anti-clockwise directions. This, however, would be sufficient to

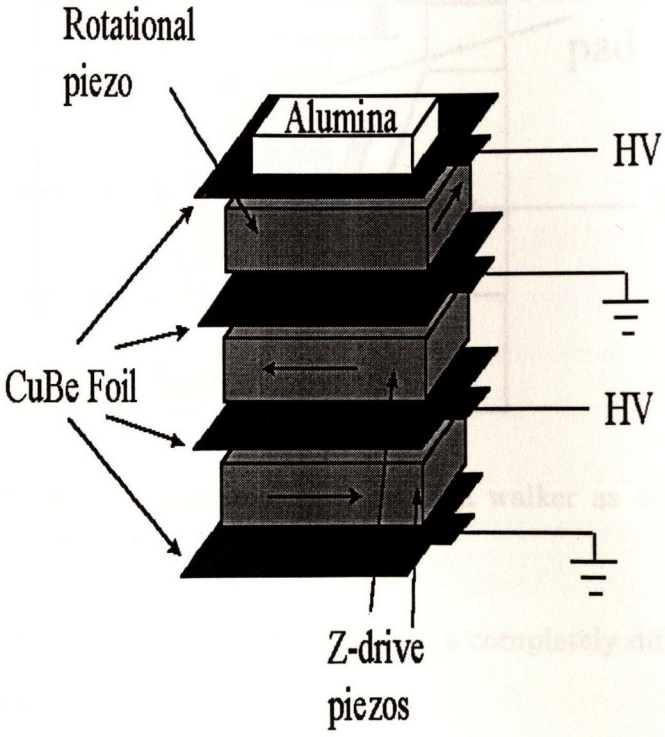

Figure 2.3: The piezo stack arrangement used in the titanium STM walker. The lower two piezo elements are for the forward and backward movement of the sample with respect to the tip. The upper piezo element is for rotational motion. Tabs on the sides of the CuBe foils are used to facilitate connection to the voltage lines.

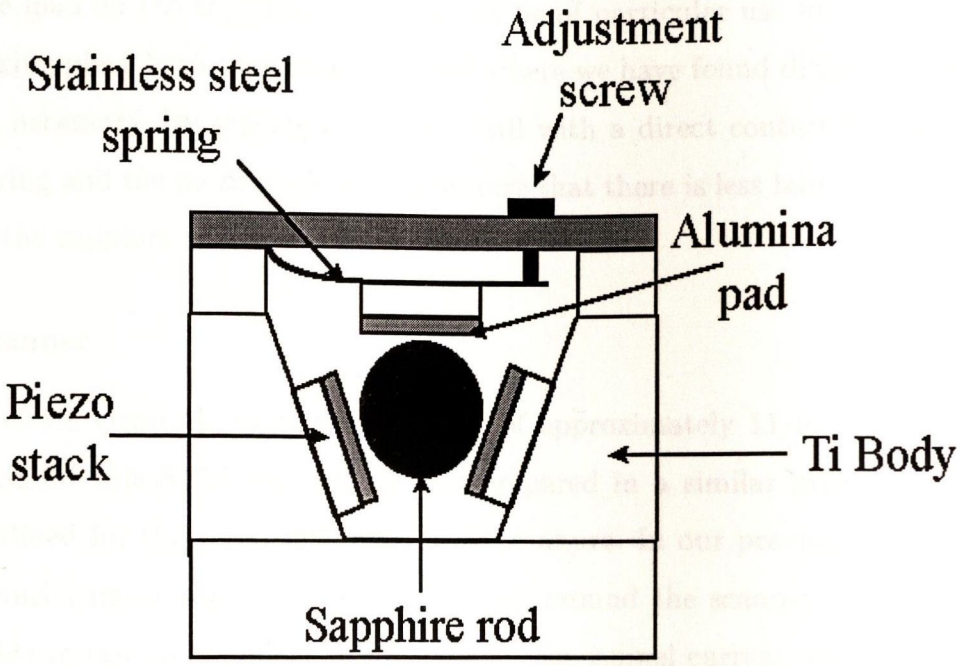

Figure 2.4: The novel spring arrangement for a walker as designed by the author.

move the sample (with respect to the tip) into a completely different area for STM experiments.

A further modification to the piezo walker previously used is in the spring system. In the original design (see [27] for further details and schematics) a spring is used to load the sapphire rod from one side. A block holds the piezo stack and this block is held in place by a ruby sphere glued to a copper-beryllium foil. If there were three ruby spheres then this arrangement would be more stable however, we have found that having only one sphere allows for too much undesirable motion of the sapphire rod leading eventually to a loss of walker efficiency. Instead of this arrangement we used the spring system shown in fig. 2.4.

The adjustment screw in fig. 2.4 can be used to increase or decrease

the load on the sapphire rod. This can be of particular use for experiments taking place both under air and UHV where we have found different loads to be necessary. By replacing the ruby ball with a direct contact between the spring and the piezo stack one can ensure that there is less lateral movement of the sapphire rod.

Scanner

A nickel electrode piezo tube scanner of approximately 11 mm length was used for this STM (fig. 2.5). It was prepared in a similar manner to that outlined for the room temperature STM above. In our previous design the tunnel current was brought from the tip around the scanner in a shielded cable to the pre-amplifier. In the TiSTM the tunnel current wire is brought through the tube scanner. The inner electrode of the scanner is grounded. This has been done to reduce the possibility of electromagnetic pick-up from the tube scanner during scanning. A copper-beryllium washer is glued to the end of the scanner and connected to the grounded inner electrode in order to shield the tip from the scanner. The tip holder assembly is considerably longer than in the room temperature STM. This is in order to facilitate tip sample transfer while the microwave cavity is in place. The disadvantage, however, is that this appears to make scanning more unstable due to the reduced resonance frequency of the tip with tip holder. This can be seen in the STM images obtained with this microscope on highly oriented pyrolytic graphite (HOPG) in air. Large scale images appear to be fine (fig. 2.6) but atomic resolution is more difficult to obtain and slower scan speeds are required. Using slower speeds creates drift which can be seen in fig. 2.7. This drift is probably more related to piezo-creep than to thermal drift. The noise on the right hand side is due to the tip dragging. It should be noted at this

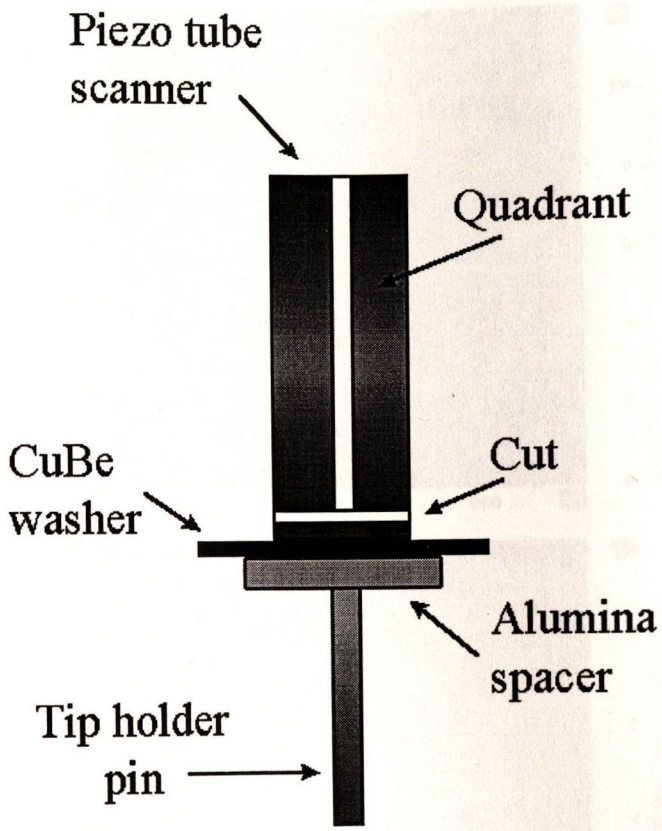

Figure 2.5: The scanner assembly arrangement for the titanium STM. The CuBe washer is glued to the part of the scanner below the cut and both are at ground for additional shielding. Two of the Z+X, Z+Y, Z-X and Z-Y quadrants are shown.

point that in these STM images and some of those to be presented in later chapters line profiles are given. These profiles relate to the unlabelled lines on the images. The lines are not labelled to avoid cluttering the images.

In normal operation the STM will be mounted inside an UHV chamber. This will eliminate the acoustic interference which was found to be significant for a STM placed on a bench in air. Once the microwave cavity has been fitted the length of the scanner will be optimised and this should improve

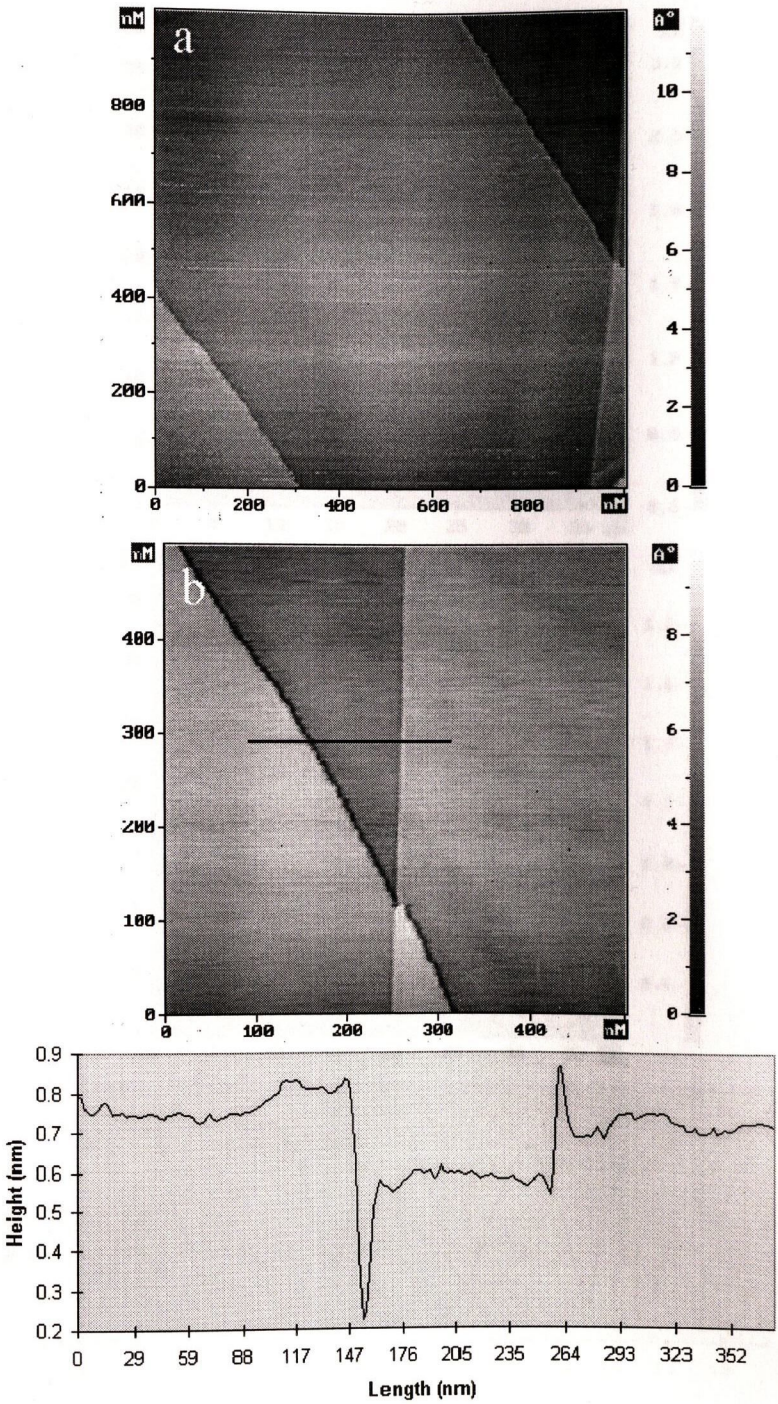

Figure 2.6: Two large scale images of graphite. A number of atomic steps can clearly be seen on both **a** and **b**. The line profile of the line marked on **b** is presented. For both **a** and **b**, V_{bias} = -50mV, I_{tunnel} = -0.15nA.

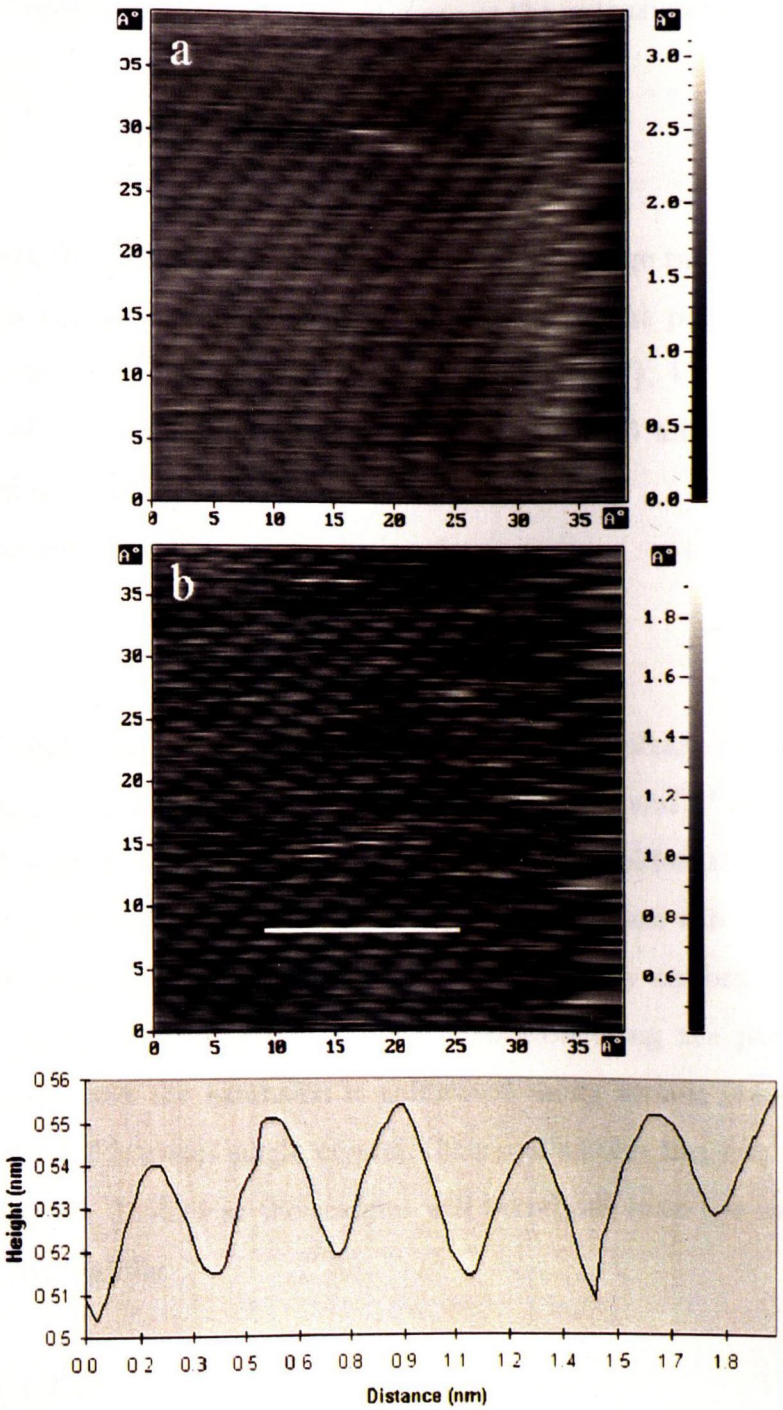

Figure 2.7: Atomic resolution images of HOPG with associated line profile. The upper image, **a**, has more drift/piezo creep than the lower, **b**, because the scan time was longer by about 35%. For **a**, V_{bias} = 50mV, I_{tunnel} = 100pA. For **b**, V_{bias} = 40mV, I_{tunnel} = 100pA.

the atomic resolution. With the present scanner the extension was calculated using

$$\Delta z = \frac{d_{31} V L}{h} \tag{2.1}$$

to be ±11,100 Å under application of the full Z-voltage range of ±140 V, where d_{31} is the piezo-electric coefficient (in this case the piezos used were EBL2 from Staveley Sensors [40] with d_{31} = -1.73 Å/V), V is the applied voltage, L is the length of the piezo scanner (11.7 mm) and h is the wall thickness of the scanner tube.

The lateral displacement was calculated using

$$\Delta y_{total} = \frac{\sqrt{2} d_{31} V L^2}{\pi D h} \left(1 + 2\frac{L'}{L}\right) \tag{2.2}$$

to be ±26,300 Å under application of the full X,Y-voltage range of ±60 V, where d_{31}, V, L and h are as defined for equation 2.1 and L' is the length of the tip-holder mount (including the pin for the tip holder, the tip holder and the tip itself) and D is the mean diameter of the piezo tube.

However, these calculation must be supplemented by calibrations. Normally the lateral displacement would be calibrated using the positions of graphite atoms and the extension is calibrated using atomic steps on the low index face of a metal single crystal. This calibration has not yet been performed on the TiSTM as the scanner will be rebuilt once the microwave cavity has been added.

2.3.3 LEED/Auger

The room temperature STM chamber is fitted with a reverse view four-grid LEED optics system from VG Microtech [41]. LEED measurements on

magnetite were taken at an energy range between 40 and 300 eV. Image capture was by means of a camera mounted on a tripod facing the LEED screen. From the images it is possible to calculate the lattice constant of magnetite. The equations used to calculate the lattice parameter from the photographs are developed in appendix B.

By rearranging the grid potentials it is possible to use the LEED optics as a retarding field analyser for Auger electron spectroscopy experiments. A 2.375 kHz sine wave is superimposed on the retarding potential. A lock-in amplifier is used to tune to the second harmonic of the modulation frequency. However, the data from this Auger set-up are of limited value due to unstable electronics, narrow energy ranges, etc.

2.3.4 Resistive heater

In this series of experiments the resistive heater was the most significant sample preparation instrument (fig. 2.8). This device is designed to hold samples either facing up (for argon ion sputtering) or facing down (for iron evaporation). For the most part the samples were annealed face down because this would give a more uniform heating. The heater filament is a coil of tungsten wire wrapped around an alumina crucible into which spiral grooves have been cut. Inside the crucible is a metal (tantalum) insert for holding the sample holder. Temperatures in excess of 1000 K can be achieved using this heater. A K-type thermocouple attached to the metal insert is used both for temperature measurement and ion current measurement during sputtering.

The temperature of the heater is controlled by a programmable power-supply. A program written by Yuri Kresnin allowed for precise control of the heater power over extended times. Using this program it was possible to maintain the required level of heating by continually checking the power

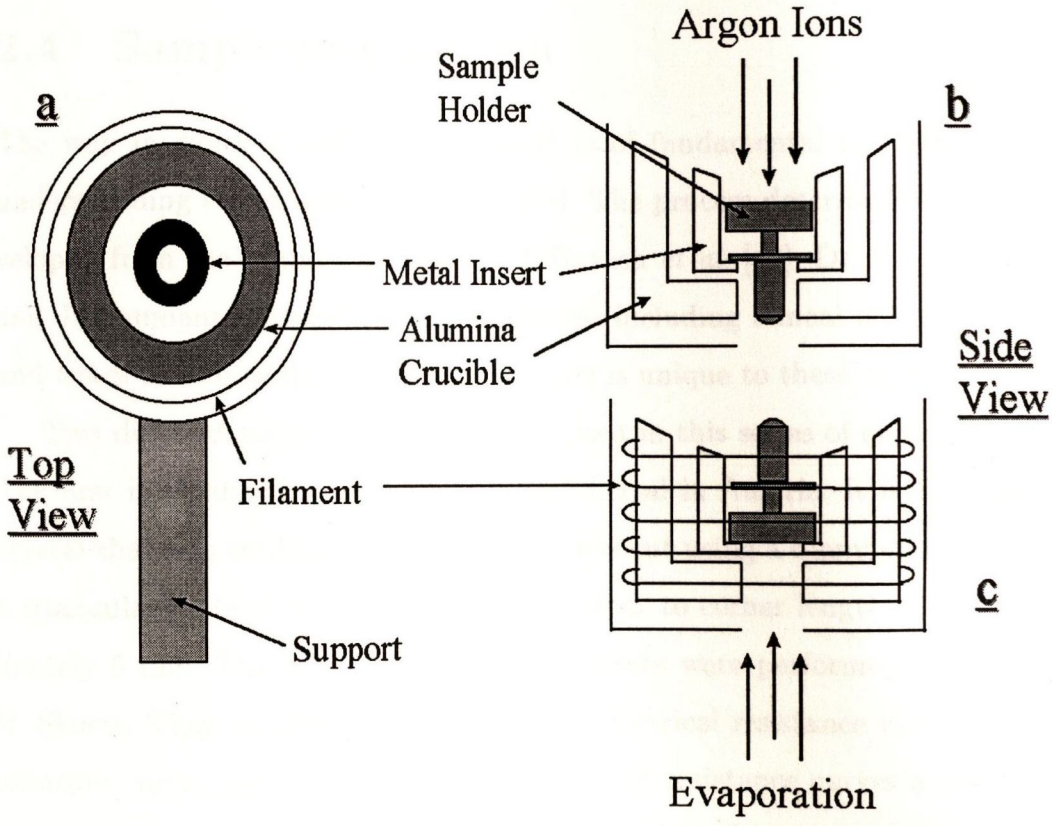

Figure 2.8: The resistive heater shown in top and side view. The sample holder can be placed either face up (for argon sputtering) or face down (for iron evaporation).

output of the power-supply and adjusting the current as necessary. Checks of the power output were carried out every few minutes over periods of several hours and so we can be confident that variations in temperature were minimised.

2.4 Sample preparation

The way in which a sample is prepared is of fundamental importance in understanding the structures seen in STM. The process described below developed from the initial experiments of Tarrach *et al.* [42], Dr. I. V. Shvets and J. Naumann. However, the final process including anneal temperatures and times as well as the polishing procedure is unique to these experiments.

Two different magnetite crystals were used in this series of experiments. The first is a natural single crystal from Zillertal in Austria. It is the same crystal that was used by Tarrach *et al.*. It was cut using a diamond saw into a triangular plate of thickness 2 mm and corner to corner length of approximately 5 mm. The initial *ex situ* measurements were performed by Dr. I. V. Shvets. They included acquisition of the electrical resistance versus temperature curves and X-ray diffraction. From the resistance curves a Verwey transition temperature [43] of 98 K was observed. As the expected transition temperature is between 115 K and 124 K [42] this indicates some degree of off-stoichiometry in the natural crystal. This could be explained by an iron deficiency of about 0.5 % [44] or by the presence of bulk impurities.

The second sample is an artificial single crystal fabricated by Prof. Honig [45]. Nuggets of this crystal were sent to RTI, Germany [46] to be cut along the [100] direction and polished. These samples are approximately 1.2 mm thick and have a diameter of about 5 mm. The crystals were polished by

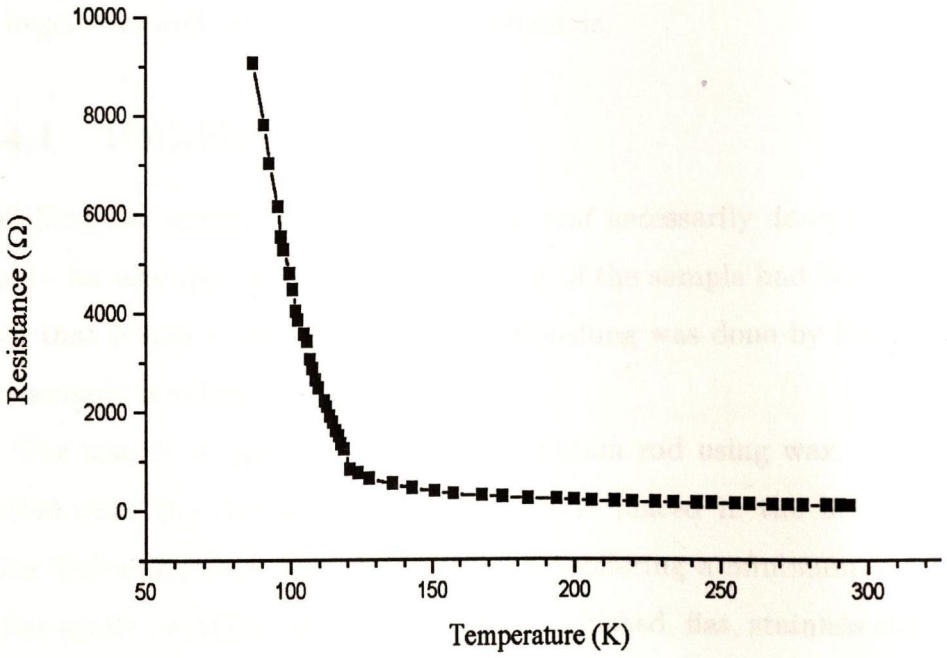

Figure 2.9: Resistance versus temperature curve for an artificial magnetite crystal. There is a sharp decrease in resistance at approximately 117 K as expected for stoichiometric magnetite.

RTI using a chemo-mechanical method. Details of this procedure could not be obtained from RTI for reasons of trade security. In this case we could not rely on this method of polishing and it was not used by us again. The cut crystals were characterised by RTI and miscuts of between $\pm 0.1^o$ and $\pm 1^o$ were reported. Resistance versus temperature measurements were performed by the author (fig. 2.9) and a Verwey transition temperature of approximately 117 K was determined thereby indicating that the artificial crystals are low in impurities and almost ideally stoichiometric.

2.4.1 Polishing

Polishing the sample was very important and necessarily done on a regular basis - for example, after iron deposition or if the sample had been annealed such that it had formed another oxide. Polishing was done by hand using a home-made levelling device (fig 2.10).

The sample is mounted onto the aluminium rod using wax. The wax is melted onto the rod and then the sample is placed in the hot wax. The three Teflon legs keep the device level while offering a minimum of friction. A fine grade polishing cloth is stuck onto a polished, flat, stainless steel base. Diamond paste is put on the cloth. Three grades of paste were used; 3 μm, 1 μm and 0.25 μm. A separate polishing cloth was used for each of these. Isopropyl alcohol was used as a lubricating agent during polishing. Polishing times of the order of hours were found to be necessary. After polishing, the samples were removed from the aluminium rod and cleaned in an ultrasonic bath using ethanol. Ultrasonic cleaning was performed in a plastic container to minimise the risk of scratching the polished surface. Similarly only plastic tools were used while handling the sample.

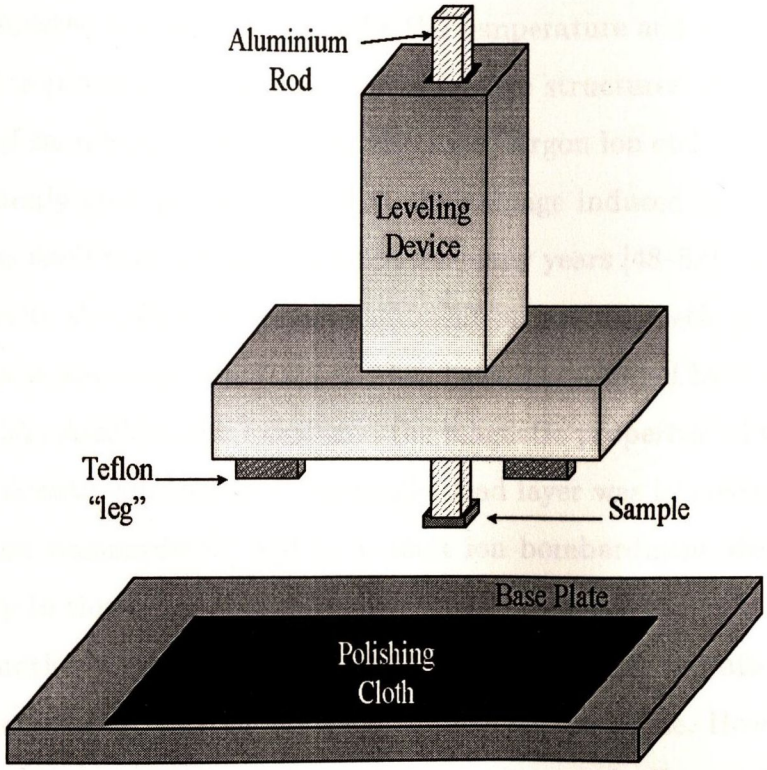

Figure 2.10: The apparatus used for polishing the samples. The pressure applied to the sample was controlled by pressing down on the top of the aluminium rod.

2.4.2 UHV preparation

Before investigating the sample surface with STM it must be cleaned. A number of different techniques are available for this and some of these have been discussed by Musket *et al.* [47]. In this series of experiments most of the sample preparation was done using the resistive heater described above. As will be discussed in chapters 4, 5 and 6 the temperature and anneal time are of critical importance in the formation of surface structures. However, other methods of sample preparation were also used. Argon ion etching the surface is a commonly used procedure. In fact the damage induced by sputtering a surface has itself been a topic of interest for many years [48–53]. In particular for magnetite the effect of ion bombardment on the magnetic properties of the surface is also very important and has been investigated by Aeschlimann *et al.* [54,55]. Aeschlimann found that the magnetic properties of the surface were significantly affected (a magnetically dead layer was formed on the surface) by ion bombardment and as a result ion bombardment was not used extensively in this series of experiments. *In situ* cleavage of single crystals in UHV is another method of preparing clean surfaces. This was attempted by Wiesendanger *et al.* [56] for the (100) surface of magnetite. However, they found that cleaving the crystals resulted in microscopically rough surfaces. This could be determined by the absence of sharp LEED spots and from the STM results.

2.5 Tip preparation

As one might expect the preparation of atomically sharp tips for STM is both difficult and important. The sharpness of the tip is a significant factor which affects the resolution of a STM [57–59]. Furthermore, a variety of different

material properties were required for this series of experiments including antiferromagnetism (MnNi tips), non-magnetic properties (PtIr and W tips) and of course stability.

A number of different methods are used for preparing sharp tips including grinding [1], mechanical cutting with a snips [60], controlled crashing [61], field emission/evaporation [62–64], ion sputtering [65, 66], fracture [67] and electrochemical polishing/etching [68–70]. Different methods are more appropriate to different tip materials. In this series of experiments we used tungsten, platinum-iridium, manganese-nickel, iron and iron deposited on tungsten tips. The method of preparation of each of these is outlined below.

Tungsten

Tungsten is by far the most commonly used tip material in this thesis. However, the method of preparation is long and tedious. In 1990 Ibe *et al.* [71] published a paper detailing an electrochemical preparation procedure for tungsten. They used 2 M NaOH in a beaker surrounded by a stainless steel foil. The tungsten wire is placed in the centre of the beaker and acts as the anode. Etching occurs at the air/electrolyte interface when a positive voltage is applied to the wire. The wire gradually thins at the interface as the tungsten dissolves to form soluble tungstate (WO_4^{2-}) anions thus producing a neck. When the neck is sufficiently small the weight of the wire in the solution snaps the wire leaving a sharp tip. However, Ibe *et al.* found that a rapid cut-off of the applied potential is critical for the formation of a sharp tip. As a result they built a high speed device for cutting off the potential which is based on the changing current detected. A similar device was built by Pat Flanagan and calibrated by the author. Calibration involves etching many tips with identical diameter (0.5 mm) and similar lengths in the etch

solution and determining the current detected immediately prior to drop-off.

After electrochemically etching the tip it is brought into UHV and bombarded with argon ions. The sputtering starts with 2 kV of accelerating potential. This is used for about 20 minutes and then the potential is reduced to 1 kV for a further 10 minutes. Finally a potential of 0.5 kV is used for the last 5 minutes. Such sputtering was shown by Biegelsen *et al.* [65] to produce 10 atomically sharp tips out of every 11. This compares favourably to 3 out of 16 from electrochemical etching alone. The ion bombardment is known to remove oxide layers and thought to improve tip shape.

Platinum-iridium

The preparation of Pt-Ir tips is the most straightforward and also the most imprecise. The basic method is to mechanically cut a Pt-Ir wire at an acute angle using a very fine wire cutters while simultaneously drawing the cutters from the wire. A wire of 0.25 mm diameter was used. The tip can be investigated using an optical microscope for an approximate degree of sharpness. As Pt-Ir does not oxidise it can be used for experiments in air and ion sputtering is not required. However, these tips have been found to be less stable and less likely to produce atomic resolution.

Manganese-nickel

Manganese-nickel is an antiferromagnetic material. As has been suggested by Minakov and Shvets [21] and Molotkov [72] an antiferromagnetic material is ideally suited to spin polarised STM experiments in that magnetostatic interactions between tip and sample are minimised. For this reason these tips are of significant interest in this work.

A form of electrochemical etching based on the "loop" technique [73]

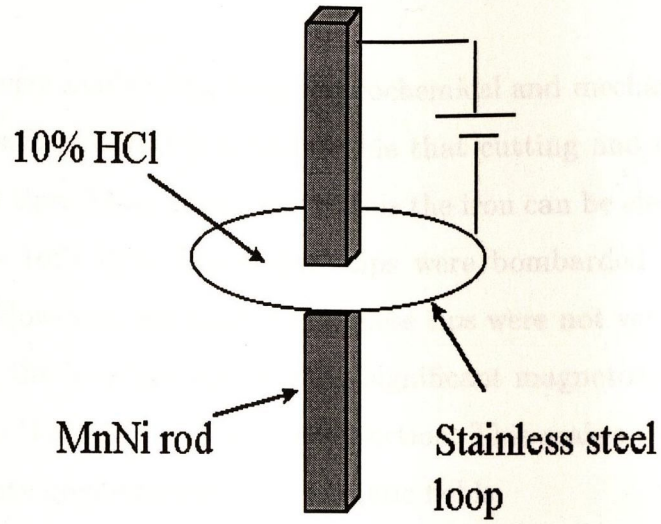

Figure 2.11: The "loop" technique used by Shane Murphy to produce atomically sharp MnNi tips. The etchant is 10% HCl and a potential of between 1.25 and 2 V was used.

was used by Shane Murphy to produce atomically sharp Mn-Ni tips [74]. In contrast to the electrochemical method used for tungsten, the stainless steel foil is replaced by a stainless steel loop (fig. 2.11). The 10% HCl etchant is suspended by surface tension inside the loop. This ensures that the etching interface is well defined. A bias voltage of between 1.25 and 2 V was applied to the tip relative to the loop.

After introduction to UHV these tips were also subjected to ion bombardment similar to that used on the tungsten tips in order to remove the oxide layer. The resultant tips reproducibly provided atomic resolution.

Iron

Iron tips were used for spin polarised STM experiments on magnetite by Wiesendanger *et al.* [12] in 1992. Using iron tips Wiesendanger *et al.* were successful in demonstrating magnetic contrast by comparison with tungsten

tips.

Iron tips were made using both electrochemical and mechanical methods. As iron is a soft material it is conceivable that cutting and drawing would produce good tips. As an alternative to this the iron can be electrochemically etched in 5 - 10% HCl. Again these tips were bombarded by argon ions prior to use. However, the results with these tips were not very encouraging. Furthermore, the iron tips are prone to significant magnetostriction when a magnetic field is applied to the tunnel junction. This makes them unsuitable for experiments involving external magnetic fields.

Iron on tungsten

In order to overcome the magnetostriction of pure iron tips we attempted to produce tips made from iron deposited on tungsten tips. Tungsten tips were prepared as described above, including the ion bombardment. Thereafter between 40 to 60 angstroms of iron were deposited on the tip. Scanning with these tips was, however, very difficult. They were very unstable and occasionally deposited large amounts of what was most likely iron on the surface. Similar tips have been used by Bode *et al.* [24] in spin polarised experiments. However, in their case the tips were heated to 600 K while the iron was evaporated onto them. Unfortunately due to experimental limitations (i.e. the stage which supports the tips during evaporation has no heating) this option was not available to us.

Chapter 3

Magnetite

It is well to observe the force and virtue and consequence of discoveries, and these are to be seen nowhere more conspicuously than in those three which were unknown to the ancients, and of which the origin, though recent, is obscure and inglorious; namely, printing, gunpowder and the magnet (i.e. Mariner's Needle). For these three have changed the whole face of things throughout the world.

Francis Bacon (1561-1626)

3.1 Historical background

Even as far back as prehistoric times man discovered uses for iron oxides. In any region where suitable deposits could be found one can now find traces of cave and rock paintings where man used iron oxides as pigments. By around 2000 BC it had been discovered that heating the oxides could result in further useful pigments of reds and browns. By the end of the last century the first synthetic iron oxide pigment had been made, Venetian Red. At present there is a total world production of iron oxide pigments of circa 600,000 tonnes.

There are sixteen iron oxides, including hydroxides and oxide hydroxides. Here we are concerned with just one of these, magnetite. Though haematite, α-Fe_2O_3 may be the oldest known iron oxide (it being the red mineral widespread in soil and rocks) magnetite is the oldest known magnetic material. Together with titanomagnetite, magnetite is responsible for the magnetic properties of rocks. Therefore it is of fundamental importance in the study of geomagnetism. By studying the grain size, magnetic orientation and composition of magnetite, geologists can tell how deep the sample was when it was formed and when it was formed. From this, valuable data can be gleaned on plate tectonics, crust formation and other geological phenomena [75].

Though man may have been using the magnet for thousands of years it has been in use by other biological organisms for much longer. These biological organisms also use magnetite for navigational purposes. Magnetite can be found in magnetotactic bacteria (where magnetotaxis means orientation and migration along geomagnetic field lines) [76]. These bacteria use the magnetite crystals (usually single domain crystals around 50 - 100 nm in size) to navigate in the earth's magnetic field. Interestingly the crystals are arranged such that the [111] direction (the direction of the easy axis in magnetite) is along the motility axis of the bacterium. It has also been noted that both honey bees and pigeons (in the skull) carry some amount of magnetite. The exact function of this is more intricate than for a simple bacterium though the principle is likely the same. Biogenic magnetite was actually first discovered in the teeth of chitons *Polyplacophora mollusca* (a type of mollusc) in 1962 by Lowensam [77]. Apparently the hard nature of magnetite has proved to be quite beneficial for grazing.

As well as being useful for navigation the magnetic properties of the

magnetic iron oxides have found application in the recording industry since the late 1940's. Even though it displays high magnetisation and coercivity magnetite is less suitable for recording devices, due to its magnetic instability [78], than is maghemite, γ-Fe_2O_3.

Magnetite, along with haematite, are the main iron oxides in industrial catalysis. Both oxides have semiconductor properties and are suitable for both oxidation and reduction reactions. Some examples of the important chemical processes involving magnetite are the Haber process for the production of NH_3 from hydrogen and nitrogen and the Fischer-Tropsch synthesis of hydrocarbons. Magnetite is particularly suitable because it is cheap, stable and it can withstand a high level of impurities without being poisoned [79]. Some properties of a range of iron oxides are given in table 3.1.

In recent times attention has focused on magnetite because it has potential in the development of spin polarised devices such as spin valve transistors [80]. Magnetite has been described as a half-metallic material [81]. Bratkovsky [82] has shown theoretically that a half-metallic material could have a tunnel magnetoresistance (TMR) of around 3000%. TMR in ferromagnetic junctions was first observed by Julliere in 1975 [10]. The observations of Meservey and Tedrow [83] that TMR could be applicable to magnetic sensors and memory devices has ignited considerable interest in this field.

3.2 Crystal structure

The spinel crystal structure was first determined by Bragg in 1915 [87] using X-ray diffraction. This structure gets its name from the mineral spinel, $MgAl_2O_4$. The general formula for a ferrite spinel is $MeFe_2O_4$ where Me represents a divalent metal ion with an ionic radius of between 0.6 and 1 Å and

	Magnetite	Haematite	Maghemite	Wüstite
Formula	Fe_3O_4	α-Fe_2O_3	γ-Fe_2O_3	FeO
Structural type	Inverse spinel	Corundum	Defect spinel	Defect NaCl
Crystal system	Cubic	Hexagonal	Cubic/ Tetragonal	Cubic
Space group	O_h^7-Fd3m	D_{2h}^{16}-R$\bar{3}$c	O_h^7-Fd3m/ $P4_32_12$	O_h^5,Fm3m
Cell dimensions (nm)	a: 0.84	a: 0.50 c: 1.38	a: 0.84/ a: 0.83 c: 2.50	a: 0.43
Colour	Black	Red	Brown	Black
Magnetic order	Ferri-	Weakly ferro-	Ferri-	Antiferro-
Curie/Neel temperature (K)	850 T_V: 119	956	820–986(1)	203–211
RT Saturation magnetisation $(JT^{-1}Kg^{-1})$	92–100	0.3	60–80	–
Density (gcm^3)	5.18	5.26	4.87	5.9
Formula units per unit cell	8	6	8	4

Table 3.1: Some properties of the iron oxides. (Cornell [79], Coey [84], Soffel [85] and Murad [86]) (1) The T_C of maghemite is uncertain because it transforms to haematite above ~713 K.

the Fe ion is trivalent. The smallest unit cell of the spinel lattice that has cubic symmetry contains eight molecules of $MeFe_2O_4$. The oxygen ions form a face centred cubic lattice. The iron atoms are arranged in two interstitial sites around the oxygen atoms. These have six-fold and four-fold symmetry and are the octahedral and tetrahedral sites respectively. In one unit cell only 8 of the 64 tetrahedral sites and 16 of the 32 octahedral sites are occupied by metal ions. These are known as the A and B sites, respectively. The arrangement of the trivalent and divalent ions within the octahedral and tetrahedral sites was originally thought to be eight divalent ions in the tetrahedral sites and the sixteen trivalent ions in the octahedral sites. This is known as a *normal* spinel. In 1932 Barth and Pasnjak [88] showed by X-ray diffraction that a spinel could also occur with the eight divalent ions in eight of the available octahedral sites and the sixteen trivalent ions distributed evenly between the eight tetrahedral sites and the eight remaining octahedral sites. This is called *inverse* spinel. Magnetite is an inverse spinel. This was confirmed by Shull *et al.* using neutron diffraction [89].

An important factor which must be mentioned in any consideration of the spinel structure is the oxygen parameter denoted u. This is a measure of the deformation to the fcc structure of the oxygen ions by the insertion of the metal ions. Quantitatively u is given by the distance between an oxygen ion and one of the oxygen fcc cube faces. For ideal fcc $u = \frac{3}{8}$. The tetrahedral sites in ferrites and many other oxidic spinels are too small to accommodate the metal ions. This results in a displacement of the oxygen ions. As a direct consequence of this the octahedral sites become smaller. It can be shown that the radii of the spheres in the A and B sites are given by

$$r_A = \left(u - \frac{1}{4}\right) a\sqrt{3} - R_o \tag{3.1}$$

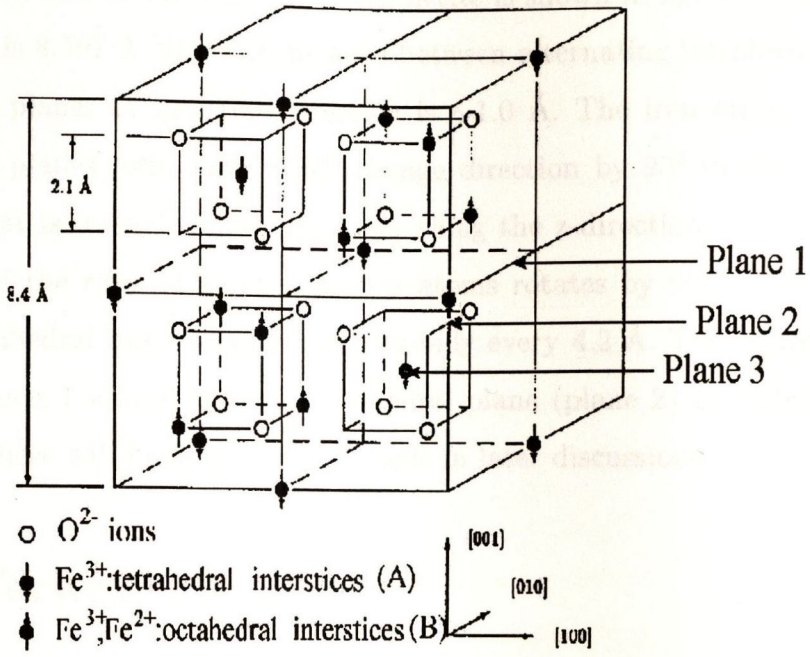

Figure 3.1: The unit cell of magnetite. Only the atoms in the front half are shown. The planes marked 1 and 3 label tetrahedral planes and plane 2 is an octahedral plane.

$$r_B = \left(\frac{5}{8} - u\right) a - R_o \tag{3.2}$$

where R_o is the radius of the oxygen ion and a is the lattice parameter. The value of the u parameter for magnetite is 0.379. From calculations of the Madelung energy for the complete lattice by Verwey *et al.* [90] it can be shown that the spinels with divalent and trivalent ions form an inverse spinel structure when the oxygen parameter $u \leq 0.379$ and the normal spinel structure when $u > 0.379$. In Fig. 3.1 we can see that the tetrahedral sites are filled by the trivalent ions i.e. Fe^{3+}. This is not unreasonable. The tetrahedral sites are smaller than the octahedral ones. The trivalent ions are smaller than the divalent equivalent and hence they occupy the smaller position.

The front half of the unit cell of magnetite is shown in fig. 3.1. The unit cell length is 8.397 Å [91]. The distance between alternating tetrahedral and octahedral planes in the [100] direction is ~1.0 Å. The iron atoms in the octahedral planes form rows which change direction by 90° in alternating planes. That is to say as one progresses along the z-direction by 2.1 Å the direction of the rows of octahedral iron atoms rotates by 90°. In the case of the tetrahedral iron atoms this occurs only every 4.2 Å. Two tetrahedral planes (planes 1 and 3) and one octahedral plane (plane 2) are labelled in Fig. 3.1. These will be of more importance in later discussions.

3.3 Verwey transition

3.3.1 Models

The electronic conductivity of magnetite is of particular interest. It was first investigated by calculating the electrostatic contribution to the lattice energy of different cation arrangements by Verwey *et al.* [90,92]. By assuming inverse spinel arrangement Verwey and de Boer could explain the electronic conductivity of magnetite [93,94]. They could also explain the low temperature transition point seen at ~120 K [43,95]. This transition point, known as the Verwey transition, T_v, [96] is a very interesting feature of magnetite. In essence the dc conductivity abruptly increases by two orders of magnitude upon heating the crystal above 120 K [97]. This Verwey transition is very important for understanding the STM images introduced in later chapters so it is worth investigating it further.

The existence of a low temperature transition in magnetite was first evident in 1929 from the work of Weiss and Forrer [98] who made measurements of magnetisation and Millar [99] who measured the specific heat changes at

120 K. They noted a deviation from cubic symmetry below 120 K. Originally Verwey *et al.* described the new symmetry as tetragonal [95]. However, Bickford calculated an orthorhombic structure [100] and later he confirmed this by measuring the strains induced during the transition [101]. This result was supported by the X-ray analysis of Abrahams *et al.* [102]. Li [103] also noted that the direction of easy magnetisation in a single crystal below the transition temperature is influenced by the direction of the magnetic field applied during cooling through the transition. This was interpreted by Verwey *et al.* as indicating that one of the orthorhombic axes is parallel to one of the original cubic axes.

Verwey *et al.* suggested that below T_v there is an ordering of the Fe^{2+} and Fe^{3+} ions in the octahedral sites. This is what accounts for the sudden change in conductivity. They predicted that successive (001) layers of octahedral sites are occupied alternately by Fe^{2+} and Fe^{3+} ions thus creating uniaxial symmetry below 120 K. This conclusion is supported by electron and neutron diffraction and nuclear magnetic resonance experiments carried out in the 70's [104–106]. From these experiments it was noted that below T_v the Fe^{2+} and Fe^{3+} sites are structurally distinguishable in a distorted crystal structure.

Above T_v the long-range order is destroyed and only a small amount of short-range order remains. The issue of order-disorder in alloys has been discussed since early this century [107, 108]. According to theories based on nearest neighbour interactions the critical temperature, T_c, for the loss of long-range order is proportional to the energy of ordering per atom, E.

$$kT_c = azE \tag{3.3}$$

where k is the Boltzmann constant, z is the co-ordination number and a is a constant dependent on the lattice type [108]. However, later calculations

by de Boer *et al.* [109] and theoretical considerations by van Santen [110] using van der Waerden's low temperature method [111] and Anderson [112] suggested that the short-range order, (SRO), is considerably stronger than originally thought and hence the ordering energy is much larger. In fact experimental evidence, namely diffuse neutron scattering [113], seemed to contend that SRO is maintained through the transition at T_v. One might then wonder why the conductivity continues to increase so dramatically through the transition [114]. Indeed there is no clear answer to this question to date [115]. Magnetite exhibits semiconductor like behaviour both above and below T_v [116,117]. However, above the temperature of maximum conductivity (300 K) magnetite behaves more like a metal and the conductivity begins to decrease with increasing temperature. Different experiments, Hall effect studies [116,118–120], and calculations [115] have not yet concluded either the number or the sign of the charge carriers in magnetite. Results ranging from $\frac{1}{4}$ electron/Fe_3O_4 molecule [116] to 1 hole/Fe_3O_4 molecule [118] have been reported.

From Mössbauer experiments [121] electron hopping times ranging from 7×10^{-9} s at 120 K to 1.1×10^{-9} s at 300 K have been calculated. From this a dc conductivity at room temperature was calculated to be 350 times too small. From diffuse neutron scattering experiments a value for the hopping time of 0.5×10^{-12} s was inferred. This yields a dc conductivity value 6 times larger than measured. The range of values for the hopping times above coupled with the inaccuracies in the calculations of the charge carriers obviously make it exceedingly difficult to fit theoretical models to experimental results. Some authors have attempted to explain the deviations from simple Drude behaviour by invoking strong electron-phonon correlations i.e. polaron effects [122,123].

Mott [114] once asked why, if the SRO persists through the transition, does the conductivity continue to increase. It was thought that photoemission (PES) and inverse photoemission (IPES) spectroscopy experiments would answer this question. With these spectroscopies it is possible to measure the spectra required to create single holes and electrons, respectively. From this one can show whether an excitation energy is required to create the free holes and electrons or whether there is a Fermi edge and thus no energy barrier as one would see with a metal. In 1995 Chainani *et al.* [124] used PES to show that a gap present in the low-temperature phase disappears as the sample is heated through T_v thus indicating that what occurs at the Verwey transition temperature is a metal-insulator transition. This would seem to imply that the SRO is not sufficiently strong to prevent the gap from collapsing. However, further work by Park *et al.* [115] actually claims the opposite. Their PES study indicated that the gap does not collapse but merely reduces by ~50 meV as the sample is heated through T_v. The differences in these results is attributed (by Park) to the different monochromaticities of the photon sources used.

By the 1970's experimental evidence [118, 125, 126] was mounting that the band model is a more appropriate description of magnetite than the ionic hopping scheme [127]. Neutron diffraction [128], electron diffraction [129] and Mössbauer spectroscopy [130] experiments all suggested a complex three-dimensional order which Cullen and Callen used to describe the semiconductor behaviour of the conductivity of magnetite above the Verwey transition temperature [127, 131]. Alvarado *et al.* [4] also used photoelectron-spin-polarisation and ultraviolet/far-ultraviolet photoemission-spectroscopy results on magnetite to show that the single ion in a crystal field (SICF) model correctly describes and explains the electronic excitation spectra of

the Fe ions.

Charge ordering due to the Coulomb interaction has been discussed theoretically by Wigner [132]. In determining whether or not a Wigner crystallisation sets in or not the important quantity is the ratio of the Coulomb interaction energy between charge carriers on nearest-neighbour sites, V_0, to the electronic bandwidth, B. V_0 is given by

$$V_0 = \frac{e^2}{4\pi\epsilon_0\epsilon a} \tag{3.4}$$

where ϵ is a background dielectric constant and a is the interatomic spacing.

Cullen and Callen [127] used self-consistent band calculations of the ground-state energy and charge orderings based on a tight-binding scheme of magnetite to obtain the following results. They found that, starting from small $\frac{V_0}{B}$, there is first a disordered state. As $\frac{V_0}{B}$ increases there are multiply ordered states (that is, fractional charges within the tetrahedra of B-site ions) with a narrow band gap followed by an ordered metallic state and when $\frac{V_0}{B} \geq 3$ an ordered insulator, i.e. Wigner crystallisation sets in. According to Coey *et al.* [133] the electronic bandwidth is considerably reduced at the surface while the interaction energy between charge carriers on nearest-neighbour sites remains largely unchanged. Therefore we can expect a Wigner crystal to form at the surface at temperatures exceeding that for bulk crystallisation.

An alternative structure to the alternating octahedral 2+ and 3+ plane system proposed by Verwey was postulated by Iida *et al.* [134, 135] in the 1980's. They proposed a model where the phase transition is due to charge freezing on the octahedrally co-ordinated sites leading to two different layered patterns. One is the formation of pairs of Fe^{2+} ions which alternate with pairs of Fe^{3+} ions along the [110] rows. The second is the formation of triplets of one species interspersed with single ions of the other species (fig. 3.2).

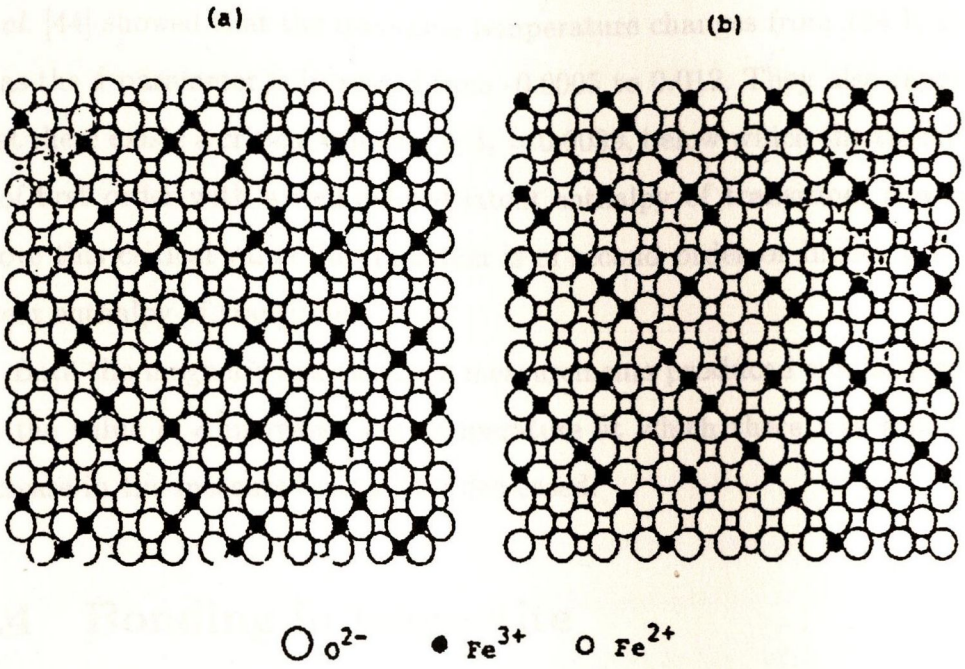

Figure 3.2: Mizoguchi's patterns of the low temperature, idealised first order structure of magnetite. The planes represent alternating octahedral planes.

These patterns were of paramount importance to Wiesendanger *et al.* in their interpretation of the spin polarised tunneling experiments on magnetite [12].

3.3.2 Nonstoichiometry

The influence of nonstoichiometry on the Verwey transition temperature in magnetite has been reported by a number of groups [136–139]. Two comprehensive investigations into this phenomenon were carried out by Aragon *et al.* [44,140]. In the first of these Aragon *et al.* investigated the effect nonstoichiometry had on T_v by means of the initial permeability in a single crystal. In the second report they researched the resistivity variations due to changes in δ.

The off-stoichiometry is quantified by the value δ as $Fe_{3(1-\delta)}O_4$. Aragon

et al. [44] showed that the transition temperature changes from 124 K to 81 K as the δ parameter is increased from -0.0005 to 0.012. They also reported that there exists a critical value for δ, $\delta_c = 0.0039$, below which the transition is of first order with a well defined latent enthalpy of transition. However, above this critical value the transition is of second order or higher with no latent enthalpy of transition.

Both the magnetic and electrical measurements produced similar results. As the value of δ increased the temperature at which there was a sudden increase in the measured parameter decreased.

3.4 Bonding in magnetite

One very controversial aspect of magnetite is the nature of the atomic bonding. Is it ionically or covalently bonded? In approaching this question it is worth keeping the observation of O'Keefe [141] in mind:

One is forced to conclude, then, that when we say that a crystal is "ionic", what is implied is that some simple properties of the crystal are well described by the ionic model. We should not consequently draw conclusions about "quantities" such as ionic radii and ionicity, which, although sometimes useful concepts, are in principle not determinable. We should not be surprised either if alternative models work equally well for the same material; indeed, they often do.

Indeed, according to LaFemina [142], *"For the relaxations and reconstructions of oxide surfaces, the same simple chemical and physical principles derived from the study of "covalent" semiconductor surfaces work not only equally well, but better."*

This is particularly important for magnetite which because of its ionic

components (Fe^{2+}, Fe^{3+} and O^{2-}) is often thought of as an ionic compound. When the surface of an ionic material is cut or cleaved it is common to think of this as simply pulling electrostatically attracting particles apart and not, as in the case of covalent bonding, breaking bonds. In fact de Groot *et al.* [143] have shown that there is significant hybridisation of the oxygen metal bonds in the transition metal oxides. Sancrotti *et al.* [144] took this further and examined the specific case of magnetite. They used ultraviolet angle-integrated inverse photoemission spectra in comparison with O 1s X-ray absorption spectra to determine a strong covalent admixture of Fe [3d;4(sp)]- and O(2p)-derived states. If magnetite can be thought of as somewhat covalent then many of the ideas and techniques developed for the understanding of semiconductor surfaces (and there has been considerably more work on these than on oxide surfaces) may be used to understand the magnetite surface. In particular, the importance of the redistribution of surface dangling bonds and dangling-bond charge density with regard to the principle of autocompensation.

3.5 Electron counting and surface autocompensation

The ideas for this particular theoretical approach to understanding surface reconstructions were originally developed to predict the missing dimer model for GaAs semiconductor surfaces by Chadi [145] in 1987. It is based on an electron counting idea [146]. This model has been proven to be justifiable in a paper by Pashley [147]. As this model is now widely used to explain the observed surface of magnetite [148, 149] it is worth introducing it at this point.

It has been shown for the case of semiconductors that the dangling-bond

energy level of the electropositive element is in the conduction band and should therefore be empty and the dangling-bond energy level of the electronegative element is in the valence band and should therefore be filled [150]. This is achieved by having the electrons from the electropositive element transfer to the electronegative element. The electron counting model requires that the number of available electrons on the surface exactly matches the number required to fill all the dangling bonds of the electronegative element. If this requirement is fulfilled the surface will be semiconducting. Otherwise partially filled dangling bonds lead to metallic behaviour. As has been mentioned above magnetite is a contentious material when it comes to the band energy. Some reports have shown there is no gap in the conduction band. However, the most recent reports indicate that there is in fact a small gap [115].

The principle of autocompensation suggests that a surface which does **not** have exactly the correct amount of electrons to fill the dangling bonds of the electronegative element is not in its lowest energy state and will reconstruct in order to provide a means for exact matching. These reconstructions take two basic forms, either the surface can add or remove some ordered array of atoms or it can shift atomic positions such that there is a different sharing of charge [149].

3.5.1 Electron counting on magnetite (100)

At this point it is worth presenting the calculations of the number of available electrons and dangling bonds on the (100) surface of magnetite. These calculations follow the work of Kim *et al.* [148] and Gaines *et al.* [149].

The basic formula unit of magnetite may be written as $[Fe^{3+}(T)Fe^{2+}(O)Fe^{3+}(O)][O^{2-}]_4$, where (O) represents an octahedral

position and (T) is for tetrahedral. Each oxygen in the bulk is associated with three octahedral irons and one tetrahedral iron. An extra complication is added when one considers that the three octahedral irons may consist of either two 3+ and one 2+ or vice versa. Either way these two options must be present in equal amounts for charge neutrality.

Each $Fe^{3+}(T)$ donates (in the bulk) three electrons between four oxygen bonds. This implies;

$$N_{Fe^{3+}(T)} = \frac{3}{4} = 0.75 \tag{3.5}$$

where N refers to the number of electrons donated per bond. Similarly

$$N_{Fe^{2+}(O)} = \frac{2}{6} = 0.33 \tag{3.6}$$

$$N_{Fe^{3+}(O)} = \frac{3}{6} = 0.50 \tag{3.7}$$

As explained above we may assume that magnetite is considerably covalent hence we expect two electrons are involved in each Fe-O bond. Recognising this the oxygen anions therefore donate 1.25, 1.67 and 1.50 electrons to each of the $Fe^{3+}(T)$, $Fe^{2+}(O)$ and $Fe^{3+}(O)$ bonds respectively. How one proceeds with the calculations from this point depends very much on the surface model assumed. For example, Kim *et al.* [148] assume that the tetrahedral and octahedral planes at the surface are close enough to be considered as one layer. In fact, if we look at fig. 3.1 we can see that there is only 1.0 Å between these layers. Due to the change in co-ordination at the surface we can expect these to contract together somewhat thereby reducing this distance further [151, 152]. On the other hand Gaines *et al.* [149] calculate for a purely octahedral plane. The result is not significantly affected. In the case of Kim *et al.* they calculate that there are 3 extra electrons per surface unit cell. Conversely Gaines *et al.* show that there are three missing electrons

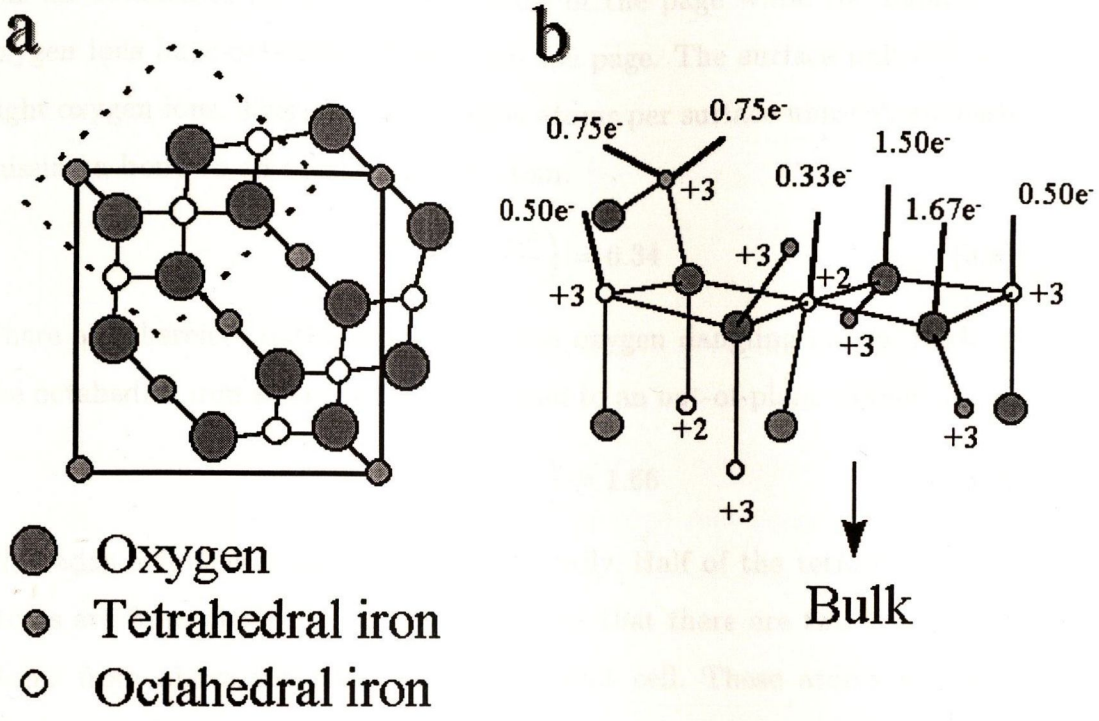

Figure 3.3: The surface unit cell of magnetite (100). In **a** the solid box outlines one 8.4 × 8.4 Å^2 unit area. The dashed box outlines the area projected 3-dimensionally in **b**. In **b** the electrons donated by various dangling bond elements are shown following Kim *et al.*

per surface unit cell. Both, however, agree that an ordered array of tetrahedral vacancies results in an electron balanced surface unit cell. Here we will present the calculations based on the approach employed by Kim *et al.* [148].

The surface unit cell is shown in fig. 3.3. This unit assumes a complete mixing of three atomic layers (marked 1, 2 and 3 in fig. 3.1) to form one surface layer [148]. A two dimensional surface cell is shown in fig. 3.3**a** and in fig. 3.3**b** a three dimensional projection of the section marked in the dotted box is presented along with the electron donation values of a selection of dangling bonds. It can be seen from fig. 3.1 that every second oxygen ion

has an octahedral bond out of the plane of the page while the remaining oxygen ions have octahedral bonds into the page. The surface unit cell has eight oxygen ions. Therefore four oxygen atoms per surface unit cell are each missing a bond to an octahedral iron atom.

$$4 \times \left(\frac{1.67 + 1.5}{2}\right) = 6.34 \tag{3.8}$$

There are therefore 6.34 electrons in these oxygen dangling bonds. Each of the octahedral iron atoms is missing a bond to an out-of-plane oxygen atom.

$$4 \times \left(\frac{0.33 + 0.5}{2}\right) = 1.66 \tag{3.9}$$

This adds a further 1.66 electrons to the tally. Half of the tetrahedral iron atoms are from above the plane. This means that there are two tetrahedral atoms from above the plane per surface unit cell. These atoms are each missing two bonds to an oxygen atom from above.

$$2 \times 2 \times 0.75 = 3 \tag{3.10}$$

Adding equations 3.8, 3.9 and 3.10 yields a total of 11 available electrons per surface unit cell. As there are four oxygen dangling bonds each requiring (for covalent bonding) two electrons, the surface needs 8 electrons. Therefore in a model which takes into account all of the tetrahedral atoms from the planes above and below the Fe-O plane there is an excess of 3 electrons per unit cell.

Both Gaines and Kim provide a method for forming an autocompensated surface. They suggest that an ordered array of tetrahedral vacancies where every second tetrahedral iron atom from above the Fe-O plane is missing would result in a balanced surface. Essentially the central tetrahedral iron atom in the solid box of fig. 3.3a is removed. This creates two extra oxygen bonds to a tetrahedral iron atom. Now there are six oxygen dangling bonds

and therefore a total of twelve electrons are needed to create a balanced surface. The number of electrons lost by removing the $Fe^{3+}(T)$ atom is half of the result of equation 3.10 which is 1.5. The number of electrons left in the new oxygen dangling bonds is 1.25 per bond (= 2.5 in total). So the surface has made a net gain of 2.5 - 1.5 = 1 electron per cell. There is now a total of 12 electrons available per surface unit cell which is *exactly* the amount needed to balance the surface. Another interesting feature of this ordered array of tetrahedral iron vacancies is that it creates a new repeat unit. As will be discussed below there are strong indications that the magnetite (100) surface forms a $\left(\sqrt{2} \times \sqrt{2}\right) R45^o$ pattern. The ordered array mentioned above follows this pattern demonstrating yet again the validity of the autocompensation model.

3.5.2 Charge balancing

Unlike the electron counting argument presented above the charge balancing considerations come from a more ionic perspective. In 1979 Tasker [153] presented three possible categories for ionic surfaces shown in cross-section in fig. 3.4. This schematic does not fully represent all atoms in a given plane.

The first type of crystal surface, fig. 3.4a, is neutral with stoichiometric proportions of anions and cations in each plane. The second type, fig. 3.4b, consists of charged surfaces with no dipole moment in the repeat unit perpendicular to the surface. However, type 3 crystal surfaces, fig. 3.4c, are charged surfaces that have a dipole moment in the repeat unit. These surfaces have an infinite surface energy and an electric field from this charged surface penetrates throughout the crystal. This counter-intuitive result can be understood as follows [153]: The stability of a surface is determined by

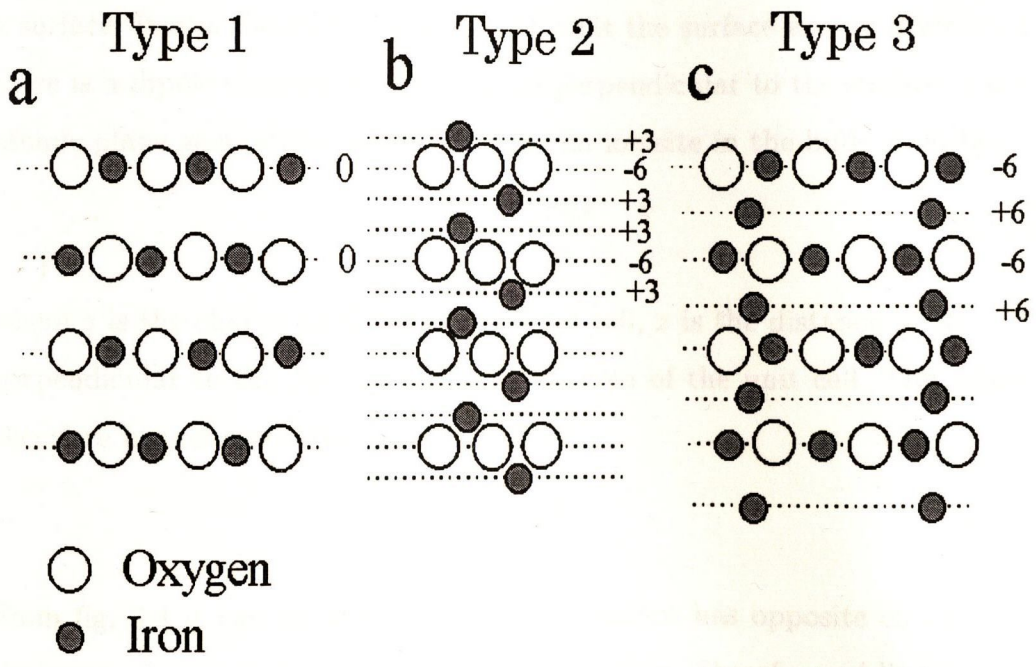

Figure 3.4: A schematic cross-section of the three surface ionic categories predicted by Tasker. **a**, **b** and **c** are the types 1, 2 and 3 described in [153]. Magnetite (100) is a type 3 surface.

the surface energy, E_s and this may be defined as

$$E_s = E_{Coh}(crystal) - N \times E_{Coh}(atom) \tag{3.11}$$

where E_{Coh}(crystal) is the cohesive energy of a finite crystal, N is the number of atoms in this crystal and E_{Coh}(atom) is the cohesive energy per atom in an infinite crystal. This is the excess energy associated with the creation of a surface. It was shown by Bertaut [154] that the surface energy diverges if there is a dipole moment in the unit cell perpendicular to the surface. Each atomic plane generates a potential, V, at an ion site in the bulk given by;

$$V(z) = \frac{2\pi qz}{A} \tag{3.12}$$

where q is the charge on the plane per unit cell, z is the distance to the ion perpendicular to the surface and A is the area of the unit cell. This plane therefore has an associated electric field of;

$$E = \frac{2\pi q}{A} \tag{3.13}$$

From fig. 3.4 it can be seen that a type 1 surface has opposite charges on the same plane which exactly cancel one another. Therefore adding planes to this crystal does not affect an ion in the bulk and hence the Madelung energy converges. A type 2 surface behaves in a similar manner with a three plane repeat unit over which the potential is cancelled out. However, for a type 3 surface the potential of the two-plane repeat unit is not cancelled out. It has a magnitude of

$$V = \frac{2\pi \mid q \mid a}{A} \tag{3.14}$$

where a is the interplanar spacing. Every time a further plane is added to the surface the energy of a particular ion in the bulk is increased. This energy therefore diverges to infinity for an infinite crystal. Obviously a surface of

this kind is not stable and there are a number of methods by which such a surface can reduce this energy. One approach is faceting. A surface may be macroscopically (100), for example, and yet have microscopic (110) facets which reduce the energy. This has been shown on (111) MgO surfaces by Henrich [155]. It is also possible to stabilise the surface by adding various foreign species to the surface like the OH^{-1} ion for magnetite [156]. Finally the surface may be reconstructed such that the terminating layer is only half-filled. In the case of magnetite (100), which is a type 3 surface, having only half of the terminating layer (either a tetrahedral or octahedral layer) effectively changes the surface into a type 2 [156]. In essence this last result is very similar to the predictions obtained from electron counting arguments. It is interesting to note that both the ionic and covalent models produce the same predictions.

3.5.3 Tapered termination theory

Tapered termination theory is a treatise on the thermodynamic excesses at interfaces in multicomponent systems introduced by Finnis [157, 158]. An excess refers to the way in which a surface termination may have an imbalance of one component with respect to the bulk crystal. The approach used in this theory is to treat a slab of the material as an ensemble of terminations and average over them. However, this theory, though useful from a bookkeeping point of view [159] makes no predictions with regard to surface relaxations or reconstructions. It merely keeps track of the stoichiometry of the surface. Therefore whether the octahedral and tetrahedral planes on the (100) surface coalesce or not cannot be determined using this model as this does not alter the surface stoichiometry [159].

Calculating the excesses for the two possible terminating planes of mag-

netite octahedral or tetrahedral (with atomic compositions of Fe_4O_8 or Fe_2 per unit cell respectively) in the manner described in [157] yields an excess of -1Fe for the former and +1Fe for the latter termination. One can conceive of the simplest situation for balancing this excess by terminating the iron poor surface with half an iron rich termination. Thus a half-filled tetrahedral layer (the iron rich layer) on top of, and coalescing with, a full octahedral layer would satisfy the excess [159]. It is interesting to note that this model produces the same prediction for the surface as both the charge balancing and electron counting arguments.

3.6 Surface characterisation work on magnetite

Magnetite has been studied extensively in the past few years using a range of surface techniques including AES [160], depth selective Mössbauer spectroscopy [161], reflection high energy electron diffraction (RHEED) [162, 163], x-ray diffraction (XRD) [164], x-ray photoelectron spectroscopy (XPS) [163,165], LEED [166,167], atomic force microscopy (AFM) [168] and, of course, STM [12, 42, 149, 169–179]

These studies have concentrated on two main areas; low index single crystalline surfaces and molecular beam epitaxy (MBE) grown films. Other magnetite film growth techniques have also been studied including reduction or oxidation of other iron oxides to magnetite [148] and pulsed laser deposition [168]. As the results to be presented in later chapters follow on from, and in some cases contradict, literature findings it is worth at this point briefly discussing the state of the field of STM magnetite research. The spin polarised experiments of Wiesendanger *et al.* [12,56,180] will be discussed in

later chapters.

3.6.1 Fe_3O_4 (100)

One of the first detailed STM studies into the effect of various preparation conditions on the surface of magnetite (100) was performed by Tarrach *et al.* [42] in 1993. They used natural single crystals from Zillertal in Austria. The samples were cleaned in vacuum using both annealing and argon ion sputtering. Three preparation conditions were examined, annealing to 810 K, annealing to 880 K and sputtering. From their results they concluded that the surface is sensitive to the preparation conditions. This is an important result for the data presented here. From previous theoretical [181] and experimental [4] work it seems that oxygen atoms are not accessible to STM hence Tarrach *et al.* associated the atomic structures they observed with the iron atoms.

In 1995 Voogt *et al.* [162] presented the results of growing magnetite by means of evaporating iron while simultaneously oxidising the film with a controlled NO_2 flux. They grew Fe_3O_4 (001) on MgO (100). From RHEED and LEED patterns Voogt *et al.* discerned a p(1 $\times$ 1) surface reconstruction on the grown films.

Gaines *et al.* presented a number of papers in 1997 on MBE grown Fe_3O_4 (100) on MgO (100) [149, 175, 176]. One point to note immediately is that in order to clean the magnetite surface Gaines *et al.* annealed the sample at 870 K. This temperature is sufficient to cause significant contamination by Mg ions from the substrate [174]. However, in this study a tendency for the surface structures to rotate by 90° is reported. In [176] reconstructed rows are reported separated by a stacking fault which causes a 90° rotation of the rows. Furthermore a p(1 $\times$ 1) surface reconstruction is presented as a displacement of the tetrahedral Fe atoms from their bulk positions. In [149] the 90° rotation

occurs on alternating terrace steps. However, in [176] the reconstructions are "elongated clusters" and not rows. The clusters are elongated along the [110] direction. Electron counting arguments suggest that some of the atomic images seen in this report are more FeO in nature than Fe_3O_4.

The MBE grown Fe_3O_4 $(\bar{1}00)$ films of Gao and Chambers [163] exhibit a $\left(\sqrt{2} \times \sqrt{2}\right)R45^o$ reconstruction as seen by LEED and RHEED. This they also attribute to the presence of an ordered array of tetrahedral vacancies. These results are taken a little further by Kim *et al.* [148] who present a surface model, fig. 3.5, of the ordered array discussed above.

The most recent publication at the time of writing is by Chambers and Joyce [179]. In this paper the authors address an on-going controversy about the conventional notation used to describe the LEED results seen by many authors on MBE grown Fe_3O_4 (100). It has been variously described as $p(1 \times 1)$ [42, 149] and $\left(\sqrt{2} \times \sqrt{2}\right)R45^o$ [148] in the literature. Chambers and Joyce provide a convincing argument that the latter is more correct. They add a further useful piece of information to the magnetite puzzle. They used x-ray photoelectron spectroscopy to determine that the top few layers of Fe_3O_4 (100) are richer in Fe^{3+} than subsurface layers. This supports the claim that the surface is terminated by filling at least some of the tetrahedral vacancies directly above an octahedral layer.

3.6.2 Fe_3O_4 (110)

Jansen *et al.* [170, 171] studied the (110) surface of artificially grown single crystals of magnetite. They used a combination of sputtering and annealing at 1200 K to prepare clean surfaces. Their justification for studying the (110) surface is that one termination of this surface contains both tetrahedral and octahedral iron atoms and hence this would be an interesting test surface for

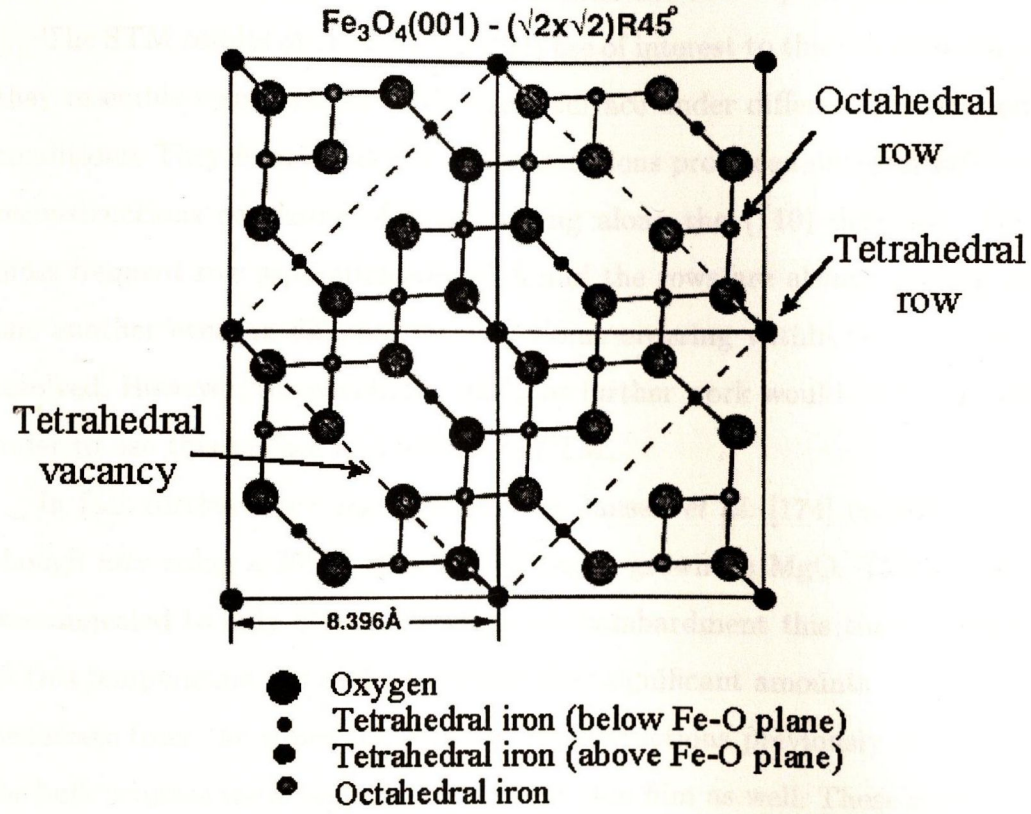

Figure 3.5: The Fe_3O_4 (100) surface as modelled by Kim *et al.*. The octahedral and tetrahedral rows are marked. Every second tetrahedral atom is from the plane above the Fe-O plane and this is represented by alternating size. An ordered array of tetrahedral vacancies is included resulting in the $\left(\sqrt{2} \times \sqrt{2}\right)$R45° pattern (dashed box).

spin polarised experiments. However, Asechlimann *et al.* [54] showed that ion bombardment produces dramatic changes in the surface magnetism of magnetite down to a depth of 50 Å. Hence this preparation technique for potential spin polarised scanning tunneling experiments has to be questionable.

The STM results of Jansen *et al.* [171] are of interest to this thesis because they resemble results found on the (100) surface under different preparation conditions. They found that the above conditions produced one-dimensional reconstructions consisting of rows running along the $(\bar{1}10)$ direction. The most frequent row separation was 25 Å and the rows are always parallel to one another even on different terraces. Some ordering within the rows was resolved. However, the conclusion was that further work would be needed in order to use this surface as a test for SPSTM.

In fact further work was presented by Jansen *et al.* [174] on this topic though now using a 500 Å thick film of Fe_3O_4 grown on MgO. This sample was annealed to only 850 K (no argon ion bombardment this time) though at this temperature the authors concede that significant amounts of Mg ions penetrate from the substrate. The row reconstructions previously described for bulk crystals were found to form on the thin film as well. These rows are modelled as being "Fe_2O_3-like" where the oxygen content is higher and the tetrahedrally co-ordinated Fe^{3+} ions are absent. The rows are found to be approximately 3 Å high which is close to twice the bulk interatomic spacing. Hence the model is based on a combination of layers.

3.6.3 Fe_3O_4 (111)

In 1994 Condon *et al.* [169] obtained Fe_3O_4 (111) on α-Fe_2O_3 (0001) by argon ion bombardment and annealing in 1×10^{-6} mbar of O_2 at 1000 K. They determined the terminating layer to be $\frac{1}{4}$ monolayer of Fe atoms.

In 1996 Lennie *et al.* produced a comprehensive STM study of the Fe_3O_4 (111) surface. Again this surface was prepared by argon ion bombardment and annealing in oxygen. They observed two distinct coexisting surface terminations with atomic resolution. These surfaces they identified with the two types of Fe (111) layers found in the bulk Fe_3O_4 structure. For reasons of surface ionic stability (see above) Lennie *et al.* proposed a model whereby for one termination (which they call termination A) an O atom caps three Fe^{2+} per (1 × 1) unit cell. The three iron atoms give a charge of +6 and the capping oxygen atom provides a charge of -2. This then stabilises the charge of -4 from the close-packed surface O atoms. For the other termination (which they call termination B) they suggest that the charge of -4 from the oxygen per (1 × 1) can be balanced by two Fe^{2+} per (1 × 1) surface unit cell. However, the authors acknowledge that other terminations are also feasible and cite ordered arrays of vacancies and surface adsorbates as possibilities.

A phenomenon known as biphase ordering had been reported on Fe_3O_4 (111) by Condon *et al.* [177,178]. Floreted LEED patterns and striking STM images show the coexistence of Fe_3O_4 (111) and $Fe_{1-x}O$ (111) islands on the surface. This coexistence is the result of reducing Fe_3O_4 (111).

3.7 Conclusion

It can be discerned quite readily from the above that magnetite is quite a complex material. This is mostly related to its inverse spinel crystal structure. Each unit cell of magnetite contains thirty two oxygen ions, sixteen octahedral iron ions and eight tetrahedral iron ions. Magnetite, as we have seen, may be regarded as having both covalent and ionic character. From this, certain predictions may be made for the formation of surface reconstructions.

In fact from the calculations of Tasker [153] it can be seen that there is a strong force driving magnetite (100) to reconstruct.

The wide variety of surface structures seen and the number of different preparation parameters used in the papers cited above serve as an indication of the level of interest in magnetite. It is of interest because of its potential as a test sample for spin polarised STM measurements. However, it is also an important oxide in catalysis and a variety of other functions. In very recent times magnetite has been investigated not only for its interesting charge ordering phenomenon [182], its transport properties [183] and half-metallicity [184], but also for a variety of other reasons including, cancer treatment [185], laser release of drugs [186], as a radiation shield [187] and in relation to the possible existence of life on Mars [188]. Judging by the current level of interest it does not seem likely that magnetite will leave the scientific arena any time soon.

Chapter 4

Terrace-scale structures on magnetite

"Everything has it's beauty, but not everyone sees it."

Confucius

4.1 Introduction

In this chapter the terrace-scale structures investigated during the course of these experiments will be discussed. By terrace-scale we refer to structures which are large (of the order of a few hundred Ångstrom) relative to atomic dimensions. Two structurally distinct surface structures have been imaged. The first type we call cubic terrace structures. The second we call reconstructions and later redefine as "nanoterraces". The preparation procedures for both will be outlined below together with the measured values of the terrace step heights and interpretations of the data. Atomic scale modelling of the structures seen is left until chapter 5. The results of this chapter have been published in *Surface Science* [189].

In the course of this work other preparation procedures were also investigated. These included annealing in oxygen and argon ion bombardment. These techniques were used as they are commonly reported to produce clean magnetite surfaces [149, 178]. They produced some quite unusual results in this study. Although these surfaces were not what was required for SPSTM experiments, and hence were not pursued further, they are worth mentioning here and are presented at the end of this chapter.

4.2 Results

Initial work on the crystals included ex-situ measurements of the resistance versus temperature curves and, in the case of the natural crystal, XRD was also performed. From the resistance versus temperature curves a Verwey transition temperature of 98 $\pm$ 3 K was obtained for the natural crystal and 117 $\pm$ 5 K for the artificial crystal. Referring back to the discussion in chapter 3 on the effect of off-stoichiometry on the Verwey transition temperature we can see that the natural crystal has some degree of impurity or off-stoichiometry and the artificial crystal is relatively stoichiometric. From the (004) and (008) peaks in the XRD of the natural crystal a lattice constant of 8.406 $\pm$ 0.01 Å was calculated. Both crystals were cut along the (100) surface using a diamond saw.

4.2.1 Cubic terrace structures

After initial polishing, the sample was annealed face-up in the resistive heater to a temperature of the order of 750 K. Scanning these images showed that the surface was unstructured. The surface also contained a scattering of large unidentified particles, fig 4.1. These particles were measured to range from

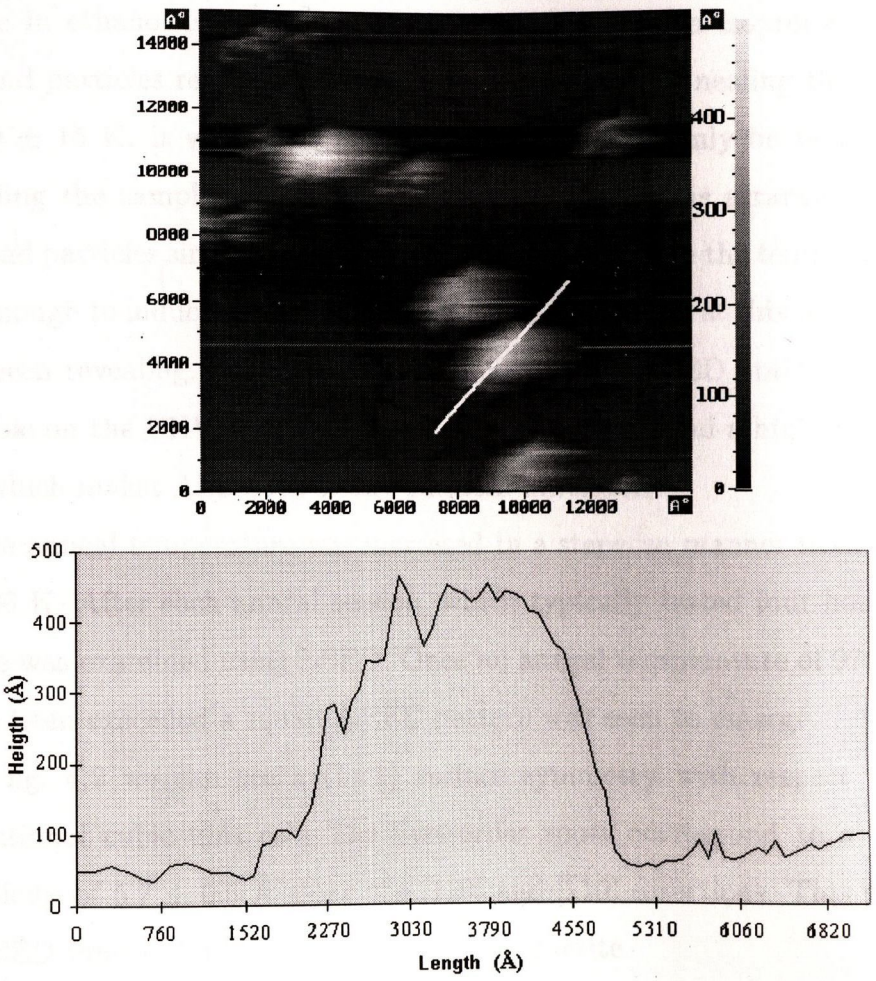

Figure 4.1: STM image of the surface of magnetite containing a number of large particles and the associated line profile. From the dimensions of the particles it was concluded that they are in fact 0.25 μm diamonds left over from the mechanical polishing procedure. $V_{bias} = 1$ V, $I_{tunnel} = 0.1$ nA.

about 0.2 to 0.3 μm in diameter. Stable tunneling was not possible above them. It was concluded that they are diamond particles left on the surface from the mechanical polishing. This is in spite of careful cleaning of the sample in ethanol in an ultra-sonic bath and rinsing in isopropanol. The diamond particles remained on the surface even after annealing the sample to 980 $\pm$ 15 K. It was found that the particles could only be removed by annealing the sample face down. We submit that in this arrangement the diamond particles simply fall from the sample surface once the temperature is high enough to induce surface mobility. AES of the surface at this point would have been revealing. Unfortunately the reverse-view LEED optics currently available on the UHV system has very poor resolution and a high electronic drift which makes AES data of any surfaces unreliable.

The anneal temperature was increased in a stepwise manner from 700 K to 1000 K. After each anneal session, which typically lasted four hours the sample was examined using LEED. Once an anneal temperature of 970 $\pm$ 15 K had been exceeded a square LEED pattern was seen to emerge.

In fig. 4.2 we can see a (1×1) surface symmetry with respect to the conventional cubic unit cell. The first order spots correspond to a lattice periodicity of 5.7 $\pm$ 0.5 Å along the [110] and [$\bar{1}$10] directions. This then is the LEED image of unreconstructed bulk magnetite.

After obtaining square LEED patterns on the sample it was introduced into the STM system. In every STM image shown from now on the tip used is tungsten (prepared as described earlier) unless specifically stated otherwise.

In figs. 4.3 and 4.4 we see two examples of a structured cubic magnetite surface. As can be seen in these images the terraces are up to several hundred Ångstrom wide. The terraces form straight edges which align along [110], fig. 4.4. This has been identified by noting the position of the sample in the LEED

Figure 4.2: LEED image of structured magnetite surface. The [110] direction is marked. Beam energy of 95 eV.

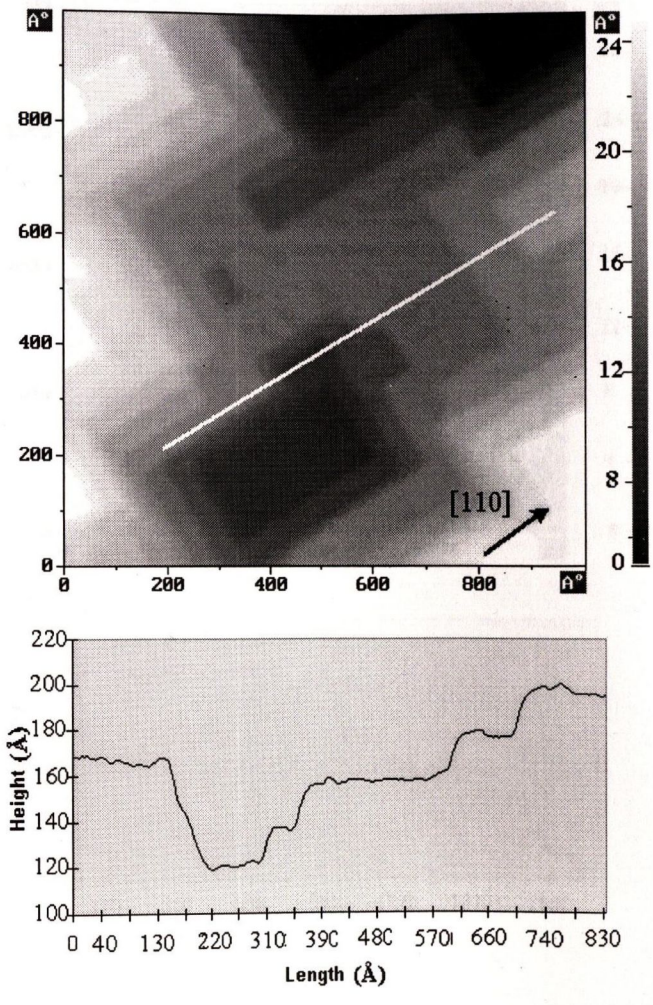

Figure 4.3: STM image of cubic terrace structures on magnetite and associated line profile. The step height between successive terraces is measured to be 2.0 ± 0.2 Å. V_{bias}= 1 V; I_{tunnel} = 0.1 nA.

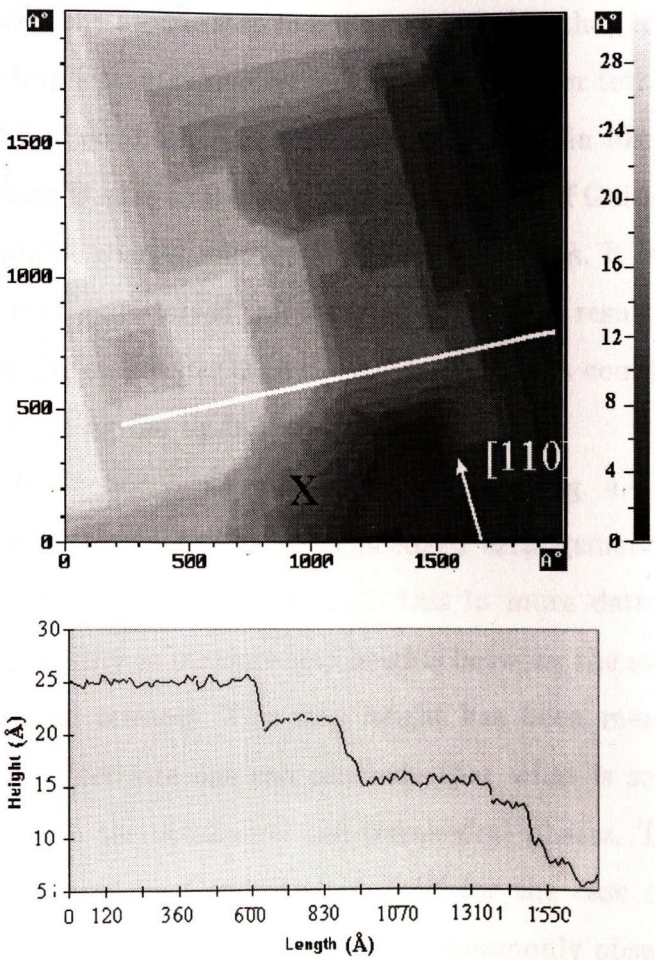

Figure 4.4: Large STM image of cubic terrace structures and associated line profile. In this image a broken terrace region is marked with an X. The [110] direction is marked. Again terrace step heights have been measured to be 2.0 $\pm$ 0.2 Å. V_{bias}= 1 V; I_{tunnel} = 0.1 nA.

and comparing this to the sample position in the STM. Using the software from both the WA scanning unit [190] and from NTMDT [31] line profiles of the terraces may be measured. These revealed terrace step heights of 2.0 ± 0.2 Å. This is twice the atomic step in bulk magnetite in the (100) direction, see fig. 3.1. The implication is that either the octahedral or tetrahedral layer is being imaged but not both. The terraces appear to join like sites, either A-sites to A-sites **or** B-sites to B-sites. Unlike the results of Gaines *et al.* [149] there is no noticeable charge build up at the terrace edges. It is conceivable that what Gaines *et al.* observed was a scanning artefact resulting from the tip scanning over the step faster than the feedback system could pull it back thus effectively crashing the tip into the step.

Upon closer inspection of the region marked X in fig. 4.4 one can see that the terraces no longer have a straight edged arrangement but form a more saw-tooth like pattern. Zooming into this in more detail in fig. 4.5 allows one the possibility to measure step heights between the straight edged and saw-tooth edged terraces. This step height has been measured to be only 1.0 ± 0.2 Å. Therefore one can conclude that what is seen here is a manifestation of both the octahedral and tetrahedral phases. This result is similar to that reported by Condon *et al.* [172] for the case of magnetite (111). However, the saw-tooth edges were not a commonly observed feature whereas the straight edge terraces were found in several scanning sessions after many anneal cycles. It would appear that the saw-tooth edges are a less stable state.

The images shown above are all for the natural magnetite crystal. Artificial crystals were also used. These were initially polished by RTI, Germany [46] using a chemo-mechanical method. Unfortunately the details of this procedure are not available. Nonetheless it is interesting to note that

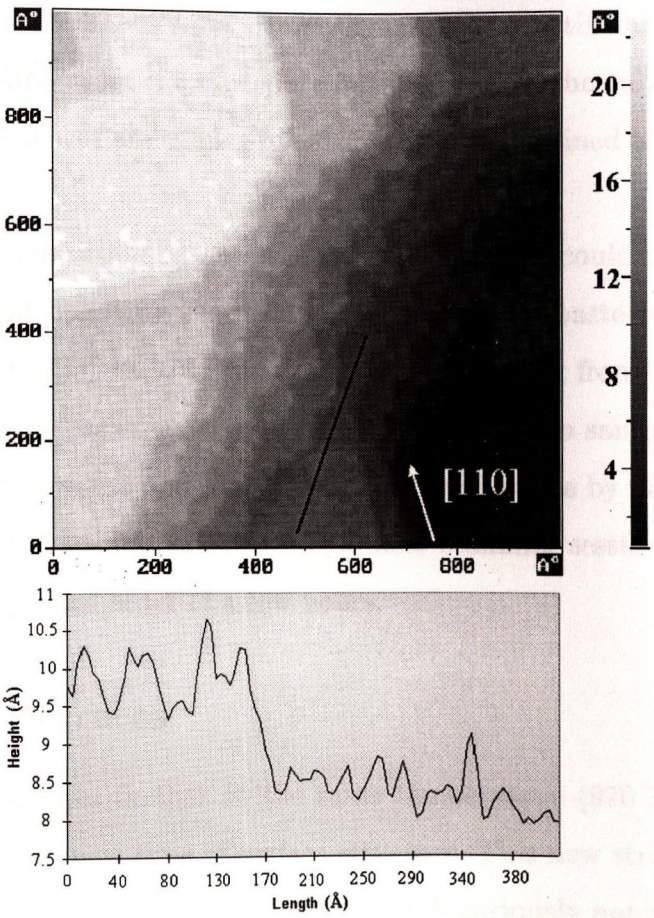

Figure 4.5: Zoom in to the area marked X in fig. 4.4. The step height (see line profile) between terraces with the saw-tooth edges and those with the straight edges is only 1.0 $\pm$ 0.2 Å. V_{bias}= 1 V; I_{tunnel} = 0.1 nA.

this polishing method produced variant surface structures after annealing at 970 ± 15 K for 4 hours, as can be seen in fig. 4.6. Even after annealing to 970 ± 15 K for more than 25 hours there are neither straight edged nor saw-toothed terraces but more rounded structures. The step heights also have been measured to be 2.0 ± 0.2 Å. However, once these artificial crystals had been hand polished using the procedure outlined earlier the cubic structures could be formed. These are similar in nature to those obtained on the natural crystal.

Finally, it is important to note that these structures could be formed at will by first hand polishing the sample using diamond paste down to 0.25 μm and then annealing at 970 ± 15 K for periods ranging from 4 to 8 hours. Therefore the structures seen could possibly be related to sample curvature or mass transfer from the polishing. They were semi-stable by nature in that they persisted on the surface for several anneal-scanning sessions where the anneal time was of the order of a few hours.

4.2.2 Nanoterraces

Annealing the samples further at the same temperature (970 ± 15 K) induced the onset of a new type of surface structure. This new structure could occasionally be seen in the LEED images though curiously not always. This is most likely due to the high step density inherent in hand polished samples due to the inaccuracies of the technique. Often the LEED patterns associated with the new surface structure were merely streaked along the [110] directions, fig. 4.7. However, occasionally satellite spots could be discerned around the principle spots in the [110] directions, fig. 4.8. These spots are approximately 1/4 of the principle spot distance thus implying a repeat structure of ~24 Å.

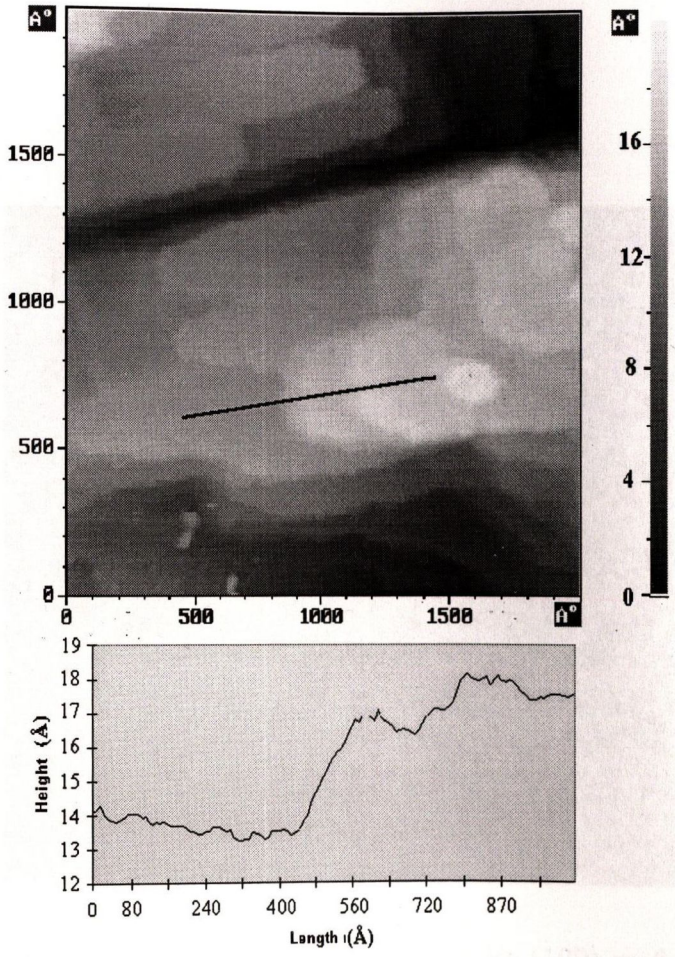

Figure 4.6: An STM image of the terrace structures seen on a magnetite surface prepared by chemo-mechanical polishing and associated line profile. The sample was annealed at 970 $\pm$ 15 K for more than 25 hours. The terrace step heights are again 2.0 $\pm$ 0.2 Å. V_{bias}= 1 V; I_{tunnel} = 0.1 nA.

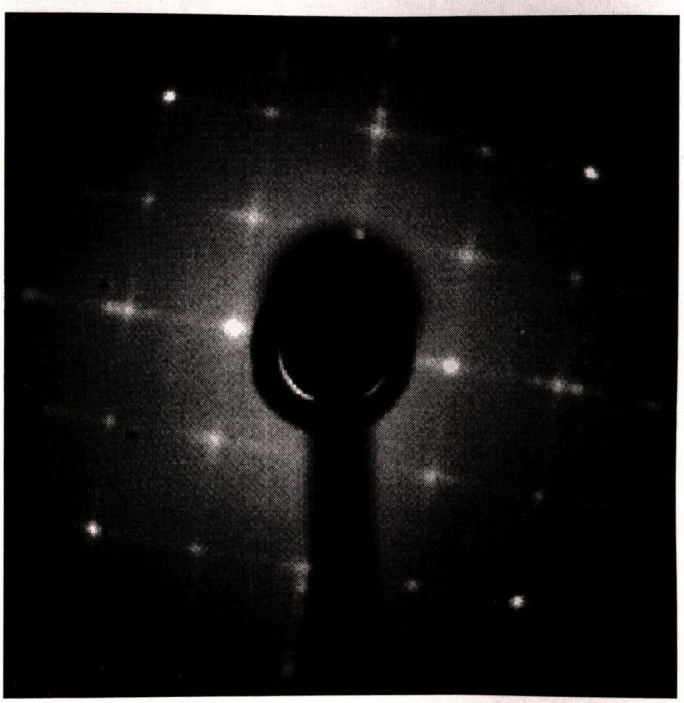

Figure 4.7: LEED image of reconstructed magnetite (100) surface. Streaking can be seen along the [110] directions. Beam energy is 96 eV.

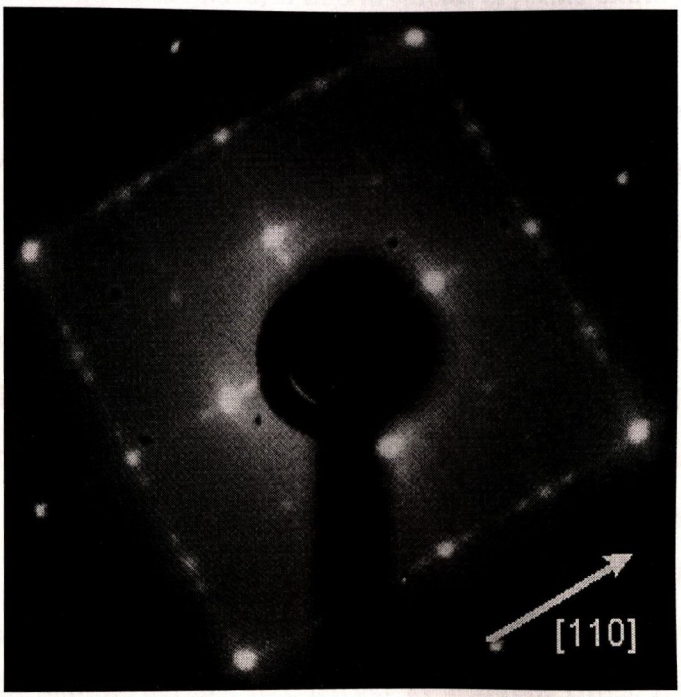

Figure 4.8: LEED image of regularly reconstructed magnetite surface as seen by Naumann [191]. Satellite spots can clearly be seen around the principle spots in the [110] direction. These satellite spots are approximately 1/4 of the principal spot distance. Beam energy is 98 eV.

The appearance of the reconstructions in the STM images occurred after a total anneal time of more than twenty hours had elapsed at an anneal temperature of 970 ± 15 K. If this was for a single anneal then the time was usually of the order of 22 hours. For sequential annealing of lesser times a total anneal time of greater than about 25 hours must elapse before the onset of reconstructions. Both the natural and artificial crystals exhibited the same behaviour.

Initially the STM images on the natural crystals revealed the reconstructions as noisy rows on the surface, fig. 4.9. However, this image was taken using an iron tip. The iron tips were found to be less stable in general than tungsten or manganese-nickel. They were prone to frequent tip changes and no atomic resolution images were obtained while using them. In fact repeating the polishing/anneal sequence for various anneal times revealed a gradual transition from square terraces to clearly defined reconstructions.

The onset and further development of reconstructions on the surface can be seen in fig. 4.10. The exact time for the transition stages is quite variable. This variation is not sample dependent but rather locally sensitive. Different locations on the sample surface reconstruct at different rates. An interesting feature of the onset of reconstructions is seen in fig. 4.11. From this figure it would appear that the reconstructions form first at the edge of the square terraces and spread inwards from there. This would imply that edge energetics play an important role in the formation of these reconstructions. Step edges are quantified for semiconductors using distribution functions such as terrace-width distribution [192] the mean-square height distribution [193], the kink length distribution function and the kink separation distribution function [194–196]. Similarly to the manner in which electron counting, which was originally formulated for semiconductors, has been extrapolated to iron

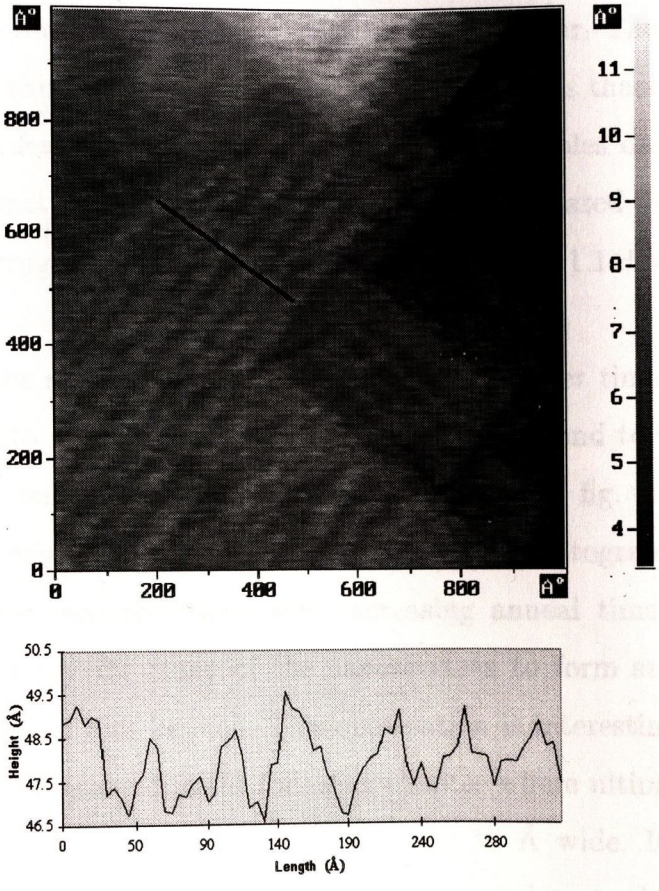

Figure 4.9: First STM image of the reconstructions on the natural single crystal. These images were taken using an iron tip which explains the poor quality. The reconstruction rows seen here are close to 40 Å wide. $V_{bias} = 1$ V, $I_{tunnel} = 0.1$ nA.

oxides it is possible that the work in semiconductor edge energetics [197] could also be valid for iron oxide studies.

In figs. 4.12 and 4.13 there are atomic scale images of the onset of reconstructions. The surface can be seen to form ripples in fig. 4.12 across the image from the bottom left corner to the top right corner. The corrugation of these ripples can be seen from the line profile to be less than 0.4 Å. After annealing for a few hours more at 970 ± 15 K the ripples can be seen to form more distinct structures (fig. 4.13). From the associated line profile we see that the corrugation at 90° to the rows is only about 1.1 ± 0.2 Å at this point.

Annealing the sample, again at 970 ± 15 K for longer times causes the reconstructions to become sharper and narrower. The trend to form narrow reconstructions can be seen using a series of histograms, fig. 4.14. The row width is plotted with respect to the occurrence in these histograms. A general shift to narrower reconstructions with increasing anneal time can clearly be seen. A tendency for many of the nanoterraces to form separations of multiples of 9 Å can also be seen. This observation is interesting in light of the models to be presented in the following chapter where ultimate stability appears to lie with nanoterraces approximately 18 Å wide. It is possible that 9 Å is the minimum unit that can be subtracted from the width of a nanoterrace. The times quoted above each histogram is further anneal time after the initial observation of reconstructions. This would seem to suggest that the narrow reconstructions are more favourable. Some examples of very clearly resolved reconstructions are shown in figs. 4.15 and 4.16.

The separation between reconstructions ranges from 24 to 40 ± 3 Å. Where the separation is large, it is easy to measure the corrugation perpendicular to the reconstruction direction and this has been measured to be 2.0

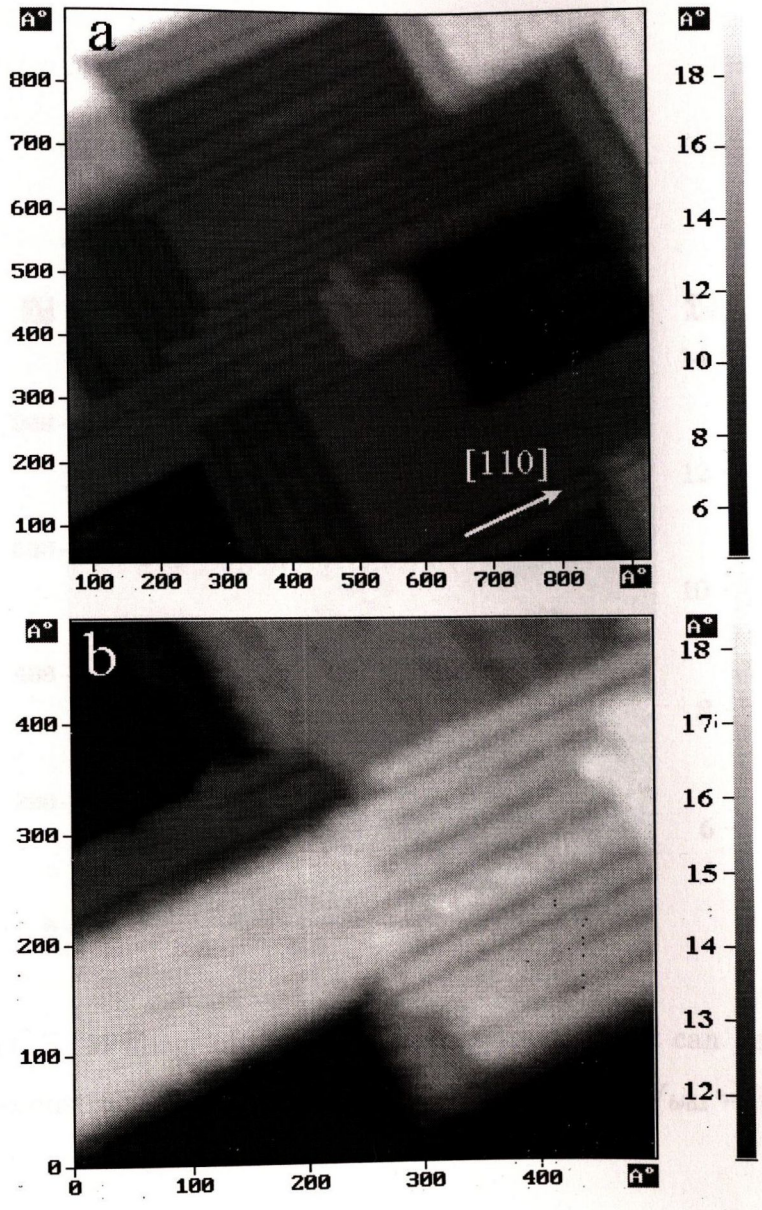

Figure 4.10: STM images of the formation of reconstructions. The remnants of flat square terraces can be seen to split along the [110] directions. These splits extend to differing degrees along the terraces. $V_{bias} = 1$ V, $I_{tunnel} = 0.1$ nA.

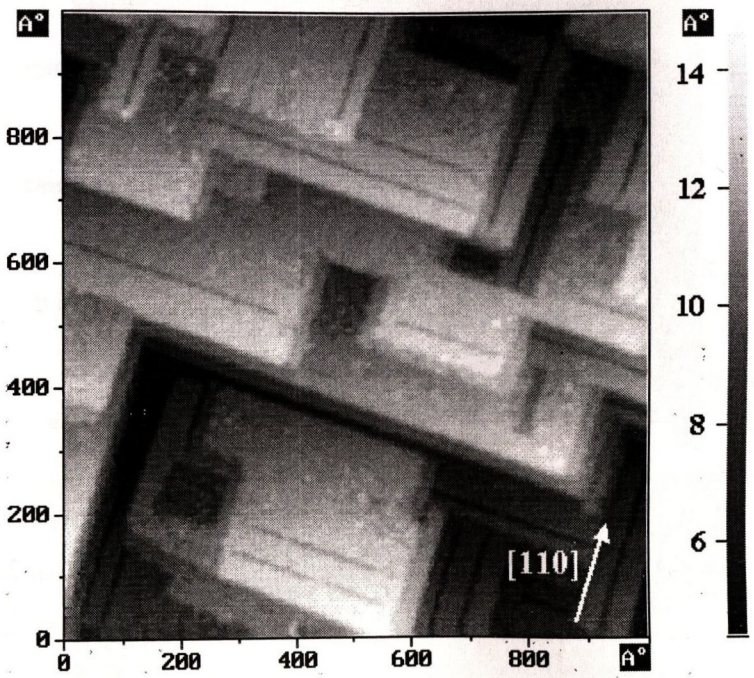

Figure 4.11: STM image of the onset of reconstructions. It can be seen here that the reconstructions begin near the edge of a terrace. V_{bias} = 1 V, I_{tunnel} = 0.1 nA.

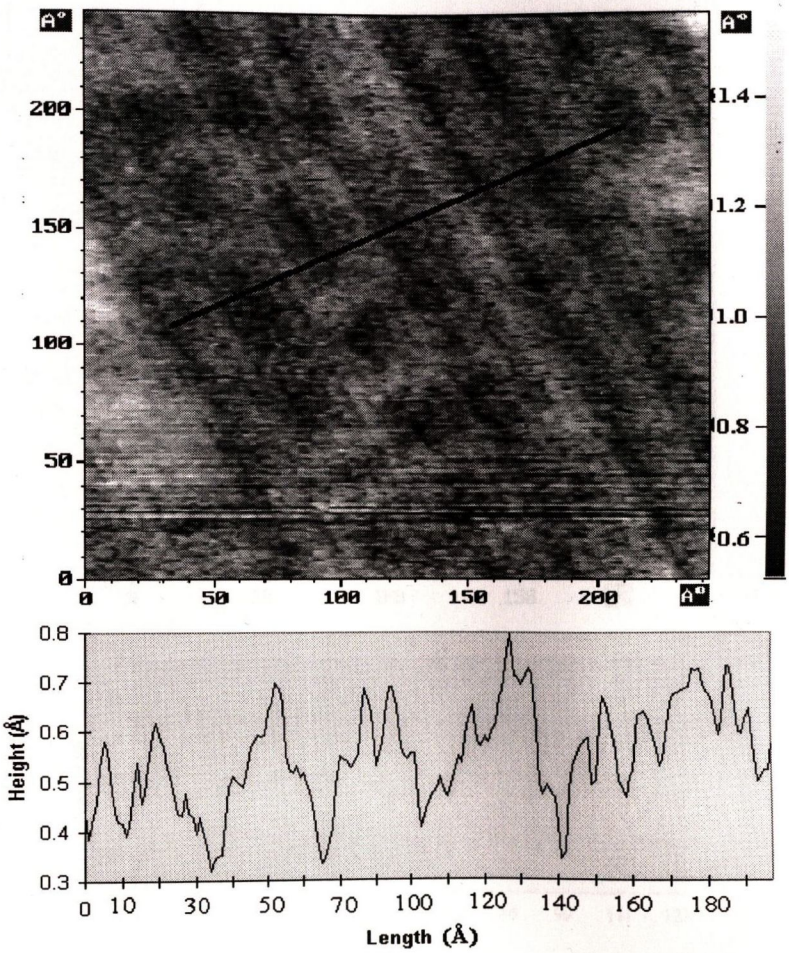

Figure 4.12: Atomic scale image of the onset of reconstructions. The surface can be seen to form ripples with a corrugation of less than 0.4 Å. $V_{bias} = 1$ V, $I_{tunnel} = 0.1$ nA.

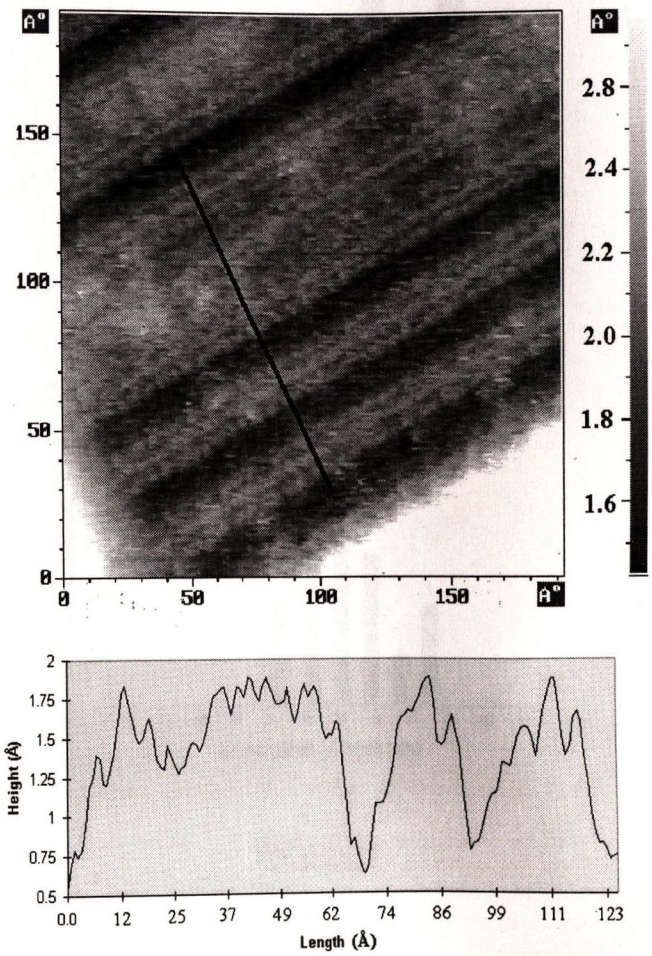

Figure 4.13: A second atomic scale image of the onset of reconstructions. In this image we see the formation of reconstruction structures though in the line profile the corrugation is still only 1.1 Å. $V_{bias} = 1$ V, $I_{tunnel} = 0.1$ nA.

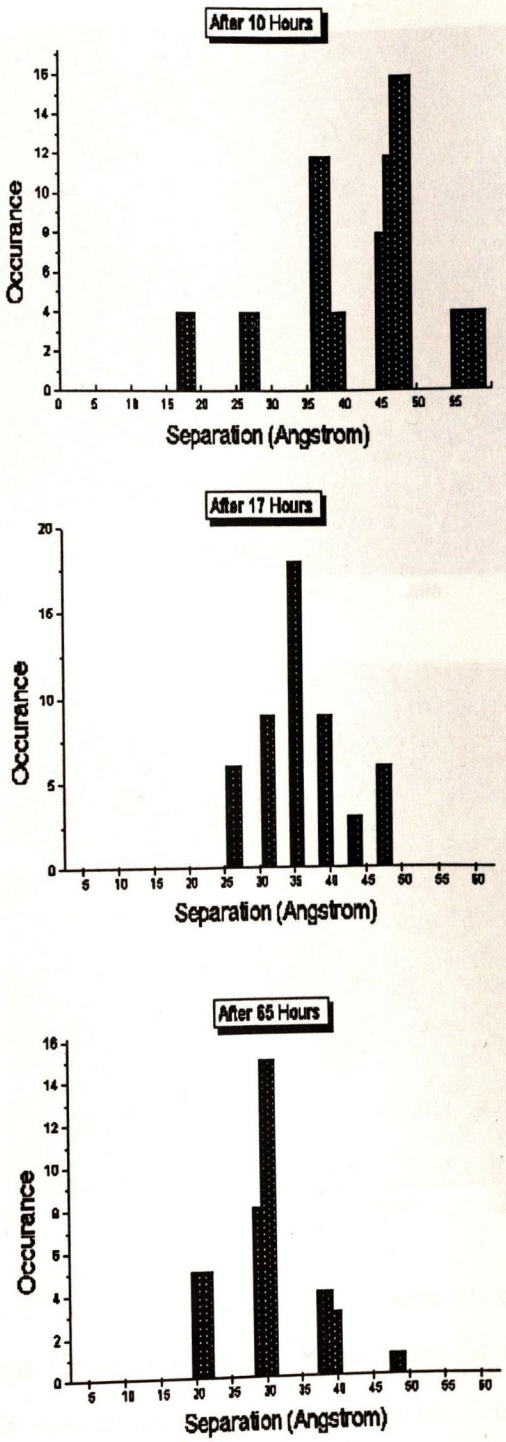

Figure 4.14: A series of histograms showing how the reconstructions become gradually narrower with increasing overall anneal time. The times quoted are for additional annealing after the onset of reconstructions is observed.

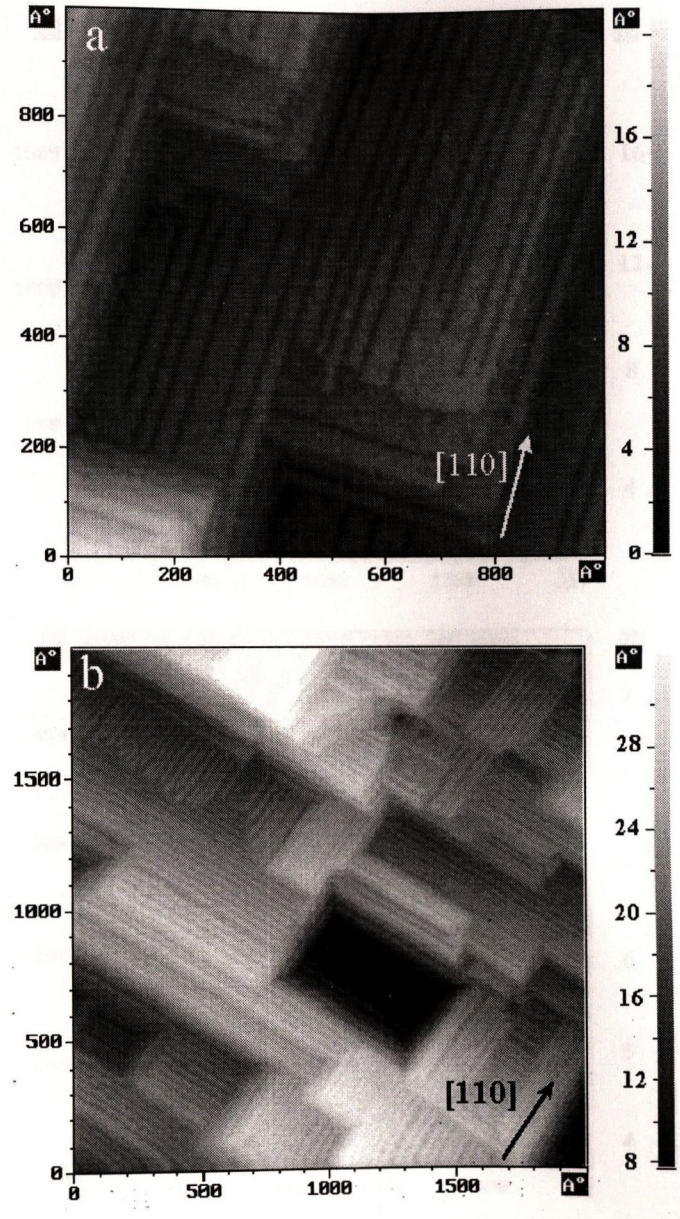

Figure 4.15: Two STM images of reconstructions on magnetite (100). The separation between the nanoterraces ranges from 24 to 40 Å. The lack of uniformity of this separation can clearly be seen. The [110] direction has been marked on the images. $V_{bias} = 1$ V, $I_{tunnel} = 0.1$ nA.

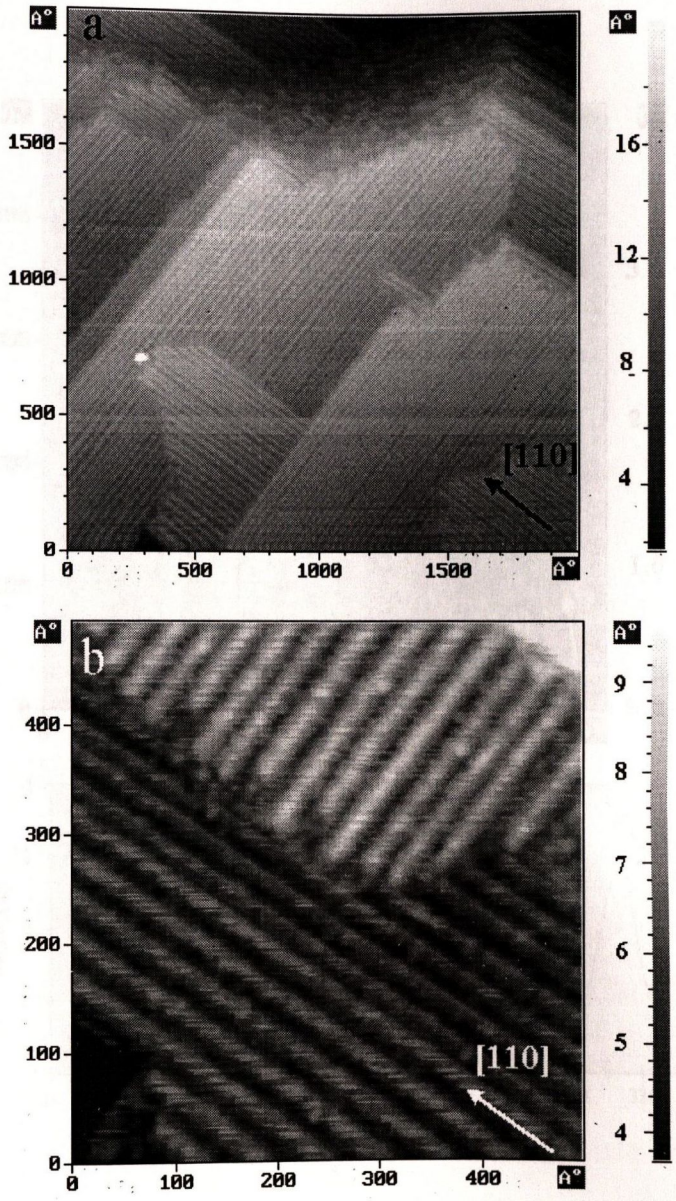

Figure 4.16: Two more STM images of reconstructions on magnetite (100). There is no discernible pattern in the corrugation along the reconstructions at this point. The [110] direction has been marked on the images. $V_{bias} = 1$ V, $I_{tunnel} = 0.1$ nA.

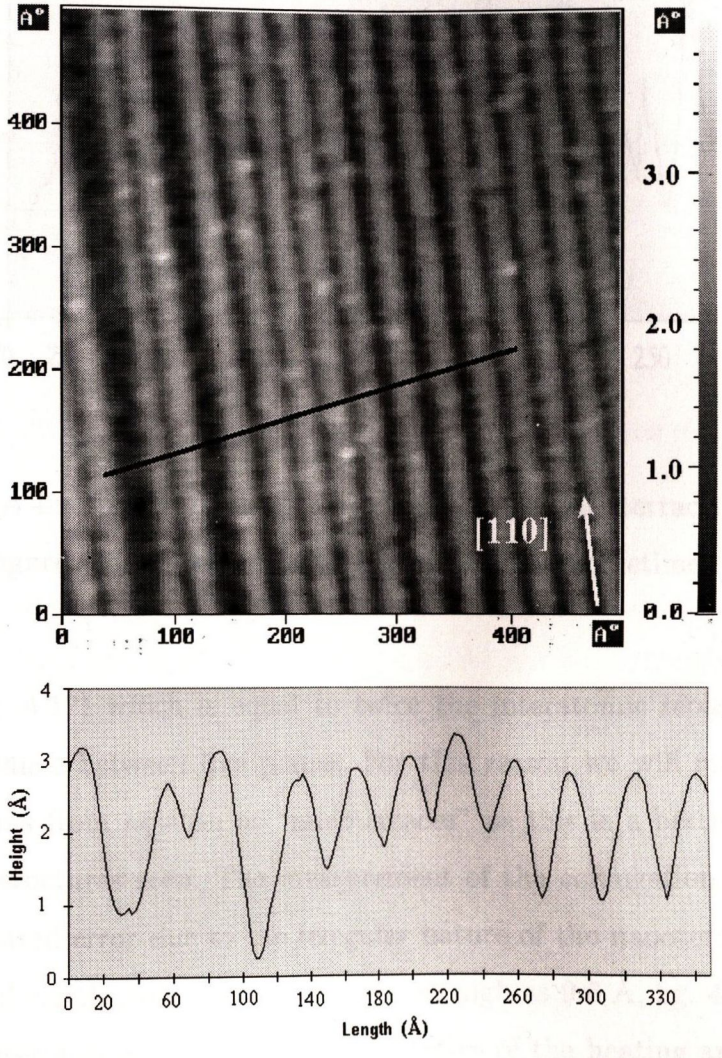

Figure 4.17: The range of separation distances between nanoterraces is clearly demonstrated in this image. Some software smoothing has been done for clarity in the line profile $V_{bias} = 1$ V, $I_{tunnel} = 0.1$ nA.

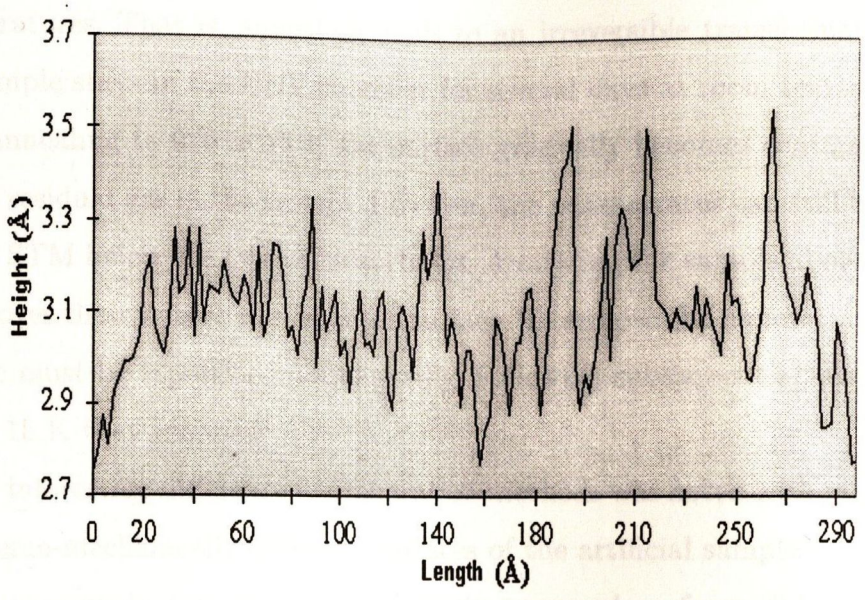

Figure 4.18: A line profile of the corrugation along a nanoterrace. It can be seen in this figure that the corrugation is irregular and sometimes as high as 0.6 Å.

± 0.4 Å (fig. 4.17) which is equal to twice the interatomic separation i.e. it is the distance between like planes. For this reason we will refer to the reconstructions from now on as "nanoterraces" as this is a better description of the structures seen. The measurement of the corrugation has quite a high associated error due to the irregular nature of the nanoterraces. The corrugation along the nanoterraces may be as high as 0.6 Å, fig. 4.18.

The nanoterraces appear to form irrespective of the heating and cooling time used. Cooling times varying from 30 minutes to 9 hours were used without any noticeable change in the surface structure. Similarly the time taken to heat the sample to its final temperature appeared to have no effect.

It is important at this point to emphasise that once the nanoterraces appeared on the surface by annealing at 970 ± 15 K they persisted even at lower

temperatures. That is, annealing leads to an irreversible transformation. If the sample stays in the UHV chamber for several days at room temperature after annealing to 970 ± 15 K the surface gradually becomes contaminated by the residual gas in the system. However, the nanoterraces can still be seen by the STM below the layer of adsorbates. Annealing the sample above ~900 K removes these adsorbates from the surface. To remove the nanoterraces the surface must be repolished mechanically. Following subsequent annealing to 970 ± 15 K they reappear.

An interesting difference in preparation methods was noted with regard to the chemo-mechanically prepared surfaces of the artificial samples. As mentioned previously the chemo-mechanically prepared surfaces did not form cubic structures upon annealing to 970 ± 15 K. Instead the terraces were more rounded, fig. 4.6. Annealing the sample at 970 K subsequent to the formation of these rounded terraces did not induce nanoterraces. Even at temperatures in excess of 1000 K the surface did not reconstruct. In fact it simply became more unstable to tunneling thus indicating that most likely a conversion to another iron oxide was occurring, e.g. to FeO or Fe_2O_3 etc. However, once the artificial samples had been repolished using the mechanical method described earlier they behaved like the natural crystals. The nanoterraces began to appear after a total anneal time in excess of twenty hours had elapsed. The dimensions of the nanoterraces are identical in nature to those on the natural crystals in terms of corrugation, separation and orientation. This would seem to indicate that the nanoterraces are naturally the most thermodynamically stable state under the conditions imposed.

4.2.3 Atomic resolution

Although most of the atomically resolved images will be dealt with in chapter 5 a number of them are relevant to this discussion. They are the images of atomic rows obtained in or around the nanoterraces. Atomic rows have been resolved previously on magnetite without any pattern of corrugation along the rows [26].

After annealing the nanoterraced surface to 1000 K and above some areas on the surface were found to resolve better. Scanning in these areas one could see an absence of nanoterraces but atomic rows running along the [110] directions could be made out (fig. 4.19). These rows have a separation of 5.8 ± 0.3 Å, as one would expect for iron rows on magnetite (100). After annealing to higher temperatures the surface becomes more unstable for tunneling. This is most likely due to the formation of other iron oxides which are more stable at higher temperature. However, as these oxides are insulators they are less suitable for STM measurements.

Atomic rows were also later found on the nanoterraces themselves (fig. 4.20). These are also separated by 5.8 ± 0.3 Å and run along the length of the nanoterrace. However, at this stage the resolution of these atomic rows was not such that a coherent model could be made.

4.3 Analysis

The most interesting feature of the cubic terrace structure is the 2.0 ± 0.2 Å separation between the terraces in the z-direction. The implication of this is that the tetrahedral and octahedral terminations cannot co-exist on the (100) surface. This result is similar to that observed previously for magnetite (100) [42] and contrary to the findings of Lennie *et al.* [173] for the (111)

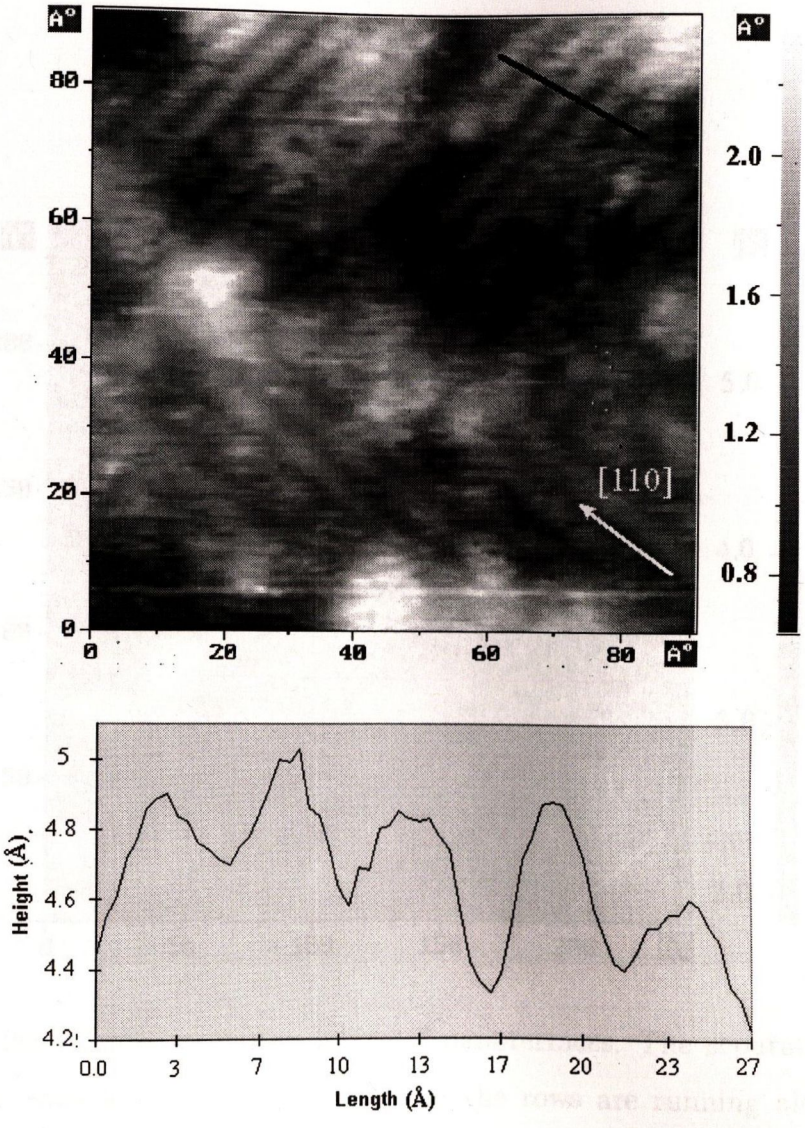

Figure 4.19: Atomic resolution image of magnetite (100) surface and associated line profile. The rows rotate by 90^o on alternating terraces and are aligned along [110]. The separation between the rows is 5.8 $\pm$ 0.3 Å. The nanoterraces are not present in this area. V_{bias} = 1 V, I_{tunnel} = 0.1 nA.

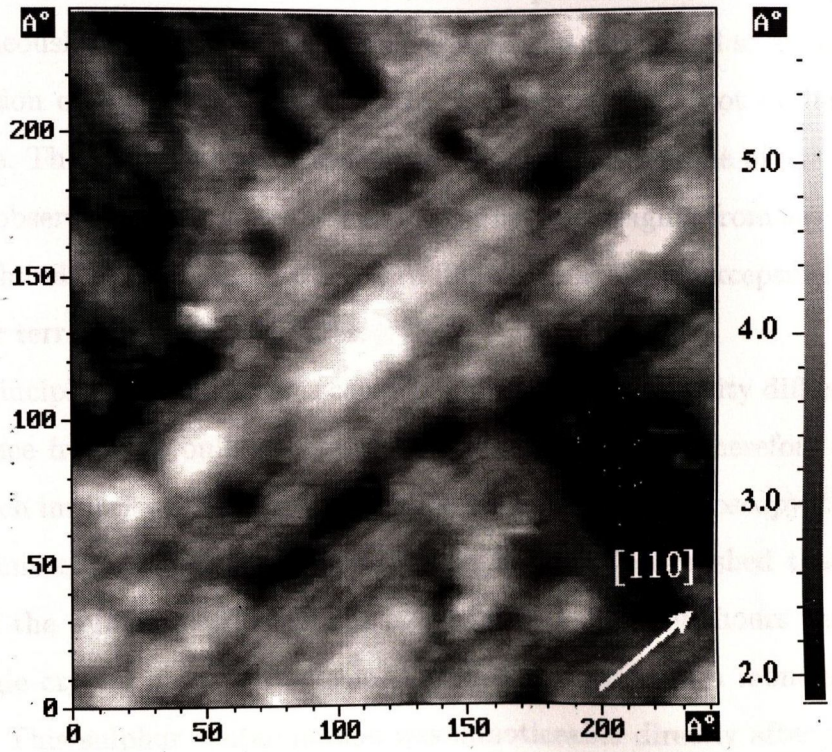

Figure 4.20: Atomic resolution image of nanoterraces. The separation between the rows is again 5.8 ± 0.3 Å and the rows are running along the nanoterraces. $V_{bias} = 1$ V, $I_{tunnel} = 0.1$ nA.

surface. In fact from an intuitive examination one would not really expect to find two inequivalent phases (i.e. simultaneous existence of individual octahedral and tetrahedral terraces on magnetite (100) surfaces) coexisting in equilibrium with the bulk [159]. This was seen by Lennie *et al.* on (111) and it is thought that in their case a surface phase decomposition hindered equilibrium. However, it seems that on occasion it is possible to have both phases simultaneously, fig. 4.5. Such images were only seen rarely and so a complete explanation of the conditions leading to their formation is not available at this time. The saw-tooth terraces resemble to some degree one of the terminations observed by Lennie *et al.* on (111). The step heights from saw-tooth to straight edged terraces is 1.0 ± 0.2 Å. This then is a rare exception to the rule that terraces connect like sites.

In principle the nanoterraces could be caused by an impurity diffusing to the surface from the bulk as a result of the annealing. We therefore examined which impurity diffuses from the bulk using Auger spectroscopy, though at the time the AES was not very reliable. We have established that as a result of the anneal at 970 ± 15 K over a period of twelve hours the natural single crystal accumulated some significant fraction of a monolayer of sulphur. This sulphur contamination was unnoticeable directly after polishing and introducing the sample into UHV but thereafter gradually increased with increasing temperature and annealing time. This could therefore be one possible explanation for the increase in the sharpness of the nanoterraces and the more regular spacing between the rows with anneal time. However, the experiments with the artificial crystal do not support this conclusion. Auger analysis of the artificial samples showed no noticeable sulphur contamination even after annealing to in excess of 970 K. Bearing in mind that the Verwey transition temperatures for the artificial and natural crystals differ by about

20 K (thus indicating a significant off-stoichiometry in the natural crystal and almost ideal stoichiometry for the natural crystal) we can suggest that the transformation of the surface to the state with nanoterraces is in fact a transformation towards a more thermodynamically stable state. In other words, the surface as mechanically polished is not in thermodynamic equilibrium and annealing is required for the surface to reach equilibrium. The equilibrium state appears to be the one consisting of rows with a periodicity of some 24 Å and a corrugation of 1.8 ± 0.3 Å. It is difficult to quantify the height of the rows of the reconstructions more precisely because of the corrugation along the rows which can be as high as 0. 6 Å (fig. 4.18). A simple pattern of periodicity in the corrugation along the rows could not be established at this point in the study.

The chemo-mechanically polished samples did not transform to the equilibrium state of nanoterraces. This may be understood by considering that the stoichiometry of a sample prepared in this way could be significantly different from that of the bulk-terminated magnetite. Effectively the surface could be modified to the extent that it becomes another stable form of iron oxide, e.g. FeO.

There is a clear reason why the magnetite (100) surface forms a stable combination of two atomic planes in each terrace. It is based on charge counting arguments. The fact is that each atomic (100) plane of magnetite, either with octahedral or tetrahedral iron is not charge neutral. Therefore, if a surface of magnetite were a plane of the bulk termination, the surface energy would have been theoretically infinitely large due to the Coulomb interaction [153]. It appears that, after mechanical polishing, the surface is in a state where it consists of the bulk terminated planes. However, as a result of the annealing a transformation occurs and each pair of planes, octahedral

and tetrahedral, combine to form a charge neutral combination to reduce the surface energy. It is important to note that in other common types of iron oxide, such as FeO or Fe_2O_3, the (100) atomic planes are charge neutral.

A second argument against the formation of bulk terminated planes on the surface is based on electron counting (see chapter 3) [147]. As outlined in chapter 3 this argument was extended to oxides by LaFemina [142] and the basic argument suggests that a minimum in the surface energy occurs when all the oxygen dangling bonds are filled and all the iron dangling bonds are empty. Assuming all the atoms on the surface have the same valency that they would have in the bulk (an assumption used by Gaines *et al.* [149] amongst others though still somewhat questionable) it was shown in chapter 3 that there is a total of 3 missing electrons per unit cell on a bulk-terminated surface. (This result is obtained by ignoring any tetrahedral iron from the plane above the topmost octahedral Fe-O plane and is similar in nature to the result where there are three excess electrons by terminating with a complete tetrahedral plane.) The missing electrons may be satisfied either by adding extra atoms to the surface unit cell or by reconstructing the surface in some manner so as to allow for charge sharing [149].

It is important to emphasise that although magnetite has been the subject of active surface investigations in recent years [148,168], including STM investigations [149,171], many of these studies could not be done under the conditions to which the samples in this study have been exposed. This applies in particular to surfaces studies on single crystalline thin films of magnetite which are in fact the most commonly studied. Such films are commonly grown on substrates of single crystalline MgO because of its good lattice match with Fe_3O_4. However, MgO is well known to diffuse to the surface from the substrate at temperatures as low as 625-675 K [198], which is 300 K lower than

the temperature required to obtain the reconstructions reported here. The diffusion of Mg at 670-700 K is so fast that a monolayer of Mg is formed on the surface of Fe_3O_4 in a matter of seconds [156]. The study carried out by Tarrach *et al.* was also on a natural crystal of magnetite with (100) orientation. However, the results presented here and those of Tarrach differ significantly in the surface structures seen. This can most likely be accounted for by the fact that the anneal temperature used by Tarrach *et al.* was approximately 100 K lower than that required to form the reconstructions reported above.

4.4 Conclusions

It is seen that at an anneal temperature of 970 $\pm$ 15 K for periods of approximately four hours the (100) surface of magnetite forms a cubic terraced structure with terrace separations of 2.0 $\pm$ 0.2 Å. Such a structure covers almost the entire surface. This implies that only octahedral **or** tetrahedral terraces are imaged, as opposed to imaging both simultaneously. However, due to the proximity of the planes (marked 1, 2 and 3 in fig. 3.1) one cannot rule out the possibility of some form of octahedral/tetrahedral combination at the surface. Further annealing (until a total anneal time of some twenty hours has elapsed) induces orthogonal rows running along the [110] directions and rotated by 90° between every second terrace separated by 2.0 Å in the z-direction which persist at room temperature. This orthogonality suggests the octahedral iron has a strong influence on the surface structures since from fig. 3.1 it can be seen that the octahedral iron atoms form rows which rotate by 90° every 2.1 Å into the bulk. However, the tetrahedral iron atoms at the surface have dangling bonds which point along the [110] directions and also rotate by 90°.

Though the structures seen could be attributed to sulphur contamination from the bulk in the natural crystal, comparison with artificial crystals do not support this. The most likely explanation is that the surface of magnetite has a stability transition point at a temperature (in UHV) close to 970 ± 15 K. This transition is driven by electron counting or charge balancing conditions and the structure formed is probably a combination of tetrahedral and octahedral planes.

Of the two main structures seen it is conceivable that the former, the square terraces, is a metastable state of magnetite. The latter state, the nanoterraces, is the stable state.

4.5 Other surface structures

A series of experiments, with the aim of producing a clean magnetite surface, was performed using annealing in oxygen and, later, argon ion sputtering. The range of possible parameters with regard to oxygen partial pressure, anneal temperature in oxygen or vacuum, anneal time, energy of argon ions, length of bombardment time, temperature of sample before during and after bombardment etc. is enormous and would take considerable time to investigate fully. In order to narrow the parameters somewhat one can use the values of other groups as a starting point. Therefore when annealing in oxygen an oxygen partial pressure of 7×10^{-6} mbar was used. The sample was annealed to 970 ± 15 K for three hours at this pressure. At this point, due to experimental conditions, the sample was brought up to atmosphere. Thereafter it was annealed in an oxygen partial pressure of 3×10^{-6} mbar at 985 ± 15 K for two hours. Then the oxygen was pumped away and the sample was annealed at this temperature for a further two hours. The results of this were

very unexpected.

In figs. 4.21 and 4.22 STM images, of progressively smaller size, are presented. The most striking feature of the surface now is the square holes. These appear to be scattered randomly about the surface. The terraces can clearly be seen though they are not well ordered relative to the results presented above. The terrace steps are ~2.0 Å as one would expect for magnetite (100) - see above. The deepest holes are 23 ± 2 Å deep. Other holes (fig. 4.21) are only 2.0 ± 0.3 Å deep. There are also some smaller holes (fig. 4.22) which appear to be square and are also about 2 Å deep. It is conceivable that the smaller holes seed the growth of the larger ones though further work is needed to draw any firm conclusions from these images.

Further annealing at 970 ± 15 K in UHV saw the return of the familiar nanoterraces. Thereafter argon sputtering was used in an attempt to remove these. The ions were accelerated using 1.0 keV for 12 minutes with no sample heating. Then the sample was heated to ~800 K for 8 minutes while the etching continued. Annealing continued after that at the same temperature for a further 20 minutes with no sputtering. The temperature of 800 K quoted is somewhat dubious because it takes several minutes for the sample and heater to reach thermal equilibrium. However, this treatment seemed sufficient to remove the nanoterraces (fig. 4.23). After the removal of the nanoterraces the sample was argon ion etched yet again. This time an accelerating energy of 1.5 keV was used for 10 minutes with no sample heating and then for a further 25 minutes with the sample heated to 900 K (again an approximate value). Finally the sample was annealed for another 10 minutes at 900 K with no etching. The results of this can be seen in figs. 4.24 and 4.25.

Fig. 4.25 is a STM zoom into fig. 4.24. The clusters seen in these images were never observed in this series of experiments before or after this. They

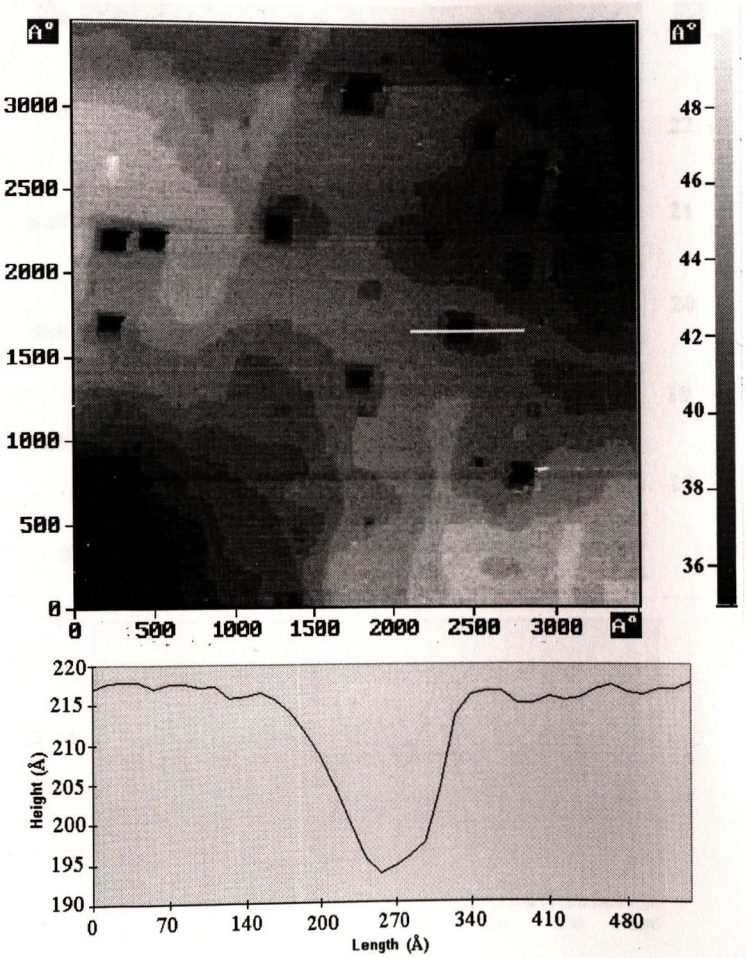

Figure 4.21: STM image of the magnetite sample after annealing in oxygen at 7×10^{-10} mbar, bringing up to atmosphere and annealing in 3×10^{-6} mbar of oxygen at 985 ± 15 K. From the line profile we see that the deepest holes are approximately 23 Å deep. $V_{bias} = 1$ V, $I_{tunnel} = 0.1$ nA.

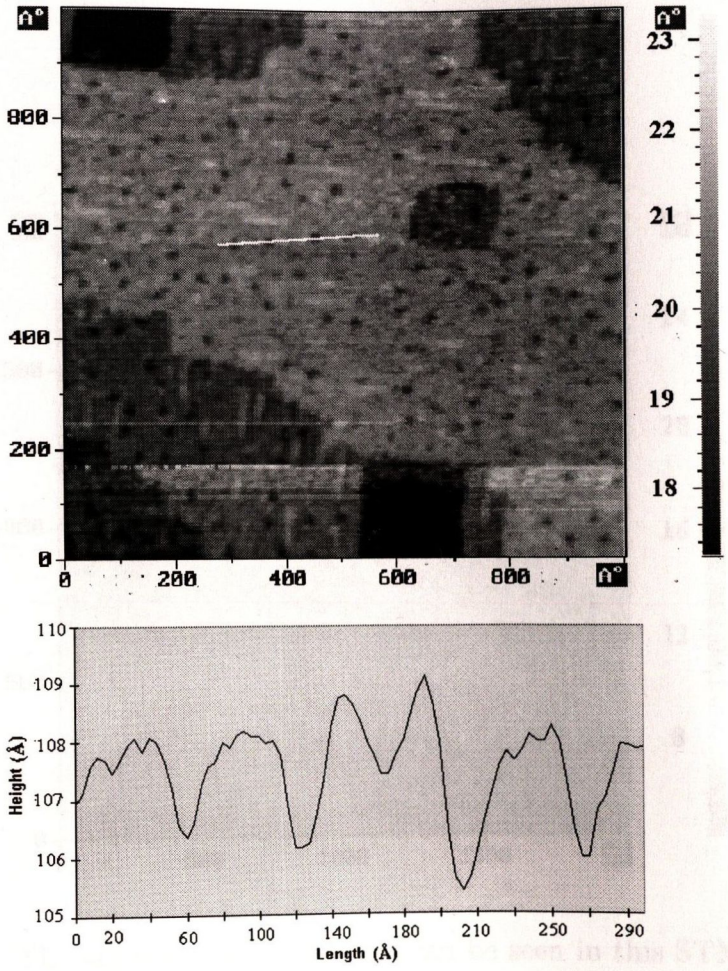

Figure 4.22: Smaller STM image of the magnetite sample after annealing in oxygen at 7×10^{-10} mbar, bringing up to atmosphere and annealing in 3×10^{-6} mbar of oxygen at 985 ± 15 K. From the line profile we see that the small holes are approximately 2 Å deep. $V_{bias} = 1$ V, $I_{tunnel} = 0.1$ nA.

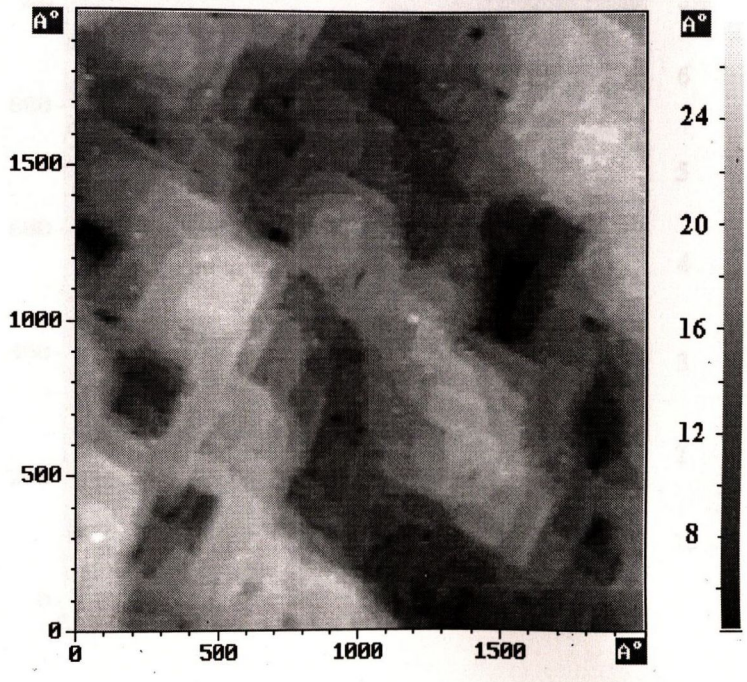

Figure 4.23: The argon ion bombardment can be seen in this STM image to have removed the nanoterraces. $V_{bias} = 1$ V, $I_{tunnel} = 0.1$ nA.

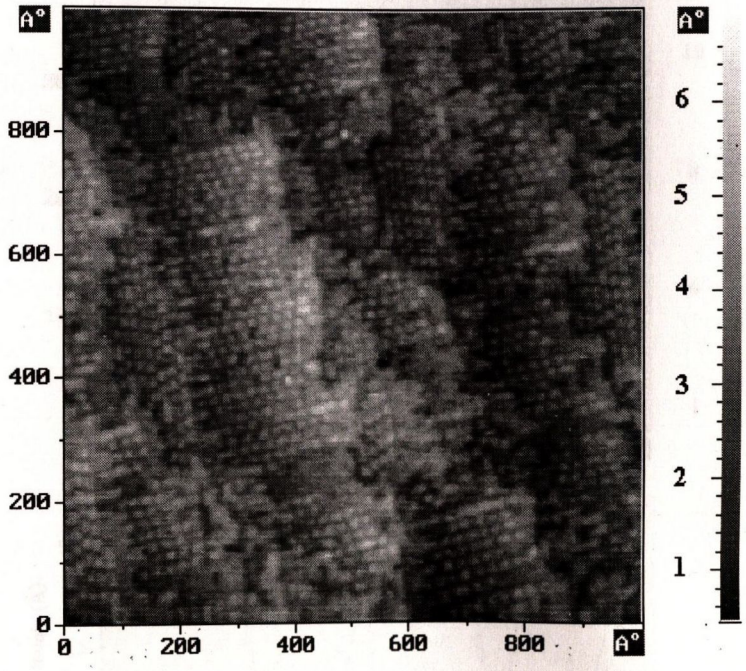

Figure 4.24: Further argon ion etching and annealing induces the formation of clusters on the surface similar to those seen by Gaines *et al.* on MBE grown magnetite (100). $V_{bias} = 1$ V, $I_{tunnel} = 0.1$ nA.

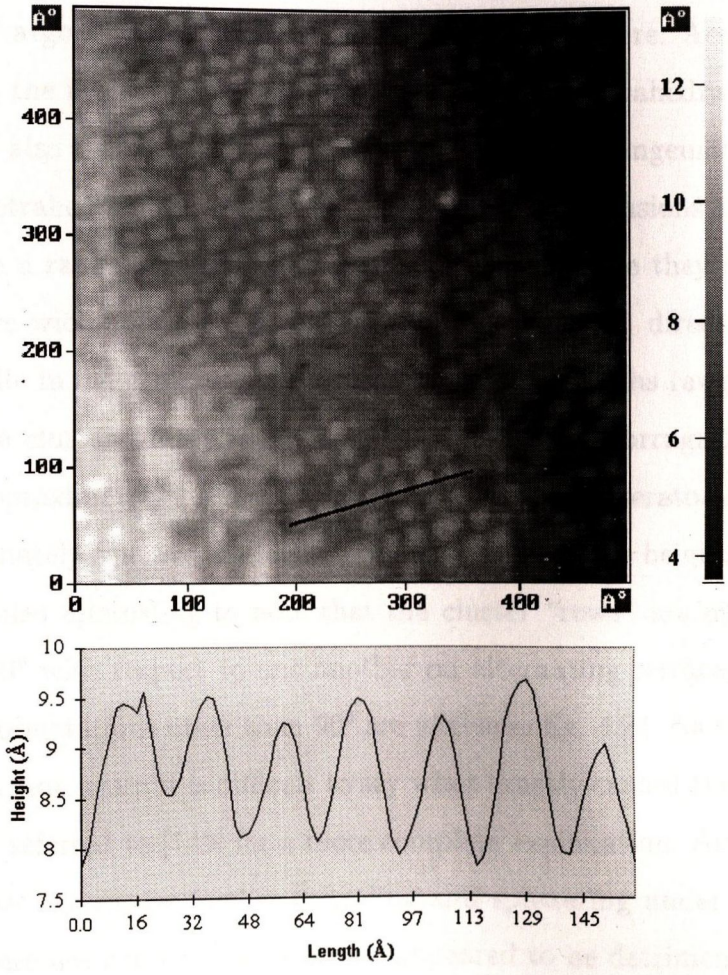

Figure 4.25: Zoom into fig. 4.24 with some software smoothing for the line profile. The line profile outlines the size of the clusters. V_{bias} = 1 V, I_{tunnel} = 0.1 nA.

are similar in nature to the clusters reported by Gaines *et al.* [149] on MBE grown magnetite (100). This is noteworthy, that almost identical results can be produced on single crystals and thin films. The anneal temperatures used by Gaines *et al.* are similar to those used here. However, Gaines *et al.* used only 500 eV argon ions compared to the 1.5 keV used here. According to Gaines *et al.* the reconstruction to clusters is driven by tetrahedral dangling bonds. They also claim that the clusters are a complex arrangement of octahedral and tetrahedral atoms which is in line with the conclusions above. The clusters have a range of lengths and widths but on average they are longer than they are wide and appear to elongate along the [110] direction. From the line profile in fig. 4.25 we can see that the cluster lengths range from 10 to 17 Å. The cluster widths range from 8 to 12 Å. The corrugation of the clusters is approximately 1.8 Å which is nearly twice the interatomic spacing and approximately equal to the terrace step and nanoterrace heights outlined above. It is also interesting to note that the cluster "rows" are not exactly rotated by 90° with respect to one another on alternating terraces. Several examples of orientations other than 90° are visible in fig. 4.24. As these clusters were not seen again it is difficult to say what exactly caused them and so the reader is referred to [149] for a more complete explanation. Attempts to reproduce the clusters by further annealing and sputtering under the same conditions were not successful and in fact appeared to be detrimental to the surface in terms of tunneling stability. Only when the sample had once again been annealed to 970 ± 15 K did the nanoterraces reform.

In fig. 4.26 STM images are presented of the nanoterraces using a novel tip arrangement. The tips used were tungsten with a 20 monolayer film of iron deposited using e-beam evaporation. Although these tips would be ideal for spin polarised experiments due to the lack of magnetostriction (compared

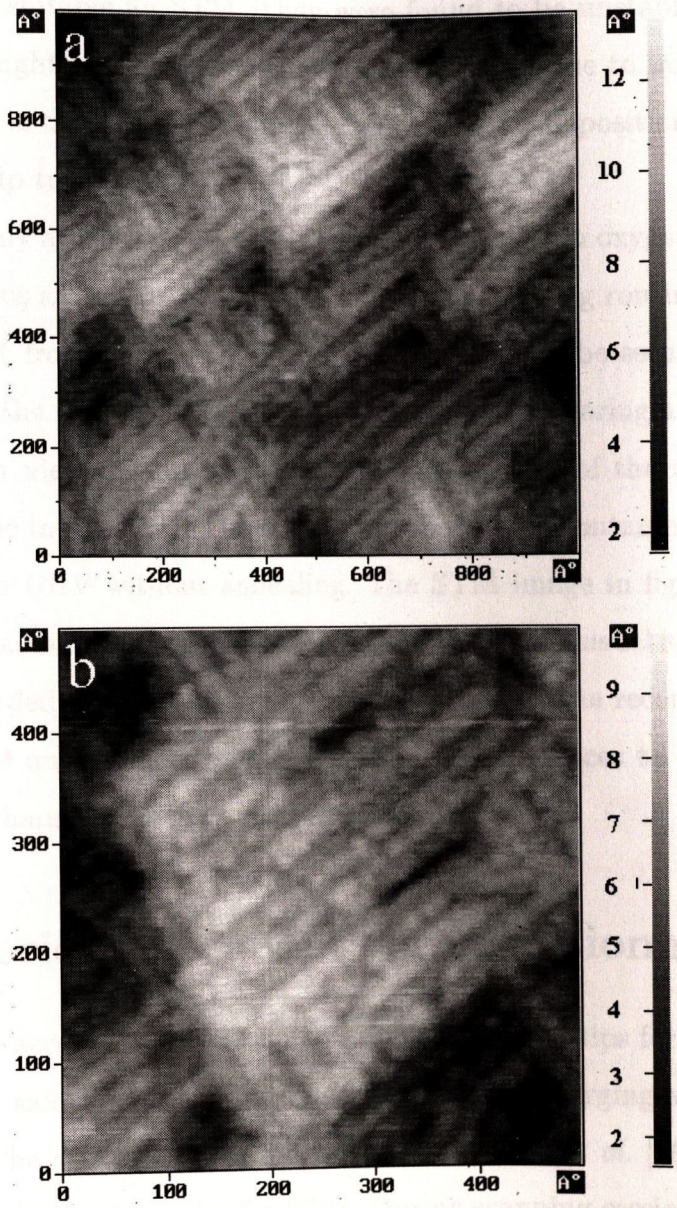

Figure 4.26: STM images using a tungsten tip covered with an e-bean evaporated 20 monolayer iron film. Although the nanoterraces can be made out in these images the resolution is poor and the tips were found to be quite unstable and prone to frequent changes. $V_{bias} = 1$ V, $I_{tunnel} = 0.1$ nA.

with pure iron tips under application of an external magnetic field) they are not, however, suitable for STM. They were found to be unstable and prone to frequent height and resolution changes presumably due to iron migrating at the end. It is thought that annealing the tips after deposition of the iron film would help to stabilise them.

It is not only argon ion bombardment and annealing in oxygen which produce anomalous structures. They were also formed during routine annealing to 970 ± 15 K from time to time. Such a structure can be seen in fig. 4.27. In this image the nanoterraces can be seen to have a smearing around them. This has been measured to be ∼ 0.8 Å below the top of the nanoterraces (see line profile in fig. 4.27). The surface had been very contaminated due to a long time in UHV without annealing. The STM image in fig. 4.27 is the result of several annealing sessions at 970 ± 15 K. This unusual surface structure was recorded only once. Perhaps it is the onset of the recombination of the octahedral and tetrahedral layers forming nanoterraces to stabilise the surface or perhaps it is merely a tip artefact.

4.6 A brief note about tip conditioning

It is generally accepted that obtaining atomically sharp tips for STM is difficult. Having said that a number of techniques are emerging at present to rectify this. The sputter-anneal process of Albrektsen *et al.* [199] routinely produces atomically sharp tips for STM. During scanning sessions it is common practice to attempt to hone the tip by means of "controlled crashing". This normally involves scanning the tip rapidly over different areas in the hope of picking up or losing something from the end of the tip. However, in the author's experience the best way to condition tips with magnetite is

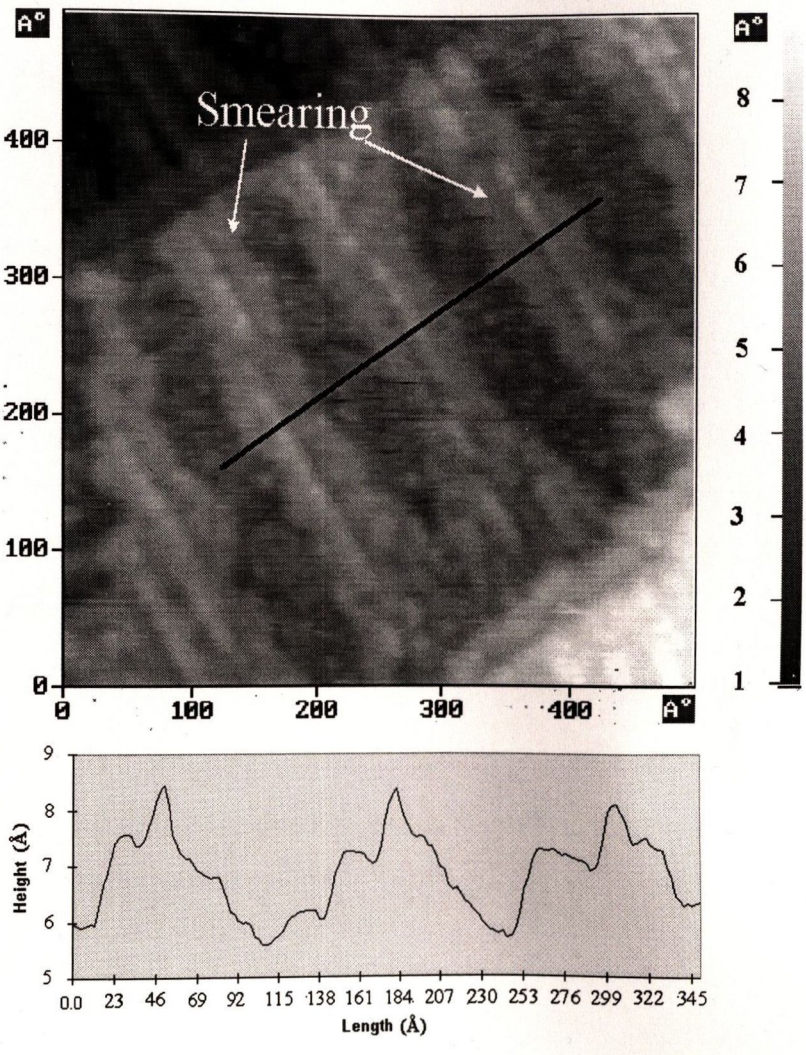

Figure 4.27: Anomalous surface structure seen only once. Perhaps this is the onset of nanoterrace formation or the combination of octahedral and tetrahedral terraces. $V_{bias} = 1$ V, $I_{tunnel} = 0.1$ nA.

by means of long, slow scans over very large areas - of the order of microns. Many materials can be scratched by the tip but with magnetite this usually leaves the surface undamaged and provides a sharp tip.

Chapter 5

Atomic scale structures

".....there is no doubt that the atomic geometry of a surface is its most fundamental characteristic. Any serious scientific effort to determine the electronic structure and properties of an interface must start with a realistic description of its atomic geometry...."

Dr. C.B. Duke, Keynote address to the Second International Conference on Solid Films and Surfaces

5.1 Introduction

As so forthrightly put by Duke, above, an understanding of the atomic arrangement of the surface of any material is vital to a full understanding of the measurable characteristics of the material. This is nowhere more true than in the case of magnetite. The varied functions of magnetite, from acting as a catalyst to a sample in spin polarised tunneling experiments, mean that a complete model of the atomic geometry is critical. However, to date there has been very little atomically resolved imaging of the (100) surface of magnetite and even less modelling of what is seen. In this chapter atomically resolved

STM images and theoretical models based upon them in conjunction with electron counting arguments [147] are presented with the aim of filling the present gap.

In chapter 4 two distinct surface structures were presented at a terrace scale level. The structures were presented with virtually no atomic resolution and certainly no atomistic modelling of the surface. The structures were identified as the metastable state and the nanoterrace state. As the metastable state appears first it will be dealt with first. The models presented below are not definitive. It is the nature of STM that chemical identification is not usually possible. Furthermore there is the added complication of whether a feature is topographical or electronic. The various valence states available to iron are difficult to distinguish and so any atomic resolution images must be approached with a degree of scepticism. Nonetheless, high quality atomically resolved images will always provide a glimpse of the true nature of a surface.

Atomic scale imaging is not necessarily concerned with imaging single atoms. In many cases on magnetite alone the atoms will form closed structures [149] which do not exhibit atomic resolution even though the structures may be no larger than a few atomic spaces. Therefore from this point atomic scale imaging will be taken to refer to any structures imaged which are of the order of unit cell dimensions. This includes both the standard and the $\left(\sqrt{2} \times \sqrt{2}\right)$R45^o unit cells.

5.2 Metastable state

5.2.1 Results

The metastable state is the one with flat square terraces on the surface. It does not persist for indefinite numbers of anneal sessions as the nanoterrace

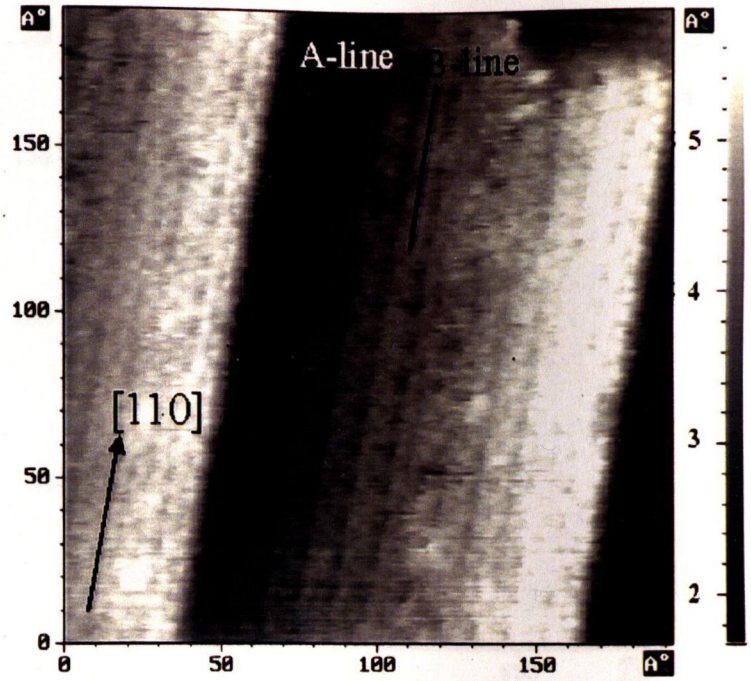

Figure 5.1: STM image of an atomic scale structure. The box marks an area of approx. 11.8 × 11.8 Å which is the correct value for a $\left(\sqrt{2} \times \sqrt{2}\right)$R45° reconstruction. V_{bias} = 1 V, I_{tunnel} = 0.1 nA.

structures do and this makes reproducible STM imaging difficult. However, in the course of this study it was possible on a small number of occasions to atomically resolve this phase.

In fig. 5.1 an STM image is shown of an 11.8 × 11.8 ± 0.4 Å structure (marked by a box) repeated over a large area. This structure corresponds to the $\left(\sqrt{2} \times \sqrt{2}\right)$R45° surface reconstruction size predicted by Kim *et al.* [148]. Further insights into the formation of this reconstruction are given below.

Scanning over the metastable state occasionally produced atomically resolved images though not often. It is difficult to know whether the tip or sample is responsible for the lack of consistent atomic resolution. The tip is the most likely candidate though it is interesting to note that the artificial

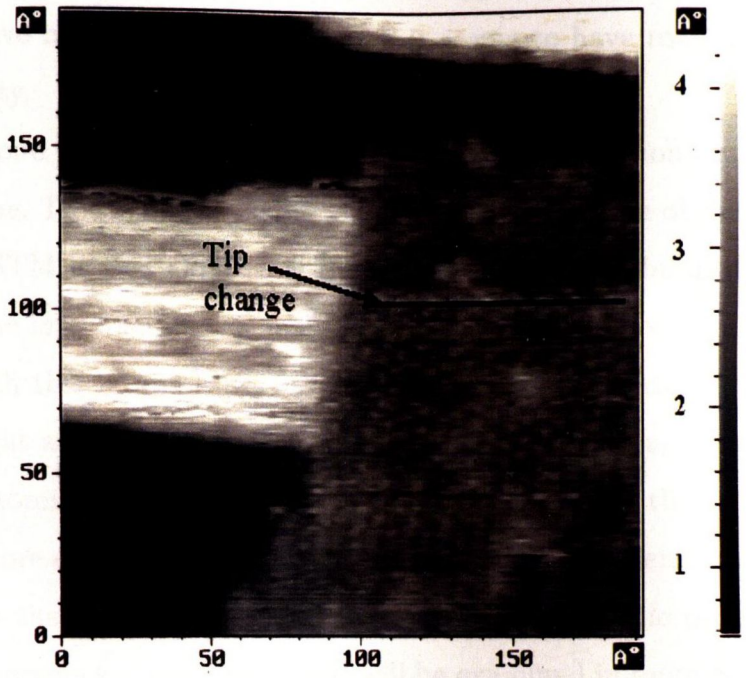

Figure 5.2: In this figure a number of different terraces are visible. The terrace on the right hand side of the image is atomically resolved. The interatomic distance, both between and along the rows, is ~5.8 Å. The location of the resolution change is marked. V_{bias} = 1 V, I_{tunnel} = 0.1 nA.

crystals produced consistently better resolution. This might be due to higher purity in the artificial crystals or improved tips at the time of investigating them.

In fig. 5.2 a number of flat square terraces are shown with a high degree of resolution on one of them. This is the only image of its kind obtained during this study. There are a number of noteworthy features to this image. Firstly it should be noted that although there is only clear atomic resolution on the right hand plane (which is in fact the middle plane in the z direction), the lowest plane (i.e. the darkest) shows an atomic structure also. Due to contrast enhancement of the middle plane the atomic detail of the lowest

plane is obscured. Interestingly enough the upper plane (the brightest) appears to have no atomic features though it seems to have rows of about 10 Å periodicity.

The second striking feature of this image is the resolution change in the middle plane. This is marked in fig. 5.2 by a solid line. One of the notorious failings of STM is the influence of the tip on the images obtained. As mentioned in the introduction the final image is a convolution of tip and sample LDOS. With this in mind it is easy to understand how a change in tip geometry might well affect the STM images. In fig. 5.2 the image changes from the usual atomic structure to more a rectangular shape on the atomic scale. (An even more dramatic version of this effect is contrast reversal. In this case a change in the atomic orbital at the tip end causes atomic protrusions to become depressions. Contrast reversal will be examined in more detail later.) Tip changes may also be related to multiple protrusions developing at the tip end. Multiple tips have the effect of doubling (or more) the topographic features of the surface.

An attempt was made to zoom-in to the atomically resolved terrace with the STM. In fig. 5.3 two approximately equivalent size STM images are presented. Fig. 5.3**a** is a software zoom-in of the middle terrace in fig. 5.2. Fig. 5.3**b** is another software zoom-in of the same area scanned immediately subsequent to fig. 5.2. As can be seen the usual atomic structure in fig. 5.3**a** has been permanently replaced by the rectangular shapes in fig. 5.3**b**. This indicates that the change in resolution in fig. 5.2 is related to the tip rather than the sample.

Examining the STM images of fig. 5.3 one sees immediately that the atoms appear to be aligned horizontally every second row across the image (lines marked on the images in fig. 5.3). In fig. 5.3**b** one can also distinguish

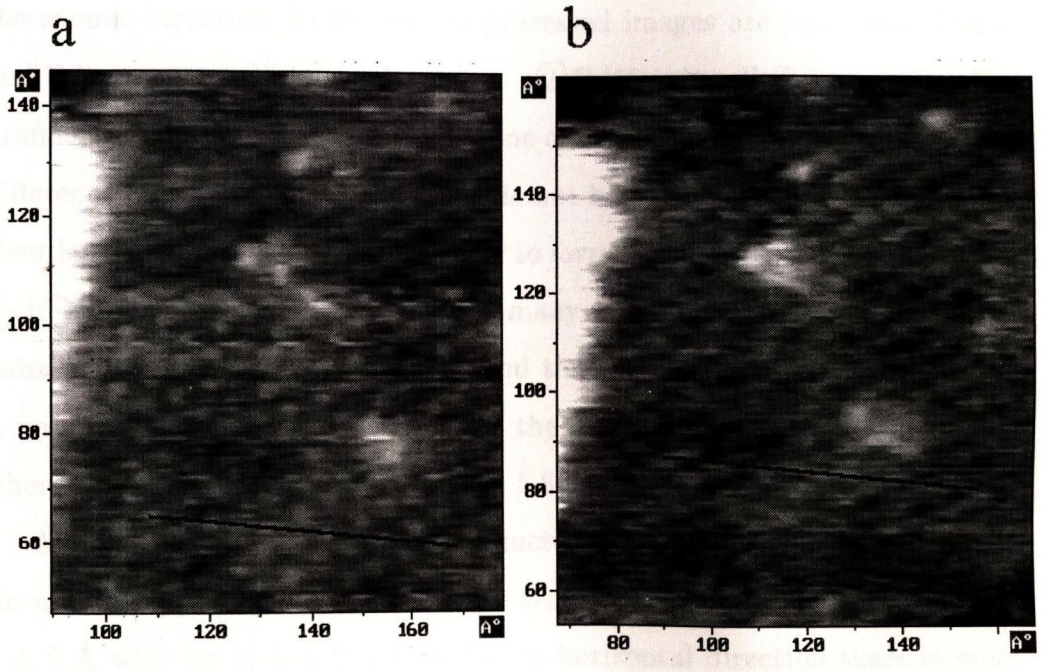

Figure 5.3: Software zoom-ins to the same area before and after the tip change. $V_{bias} = 1$ V, $I_{tunnel} = 0.1$ nA.

between two distinct rows. One row contains much darker depressions in general than the other. These we will call A-lines and the essentially brighter lines we will know as B-lines. In fact these A and B lines can also be seen in fig. 5.1.

Using the NTMDT [31] software it was possible to improve the contrast in fig. 5.3**b** by means of fourier filtering, smoothing and contrast enhancement. It was found that presenting the image in a 3-D form made it easier to view the atomic structure. In fig. 5.4 the processed images are presented. The A and B lines are marked as is the $\left(\sqrt{2} \times \sqrt{2}\right)$R45^o unit cell. By measuring line profiles (fig. 5.5) along A and B lines one can see that there is a considerable difference between them. The A lines do not have the same periodicity along their length. In fact the A-lines appear to form a pair-gap arrangement along their length. Careful measurement of many of these profiles show that the pairs are separated by 4.4 $\pm$ 0.3 Å and the gaps in between are 7.4 $\pm$ 0.3 Å wide. This is in marked contrast to the regular spacing found on B-lines where the spacing was measured to be 5.8 $\pm$ 0.2 Å.

Another interesting atomic scale structure is seen in fig. 5.6. In this image the surface appears to form a fish-scale type pattern. The "scales" are about 7 $\pm$ 2 Å wide by 11.5 $\pm$ 2 Å long. In the horizontal direction there is more of a gap between the structures then in the vertical direction. The result is that we get again the $\left(\sqrt{2} \times \sqrt{2}\right)$R45^o symmetry. It might be argued that the "scale" structures are as a result of a blunt tip. However, this structure was not seen on the other terraces imaged in the same scan. It was not seen again on any other occasion.

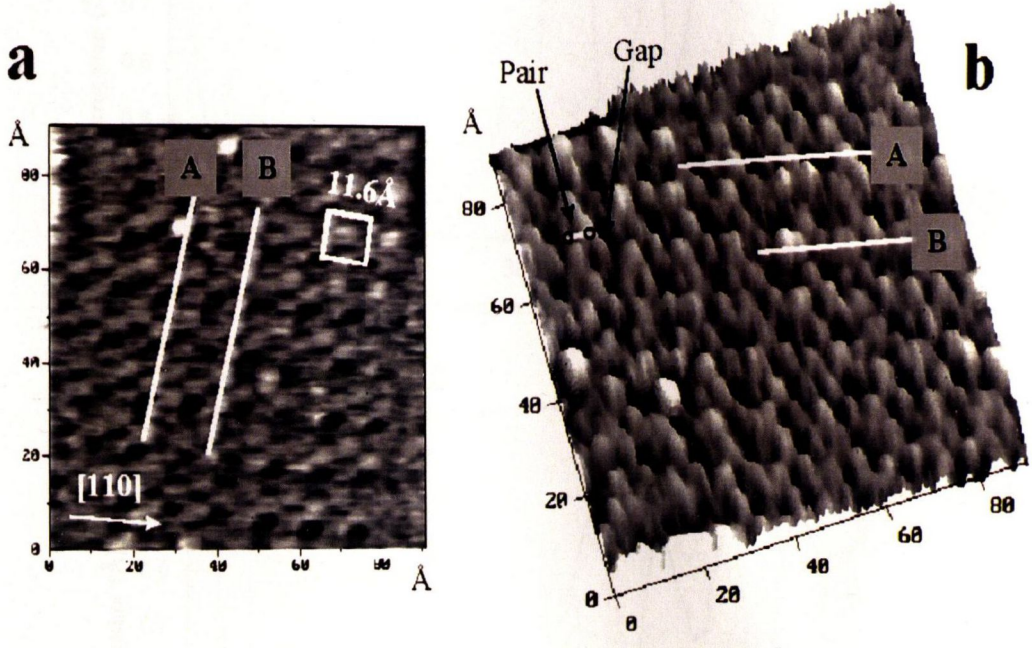

Figure 5.4: **a** is a 2-D STM image of the area of interest. **b** is a 3-D projection of the same image. The $\left(\sqrt{2} \times \sqrt{2}\right)$R45° unit cell is marked as are the A and B lines. Also marked is a sample of atomic pair arrangement on an A line. $V_{bias} = 1$ V, $I_{tunnel} = 0.1$ nA.

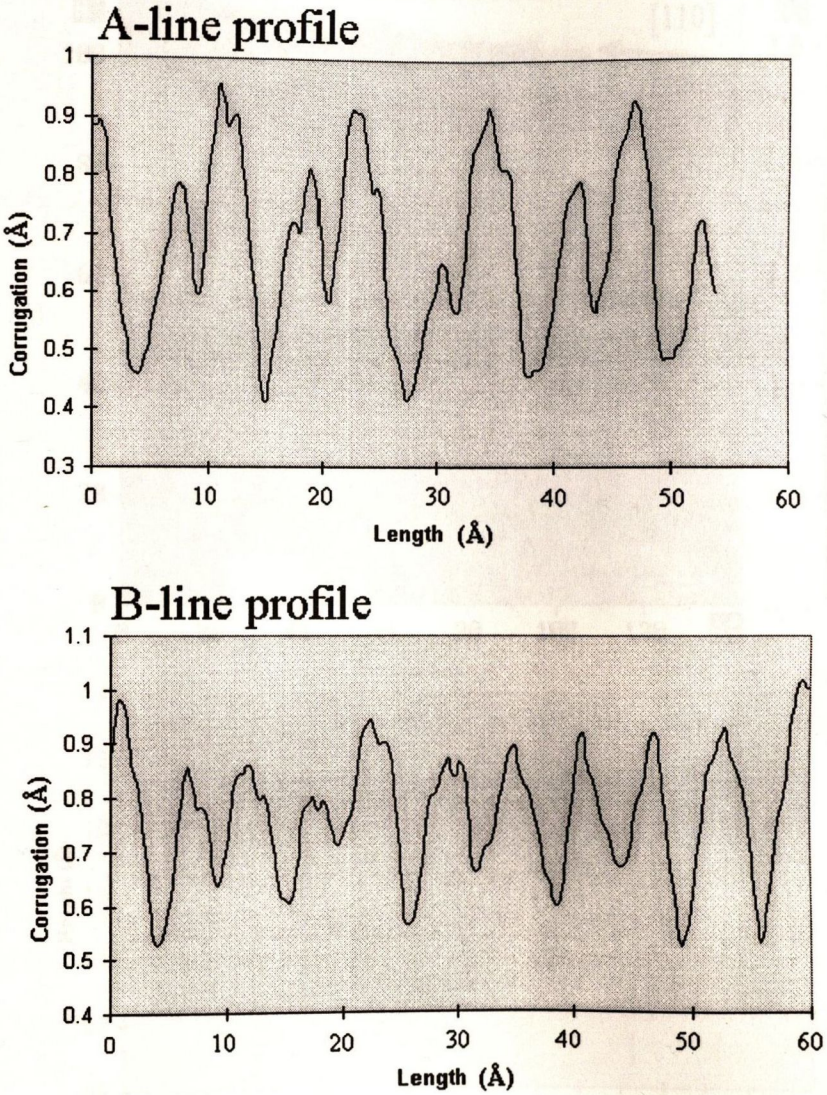

Figure 5.5: Line profiles of the A-lines and B-lines. The pair-gap arrangement is clearly seen along the A-lines in comparison to the regularity of the atomic spacing along B-lines.

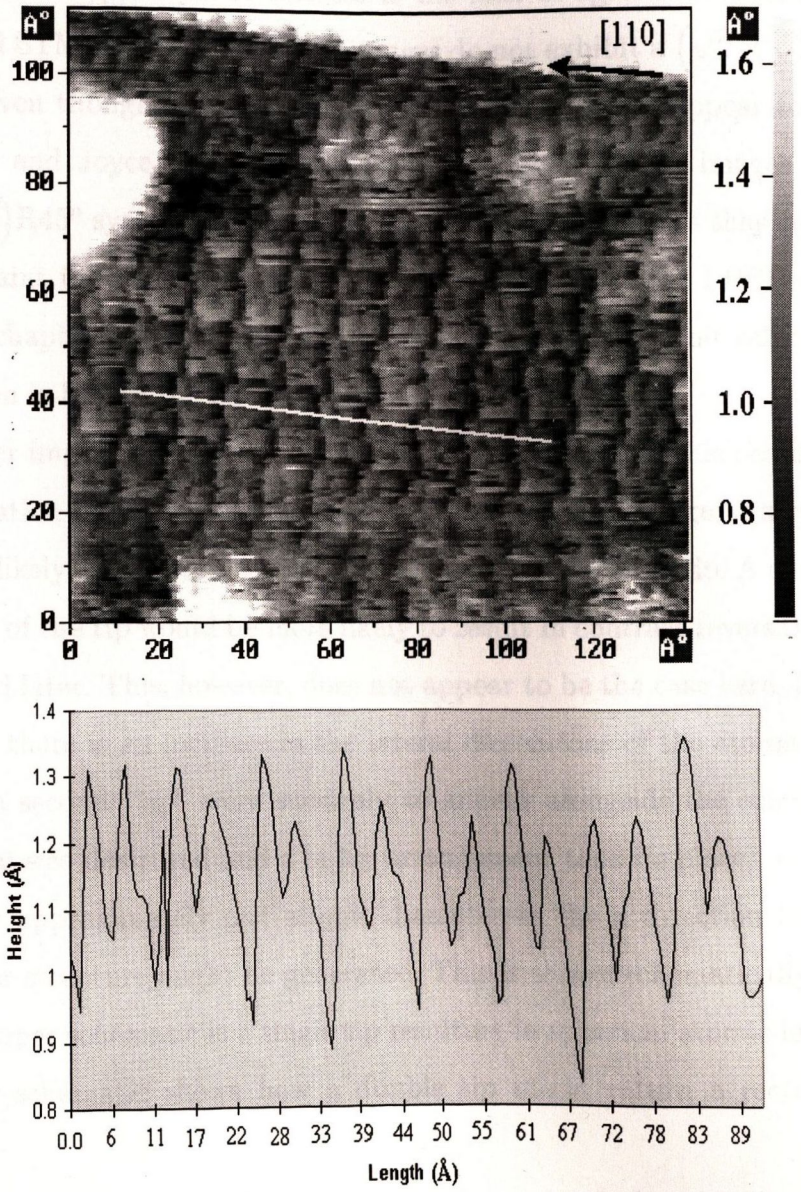

Figure 5.6: STM image of fish-scale type structures and associated line profile. The individual "scales" are each 7 ± 2 Å wide and 11.5 ± 2 Å long. V_{bias} = 1 V, I_{tunnel} = 0.1 nA.

5.2.2 Analysis

One of the first questions to address is the lack of agreement between the LEED and STM results. The LEED images do not exhibit a $\left(\sqrt{2} \times \sqrt{2}\right)$R45^o unit cell even though the atomically resolved STM images appear to do so. Chambers and Joyce have previously reported [179] LEED images with a $\left(\sqrt{2} \times \sqrt{2}\right)$R45^o symmetry. However, the reconstruction spots they reported are very faint indeed. Therefore it is quite possible that the LEED images shown in chapter 4 do in fact exhibit the $\left(\sqrt{2} \times \sqrt{2}\right)$R45^o unit cell but the information is lost in the background.

Another important issue is the nature of the tip change which caused the transformation from the usual atomic structure to the rectangular structure. The most likely explanation is that the tip became a multiple tip. A change in the LDOS of the tip would be more likely to result in contrast reversal as will be outlined later. This, however, does not appear to be the case here. Instead it appears there is an increase in the lateral dimensions of the atoms. If, for example, a second "tip" were suddenly to appear alongside the original (or the original was destroyed and a bi-tip arrangement took its place) displaced from it by approximately one atomic diameter in the x direction then the rectangular structure might be generated. This is shown schematically in fig. 5.7. The upper schematic is a single tip resulting in spherical atomic imaging. The lower schematic shows how a double tip might return a rectangular pattern.

Returning to the A and B lines. This is the major finding of this section. The pair-gap arrangement reported here is not in fact completely unique. A somewhat similar result was published previously by Gaines *et al.* [176] on MBE grown magnetite (100). However, in their case the pairing was found to occur on every row and not on alternate rows as seen here. Nonetheless it is

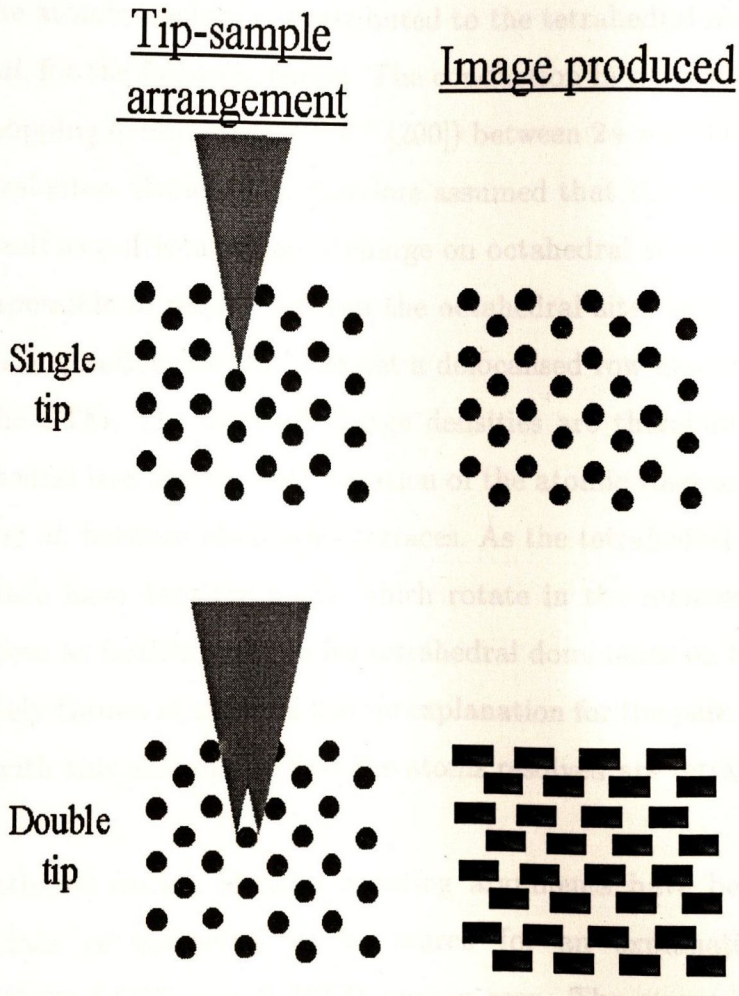

Figure 5.7: A schematic of how a double tip can change the appearance of the atomic-size features on a surface.

instructive to examine these results and they help in the formulation of the model presented below. Gaines *et al.* measured the gap to be approximately the same as seen here. This they attribute to a shifting of the tetrahedral iron atoms along the [110] directions by 0.75 Å in such a way that pairs are formed. The atomic resolution is attributed to the tetrahedral iron atoms by Gaines *et al.* for the following reason. The conduction in magnetite is due to the rapid hopping of electrons (10^{12} s^{-1} [200]) between 2+ and 3+ iron atoms in octahedral sites. Gaines *et al.* therefore assumed that this hopping would manifest itself as a delocalisation of charge on octahedral sites which should make it impossible to resolve between the octahedral sites with STM. This assumption is questionable [201] and yet a delocalised row is seen by Gaines *et al.* in the STM. The localised charge densities are therefore associated with tetrahedral iron atoms. A 90° rotation of the atomic rows was observed by Gaines *et al.* between alternating terraces. As the tetrahedral iron atoms at the surface have dangling bonds which rotate in the manner described this was taken as further evidence for tetrahedral dominance on the surface. Unfortunately Gaines *et al.* could find no explanation for the pairing. We will also work with this assumption that the atoms resolved are tetrahedral iron atoms.

As mentioned earlier, electron counting arguments have been applied to the surface of magnetite in the search for an explanation of the $\left(\sqrt{2} \times \sqrt{2}\right)$R45° LEED and RHEED images seen. The structure seen by Gaines *et al.* could not be made to satisfy electron counting arguments. However, we will attempt to show now how the A and B lines reported above can produce the $\left(\sqrt{2} \times \sqrt{2}\right)$R45° unit cell seen in the STM images and account for electron counting arguments and thus surface energy reduction. The model presented in fig. 5.8 is based on the magnetite (100) surface model pub-

lished by Kim *et al.* [148]. This rather complicated looking system has all the octahedral and tetrahedral iron atoms and all of the oxygen atoms on the surface together with their respective bonds. Following the work of Kim *et al.* (fig. 3.5) we will work with the idea that tetrahedral iron from both the planes above and below the Fe-O plane can be present at the surface.

In fig. 5.4 the way in which pairs of atoms on A lines are arranged symmetrically about every second atom on B lines is visible - though admittedly not immediately. In order to model this we must take into account whether the pairs are from the tetrahedral plane above or below the octahedral plane. From the Kim model (fig. 3.5) a separation along either [110] direction of ~6 Å implies that the atoms are from the same plane. Hence we can safely assume that the B line atoms are all from the same tetrahedral plane. The situation is not so straightforward for the A lines. There are a number of possible combinations.

1) The pair forming the pair-gap arrangement of the A line is composed of iron atoms from a plane different to the plane forming B lines. This means that the atoms each shift by ~0.75 Å towards one another along [110].

2) The pair is formed by iron atoms from the same plane. In this case the atomic displacement is not symmetric. One atom moves by ~2.2 Å and the other moves by ~3.6 Å along [110].

3) The pair is formed by one iron atom from each of the two tetrahedral planes. In order for this to work, the iron atom from the different plane again moves by ~0.75 Å and the one from the same plane as the B lines moves by ~2.2 Å.

Given the three options above option 1 seems the most likely. There is the least amount of movement of the atoms on the surface and it is the only option which is symmetrical.

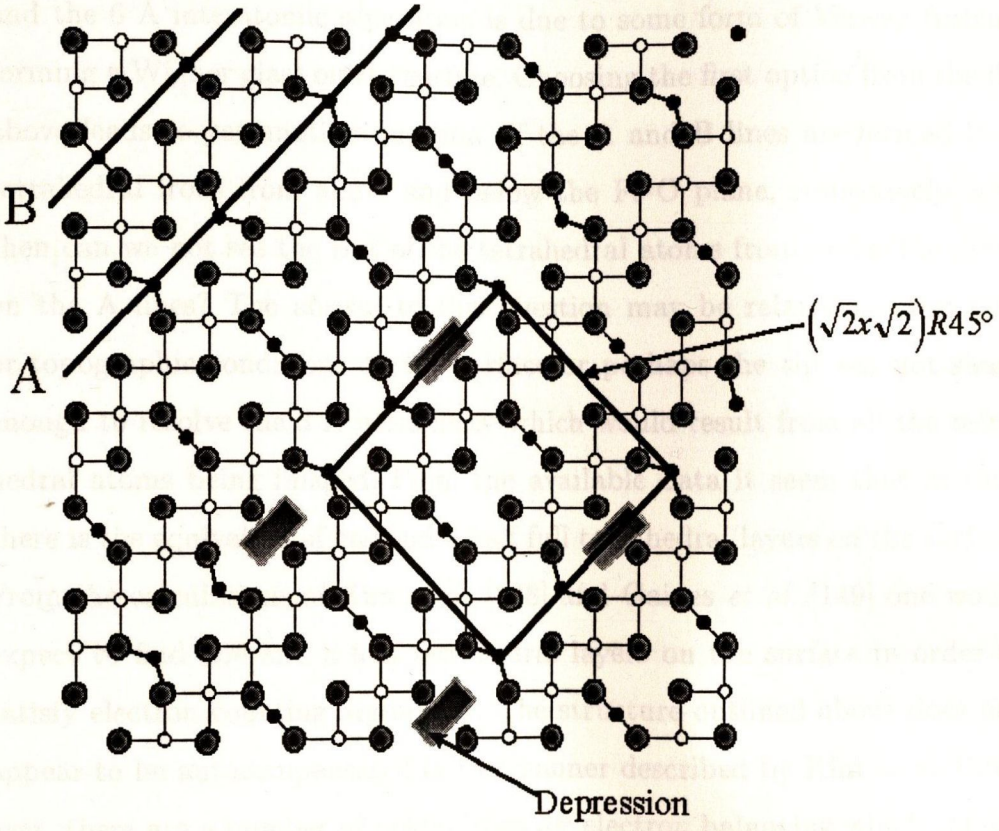

Figure 5.8: A model of the (100) surface of magnetite including the pair-gap arrangement. The A and B lines are marked. The square marks a $\left(\sqrt{2} \times \sqrt{2}\right)$R45° unit cell. The larger dark circles represent the oxygen ions, the small dark ones the tetrahedral iron and the small open circles represent the octahedral iron. The positions of the depressions seen in fig. 5.4 are filled by dark rectangles.

Of course it is not possible to determine with the STM which of the above cases is correct. Indeed it is even debatable whether it is tetrahedral iron which dominates. Perhaps the octahedral iron is dominant on the surface and the 6 Å interatomic separation is due to some form of Verwey freezing forming a Wigner glass on the surface. Choosing the first option from the list above leads to yet another question. If the A and B lines are formed from tetrahedral irons from above and below the Fe-O plane, respectively, why then can we not see the rest of the tetrahedral atoms from below the plane on the A lines? The answer to this question may be related to electronic or topographic conditions on the surface or perhaps the tip was not sharp enough to resolve the 3 Å periodicity which would result from all the tetrahedral atoms being imaged. From the available data it seem that in total there is the equivalent of one and a half full tetrahedral layers on the surface. From the calculations of Kim *et al.* [148] and Gaines *et al.* [149] one would expect to find one and a half tetrahedral layers on the surface in order to satisfy electron counting arguments. The structure outlined above does not appear to be autocompensated in the manner described by Kim *et al.* However, there are a number of possibilities for electron balancing which cannot be excluded using the STM. For example, the oxygen atoms at the surface may be rearranged or the iron atoms may exist in valence states, or amounts, significantly different from those of the bulk.

However, by combining the STM data above with electron counting arguments it is possible to account for the atomic pairing, the $\left(\sqrt{2} \times \sqrt{2}\right)\mathrm{R}45^{o}$ unit cell and show that the surface is electronically balanced. This model is outlined below.

Every surface oxygen atom has either a tetrahedral or an octahedral dangling bond (where we define an oxygen tetrahedral/octahedral dangling

bond to be a bond broken with a tetrahedral/octahedral iron atom). The octahedral dangling bond is normal to the plane of the surface. The tetrahedral bond is at an angle out of the plane. From fig. 5.9 we see that every octahedral iron atom forms six bonds and every tetrahedral atom forms four. On the surface (and here we are assuming coalescence of tetrahedral and octahedral layers at the surface) each octahedral atom is missing just one bond to oxygen. However the tetrahedral surface atoms are different. Those from the plane below the Fe-O plane are not missing any oxygen atoms. Conversely, those from the plane above the Fe-O plane are each missing two bonds. In calculating the numbers of dangling bonds and available electrons below we are making the following assumptions. Firstly we are assuming that the B-lines are due to iron atoms from the tetrahedral layer below the Fe-O plane. Secondly we assume that the A-lines are due to tetrahedral iron atoms from the layer above the Fe-O plane. Lastly we assume that the tetrahedral iron atoms from below the Fe-O plane in the A-lines are present even though they are not imaged. The reason for the pair-gap arrangement could be related to this. Taking into account the above assumptions the electron counting calculations for a $\left(\sqrt{2} \times \sqrt{2}\right)$R45° cell go as follows:

1) There are 8 octahedrally co-ordinated oxygen dangling bonds in such a cell.

2) There are 4 tetrahedrally co-ordinated oxygen dangling bonds (on the B-line).

3) This gives a total of 12 dangling bonds needing 24 electrons. Also from the calculations for electron counting in chapter 3 we see that these dangling bonds donate $12.68 + 5.0 = 17.68$ electrons to the surface.

4) Each of 8 octahedral iron atoms has a dangling bond out of the plane.

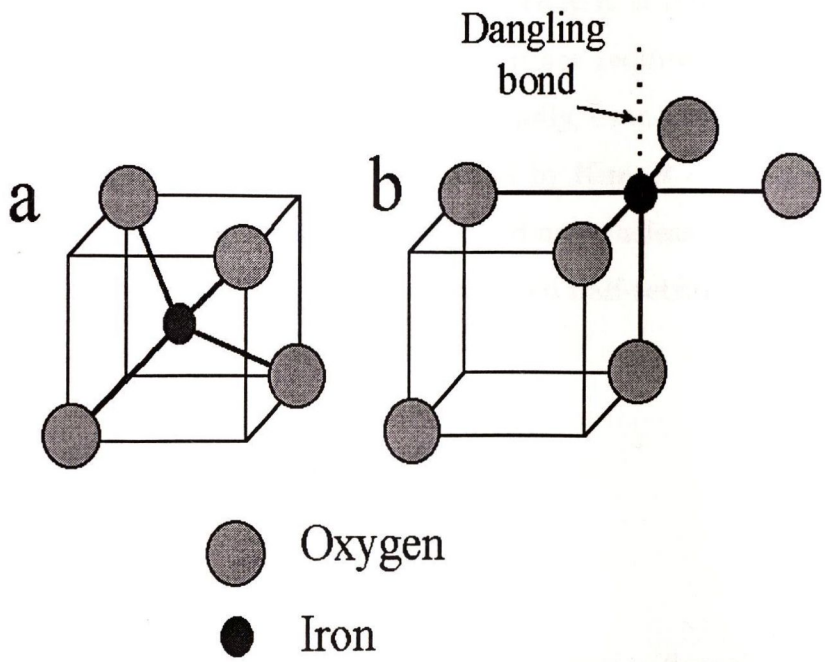

Figure 5.9: Schematics of the two standard interstitial sites in magnetite - tetrahedral and octahedral (a) and (b) respectively.

This provides for another 3.32 electrons.

5) Finally there are, on average, two tetrahedral iron atoms from above the Fe-O plane per cell which donate a further 3 electrons.

6) There is a total of 24 electrons available and 24 required.

From the calculations above it appears that the surface is exactly electron balanced. This is an interesting result. Firstly it is interesting in that, as predicted [148, 179], the magnetite (100) surface requires termination by half a tetrahedral iron layer for stability. Secondly, even though the atomic positions used are different to those suggested by Kim *et al.* for generation of a $\left(\sqrt{2} \times \sqrt{2}\right)$R45° unit cell, the cell is formed nonetheless. To the author's knowledge this is the first time that the predicted half-tetrahedral-layer termination might have been observed directly.

5.3 Nanoterraces

5.3.1 Results

The results presented from this point onwards differ significantly from those presented so far. In the previous images, for example, the best results were obtained using tungsten tips prepared as described in chapter 2. However, from now on the most interesting images are obtained using antiferromagnetic manganese-nickel tips. Furthermore, in this section atomic resolution images of the nanoterraces will be presented. To the author's knowledge no other group has succeeded in atomically resolving the row reconstructions found on many of the surfaces of magnetite. The transformation of the surface from square terraces to nanoterraces can be understood in terms of electron counting arguments. The electron balance of the $\left(\sqrt{2} \times \sqrt{2}\right)$R45° unit cell is

necessarily upset at line defects (i.e. step edges). There are a large number of such line defects on the surface and as has been seen in chapter 4 the nanoterraces appear to begin near step edges. Therefore we can conclude that the nanoterraces are in some way balanced by the presence of step edges.

In fig. 5.10 an atomically resolved image of the nanoterraces is presented. Fig. 5.10 is not as clearly resolved as fig. 5.11. However, it has two features in common. The first thing to note is that in these images the nanoterraces appear to be generated from only three or four atomic rows. It can be seen also in fig. 5.11 that one of the four atomic rows stops suddenly along two different nanoterraces. This type of defect was not observed frequently. The second feature common to all three images is the presence of adsorbates along the nanoterraces. These appear as random bright spots. The positions of the atoms will be discussed in later, clearer, images.

In fig. 5.12 the nanoterraces seem to be composed of up to six atomic rows. Furthermore there are now less adsorbates on the nanoterraces. In **a** and **b** one can see how the previously observed [26] atomic rows begin to resolve into individual atoms. The separation between the atomic rows perpendicular to their direction is 5.8 ± 0.3 Å. The corrugation along the rows has approximately the same separation. As can be seen from fig. 3.1 the separation between tetrahedral atoms on the same plane is also $\sim 6 \times 6$ Å. The [110] direction is marked.

Higher resolution images are shown in figs. 5.13 and 5.14. Atomic rows on a number of different terraces can be observed. The atomic rows rotate by 90° every 2.0 ± 0.2 Å in the z-direction. It is interesting to note that there is an apparent difference between the atomic density on the nanoterrace aligned along the marked [110] direction in fig. 5.13, the middle terrace, and the other

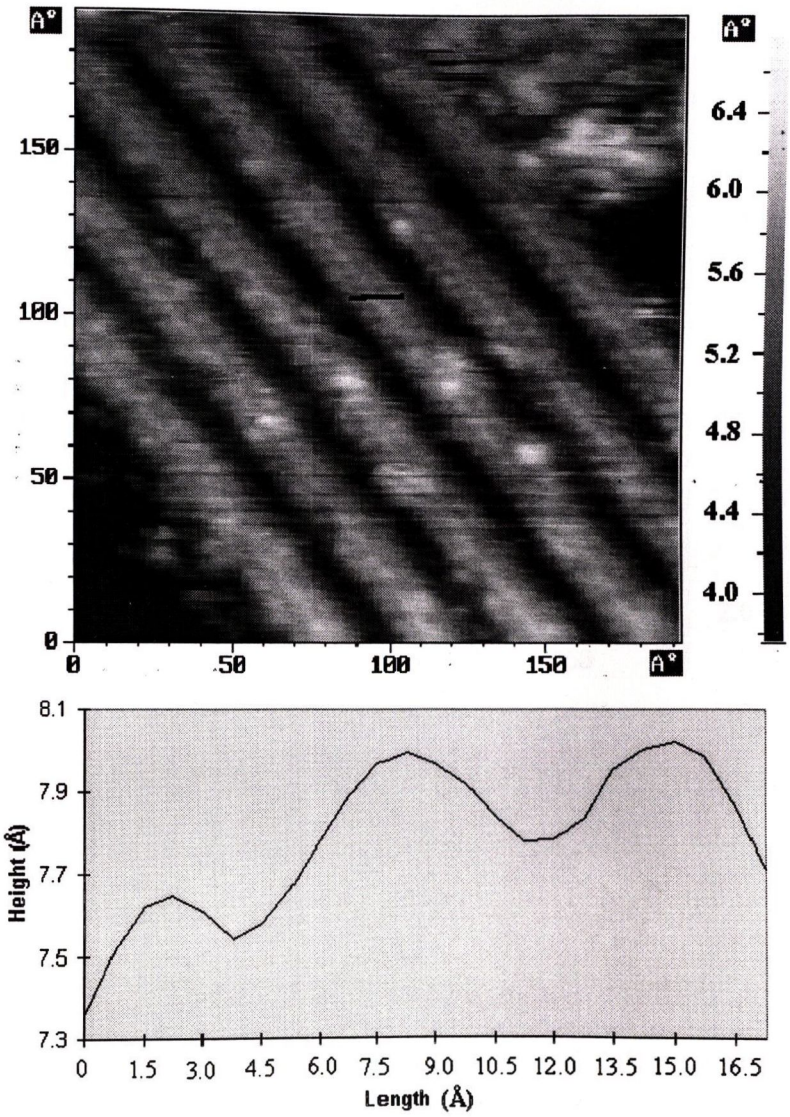

Figure 5.10: Atomic resolution image of the nanoterraces. The nanoterraces appear to be composed of three or four atomic rows (see line profile). Adsorbates can be seen as random bright spots along the rows. MnNi tip. V_{bias} = 1 V, I_{tunnel} = 0.1 nA.

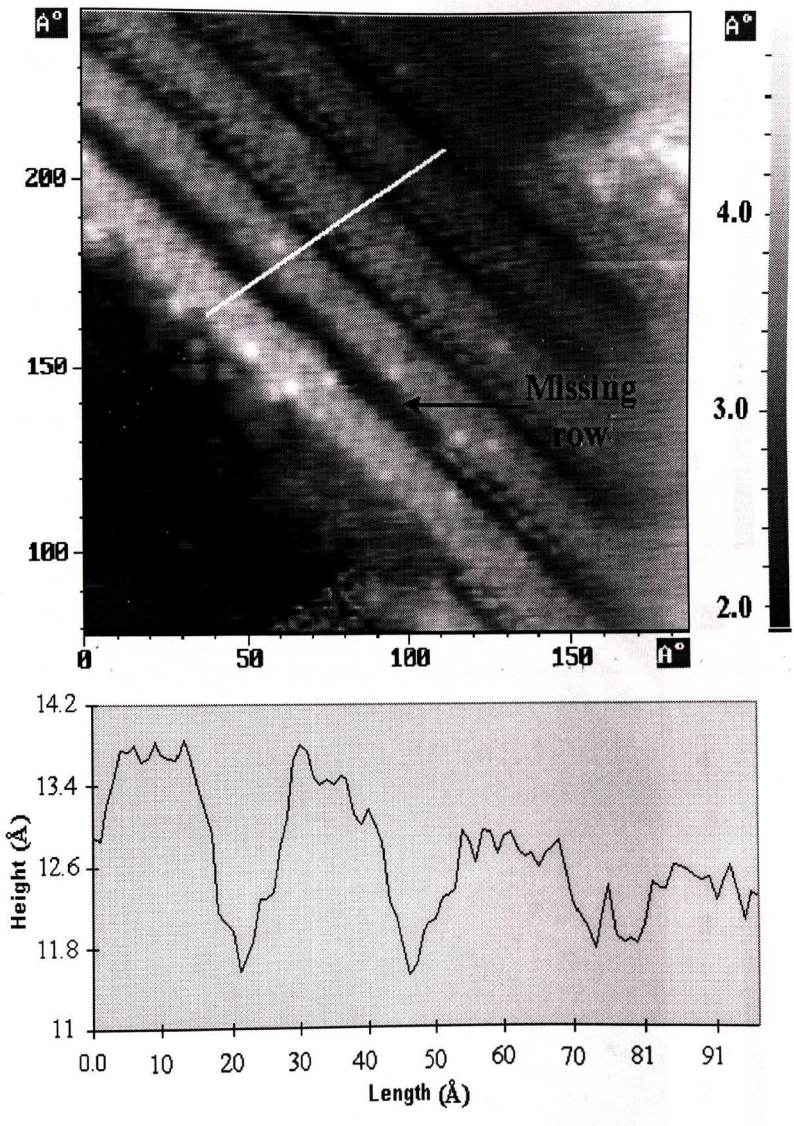

Figure 5.11: Atomic resolution images of the nanoterraces. Missing atoms are marked. From the line profile we see that the nanoterraces are composed of three or four atomic rows. Adsorbates can again be seen. MnNi tip. V_{bias} = 1 V, I_{tunnel} = 0.1 nA.

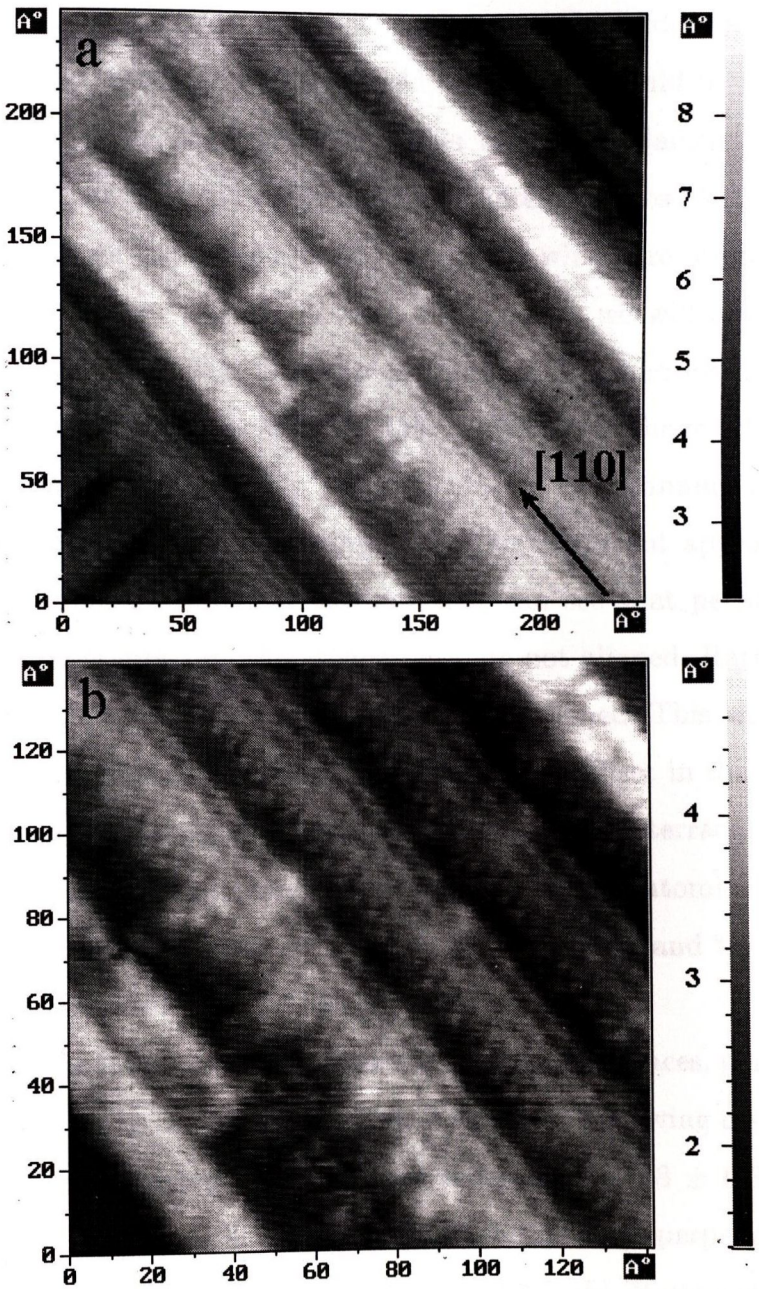

Figure 5.12: Two atomically resolved images of the nanoterraces. The previously noted atomic rows can be seen as well as further resolution to individual atoms along the rows. MnNi tip. $V_{bias} = 1$ V, $I_{tunnel} = 0.1$ nA.

two. The other two nanoterraces are above and below the one in question. There seems to be a greater density of atoms on the middle nanoterrace whereas the other two have well separated atoms. This could be a scanning artefact relating to an asymmetric tip. This may be explained as follows. If one examines fig. 5.14 carefully, one immediately notices the manner in which the atoms on the middle terrace form lines which are approximately vertical, i.e. along the y-axis. This form of alignment we will now call the α-lines. Bearing in mind that the tip was scanning back and forward in the x-direction for this image it is apparent that the atoms on the middle terrace have their α-lines approximately perpendicular to the scanning direction. Therefore the other two terraces would have this alignment approximately along the scanning direction. Furthermore one can see that perpendicular to the nanoterrace direction the atomic rows are not aligned. Rather every second atom along the perpendicular direction is aligned. This we will call a staggered arrangement. One could say there was an offset in the positions of the atoms on alternating rows perpendicular to the nanoterrace direction. Hence if the tip is scanning along the x-direction the interatomic spacing is greater on the middle nanoterrace than on the other two and this is what results in the superior resolution on this terrace.

Measuring the inter-atomic distances along the nanoterraces, perpendicular to them and along the α-line direction leads to the following results. The atoms along the nanoterrace direction are separated by 5.8 ± 0.3 Å. This holds for all the atomic rows. Measurement of the spacings perpendicular to the nanoterrace direction is more complicated (fig. 5.15). It appears in most cases that this distance is 11 ± 1 Å. Along the α-line direction the interatomic spacing is found to be 3.5 ± 0.4 Å. There is a large associated error with this due to the difficulty in resolving the individual atoms. The angle,

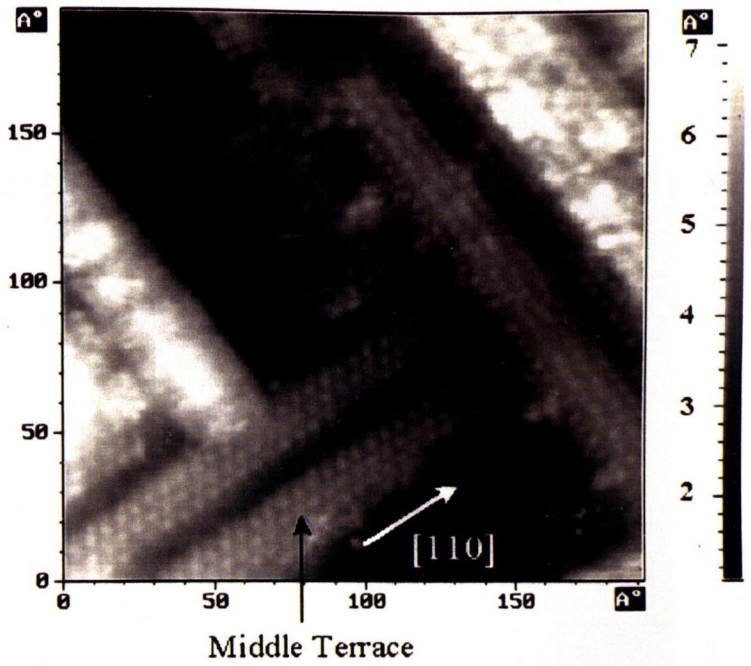

Figure 5.13: Resolution of individual atoms on a nanoterrace. There is an apparently higher atomic density on the middle terrace than on the other two though this is most likely a scanning artefact. MnNi tip. V_{bias} = 1 V, I_{tunnel} = 0.1 nA.

α, marked in fig. 5.15 has been measured to be 66° ± 3°.

5.3.2 Analysis

In fig. 5.16 a model of the atomic positions is presented. Unlike in fig. 5.8 the atomic bonds are not shown for clarity. Three types of iron atoms are distinguished, octahedral iron, tetrahedral iron from below the Fe-O plane and tetrahedral iron from above the Fe-O plane. It can be seen that all three types are required for the model. It is not possible to say from the STM images which iron atoms are which. This might be possible using spectroscopy though it is argued that spectroscopy works best with blunt tips [15] and

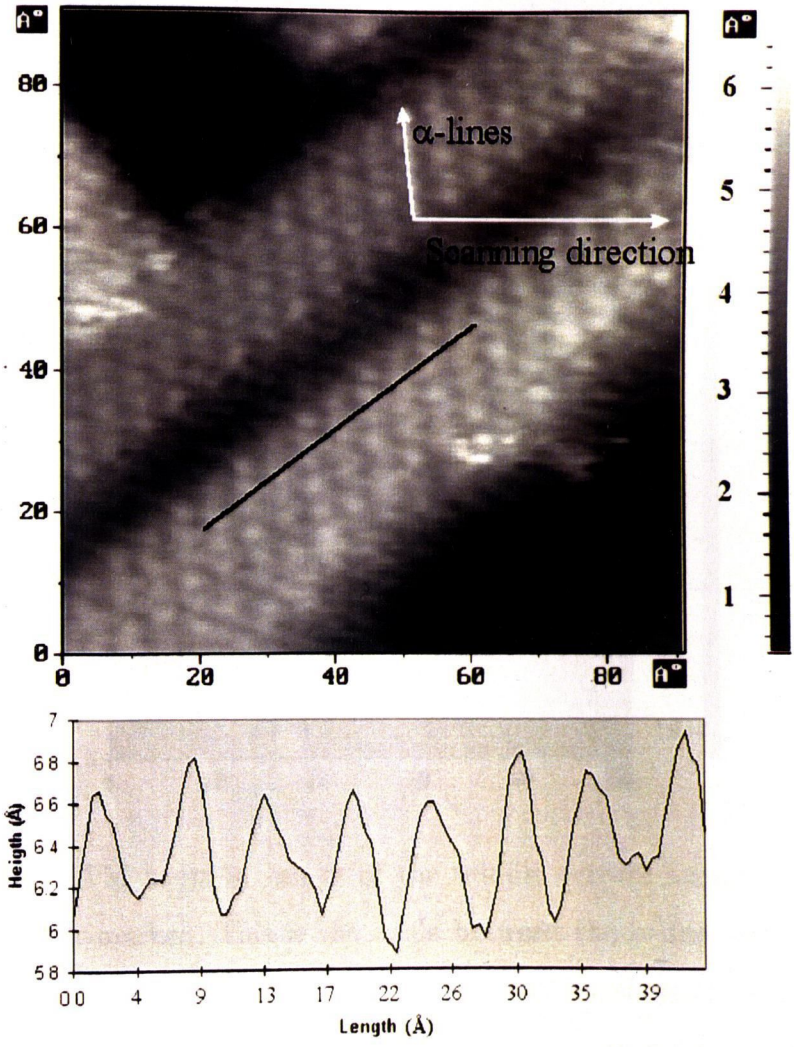

Figure 5.14: A high resolution STM image of nanoterraces. The scan direction and the α-line direction are both marked on. MnNi tip. V_{bias} = 1 V, I_{tunnel} = 0.1 nA.

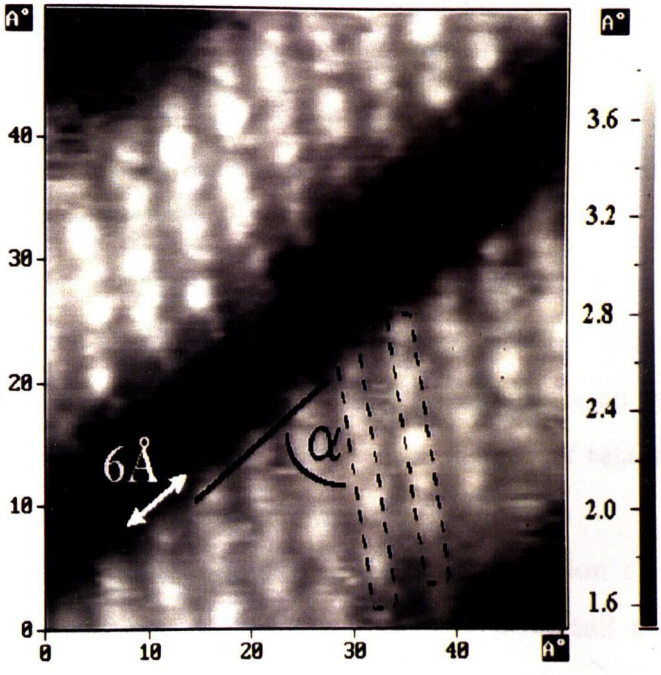

Figure 5.15: STM zoom-in image of the middle terrace seen in fig. 5.13. The angle α is marked. This is the angle between the α-line direction and the nanoterrace direction. The inter-atomic separation along the nanoterrace direction of $\sim$6 Å is also marked. The dashed rectangles cover two of the α-lines. MnNi tip. $V_{bias} = 1$ V, $I_{tunnel} = 0.1$ nA.

hence is not normally useful on the atomic scale. As can be seen from fig. 3.5 if all the octahedral and tetrahedral (from both planes) atoms are present then the inter-atomic distance along the iron rows is only ~3 Å. Similarly the distance between the rows is also only ~3 Å. However, this is clearly not the case in the atomic resolution images of the nanoterraces (figs. 5.13, 5.14 and 5.15). The spacing between the rows is indeed ~3 Å but the inter-atomic distance along the rows is a regular 6 Å. This means that for some reason every second atom along the row is not seen. There are two possible generic reasons for this. Either the atoms are physically absent **or** they are not imaged by the STM.

The physical absence of a quarter of the total number of tetrahedral atoms would be in line with the predictions of Kim *et al.* [148] for electron counting arguments. However, if we assume that every second atomic row imaged is tetrahedral then it seems that half of the total number of tetrahedral atoms is missing. This is not a balanced arrangement.

In the generation of the model in fig. 5.16 the selection of which atoms are imaged is not arbitrary. We will go through it in detail now. From the STM images we know that the inter-atomic distance along the rows is ~5.8 Å as opposed to 3 Å if all the atoms are present. We also know that the α-lines are at an angle of ~63^o to the nanoterraces. Using this information we see that, beginning with any atom, the position of the next atom across is determined. The first row of iron atoms in fig. 5.16 is arbitrarily chosen to be octahedral iron. The next atom down will necessarily be tetrahedral though it could be in either of two locations, marked A and B. It is obvious that if the next atom were to be placed in position A instead of B then the α-line structure would no longer be at 63^o to the nanoterrace. Similarly the locations of the rest of the atoms are all determined once the first line has

been selected. Knowing this we see that the three types of iron (octahedral, tetrahedral below the Fe-O plane and tetrahedral above the Fe-O plane) are required to satisfy the model. An interesting point to note is that the α-lines do not line up across two different nanoterraces in the STM images. There is an exact shift of the α-lines such that a straight line from an α-line on one nanoterrace passes through a trough in the next nanoterrace. This offsetting of the α-lines can be generated in the model of fig. 5.17 by allowing a 12 Å separation between the nanoterraces. Careful measurement of the separation in the atomically resolved STM images yields a separation of 11 ± 2 Å.

A test of this model is whether or not electron counting arguments are satisfied. Unfortunately this is difficult to determine because we cannot identify the different atomic species. There is also the possibility of alternative valence states existing on the surface. However some calculations can be made. Firstly it does not seem reasonable to conclude that every second octahedral atom is not present. It is more likely that they are merely not imaged. If half the octahedral atoms at the surface were physically absent this would create oxygen dangling bonds 2.1 Å below the surface as well as four oxygen dangling bonds per missing octahedral atom at the surface. It seems unlikely that a reconstruction driven by electron counting arguments could account for the increased energy associated with such an arrangement. Similarly for the tetrahedral iron atoms below the Fe-O plane it does not seem reasonable that they are physically missing due to the large number of extra oxygen dangling bonds this too would cause.

The electron counts for a number of possible arrangements of a thermodynamically stable model were calculated. In all cases it was assumed that the atoms both in and below the Fe-O plane were present whether imaged or not. This assumption is based on the energy argument above. The number

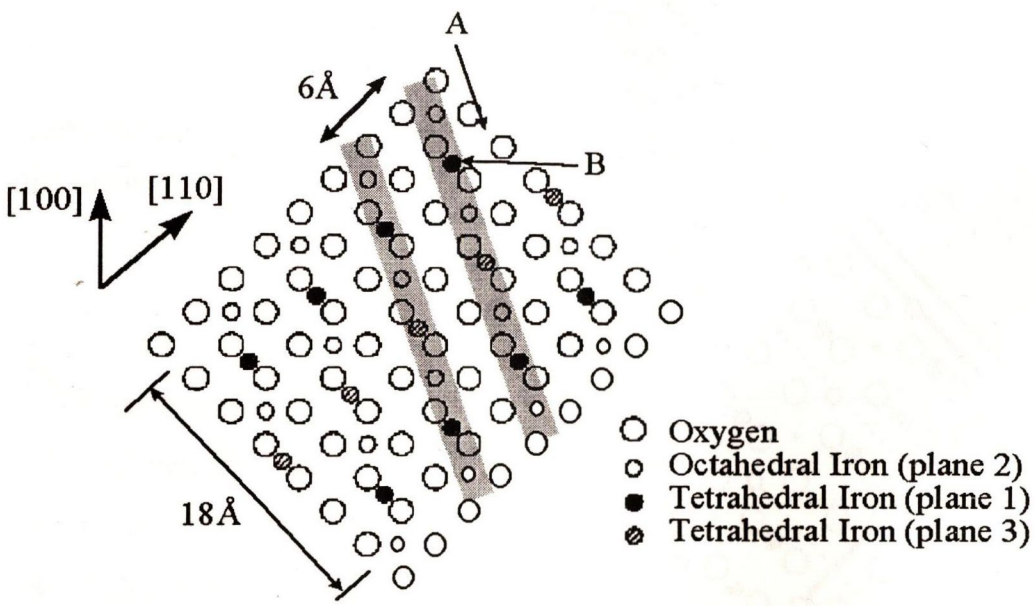

Figure 5.16: A model of the atomic resolution image of fig. 5.15. The atomic bonds used in fig. 5.8 are left out for clarity. The shaded rectangles mark an equivalent area to the dashed rectangles marked in fig. 5.15.

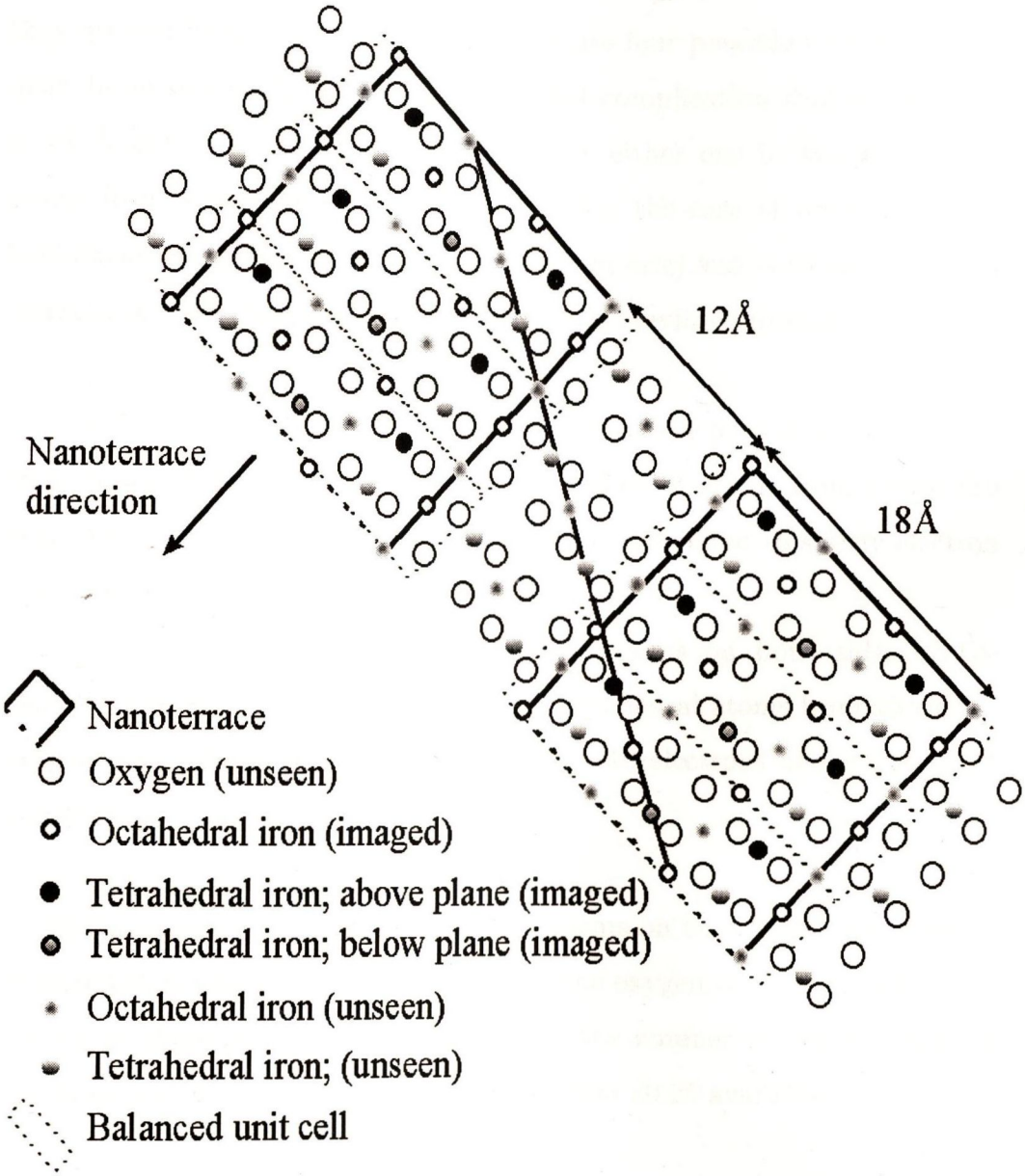

Figure 5.17: In this model two nanoterraces are formed by displaying all the atoms, those seen in the STM and those expected to be present. Each nanoterrace is terminated by octahedral oxygen atoms on both sides. Nanoterrace width is ~18 Å.

of oxygen atoms involved in the calculations is difficult to estimate because they are not imaged with STM. But there are four possible unit cells which must be examined. There is also the added complication that in each 6 Å × 18 Å unit cell (see appendix C) there is either one or two tetrahedral atoms from above the Fe-O plane (except for the case of tetrahedral iron boundaries on the nanoterraces which is symmetric) and both cases must be investigated. The results are given below in abbreviated format;

1)a) Nanoterraces have octahedral iron atoms on both sides of the nanoterraces with one of the three visible tetrahedral atoms from above the oxygen plane. In this case there are 20 electrons required to satisfy electron counting criteria and 22.65 available.

1)b) Nanoterraces have octahedral iron atoms on both sides of the nanoterraces with two of the three visible tetrahedral atoms from above the oxygen plane. Now the surface requires only 16 electrons and it has 21.65 available.

2) Nanoterraces have tetrahedral iron atoms on both sides. The number of tetrahedral iron atoms above and below the oxygen plane seen in this cell is even so there is only one case. Counting the number of oxygen dangling bonds we see we need 18 electrons and we have 20.25 available.

3) Nanoterraces have oxygen atoms next to tetrahedral iron rows on both sides. Again this case is symmetric with regard to the number of tetrahedral atoms from above and below the oxygen plane. There are 24 electrons required and only 23.17 available.

4)a) Nanoterraces have oxygen atoms next to octahedral iron rows on both sides and one tetrahedral iron atom above the oxygen plane. In this case 28 electrons are required and there are only 25 available.

4)b) Nanoterraces have oxygen atoms next to octahedral iron rows on both sides with two tetrahedral iron atoms above the oxygen plane as in fig. 5.16. In this case there are 24 electrons required and 24 available. This is a balanced surface.

Option 4)b) above is electron balanced. That is, there are sufficient electrons available per unit cell to fill the dangling bonds of every electronegative element per unit cell. It should be pointed out that though option 4)b) is balanced it may not be unique. It was, however, the only balanced arrangement found by the author. Furthermore, the many assumptions made in fig. 5.16 may not be valid, especially where it has been assumed that the atoms from on, or below, the Fe-O plane which are not imaged are still present. As mentioned above there are many possible combinations of valence states, of iron and oxygen positions and even different iron oxides which could also account for the nanoterrace formation.

Having said all that, this result is very interesting in the context of reconstruction driving forces. As we saw in fig. 4.11 the onset of the nanoterrace reconstructions appears to occur at step edges. From fig. 4.10 we can see that the reconstructions do not form instantly along the full length of the square terrace but gradually propagate along the terrace with further annealing. From the electron balancing arguments presented above it seems that the gap between the nanoterraces is due to two rows of tetrahedral iron atoms and an octahedral iron row. As the nanoterraces form a stable unit and become narrower with longer annealing times these iron atoms probably relax

more into the layer below the layer of the nanoterrace thus forming the gap.

In order to find a balanced structure it was assumed above that though some atoms could not be imaged they were in fact still present on the surface (it is possible that some way could be found to show that the missing atoms can lead to a balanced surface though this will be difficult). There are two ways now to account for the "invisible" atoms. One is to assume that the Verwey transition at the surface occurs above room temperature and the other is to assume some form of spin polarised tunneling with the antiferromagnetic manganese-nickel tip.

The possibility of a Verwey transition at the surface being significantly higher than in the bulk has been discussed before [133]. Indeed there are experimental indications that this effect exists [26]. Essentially the charge fluctuations in the octahedral iron 2+ and 3+ states is frozen out at the surface even at room temperature. This is caused by the change in co-ordination at the surface. Each octahedral iron atom is missing one oxygen atom from out of the plane. This reduces the site symmetry from cubic to tetragonal. As a result the t_{2g} levels of the hopping electron are split. In terms of the Wigner criterion discussed earlier the bandwidth, B, is dramatically reduced at the surface while the Coulomb interaction, V_0 remains essentially unchanged [133]. As discussed, when V_0/B is greater than about 3, Wigner crystallisation sets in. If B is reduced at the surface we can expect the Wigner crystallisation to set in at much higher temperatures at the surface.

There are two missing species, half the octahedral irons and a number of the tetrahedral atoms from the plane below the Fe-O plane. As regards these latter atoms it is possible that a similar explanation for the case of the metastable state exists. That is, the presence of some tetrahedral atoms from above the plane may make it difficult to see the tetrahedral atoms

below the plane because the lateral distance between them is only ~3 Å. Obviously the atoms from the plane above would be expected to dominate. The reason why only half the octahedral atoms are seen is more interesting. It is not clear exactly what positions the 3+ and 2+ iron states take along any octahedral row. They could be alternating or they could form pairs as originally postulated by Mizoguchi [200] and later by Iida *et al.* [134] and Kita *et al.* [202]. In fact the spin polarised experiments of Wiesendanger *et al.* on magnetite (100) [12,56] based the interpretation of the results on the Mizoguchi pair structure. Static arrays of Fe^{2+} and Fe^{3+} atoms were imaged using an iron tip. However, the contrast was attributed to the 2+ ions rather than the 3+ ions. In the case of the results presented above it would appear that if tetrahedral iron atoms are imaged we are also imaging the 3+ valence state.

5.4 Contrast reversal

An interesting feature occasionally observed in STM is that of contrast reversal (also known as corrugation inversion) [16]. An example of this effect can be seen in fig. 5.18. This is an STM image similar to fig. 5.15 in that the same tip, bias and tunnel current conditions were used. However, it can clearly be seen in fig. 5.18 that where there should normally be protrusions there are depressions. The spacings of the depressions are approximately equal to the inter-atomic distances measured above. Hence we can conclude that this image is contrast reversed.

Contrast reversal is a phenomena related to the apical tip orbital (fig. 5.19). According to Chen [203] one can expect a sharp peak centred at the atom site for an apical d_{z^2} orbital. In fact the d_{z^2} tip state enhances the

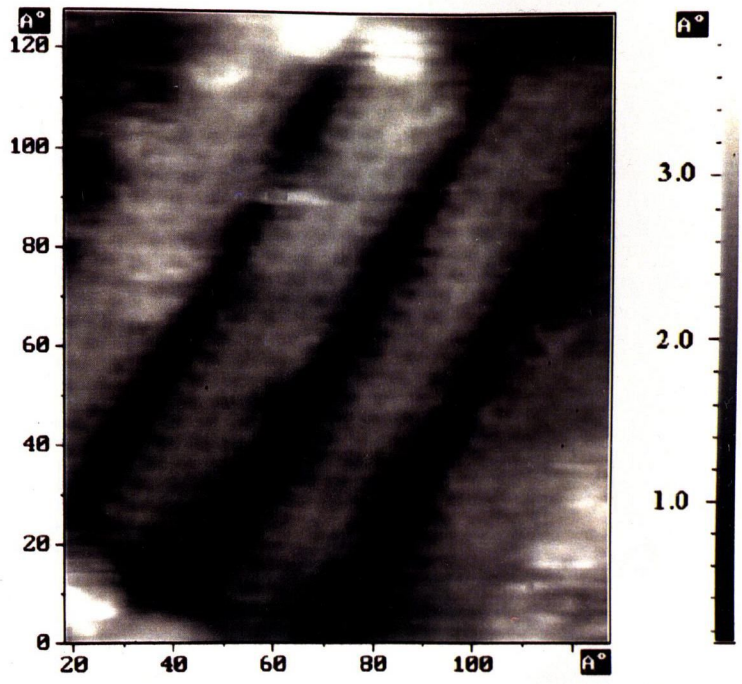

Figure 5.18: STM image exhibiting atomic contrast reversal. MnNi tip. V_{bias} = 1 V, I_{tunnel} = 0.1 nA.

atomic corrugation seen relative to an s-wave tip state. However, the other tip states (fig. 5.19) exhibit a more ring-shaped LDOS. The tunnel current distribution for a single atom is proportional to the tip LDOS and so for the d_{xz}, d_{yz}, d_{xy} and $d_{x^2-y^2}$ orbitals contrast reversal can be expected.

5.5 Conclusions

The two main surface structures detailed in chapter 4 have been atomically resolved. In the case of the metastable state of flat terraces there are not very many atomically resolved images. This is mainly related to the transience of the structure. However, from the atomic resolution images it is apparent that a $\left(\sqrt{2} \times \sqrt{2}\right)$R45° unit cell structure dominates. It has been possible to con-

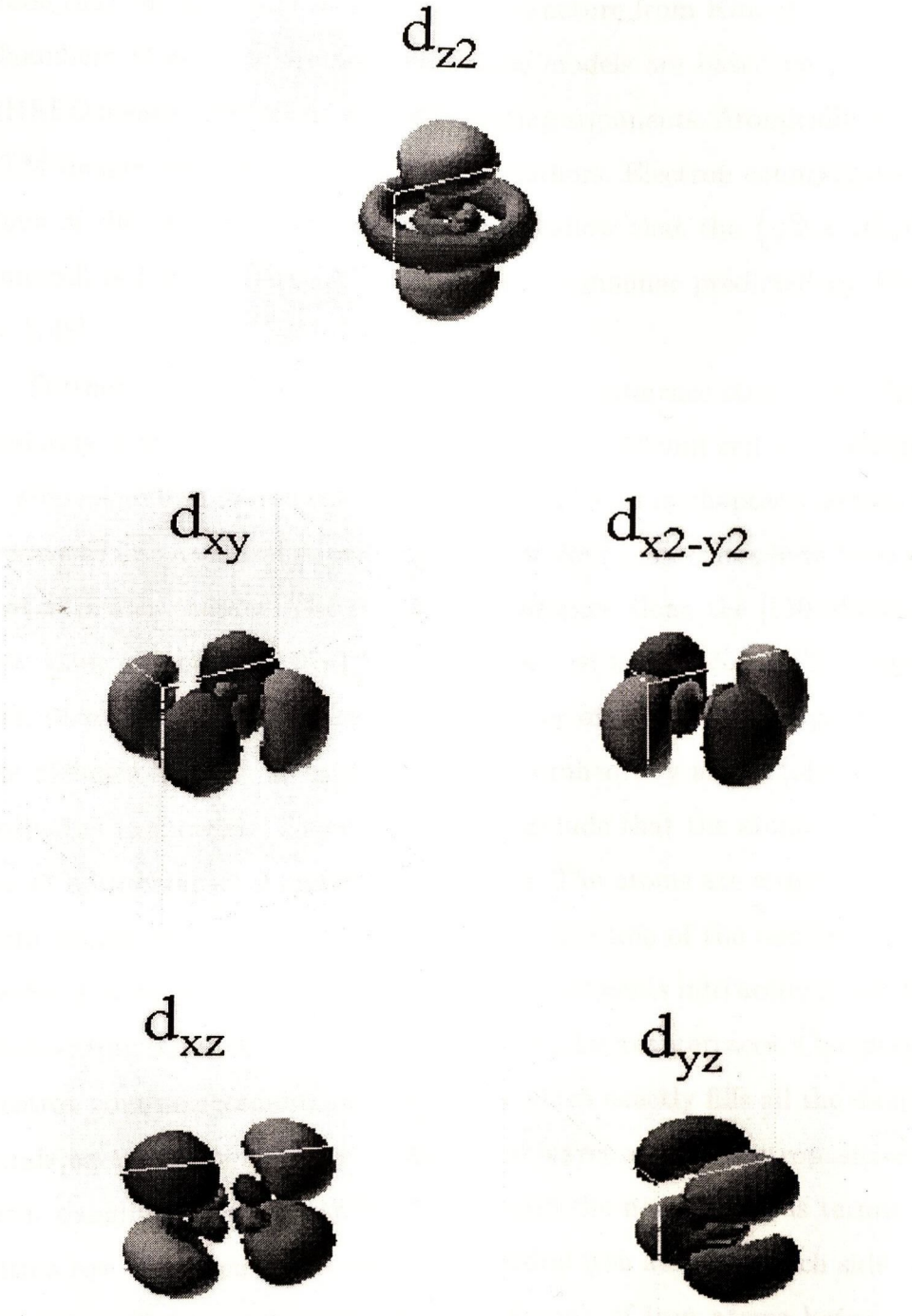

Figure 5.19: Representations of the atomic orbitals possible at the end of a manganese-nickel tip.

clude that the predicted models for this structure from Kim *et al.* [148] and Chambers *et al.* [179] are not seen. These models are based on LEED and RHEED measurements and electron counting arguments. Atomically resolved STM images were not available to these authors. Electron counting calculations of the atomic structures we obtained show that the $\left(\sqrt{2} \times \sqrt{2}\right)$R45^o unit cell is balanced though not quite in the manner predicted by Kim *et al.* [148].

Further annealing sees the advent of the nanoterrace structures. This is probably related to the fact that the $\left(\sqrt{2} \times \sqrt{2}\right)$R45^o unit cell is not balanced at step edges and indeed the nanoterraces were seen in chapter 4 to begin at terrace edges. Atomically resolved images of the nanoterraces have been presented in this chapter. The inter-atomic distance along the [110] directions (i.e. along the nanoterraces) has been measured to be ~5.8 Å. The separation between the atomic rows is of the order of 3 Å. This is equivalent to the distance between alternating rows of tetrahedrally and octahedrally coordinated iron atoms. Therefore we can conclude that the atomic rows seen are of both octahedral and tetrahedral iron. The atoms are also observed to form α-lines at an angle of $66^o \pm 3^o$ to the direction of the nanoterraces. A model is presented which takes all these measurements into account and from them extrapolates the atomic composition of the nanoterraces. One possible electron counting scenario has been found which exactly fills all the dangling bonds on the electronegative elements and leaves all the electropositive element dangling bonds empty. In this scenario the nanoterrace is terminated with a row of oxygen atoms next to octahedral iron atoms on each side. This symmetry of the nanoterrace leaves three rows of iron atoms between the nanoterraces which gradually relax onto the layer below the topmost oxygen layer thus forming the gap observed.

It is interesting to note that the calculation of the electron balancing arrangement for both terrace scale structures is based on the assumption that atoms which are not imaged by the STM are nonetheless present on the surface. In fact what we are saying is that the surface is frozen into a Wigner crystal. This is further experimental evidence that as predicted by Coey *et al.* [133] the Verwey transition temperature is much higher at the surface than in the bulk. A charge fluctuation time of $\sim 10^3$ s was calculated by Coey *et al.* Here we have found the atoms to form an ordered array that persists over the entire image. A typical atomically resolved image can take of the order of 100 to 200 seconds (depending on image size) to complete. This would seem to indicate that the charge fluctuation time is of the same order in these experiments. This is a change of about 14 orders of magnitude when compared with the fluctuation times discussed in chapter 3. As the inter-atomic separation along the [110] direction of octahedral rows is ~ 6 Å we must conclude that the surface has already undergone the Verwey transition at room temperature.

Chapter 6

Iron growth experiments

My own beliefs are that the road to a scientific discovery is seldom direct, and it does not necessarily require great expertise. In fact, I am convinced that often a newcomer to a field has a great advantage because he is ignorant and does not know all the reasons why a particular experiment should not be attempted.

I. Giaever, Nobel Prize address, 1973

6.1 Introduction

In order to progress towards actual spin polarised experiments there are two further areas to be examined. The first is how to prepare the surface such that any desired surface structure can be maintained without transforming to another surface and this is the subject of this chapter. The second is the effect of applying a magnetic field to the instrument and the sample and this will be discussed in chapter 7. Prior to this we have seen how two distinct surface structures can be formed by annealing for different times. However, the flat square terraces are transient. That is, they transform to the nanoter-

race structures once a total anneal time of something greater than 20 hours is achieved at the transition temperature of 970 ± 15 K. Although the nanoterrace structures are themselves interesting, their high corrugation would make it difficult to measure height changes due to spin-polarised tunneling. Annealing at lower temperatures prevents the onset of nanoterraces though this does not clean the surface as effectively. Therefore, in order to stabilise the flat square terraces we attempted to alter the iron-oxygen balance on the surface by depositing a thin iron film. The question of whether or not additional iron atoms on the surface would inhibit the formation of nanoterraces could now be addressed. The results of these investigations were most unexpected.

6.2 Iron growth

The growth morphology of iron has been exhaustively studied for a number of substrates including Cu [204], Pd [205], Mo [206] and W [207,208]. However, most of the work with iron films deposited on a metal substrate has been directed towards studying the films formed. The experiments are intended to investigate the manner in which the films grow, the structures formed by the films or their magnetic properties. The ultimate goal is the fabrication of electronic and magnetic structures at the atomic level. It is thought, for example, that wedge shaped islands of iron grown on various substrates would make suitable test structures for spin polarised STM and indeed work has continued in that vein in this group [209].

However, in this series of experiments the iron was deposited in order to investigate the manner in which it affects the formation of nanoterraces rather than with the aim of growing films. To the author's knowledge there is

no comparable study on record. In fact the only publication where iron was deposited on magnetite, was a scanning electron microscopy (SEM) study in 1973 [210].

6.2.1 Results

The range of possible experimental parameters for these experiments is considerable. These include the times and temperatures of pre-deposition anneal treatment, the sample temperature during iron deposition, the amount of iron deposited, the vacuum pressure and the post-deposition annealing time and temperature. Below we outline the two combinations investigated so far. The experiments described in this chapter have all been performed on artificial single crystal magnetite (100).

Experiment (1)

The first experiment was done on a hot sample. The sample was pre-annealed to about 920 ± 15 K for 3.5 hours. Then the anneal temperature was increased to 970 ± 15 K for about ten minutes. At this point approximately 1.5 Å of iron was deposited in ~70 seconds using an electron beam evaporator on the hot sample. This was done at a pressure of 6×10^{-9} mbar. After iron deposition the sample was annealed for a further 2.5 hours at 970 ± 15 K. STM investigations revealed a vague outline of surface structure but nothing could be clearly discerned. Annealing for a further 12 hours, again at 970 ± 15 K had quite a different result. The STM images were stable and an interesting feature was observed (fig. 6.1). In this image one can see very wide, ~ 30–70 Å, rows running the length of the image. This is most likely related to a change in the polishing procedure. For this sample a mechanical lapping machine was used which results in a more uniform polishing. Fig. 6.2

is a close-up of fig. 6.1 and in it we can see the terrace structure once more. The terraces are quite rough but a step height of 2.0 ± 0.3 was measured.

The sample was annealed for a further 29 hours at 970 ± 15 K. This has invariably proven in the past to produce nanoterraces. In this case, however, it did not. What this long anneal session did achieve was a more right-angled structuring of the terraces. In fig. 6.3 one can see both square and unstructured terraces co-existing. When after annealing for more than 50 hours at 970 ± 15 K no nanoterraces were formed we subjected the sample to a further 70 hours of annealing at the same temperature. The results of this can be seen in fig. 6.4. There are three notable features of these images. Firstly the terraces are now mostly square. Secondly there is some form of cracking of the terraces, reminiscent of the onset of nanoterraces. Finally there is a notable amount of adsorbate material visible in the two images. Atomic resolution can just be made out beneath the adsorbate layer in the lower image. Many of the images seen at this stage have a high adsorbate content. This is an unexpected result because one would expect the sample to be particularly clean after such a long anneal time, though we cannot completely exclude the possibility that impurities diffused from the bulk to the surface. Further annealing failed to remove these adsorbates completely or to generate the nanoterraces and the sample was removed from the UHV system and repolished. The nanoterraces could be readily formed as described in chapter 4 once the surface had been removed from the UHV system and repolished manually.

Experiment (2)

Almost the reverse procedure to that outlined above was attempted on the (100) surface of another magnetite crystal. After polishing, the sample was

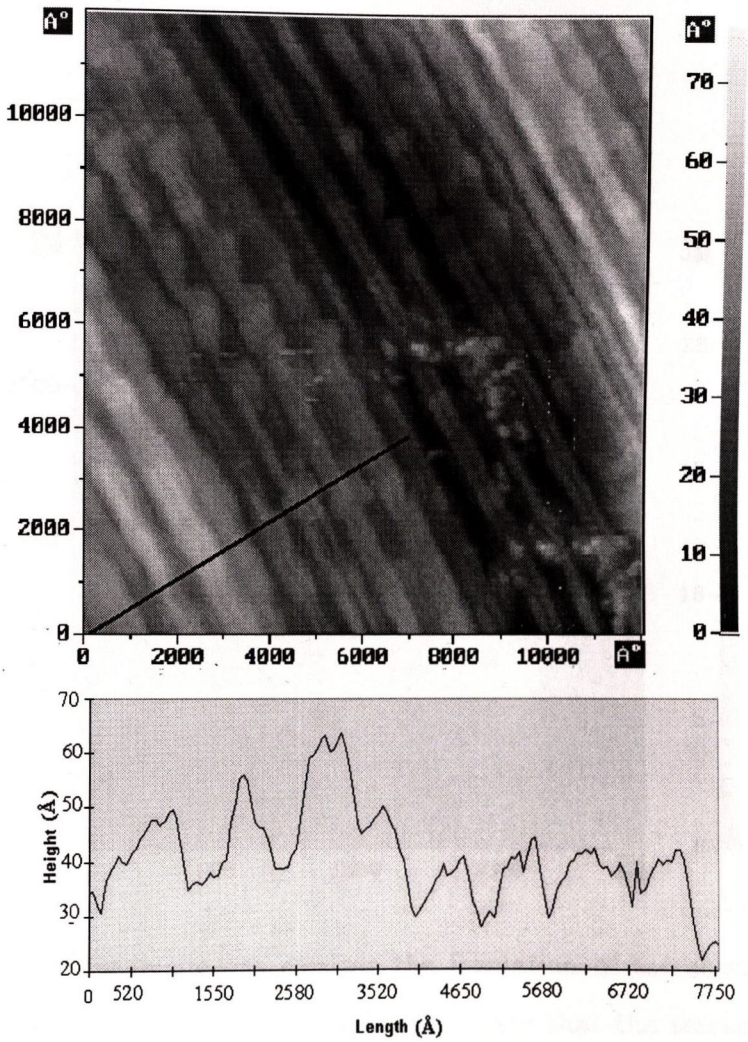

Figure 6.1: An STM image showing the wide rows seen after polishing with a lapping machine to 0.1 μm and deposition of 1.5 Å of iron at 920 $\pm$ 15 K and post-deposition annealing to 970 $\pm$ 15 K for $\sim$ 15 hours. V_{bias} = 1 V, I_{tunnel} = 0.1 nA.

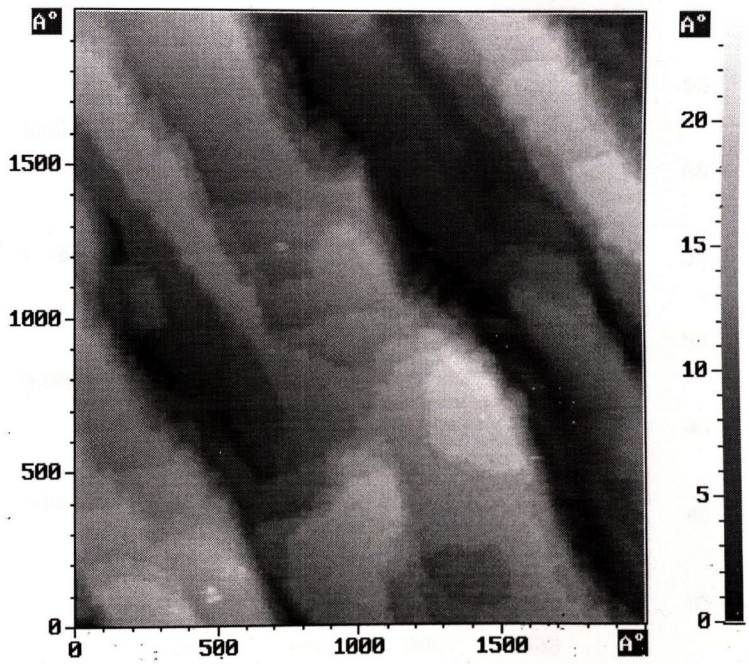

Figure 6.2: In this image one can see the formation of terraces. The step height is $\sim$ 2 Å. It can also be seen in this image that the terraces are not square but rather irregular in shape. $V_{bias} = 1$ V, $I_{tunnel} = 0.1$ nA.

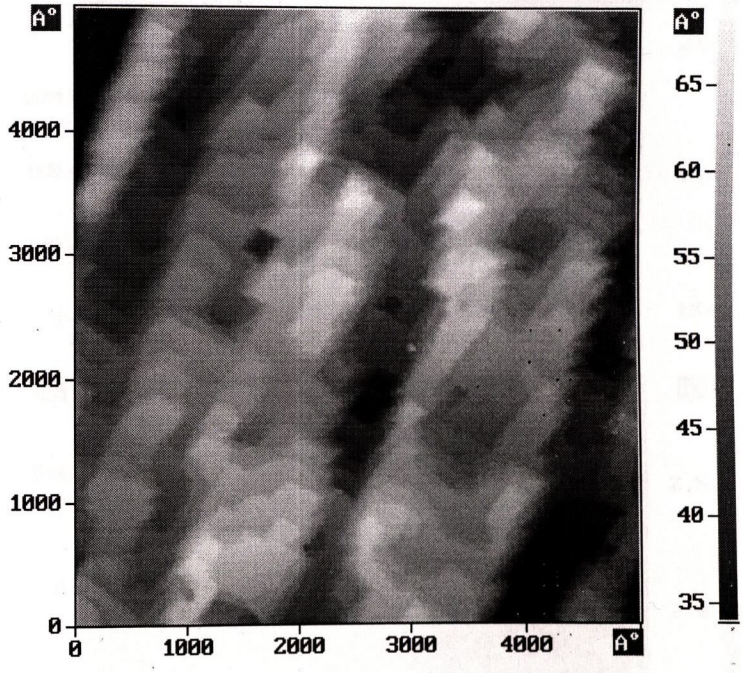

Figure 6.3: The terraces can clearly be seen here to be more square than in fig. 6.2. This is due to annealing the sample for 29 hours at 970 ± 15 K. V_{bias} = 1 V, I_{tunnel} = 0.1 nA.

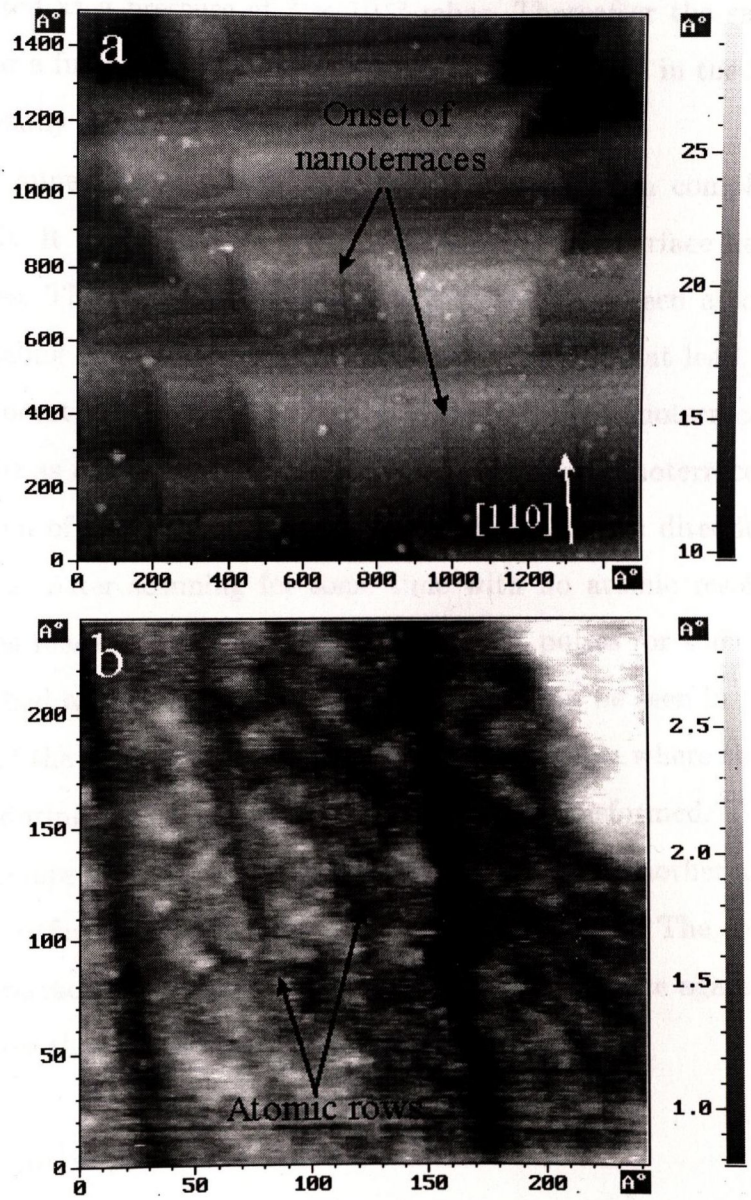

Figure 6.4: These STM images are the result of more than 120 hours of post-deposition annealing at 970 ± 15 K. $V_{bias} = 1$ V, $I_{tunnel} = 0.1$ nA.

annealed to 970 ± 15 K for three hours prior to deposition. The deposition was done at a sample temperature of about 850 K. A total of 6 Å of iron was deposited at a pressure of 3×10^{-9} mbar. Thereafter the sample was annealed for a further 80 minutes at ~850 K. This resulted in the formation of an essentially unstructured surface.

Further annealing at 970 ± 15 K for 12 hours gave a completely different result. It can clearly be seen in fig. 6.5 that the surface has formed nanoterraces. This is interesting in that there has only been a total of 15 hours annealing at 970 ± 15 K whereas normally it takes at least 20 hours at this temperature to form nanoterraces. However, the nanoterraces do not appear to be as clear as usual. Closer inspection of the nanoterraces reveals a corrugation of only ~0.5 Å or less perpendicular to the direction of the nanoterraces. After scanning for some time with no atomic resolution an attempt was made to condition the tip using HV pulses for some milliseconds. This had a dramatic effect on the surface as can be seen in fig. 6.6. A large area of the surface (~ 12,000 Å × 12,000 Å) below where the tip was positioned during the conditioning was completely transformed. There is no regular structure in this area. When the tip was moved to another area of the sample the surface reconstructions could again be resolved. The corrugation of the nanoterraces perpendicular to their direction was once again ~ 2.0 Å. This indicates that the HV pulse created a sharper tip.

6.2.2 Analysis

The most important aspect of both experiments above, in the light of the anomalous results to be presented below, is that the sample had been heated to 970 ± 15 K (albeit for different times) prior to iron deposition.

The reason for depositing the film at 970 ± 15 K is that this is known

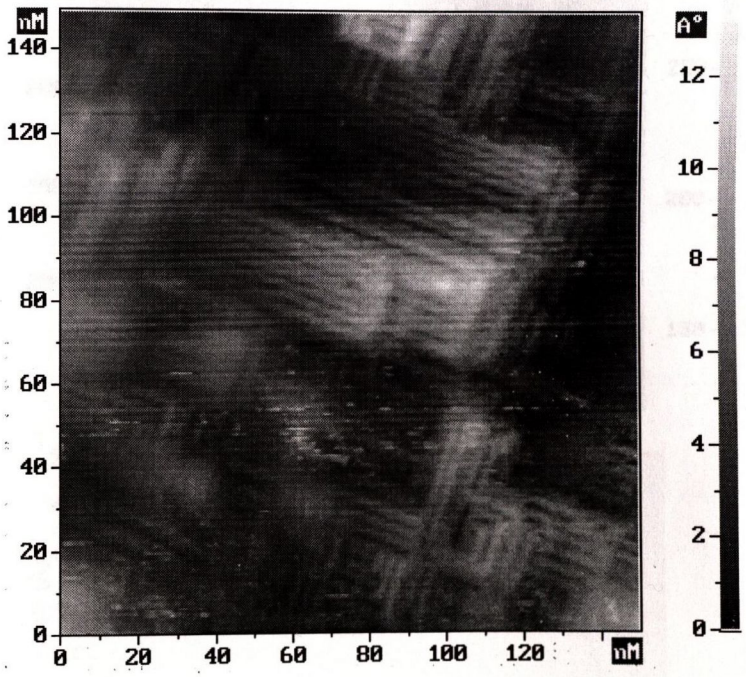

Figure 6.5: Formation of nanoterraces after iron deposition and annealing to 970 $\pm$ 15 K for only 12 hours. V_{bias} = 1 V, I_{tunnel} = 0.1 nA.

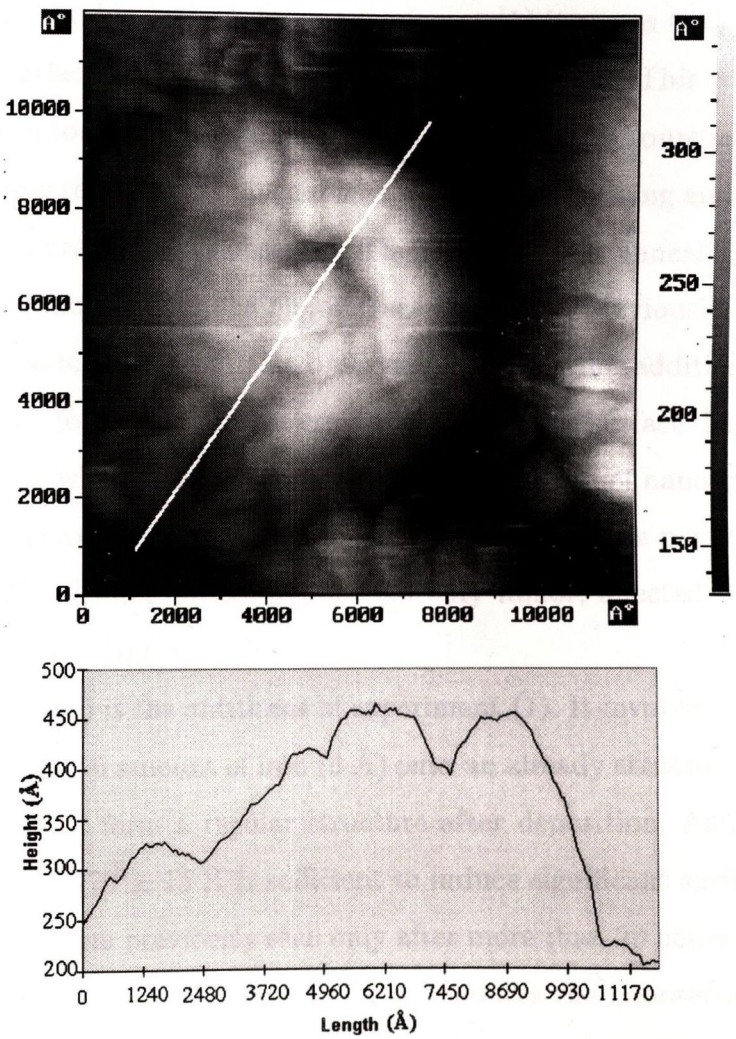

Figure 6.6: HV pulses were used to condition the tip and the result of this was the formation of the non-structured surface seen here. $V_{bias} = 1$ V, $I_{tunnel} = 0.1$ nA.

from our previous experiments to be a critical temperature for the formation of a structured surface. Therefore depositing iron onto the surface before it has reached a stable state will obviously have more impact than on an already structured and stable surface. From experiment (1) it seems that depositing iron on the surface inhibits the formation of nanoterraces. This is an important result as a tool for tailoring the surface. A total of 120 hours annealing at 970 ± 15 K was required to induce some form of nanoterracing and even then only a form of cracking was observed. Thereafter further annealing failed to enhance this cracking into the nanoterrace structures previously seen. The most logical conclusion from this observation is that the addition of extra iron during the formation process creates a more stable surface. Perhaps the dangling bonds which are thought to drive the formation of nanoterraces are satisfied by the extra iron. However, we cannot rule out the possibility that the change in polishing procedure, though only minor, affected the surface in an unexpected manner.

Experiment (2) is the antithesis of experiment (1). It involves the deposition of a substantial amount of iron (6 Å) onto an already structured surface. The film does not form a regular structure after deposition. Annealing for only 12 hours at 970 ± 15 K is sufficient to induce significant surface reconstruction of the form previously seen only after more than 20 hours annealing at this temperature. It seems that the iron enhances the nanoterrace formation. Furthermore there is the interesting result caused by pulsing the tip. It is conceivable that a large amount of collected iron fell from the tip onto the surface. However, the amount seems quite large for this explanation.

Clear atomic resolution was not obtained in either of the two experiments. This is unfortunate in that it might have provided valuable information on the exact nature of the influence the iron film has on the surface.

6.3 Iron film induced transformation in the bulk

Though the results above are interesting, repetition is required for a proper scientific study. The intention was to study the way iron affects the onset of nanoterraces and thereafter to study the growth kinetics of iron on structured magnetite surfaces. However, a slightly different approach this time (iron deposition on an unstructured surface) yielded completely unexpected results.

6.3.1 Results

Fe films were grown once on each of three separate samples. The film thicknesses were 0.5, 1.0 and 1.5 Å. Prior to deposition each sample was hand polished in the manner previously described and then annealed in UHV for 2 hours at 920 ± 15 K. Then they were cooled to temperatures ranging from 310 to 350 K. Shortly after deposition the samples were investigated using LEED. However, there were no spots visible, only a diffuse image. The samples were annealed at 970 ± 15 K repeatedly for times ranging from 4 to 20 hours with no improvement in the LEED pattern. No stable tunnel current could be obtained with STM on the samples. The samples were then removed from the UHV system.

The most striking feature of the samples after post-deposition annealing was the colour change. After annealing the sample for 20 hours or more at the transition temperature of 970 ± 15 K the samples all acquired a series of colours ranging from blue at one corner of the sample, through red, to brown at the other side. The only place where there was no colour change was underneath the tantalum cap that screws down over the sample to hold it

Sample	Film Thickness (Å)	Sample Temperature (K)	Pressure (mbar)
No.1	1 ± 0.3	317 ± 7	3×10^{-9}
No.2	0.5 ± 0.2	318 ± 7	4×10^{-10}
No.3	1.5 ± 0.3	346 ± 7	5×10^{-10}

Table 6.1: The iron film deposition parameters

in place and the underside of the sample. Therefore it is safe to conclude that the colour change is due entirely to the iron film. This film can be removed quite easily by hand polishing the surface with diamond paste for some 10 seconds. From this we estimate the thickness of the film to be of the order of 0.2 ± 0.1 μm because a complete polishing session removes approximately 30 μm of magnetite from the surface. After a full polishing session each sample was returned to the UHV system and annealed again at 970 ± 15 K for 20 hours or more. Surprisingly this induced the return of the coloured film! The film also recreated its initial blue to red structure each time. Again no LEED spots could be obtained and the samples were unstable to STM investigation.

The lack of tunneling stability is due to the increased resistance of the film. It has a room temperature resistance of some hundreds of ohms compared to the normal value of just a few ohms.

As can be clearly seen in table 6.1 there is quite a spread of experimental conditions. The film thickness, deposition temperature and system pressure were all variable. In spite of this the sample behaved in an identical manner each time.

The range of colours associated with the sample could be attributed to the movement of the sample across the iron deposition plume. The method employed for iron deposition involves evaporation of the iron films onto a

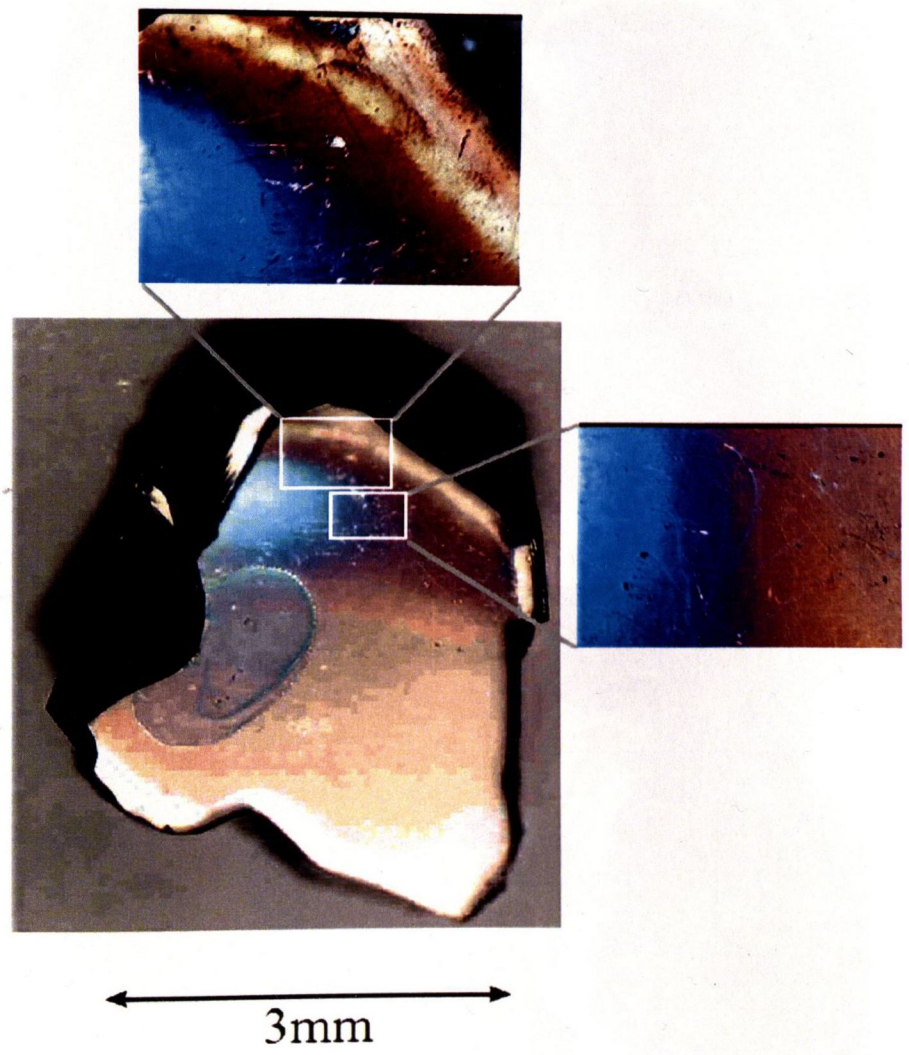

Figure 6.7: Photograph of one of the coloured films. Zoom-ins using a reflection mode microscope are also provided. The crystal is approximately 3 or 4 mm across. The range of colours mentioned in the text is clearly visible.

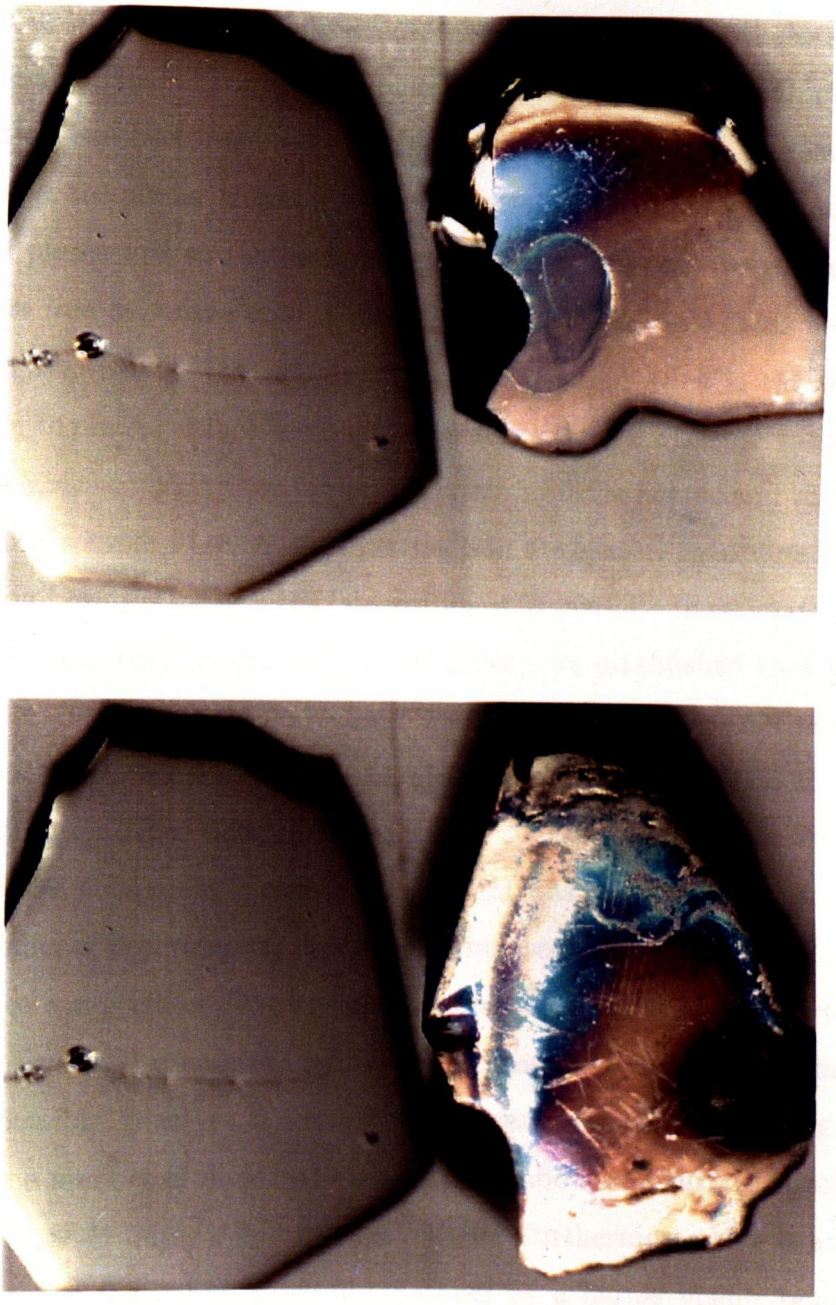

Figure 6.8: Two of the coloured samples compared to a polished magnetite sample. The magnetite sample reflects the light and so appears white even though the crystal is black.

quartz crystal until a stable deposition rate has been achieved. This crystal is on the same drive as the sample holder and displaced from the sample by about 45 mm. This is known to be greater than the plume width. Once stable evaporation has been attained the drive is withdrawn until the sample is directly over the plume. However, during this time the sample is not protected from the plume and so the leading edge of the sample can be expected to have more iron deposited onto it than the rest of the sample. This has been tested approximately. The sample orientation is noted when in the wobble-stick prior to placing it face down in the heater (see fig. 2.8). Unfortunately it is not possible to observe the sample orientation in the heater and there is a good deal of sample rotation while placing it in the heater. By comparing the orientation both before and after deposition it is possible to estimate which was the leading edge of the sample and indeed we established that this is the edge that develops the blue colour. The time taken to cross the plume is approximately 10 seconds. In the cases of samples 1 and 2 this leads to about 0.1 Å extra iron deposition on the leading edge. For sample 3 this time was increased and consequently the colour gradient was more spread out.

A number of experimental techniques were used in an attempt to identify the surface composition. The sample was placed in a scanning electron microscope. Due to the magnetic nature of the sample high resolution imaging was not possible. However, a number of features could be resolved (fig. 6.9). There are a number of dark features scattered about the surface. Dark features in the SEM imply a lack of conductivity. Furthermore there is an area on the right of the image which is separated by a barely visible boundary from the rest of the sample. This is where the shadow of the sample-holder cap blocked iron deposition and this is magnetite.

Energy dispersive x-ray analysis was performed in the SEM. A number of

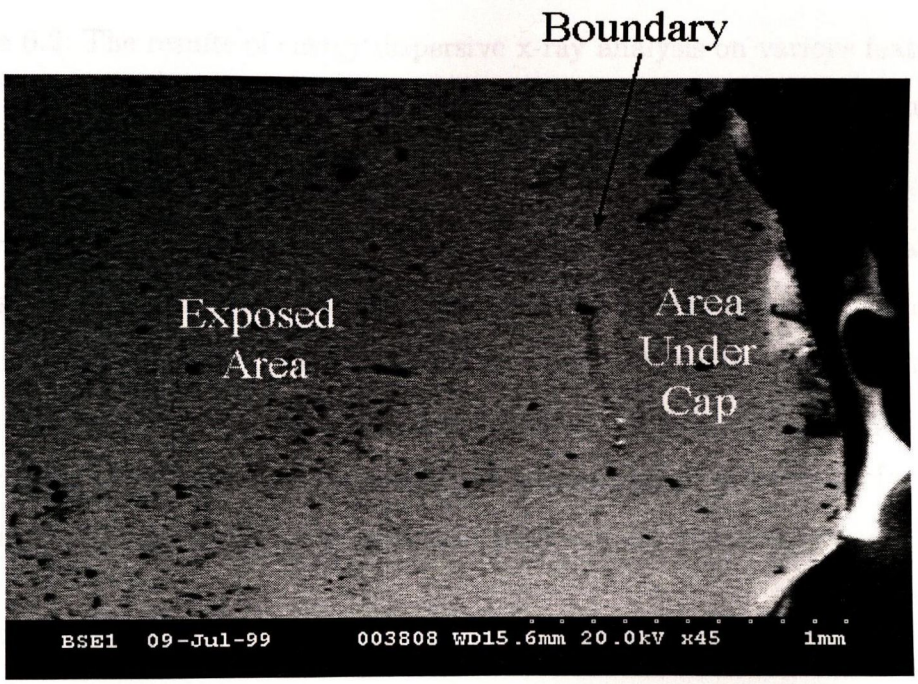

Figure 6.9: SEM picture of the iron film on magnetite. The colours obviously can't be distinguished but there is an area on the right which is bounded off from the rest and this is where no film was grown due to the sample-holder cap.

Feature	% Fe	% O	% Ta	% Na	% Cl
Undercap	47.69	49.88	0.19	1.62	-
Exposed	43.64	49.44	0.48	5.07	-
Dark1	41.17	48.74	0.70	7.76	0.50
Dark2	39.72	49.81	0.53	5.41	0.73

Table 6.2: The results of energy dispersive x-ray analysis on various features seen in the SEM. The features called *Dark* refer to the dark blobs seen in fig. 6.9.

different features were examined, the area under the cap, the exposed area, and some of the dark features. The results of this proved to be inconclusive largely due to the significant drift of the image during the time taken to do this measurement. Considering the magnetic nature of the sample the differences noted may well be within the experimental error range for the instrument. The details are tabulated in table 6.2 for completeness.

6.3.2 Analysis

At this point any explanation or model will necessarily be highly speculative. There is not yet enough data to support any definite conclusions. Further experiments are required (and some of these are outlined below) in order to arrive to a complete explanation. Nonetheless from the available data some possible models have been developed by the author, Dr. I.V. Shvets and G. Mariotto. In our explanations we assume that the deposited iron bonds with oxygen from the bulk and make use of the fact that there are three main, stable forms of iron oxide; FeO, Fe_2O_3 and Fe_3O_4.

The first model involves the formation of extra iron-oxygen bonds in an

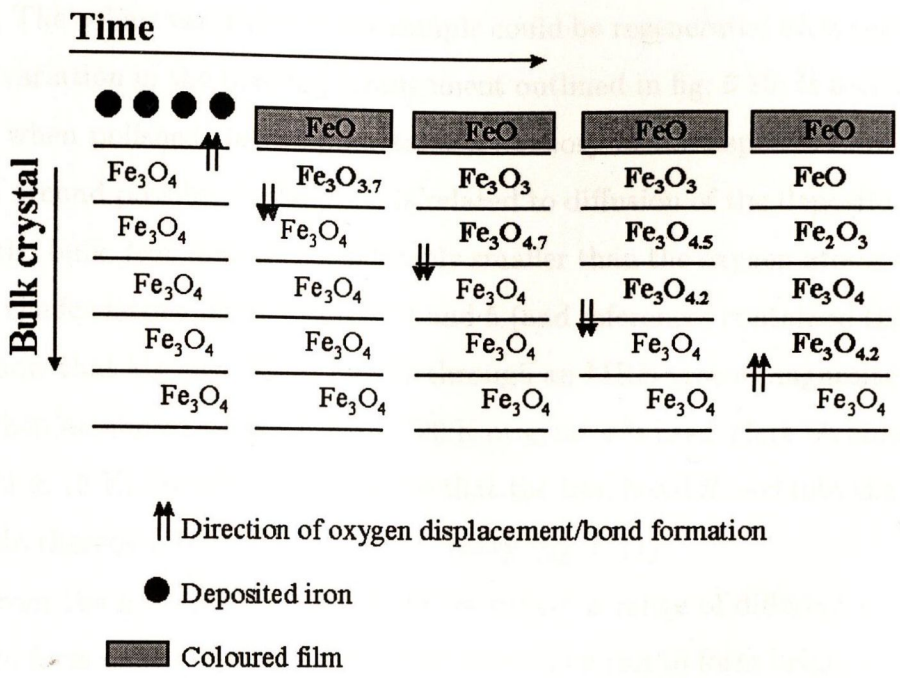

Figure 6.10: A model of the manner in which the presence of extra iron on the surface could cause a cascade effect in a wave-like manner into the bulk crystal.

attempt to balance the extra iron on the surface. As iron was deposited on the surface of Fe_3O_4 (100) the iron to oxygen ratio was radically altered. We suggest that when the sample was annealed to the transition temperature of 970 $\pm$ 15 K the surface iron was oxidised by forming bonds with oxygen atoms below. This then created an imbalance in the layer immediately below the surface layer such that this layer was no longer one of the stable forms of iron oxide. This layer would then attempt to form bonds with the layer below that again in order to stabilise itself. A succession of such layers could permeate in a wave-like manner into the bulk (fig. 6.10).

From a measurement of the amount of the sample already removed we can see that this cascade must penetrate at least some hundred microns into the

bulk. The colour variations in the sample could be regenerated after polishing by a variation in the bonding arrangement outlined in fig. 6.10. It seems that even when polished the sample retains a memory of the deposited film.

A second possible explanation is related to diffusion of the deposited iron into the bulk. Iron ions are considerably smaller than the oxygen atoms which form the fcc lattice. From chapters 4 and 5 (and references contained therein) we know that Mg can diffuse readily through an MBE-grown magnetite sample when an anneal temperature of 720 K or greater is used. Here we annealed at 970 $\pm$ 15 K, therefore it is possible that the iron has diffused into the bulk sample thereby offsetting the stoichiometry (fig. 6.11).

From the models presented above we expect a range of different iron oxides to form on the surface. Iron oxides are well known to form bright colours. For example, Fe_2O_3 is found naturally in a range of colours from red to brown and, indeed, red and brown dominate the surface of our films. Both FeO and Fe_3O_4 are black. Hematite (Fe_2O_3) is used in paints to create an effect known as "lustre flop" [79]. In this case the effect is created using thin mica plates (200-500 nm) upon which thin layers of transparent haematite particles (50-150 nm) are deposited by precipitation of Fe^{3+} oxide from an aqueous Fe^{2+} salt solution followed by calcination at 950-1150 K. This results in brilliantly coloured iridescent surfaces with colours ranging from red to green depending on the thickness of the haematite film. Fine haematite particles are transparent so the colours are the product of interference patterns. Haematite is also known to form blue and purple colours. This depends on particle size. Kerker *et al* [211] found that suspensions of haematite with particle sizes < 0.1 μm were orange, those between 0.1 and 0.5 μm were red and those > 1.5 μm had a strong enough reflectance in the blue region (440-480 nm) to appear purple. Particle size and shape also plays a significant role in the colour of

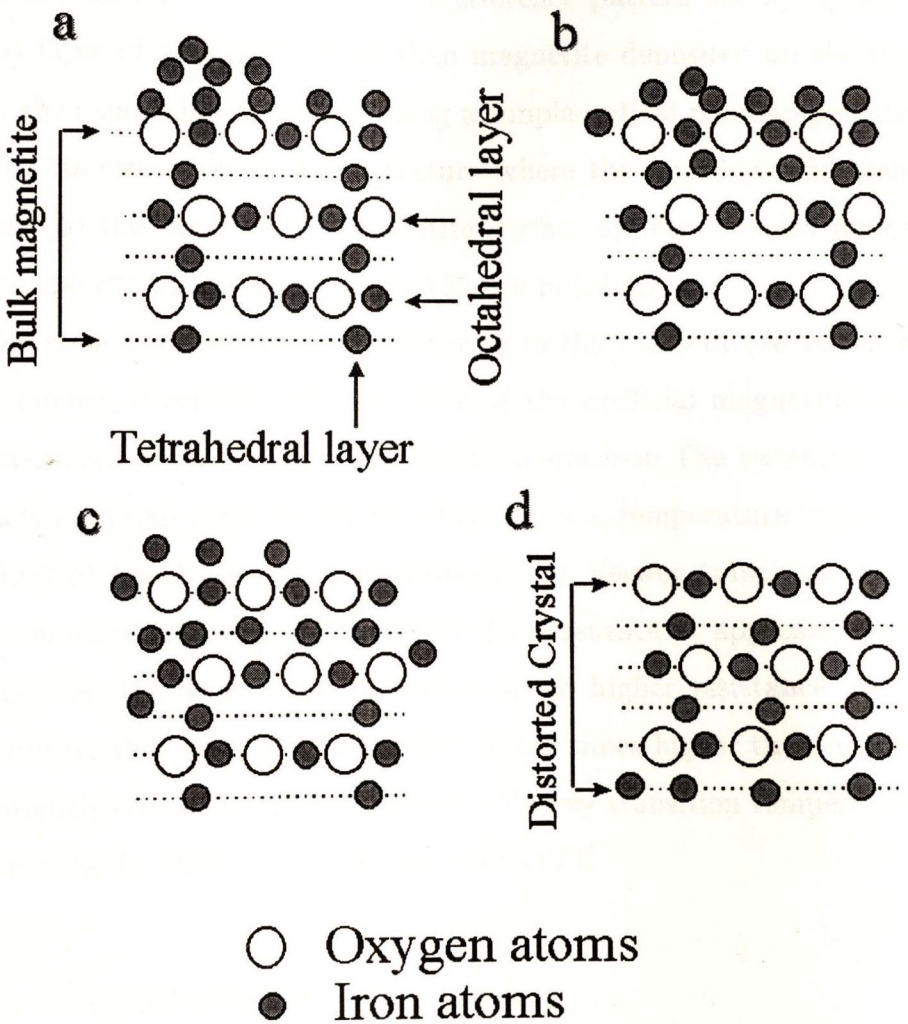

Figure 6.11: A model of the manner in which the deposited iron diffuses into the bulk.

the crystal. Hund [212] showed that smaller particles are redder and more symmetric particles (e.g. cubic) tend to reflect more in the blue end of the spectrum.

So it seems that there is a an interference pattern set up by a wedge shaped layer of some oxide other than magnetite deposited on the surface. When the sample is investigated using a simple optical microscope it is possible to discern a grainy surface texture where the sample is iridescent. In contrast to this the polished magnetite surface appears smooth under the microscope except for the marks of 0.25 μm polishing.

The second measurement of interest is in the temperature versus resistance curves. Previously the resistance of the artificial magnetite crystals was measured down to liquid nitrogen temperatures. The resistance of the magnetite crystals range from a few ohms at room temperature to some tens of kohms at liquid nitrogen temperatures. The Verwey transition temperature is marked by a sudden increase in the resistance at approximately 115 K. However, the iridescent films have a much higher resistance. At room temperature they have a resistance five to ten times higher than magnetite. The brightly coloured films also exhibit a Verwey transition temperature (as measured by G. Mariotto) in the region of 115 K.

6.4 Conclusions

The iron growth experiments are very promising. It would appear from experiment (1) that it is possible to prevent the formation of the nanoterrace surface structure by the deposition of 1.5 Å of iron onto a hot sample (970 $\pm$ 15 K). This resulted in quite a rough surface and some fine tuning may well produce a more useful surface. In any case, it is now possible to maintain

the square terraced surface for at least 120 hours of annealing at 970 ± 15 K. Atomic resolution images of this stabilised surface showing where the extra iron is positioned on the surface would be very interesting. It is possible that the stability and the increased surface roughness are linked. Information on the nature of the surface reconstructions on magnetite and their driving forces could be obtained from this study.

A range of film thicknesses should be deposited under the same conditions of sample preparation outlined in experiment (2) to determine how exactly the deposition of large amounts of iron on a structured surface aids the formation of nanoterraces.

A series of experiments was planned to investigate both results further. However, the discovery of the brightly coloured films due to iron deposition prevented this work. These films can be removed quite easily by diamond polishing and reformed thereafter without the need for further iron deposition by annealing in UHV at 970 ± 15 K. This indicates that the thin iron film deposited on the surface creates a cascade effect deep into the bulk of the crystal and this acts as a memory of the deposited film.

Chapter 7

STM experiments with magnetic field

"Find out what you're doing wrong and stop doing it....!"

Prof. J.M.D. Coey, 1993

7.1 Introduction

Before one can begin in earnest to perform spin polarised STM experiments one has to eliminate all possible sources of extraneous noise that could affect the interpretation of the results. We need to know how the sample behaves in the STM under an applied magnetic field. There are only a few experiments where STM measurements have been made in an external magnetic field so it is important to understand the experimental conditions that may influence the results which are not related to spin polarisation. For example thermal drift induced by the warming electromagnet electrodes or electromagnetic pick-up on the tunnel current from the electromagnet's power supply. Magnetite is a magnetic sample so the influence of a magnetic field on the bulk

sample in an STM experiment has also to be considered and examined. In essence, we need to test the present set-up to see if it is suitable for sensitive spin polarised STM experiments.

7.2 Magnetic investigations

As mentioned above, there are two fundamental questions to be answered before the in-situ electromagnet around the STM can be used for spin polarised experiments. The first is how the instrument will behave when a magnetic field is applied including questions of electromagnetic noise pick-up and general stability. The second feature is the behaviour of the sample under the influence of an applied field. If, for example, the sample were found to mechanically move this would displace the area under study in an uncontrolled manner under the tip or could even lead to a tip crash. The simple answer to both questions, as we shall see, is that the present system is not suitable for spin polarised experiments.

7.2.1 Results

The instrument

Initial experiments were centred around the possibility of electronic noise pick-up in the STM due to the applied field. The most straightforward method of testing this is to scan a non-magnetic sample with a non-magnetic tip while the electromagnet is operational. To this end a copper sample was scanned using a platinum-iridium tip by Dr. I.V. Shvets. The conclusion was that there was no detrimental effect except some thermal drift from heating of the electromagnet poles. The electromagnet is fitted with vacuum feedthroughs to allow for water or nitrogen cooling. However, nitrogen

cooling would probably generate far too much mechanical noise for high resolution STM imaging. When a magnetic field of 100 mT is generated by the electromagnet (which is the highest field that can be generated without risk of burning the coils) the temperature at different points of the electromagnet ranges from 330 to 360 K, being lower at the poles than in the centre of the windings. The time taken to reach these temperatures was measured by J. Naumann [191] to be of the order of 30 minutes. This temperature rise in the magnet is enough to induce significant thermal drift. Therefore there are two limitations to using the electromagnet. The magnet can be used either in the low field range (10-20 mT), in which case the temperature only rises by a couple of degrees over several hours or, if higher fields are required, time must be allotted to allow for thermal equilibrium. This experimental limitation, though not significant for the time being, will have to be dealt with in the future. Cooling the electromagnet will necessarily be re-examined.

From a purely mechanical point of view the present room temperature STM is unsuitable for magnetic experiments with fields greater than 60 mT. Although great care was taken to avoid standard magnetic eddy current damping so that this instrument would be suitable for magnetic experiments, the presence of nickel in the springs of the sample holder mount within the STM is a cause for concern. The springs from Coda Systems Ltd. [213] are designed to withstand repeated use and nickel is a major component of the materials used. Furthermore, some of the stainless steel components were found to develop significant magnetic permeability after work-induced heating.

The sample

At present the magnetite samples used have thicknesses of up to 1.2 mm and a lateral size in the region of 5 mm (due to the irregular nature of the original nuggets the samples are not disc shaped). When subjected to high magnetic fields this sample is attracted strongly to the poles of the electromagnet. In fact, the magnetite samples in conjunction with the nickel sample-holder-mount springs (which are also affected by the magnetic field) limited the maximum applied magnetic field to ~60 mT. Any higher field than this and the entire STM would be pulled towards the electromagnet poles. The field required for magnetisation saturation of the crystals was measured by the author to be of the order of 200 mT. The saturation magnetisation was found to be around 110 J/T Kg. Calculation of the field required for saturation is not trivial in the case of irregular shaped samples like the ones used in this thesis. Most calculations are done for the case of rods or ellipsoids [214]. In spite of not being able to apply the saturation field a number of interesting results emerged from these preliminary investigations of the influence of an external magnetic field on the surface of magnetite as seen by STM.

The first and most obvious finding was magnetostriction. When the external magnetic field is applied the surface can be seen to move away from the tip. This is a highly reproducible result. In the STM images the areas where an external magnetic field is applied look like depressions on the surface. For contrast purposes two images are shown in fig. 7.1. They are of the same area though in fig. 7.1**a** there is no applied magnetic field and in fig. 7.1**b** there is an applied field between the vertical 300 Å and 700 Å positions of 18 ± 2 mT. In fact there is a delay as the magnetic field is applied over a few scan lines rather than instantaneously so the effect can be seen to occur sometime after the 300 Å and 700 Å positions. We can see from the line profile that the

height change due to the magnetic field is of the order of 10 Å. There are two other interesting features to be seen in fig. 7.1**b**. One is the tip change due to some contaminant near the bottom of the image. The other is the large tip crash crater in the centre of the image. This is most likely due to the rapid application of the magnetic field at some point between the time when the two scans were taken though there is no record of this.

A great many images have been recorded with the same magnetostrictive effects. Generally the greater the applied field the larger the depression with actual values dependent on the relative orientation of the sample with respect to the applied field. The magnetostriction effects were considerably enhanced when the tip was ferromagnetic. Typically an iron tip would be some 3 to 5 mm long and the diameter of the wire used is 0.25 mm. In fig. 7.2 the effect of small changes in the external magnetic field is very pronounced. A line profile of these effects is shown directly below the STM image. In table 7.1 the changes in magnetic field along with the associated height changes are given. It can clearly be seen that this is quite a linear effect and also that only a **very** small change in magnetic field is required to induce a large magnetostrictive effect!

In one particular scanning session where the electromagnet was used with a PtIr tip, the magnetostriction was not linear. The variations of the sample height are shown graphically in fig. 7.3. The graph shows how the sample initially moved out towards the tip and then as the external magnetic field increased beyond 20 mT it contracted away from the tip until the field was greater than 50 mT at which point the sample again moved towards the tip rapidly up to the maximum value that could be applied of $\sim$63 mT. It is noteworthy that this curve was not due to a once off movement of the sample and was highly reproducible in several different scans. There are so

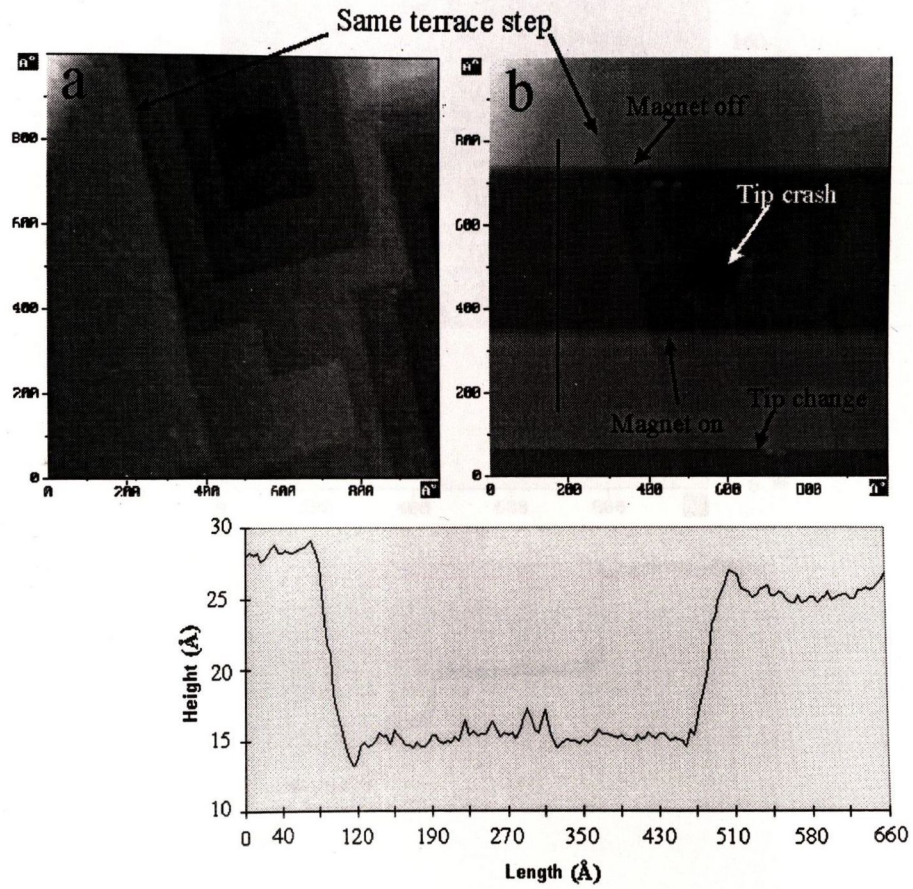

Figure 7.1: Two STM images of the same area. However, in **b** there is an applied magnetic field of 18 $\pm$ 2 mT between the vertical 300 Å and 700 Å positions. One can also see a tip change in the lower part of **b** and a notable tip crash crater in the centre of the image. PtIr tip. V_{bias} = 1 V, I_{tunnel} = 0.1 nA.

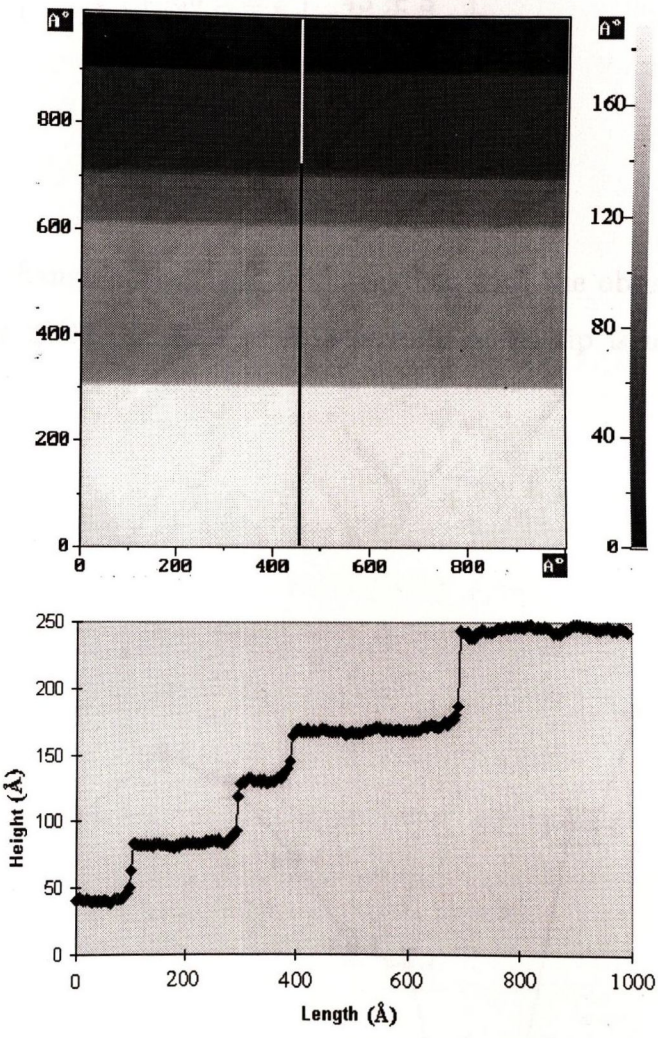

Figure 7.2: STM image and associated line profile of the cumulative magnetostrictive effect when a ferromagnetic tip is used to scan magnetite. The changes in magnetic field together with their associated height changes are shown in table 7.1. Fe tip. $V_{bias} = 1$ V, $I_{tunnel} = 0.1$ nA.

ΔB (mT)	% Δz (Å)
0.3 ± 0.1	43 ± 3
0.3 ± 0.1	48 ± 3
0.3 ± 0.1	38 ± 3
0.7 ± 0.2	78 ± 3

Table 7.1: The change in magnetic field together with the observed change in height in the STM (fig. 7.2) when a ferromagnetic tip is used to scan magnetite.

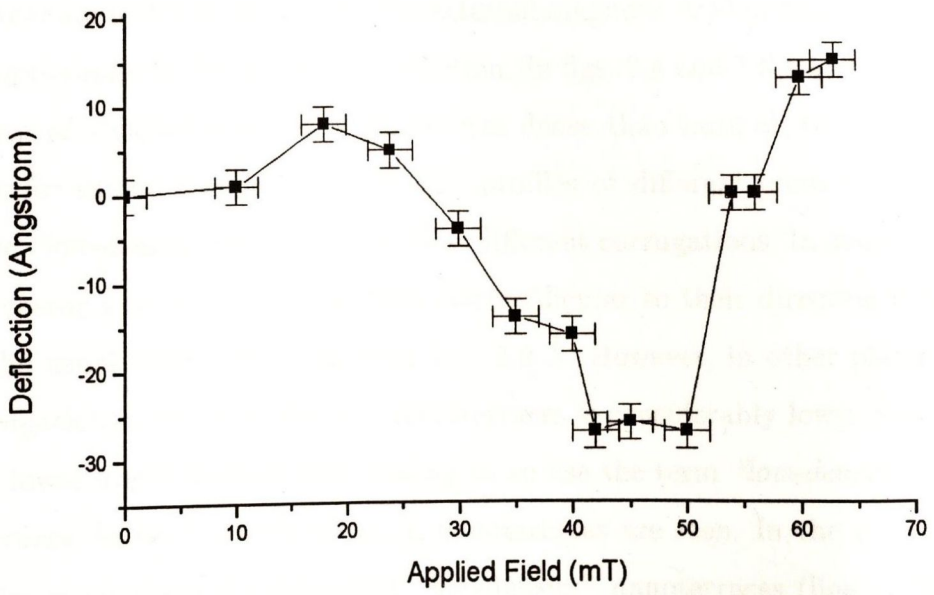

Figure 7.3: A graph of the movement of the sample relative to the tip along the z-direction due to an external magnetic field.

many possible influences on the magnetostriction seen here that it is difficult to say how much is due to the magnetite crystal itself and how much comes from other sources. It is possible, for example, that the crimp connectors that hold the STM tips and the spring probes that hold the samples (both of which we have found to be magnetic) could be affected by the changing magnetic field thus contributing to the height changes. Furthermore, the irregular shape of the sample coupled with the clamping of the sample by the cap screwed over it could lend itself to a range of strains that can not be modelled in a simple manner. This therefore, is an effect which will only be investigated properly when the TiSTM is in use.

The nanoterraces provided yet another interesting effect under the application of an external magnetic field. The effect was seen to appear only under certain sample orientations with respect to the applied field direction when a manganese-nickel tip was used. The external magnetic field in figs. 7.4 and 7.6 is approximately along the [110] direction. In figs. 7.4 and 7.6 two images are shown of nanoterraces which appear less dense than normal. By less dense we refer to the manner in which line profiles of different cross sections of these "low-density" nanoterraces yield different corrugations. In some places the corrugation of the nanoterraces perpendicular to their direction is close to the usual value seen in chapter 4 of 2.0 Å. However, in other places the corrugation of the "low-density" nanoterraces is considerably lower resulting in a lower overall average and leading us to use the term *"low-density" nanoterraces.* In fig. 7.4 both types of nanoterraces are seen. In the upper left of the image there is a terrace of "low-density" nanoterraces (line profile A in fig. 7.5). On the extreme right one can see the usual nanoterraces with the standard separations and corrugations (line profile B in fig. 7.5). From software measurements the most accurate interpretation can only be that

there is a lesser atomic density in the fainter terraces. This gives rise to the illusion when one first measures the corrugation of a significantly reduced corrugation. However, on closer inspection of the "low-density" nanoterraces one finds that the corrugation can be as high as normal, just not uniformly so throughout the nanoterrace.

A very strong piece of corroborating evidence for magnetic field influence is that when the connections to the coils of the electromagnet were reversed, such that an identical electric current (and hence temperature) was used but no magnetic field was generated, the effect could no longer be found anywhere on the surface. Furthermore atomic resolution images (fig. 7.7) were obtained. The resolution is not, however, as good as that seen in chapter 5 though it is still possible to discern atomic corrugation along the length of the nanoterrace (line profile of fig. 7.7). The interatomic spacing along the length of the nanoterrace is 5.7 ± 0.3 Å. This is approximately what was obtained earlier (chapter 5) in the absence of an external magnetic field. However, the atomic rows at either edge of a nanoterrace appear significantly reduced, particularly on the lower edge. This could easily be a scanning artefact related to the speed at which the tip passes from a trough to the first atomic row which is a greater height change than that going from atomic row to atomic row.

Fig. 7.6 takes a closer look at another region exhibiting the same unusual "low-density" nanoterraces. Unlike all the images previously shown this image differs in that it is a y-direction scan and instead of 256×256 resolution it is 512×512 points. However, even under this resolution it was not possible to obtain clear atomic resolution, though some atomic scale features are resolved. A careful measurement of the corrugation along these nanoterraces reveals a 12 Å periodicity along the direction of the nanoterraces. Further-

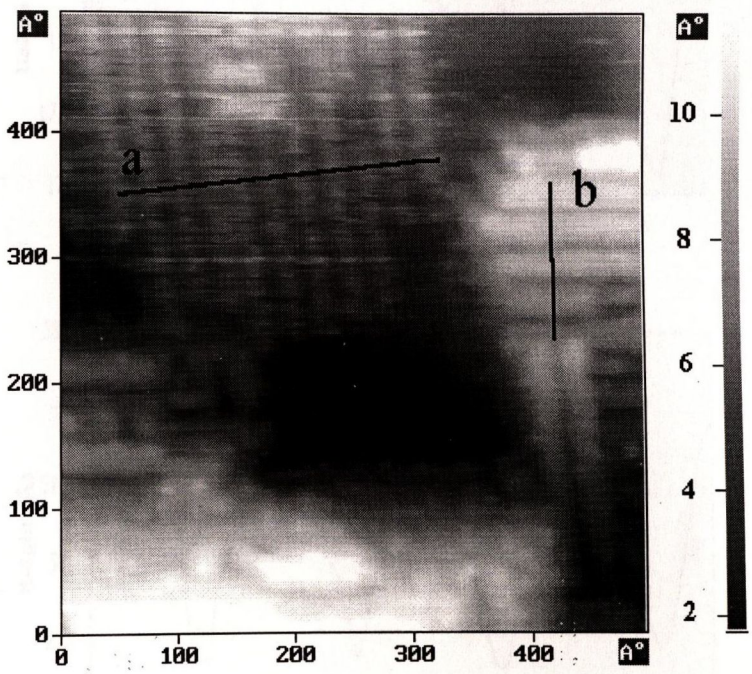

Figure 7.4: The unusual "low-density" nanoterraces can clearly be seen in the upper half of this image. On the right one can see an example of the normal nanoterraces. MnNi tip. $V_{bias} = 1$ V, $I_{tunnel} = 0.1$ nA.

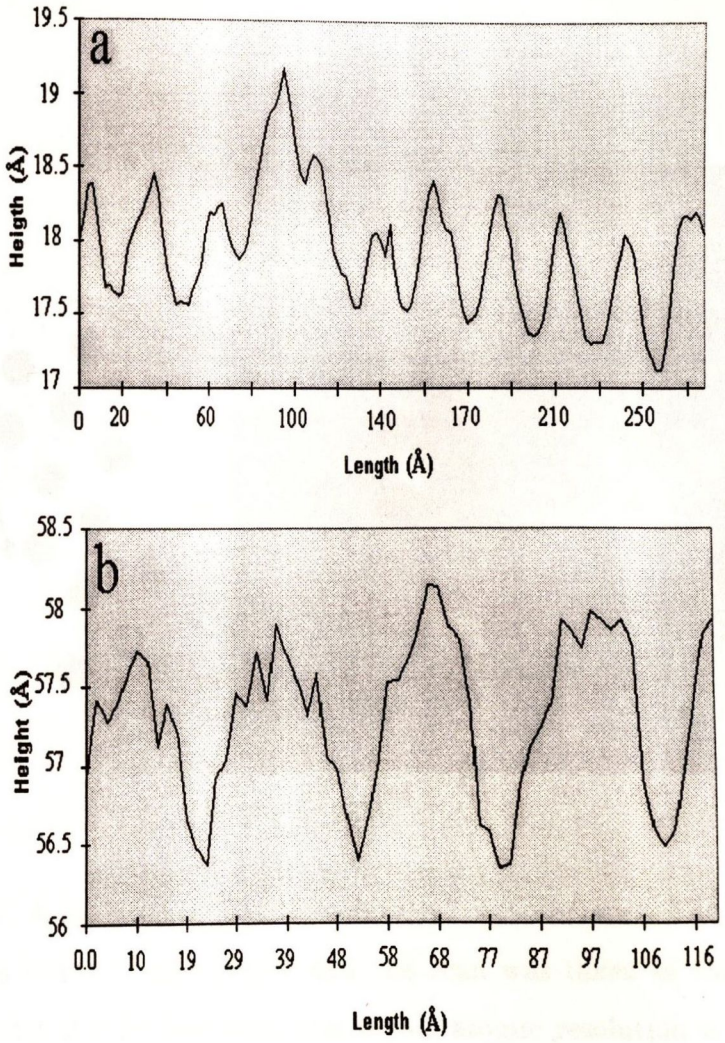

Figure 7.5: Line profiles of both the unusual "low-density" nanoterraces (upper left half of fig. 7.4) and the normal nanoterraces (right side of fig. 7.4). MnNi tip. $V_{bias} = 1$ V, $I_{tunnel} = 0.1$ nA.

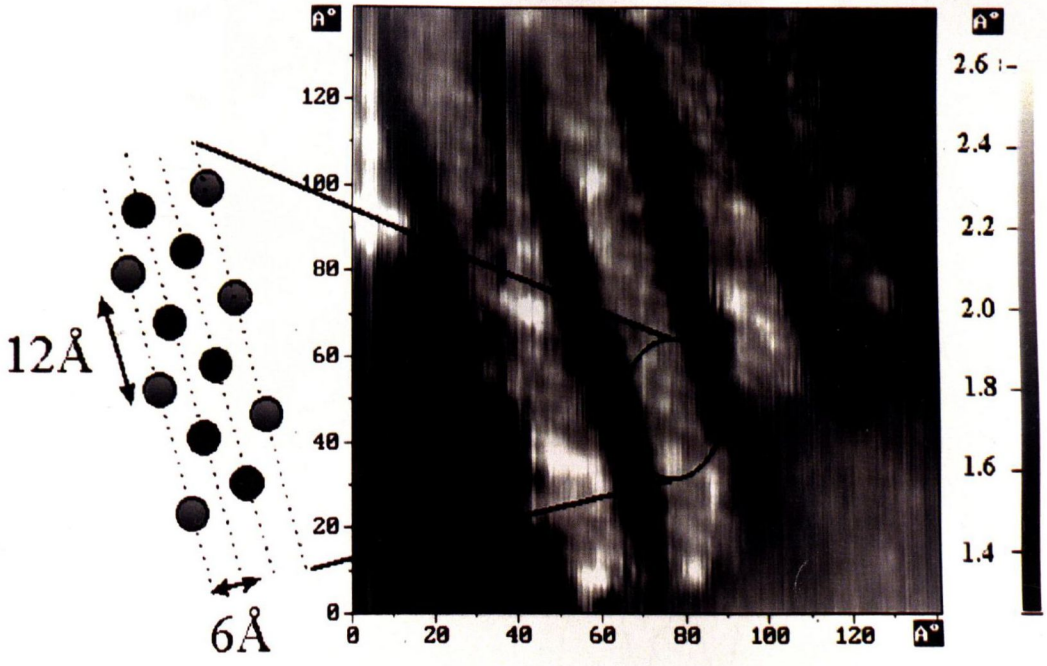

Figure 7.6: A close up of the "low-density" nanoterraces. The resolution of this image is 512 × 512 points and the scan was taken in the y-direction. A ball model of a section with reasonable atomic resolution is given. There appears to be a 12 Å periodicity along the nanoterrace. MnNi tip. V_{bias} = 1 V, I_{tunnel} = 0.1 nA.

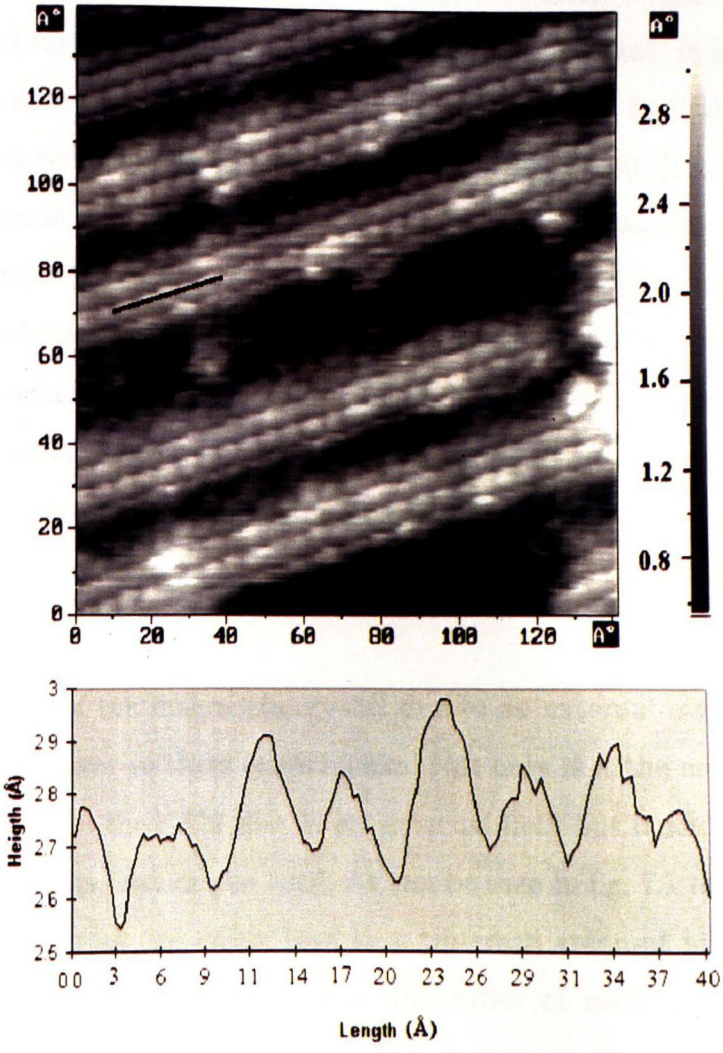

Figure 7.7: Atomic resolution image of a "normal" nanoterrace while in an external magnetic field of ~60 mT. The interatomic spacing along the length of the nanoterrace is 5.8 ± 0.2 Å. The atomic rows at the edges appear significantly reduced. MnNi tip. V_{bias} = 1 V, I_{tunnel} = 0.1 nA.

more the two central rows appear raised with respect to the other atomic rows along the nanoterraces. This is represented in the ball model of fig. 7.6 by darker balls. Unfortunately this is the best resolution obtained of these structures and further speculation is unjustified at this point. It is however, interesting to note that a 12 Å periodicity was taken before, by Wiesendanger *et al.*, as evidence for magnetic resolution on magnetite (100) [12,56,180]. In these experiments a 12 Å periodicity was obtained when scanning magnetite with an iron tip which was not observed when scanning with a tungsten tip.

The most obvious way to obtain a fuller understanding of this effect would be to observe what happens as the magnetic field is reduced. Unfortunately reducing the applied external magnetic field from 60 mT results in a completely different area being under the STM tip.

7.2.2 Analyses

Magnetostriction of the magnetite crystal due to an external magnetic field is the dominant factor in these experiments. Not only is it the most striking phenomenon seen in the STM due to an external field but it also limits the range of experiments that can be used. As can be seen in fig. 7.1 the use of an external electromagnet can easily lead to a tip crash amongst other effects. Fig. 7.2 gives a clear indication of the difficulties of using ferromagnetic probes in conjunction with a ferrimagnetic sample in the presence of an external magnetic field.

There is some very strong evidence that the appearance of the "low-density" nanoterraces described above is related to the magnetic field. Firstly there is the result that when the coils of the electromagnet were reversed no more "low-density" nanoterraces could be found. Of course, if it had been possible to observe the effect disappearing as the field was reduced then

the evidence would have been conclusive. For the time being that is not an option. However, in the near future with the advent of the TiSTM and using significantly thinner crystals it may be possible to do this. The reason is that thinner crystals could be saturated or remagnetised along their surface in a much smaller magnetic field. In addition the attractive force exerted by the magnet on the sample would be reduced at any value of the field due to the reduced volume of the sample.

Secondly there is the interesting observation that when the sample was rotated such that the electromagnet poles were no longer along the [110] direction but along [100] the "low-density" nanoterraces could not be found. This is in spite of all other conditions being identical, magnetic field, surface preparation conditions and the tip being unmoved. At room temperature (the temperature at which all these experiments were carried out) the easy axis of magnetisation for magnetite is along the [111] direction while the hard axis is along [100]. Therefore, knowing the directions of the easy and hard axes, one can expect that any magnetic field induced effects would occur more readily when the sample is orientated such that the magnetic field is applied along the [110] direction than along [100]. However, this is only the case for disc-shaped samples. In the present case the sample does not have a regular shape and therefore the field necessary to magnetise it largely depends on the shape of the sample. The sample is in fact elongated in approximately the [010] direction. Again this supports the conclusion that a magnetic field along [100] might not produce an effect as readily as a magnetic field along [110]. However, a change in the magnetic structure of the tip end can not be ruled out completely. In fact, one of the major draw-backs to this system is the complete lack of information about the magnetism of the tip end. The only way to deal with this at present is to avoid moving or damaging the

tip in the hope that it will remain unchanged. This was indeed the case for this series of experiments. The sample was annealed a number of times and so its orientation with respect to the magnetic field changed. However, the tip was not moved. Therefore, assuming there was no significant change to the magnetism at the tip end (even though we cannot observe this directly) one has to accept that the presence of "low-density" nanoterraces is due to the orientation of the sample in the magnetic field. However, it is also worth mentioning the possibility of multiple tips. It could be that applying a magnetic field of some 60 mT causes magnetostriction in the sample and/or the tip such that tunneling is now via a different tip or from a different part of the sample. This could explain why atomic resolution could be obtained when no magnetic field was applied and could not be obtained while the field was on. Multiple tip effects were clearly seen by Osing [209] using this tip on a different system.

Finally it must be remembered that over the course of this thesis hundreds of images have been recorded of nanoterraces. None of these exhibited the same unusual-looking nanoterraces as were seen when an external magnetic field was present.

The most obvious question at this point is "what is the effect"? If, indeed, there is an effect on the sample due to the external magnetic field. A quantifiable measure has not yet been obtained as it is still unclear whether the corrugation of the affected nanoterraces is truly lower or the atomic density within each nanoterrace is apparently lower. The images shown in figs. 7.4 and 7.6 come from separate scanning sessions. Several days passed between these sessions and the sample was annealed in this time to 970 ± 15 K. However, from figs. 7.4 and 7.6 one can clearly see that there is a rotation of no more than $\pm 5^o$ between them. That is, the magnetic field orientation with

respect to the crystal axes is approximately identical for these two scanning sessions.

Examining figs. 7.4 and 7.6 one might be forgiven for thinking that the effect occurs on all nanoterraces aligned in the vertical direction (y-direction). In fig. 7.4 however, there are two vertical nanoterraces which have a normal appearance. Unfortunately they are not well resolved and measuring the corrugation between them results in a large associated error. Therefore, even this evidence is inconclusive at this point.

Although recognising that these experiments are only preliminary and certainly not conclusive, the fact remains that there is an apparent effect on the sample topography due to the presence of an external magnetic field.

7.3 Conclusions

The magnetic experiments must be repeated and investigated further in order to make any definite conclusions. However, what this chapter serves to provide is some interesting milestones along the way to obtaining spin polarised STM.

Applying a strong magnetic field showed up very clearly the weaknesses of the present system. A combination of both a magnetic sample and some magnetic parts in the STM prevent fields any higher than $\sim$60 mT from being applied. Furthermore the magnetostriction associated with such a field means that STM imaging of a particular area cannot be maintained if the field is changed by anymore than a few mT. As a result it is difficult to prove conclusively that a particular result is due to the magnetic field or simply a scanning artefact.

Aside from the effects of magnetostriction a curious phenomenon was

observed in the presence of an external magnetic field of some 60 mT. A number of the nanoterraces were seen in the STM to become fainter when a field was applied along the [110] direction. Clear atomic resolution could not be obtained while the field was on. However, from what resolution could be obtained an apparent corrugation of ~12 Å was measured along the nanoterraces compared with the 6 Å normally seen. The corrugation perpendicular to the direction of the nanoterraces appears considerably less than the 2.0 Å normally measured though as mentioned above this may be due to the apparently lower atomic density. Possible explanations for this effect abound. They include multiple tip effects or simply an unusual phenomenon not associated with the magnetic field. Nonetheless it is difficult to ignore the possibility of some sort of spin polarised effect. Especially considering that the effect could not be found once the coils of the electromagnet were reversed and the magnetic field cancelled out. One explanation could be that due to the magnetic field one of the two iron configurations in magnetite (Fe^{3+} or Fe^{2+}) is no longer accessible to the tip and so the nanoterrace appears less dense. However, due to the limitations of the experimental set-up this can not yet be proven conclusively.

On the positive side, we found by scanning a non-magnetic sample, that the electromagnetic noise pick-up in the STM from the electromagnet is negligible. However, the present system is not suitable for spin polarised experiments. In spite of efforts to avoid any magnetic materials the STM still has some magnetic parts such as the springs for the sample holder mount and the stainless steel springs on the vibration damping stages. The magnetite samples currently in use are too thick making it necessary to use a high magnetic field. In the future when the TiSTM comes online and with thinner samples spin polarised experiments should be possible.

Chapter 8

Conclusions and further work

"Truth is rarely pure and never simple"

Oscar Wilde

8.1 Conclusions

The aim of this thesis from the beginning has been to prepare and fully characterise the surface of magnetite (100) in such a way that it could be used as a test surface for spin polarised STM experiments. As the work progressed a number of results, both expected and unexpected, explicable and inexplicable, were uncovered. The results can be broken into four categories; terrace scale structures, atomic scale structures, iron growth experiments and the results of applying an external magnetic field while scanning the surface with ferromagnetic and antiferromagnetic probes.

Two types of terrace scale structures were seen. The first was flat cubic terraces with a 2.0 ± 0.2 Å separation between them in the z-direction. We use the term "cubic" to describe the manner in which the surface was arranged with straight edges along [110] and 90° corners. The surface was

formed by annealing the sample in UHV to 970 ± 15 K for about 4 hours. Due to the high step density the cubic terraces had a wide range of sizes ranging up to more than 600 Å at times and down to some tens of angstroms on other occasions. This can be related directly to the mechanical polishing which was done by hand. However, the cubic terrace structures were a transient state and usually after a total anneal time of some 22 to 25 hours at 970 ± 15 K had elapsed, the surface transformed into a reconstructed surface structure which we call nanoterraces.

Nanoterraces have a range of widths from about 18 Å to 42 Å. The length of a nanoterrace is as variable as the size of the cubic terraces previously mentioned. The direction of the nanoterraces is along [110] and this rotates by 90^o every 2.0 Å in the z-direction. We use the term nanoterrace because the corrugation perpendicular to the direction of the nanoterraces is 2 ± 0.3 Å which is approximately the distance between consecutive octahedral **or** tetrahedral planes. Our belief is that the nanoterraces are the result of fragmentation of the cubic terraces into strips of narrow terraces.

It was only when atomic resolution images were obtained on both surface arrangements that we could start to form a model of what was driving the surface reconstructions. This model is based on electron counting arguments. Calculating the number of available electrons with respect to the number of electronegative element dangling bonds for the structures seen is very difficult and largely speculative. One of the limitations with STM is that one does not know which iron atom one sees. Even though we have atomic resolution images of the surface it is difficult to determine exactly which species we are observing and even to be sure from which atomic plane they originate.

Atomic resolution images of the cubic terrace structures were difficult to obtain and never very clearly resolved. However, when they were obtained it

was possible to observe a pairing of the iron atoms along every second row in the [110] direction. This formed a $\left(\sqrt{2} \times \sqrt{2}\right)$R45^o surface structure which approximately matched the predictions of Kim *et al.* made from LEED and RHEED observations. We determined that the surface (as predicted by Kim) is terminated by a half-filled tetrahedral layer. By combining this extra layer with an octahedral layer (Fe-O plane) and a second tetrahedral layer from below the Fe-O plane we could show that this surface is electron balanced. However, line defects (e.g. step edges) upset the balance of this cell. We have seen that nanoterraces begin at step edges. Therefore we can conclude that the nanoterraced surface is stabilised by the creation of more step edges.

Again using the model originally proposed by Kim *et al.* [148] and comparing with the STM images we have, it was possible to model the iron atoms in the nanoterraces. A balanced arrangement was found which is dependent on the formation of step edges every 18 Å. It is interesting to note that the staggered atomic arrangement imaged can only be modelled when three atomic planes are included in the model (one octahedral plane and one tetrahedral plane from either side of it).

As the cubic terrace structures did not persist for extended periods of time they could not be investigated carefully. Due to their regular nature when compared with the nanoterraces they might make a more useful test surface for spin polarised experiments. Therefore stabilisation of the cubic terrace structure was attempted. To this end iron was deposited onto the surface. The reasoning behind this was that the surface reconstructed because it wasn't electron balanced. Perhaps deposition of extra iron could provide a balance. Indeed the result of this was that deposition of 1.5 Å of iron onto a hot magnetite surface (970 $\pm$ 15 K) stabilised the cubic structures. Even after more than 120 hours annealing at 970 $\pm$ 15 K the surface did not form

nanostructures (though some cracking of the terraces could be observed) whereas normally 22 to 25 hours annealing at 970 ± 15 K is enough to create nanoterraces. Though not yet repeated, this seems to be a very successful approach.

We also found that depositing 6 Å of iron onto the surface at 850 ± 15 K after pre-annealing to 970 ± 15 K for 3 hours appeared to aid the formation of nanoterraces. It took only 12 more hours of annealing at 970 ± 15 K for nanoterraces to form. This is considerably less than the 22 to 25 hours normally required.

A very unexpected result was uncovered when iron was deposited on the unstructured magnetite (100) surface at room temperature and post-deposition annealed to 970 ± 15 K. The iron was seen to from a luminescent film on the surface. LEED images were diffuse and STM was unstable on these films. The films have a resistance nearly an order of magnitude higher than normal magnetite. It was only when the samples had been polished to remove the films and annealed in UHV that the truly surprising result appeared. The luminescent film reformed spontaneously without deposition of additional iron. Apparently the deposited film causes a cascade transformation deep into the crystal which retains a memory of the film. We speculate that this transformation is related to a tiny off-stoichiometry in the bulk induced by the extra iron bonding with oxygen atoms on the magnetite surface.

Magnetic experiments concentrated on determining whether or not the current set-up was suitable for spin polarised experiments or not. We examined the effect of applying an external magnetic field on the instrument and the sample. We found that approximately 60 mT is the highest field that can be applied without attracting the STM to the electromagnet poles. The main effect seen in the STM images is undoubtedly magnetostriction. From

the amount of magnetostriction seen we can conclude that ferromagnetic tips are unsuitable and the best hope is using antiferromagnetic tips.

When the magnetic field was applied along the [110] direction an unusual effect was seen. A number of the vertical nanoterraces were seen to become apparently fainter or to have a lower corrugation. This we termed "low-density" nanoterraces because different cross-sections of these nanoterraces have different corrugations which is related to the presence or absence of atoms along the nanoterraces. The probe in this case was antiferromagnetic MnNi. Reversing the electromagnet coils such that the magnetic field was cancelled out resulted in the disappearance of this effect. However, as a field of 60 mT causes such a considerable magnetostriction, the tip had to be withdrawn beforehand. Therefore scanning afterwards is in a different area. Even so it is interesting that this effect cannot be found when there is no field and all the nanoterraces appear identical. Furthermore, applying the field along [100] does not generate the same effect. It is conceivable that this was an observation of a spin polarised effect.

8.2 Further work

There is no doubt that an enormous amount of work remains to be done on magnetite. In the course of this thesis the parameters necessary for the formation of interesting stable surface structures were found. Furthermore considerable characterisation of the surface from atomic resolution imaging was possible in conjunction with speculations based on electron balancing and charge counting arguments. One of the most important additions to this work now would be a detailed investigation using Auger spectroscopy. A new cylindrical mirror analyser Auger system recently installed will be a useful

tool for this study. There is also the whole area of annealing the sample in various oxygen partial pressures to be investigated. It is possible that by oxidising and subsequently reducing the surface, important information may be gleaned on the atomic make-up of the surface. Furthermore, the rate of nanoterrace formation relative to square terrace width (just prior to nanoterrace formation) would be an interesting study.

The work on iron growth experiments has only just begun. There is an enormous amount of possible combinations of iron growth conditions to be investigated - the amount of iron deposited, sample deposition temperature, pre- and post-anneal temperatures and times etc. The luminescent films also need to be investigated further and promise to be a very interesting result. This work should include resistance versus temperature curves, Mössbauer, X-ray diffraction and Kerr effect measurements as well as a range of spectroscopic investigations.

Finally there is a lot of work to be done on the magnetic characterisation of the surface. This work should begin by replacing the current STM with the TiSTM built by the author. The magnetic components of the current STM could be partly responsible for the displacement of the sample relative to the tip when a magnetic field is applied. The TiSTM does not contain these components and the difference between the effects of the magnetic field on the two microscopes should be investigated carefully. The magnetite single crystals should also by ground down to as thin a sample as possible - preferably somewhere in the region of 50 to 100 μm. This should allow a higher magnetic field to be applied and reduce the magnetostriction. Thereafter spin polarised STM experiments can begin in earnest....

Appendix A

TiSTM Photos

The titanium scanning tunneling microscope was designed by Dr. I.V. Shvets, Dr. A. Quinn and C. Kempf and built by the author. Modifications to the original design made by the author are discussed in chapter 2. Below are three pictures of the TiSTM. The first (fig. A.1) is a view of the entire system including the 10 inch base flange, the stainless steel support rods and the two spring stages. Macor spacers are used to guide the various wires through the spring stages to the electrical feedthroughs.

The STM head stage is shown in fig. A.2. This stage contains a number of Macor blocks for crimp connectors. The pins in these blocks can be unplugged thus allowing for a certain degree of modularisation of the STM. The springs used are made from CuBe and these are connected via viton rings to the support rods. The viton rings serve to dampen vibrations which might otherwise have propagated along the springs. In this figure we can see that the walker is almost completely housed in stainless steel.

The third figure (fig. A.3) is a close-up of the TiSTM head itself. The titanium support rods for the microwave cavity run along either side of the STM head. The tip and sample holders are visible.

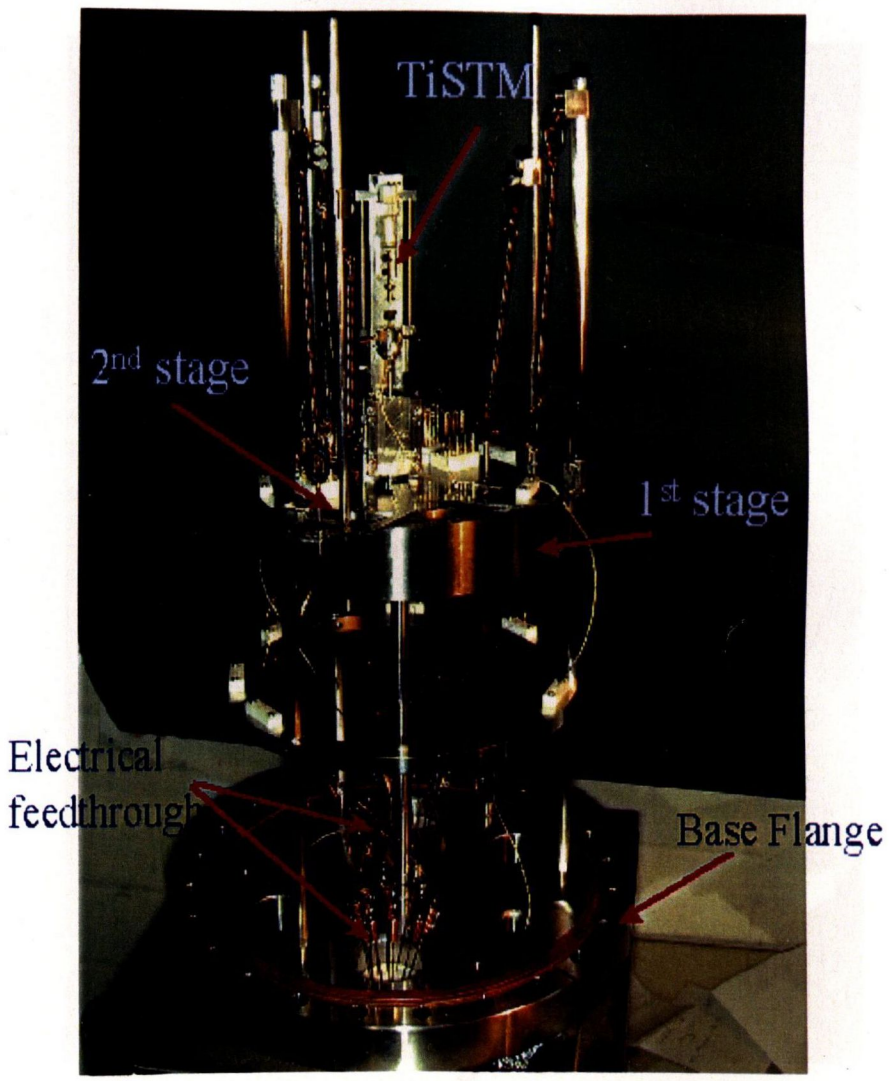

Figure A.1: View of the entire STM including base flange and spring stages.

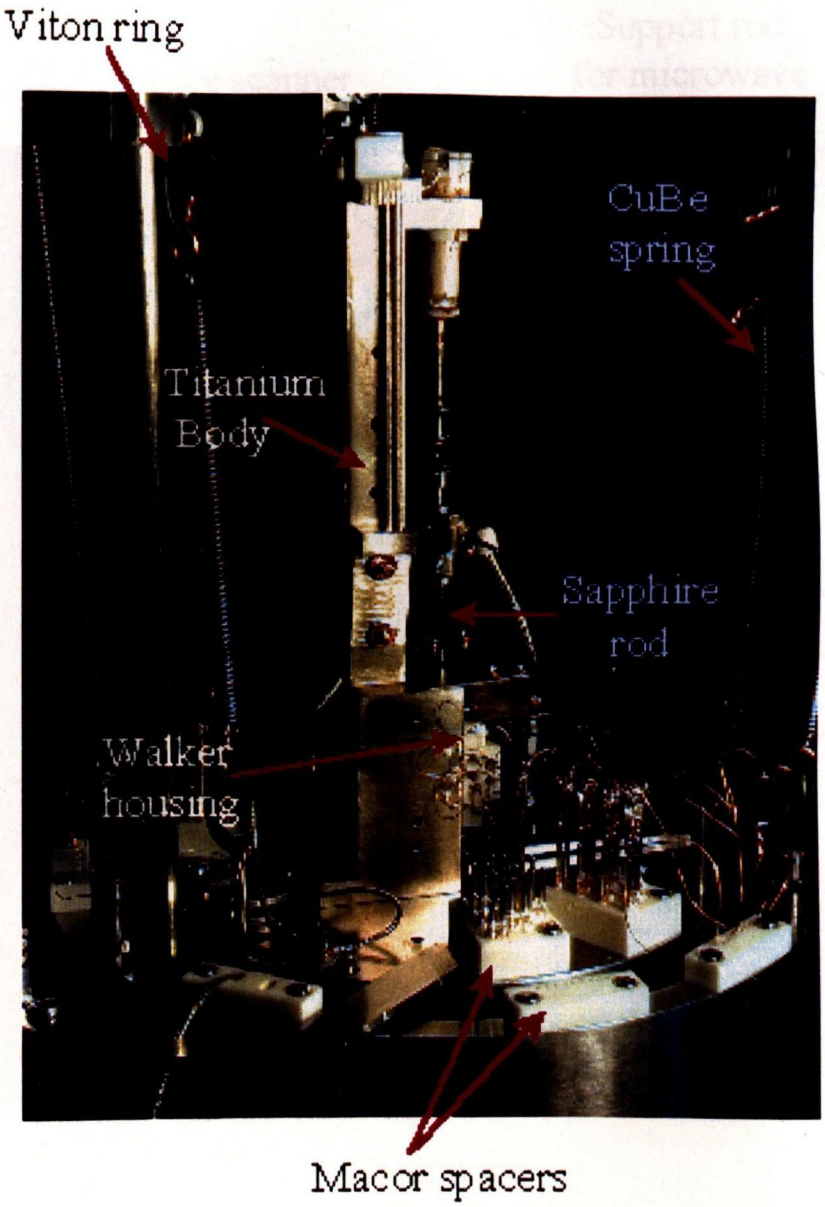

Figure A.2: A view of the TiSTM head and walker stage

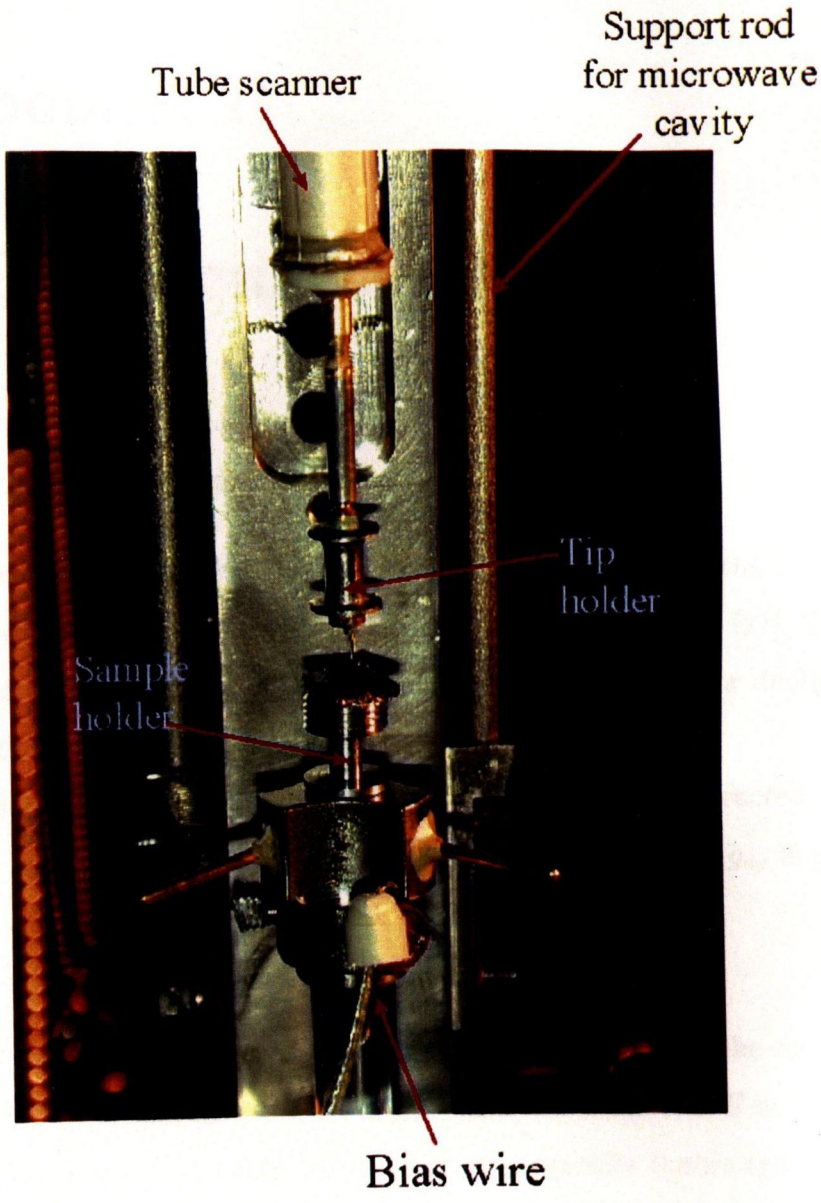

Figure A.3: A close-up of the TiSTM head.

Appendix B

LEED calculations

B.1 Equations

The formulae for the calculation of lattice parameters from the LEED system in our set-up were developed originally by Dr. A. Quinn [27]. They are presented here for completeness. Thereafter the procedure for dealing with magnetite LEED images is addressed.

An incident beam of electrons normal to the sample is diffracted through an angle α (fig. B.1). The associated reciprocal lattice vector g_{np} is given by

$$\mid g_{np} \mid = na^* + pb^* = k_d Sin\alpha = \frac{\sqrt{2mE}}{\hbar} Sin\alpha \tag{B.1}$$

where a^* and b^* are the reciprocal mesh basis vectors, k_d is the momentum of the diffracted electron beam, m is the electronic mass and E is the energy of the incident electron beam. In the case of magnetite (cubic symmetry)

$$\mid a^* \mid = \mid b^* \mid = \frac{2\pi}{a} \tag{B.2}$$

where a is the lattice parameter. Equation B.1 now reduces to

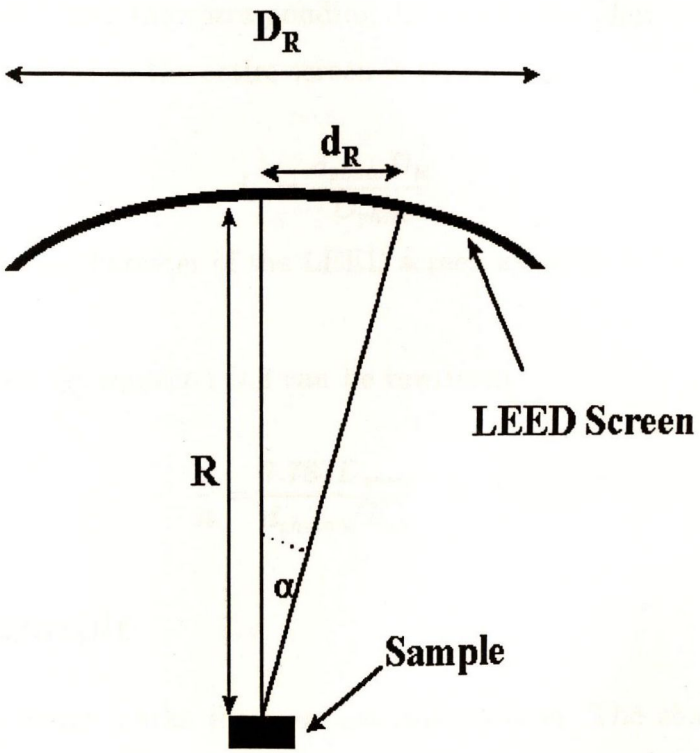

Figure B.1: A schematic of the LEED set-up

$$\frac{a}{n} = \frac{h}{Sin\alpha\sqrt{2meE_{eV}}} = \frac{12.2643}{Sin\alpha\sqrt{E_{eV}}} \text{ Å} \tag{B.3}$$

where E_{eV} is the beam energy in eV.

The LEED images are usually photographed using a tripod mounted camera. The radius of curvature of the LEED screen is 66 mm and its diameter, D_R, is 104 mm. The real distance, d_R, of a spot from the centre of the screen can be calculated from the corresponding distance in the photograph, d_{photo}, if a calibration photo of the entire screen is taken, i.e.

$$d_R = \frac{d_{photo}D_R}{D_{photo}} \tag{B.4}$$

where D_{photo} is the diameter of the LEED screen as measured in the photograph.

Since $Sin\alpha = \frac{d_R}{66}$ equation B.3 can be rewritten

$$\frac{a}{n} = \frac{7.783D_{photo}}{d_{photo}\sqrt{E_{eV}}} \text{ Å} \tag{B.5}$$

B.2 Example

In fig. B.2 an arrow marks the measurement position. The shadow of the electron gun is not exactly central but it still blocks the central spot. So the arrow shown is twice the value d_{photo}. The energy of the electron beam was 95 eV.

Measuring the distance between successive spots along the (110) direction as shown yields a value of 31 mm. The value of D_{photo} in this image is 108 mm. Putting these figures in equation B.5 gives a value for the lattice parameter of 5.56 Å in the (110) direction. This is expected to be 5.93 Å. Therefore there is a 6% error in the set-up. The error probably relates to the position

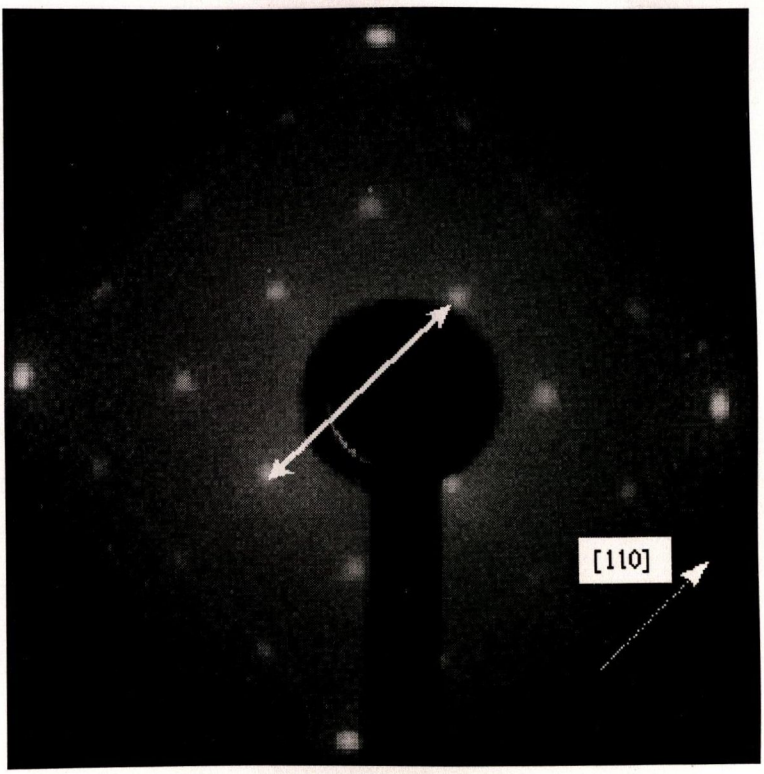

Figure B.2: An example of a LEED image for calculations.

of the sample in the UHV magnetic drives and the position of the magnetic drive itself as well as the error associated with camera optics, measurements of the LEED spots, etc.

Appendix C

Electron counting

In chapter 5 the result of electron counting on the nanoterraces is presented without detailed calculations. In the following, the details of the calculations leading to the balanced structure presented are outlined.

Every oxygen atom in the bulk magnetite crystal has four bonds to iron. Three of these are to octahedral iron atoms and the fourth is to a tetrahedral iron. Of the three octahedral iron-oxygen bonds two are in the plane of the oxygen atoms and the third is from either the plane above or the plane below the oxygen plane. This alternates every second oxygen atom. Similarly every second tetrahedral iron-oxygen bond is from above the oxygen plane and the other is from below. The result is that for a sample cleaved along the [100] direction every second oxygen atom is missing one bond to an octahedral iron atom and one to a tetrahedral iron atom.

In fig. C.1 a balanced unit cell which has a width of ~18 Å and a length of ~6 Å is shown. This cell represents the atomic resolution images of nanoterraces. As mentioned in chapter 5 it is assumed that all the octahedral iron atoms in the oxygen plane and all the tetrahedral iron atoms from below this plane are present whether imaged in the STM or not. Those atoms which

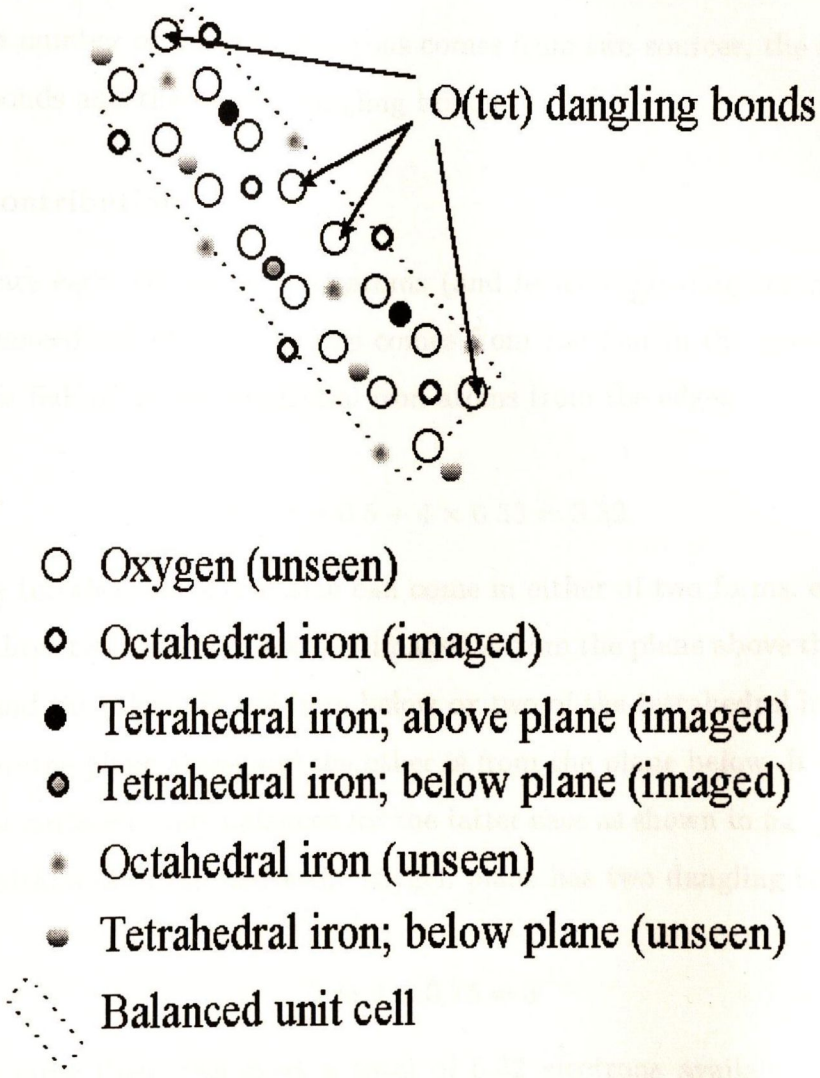

Figure C.1: A balanced unit cell of nanoterrace. The cell is approximately the width of a nanoterrace (~18 Å) and 6 Å long. Both imaged and unseen atoms are marked.

are present on the surface but not imaged by the STM are shown without outlines in fig. C.1. Also, as mentioned in chapter 3 the oxygen atoms are not imaged.

The number of available electrons comes from two sources, the iron dangling bonds and the oxygen dangling bonds.

Iron contribution

There are eight octahedral iron atoms (and hence eight dangling bonds) in the balanced cell of fig. C.1. This comes from the four in the middle of the cell plus half of all the octahedral iron atoms from the edges.

$$8 \Rightarrow 4 \times 0.5 + 4 \times 0.33 = 3.32 \tag{C.1}$$

The tetrahedral contribution can come in either of two forms; either one of the three tetrahedral iron atoms imaged is from the plane above the oxygen plane and the other two are from below **or** two of the tetrahedral iron atoms are from the plane above and the other is from the plane below. It turns out that the surface is only balanced for the latter case as shown in fig. C.1. Each tetrahedral atom from above the oxygen plane has two dangling bonds.

$$2 \Rightarrow 4 \times 0.75 = 3 \tag{C.2}$$

Summing these two gives a total of 6.32 electrons available from iron contributions.

Oxygen contribution

There are in total 16 oxygen atoms in the balanced cell (the oxygen atoms at the edge of a nanoterrace are assumed not to be shared with neighbouring

nanoterraces). As mentioned above every second oxygen atom is missing an octahedral iron from the plane above it.

$$8 \Rightarrow 4 \times 1.5 + 4 \times 1.67 = 12.68 \tag{C.3}$$

Marked on fig. C.1 are the positions of the tetrahedral oxygen dangling bonds. One would normally expect eight oxygen dangling bonds from tetrahedral iron atoms missing from the plane above. However, from STM images it appears that some of these iron atoms are present. Therefore there are only four tetrahedral oxygen dangling bonds.

$$4 \Rightarrow 4 \times 1.25 = 5 \tag{C.4}$$

Adding C.1, C.2, C.3 and C.4 gives a total of 24 available electrons.

There are 8 octahedral oxygen dangling bonds and 4 tetrahedral oxygen dangling bonds. This is a total of 12 oxygen dangling bonds. Therefore 24 electrons are needed to balance the surface. This is exactly what we have so this surface is electron balanced.

Bibliography

[1] G. Binnig, H. Rohrer, Ch. Gerber, and E. Weibel. *Phys. Rev. Lett.*, 49(1):57, 1982.

[2] B. Feuerbacher, B. Fitton, and R.F. Willis. *Photoemission and the electronic properties of surfaces.* J. Wiley and Sons, Chichester, UK, 1978).

[3] S.F. Alvarado, W. Eib, F. Meier, D.T. Pierce, K. Sattler, H.C. Siegmann, and J.P. Remeika. *Phys. Rev. Lett.*, 34(6):319, 1975.

[4] S.F. Alvarado, M. Erbudak, and P. Munz. *Phys. Rev. B*, 14(7):2740, 1976.

[5] E. Kay, R.A. Sigsbee, G.L. Bona, M. Taborelli, and H.C. Siegmann. *Appl. Phys. Lett.*, 47(5):533, 1985.

[6] M. Campagna, D.T. Pierce, F. Meier, K. Sattler, and H.C. Siegmann. *Adv. Electronics and Electron Phys.*, 41:113, 1976.

[7] J. Kessler. *Rec. Mod. Phys.*, 41(1):3, 1969.

[8] S.F. Alvarado and P. Renaud. *Phys. Rev. Lett.*, 68(9), 1992.

[9] P.M. Tedrow and R. Meservey. *Phys. Rev. Lett.*, 26:192, 1971.

[10] M. Julliere. *Phys. Lett. A*, 54:225, 1975.

[11] R. Wiesendanger, H.J. Güntherodt, G. Güntherodt, R.J. Gambino, and R. Ruf. *Phys. Rev. Lett.*, 65:247, 1990.

[12] R. Wiesendanger, I.V. Shvets, D. Bürgler, G. Tarrach, H.J. Güntherodt, J.M.D. Coey, and S. Gräser. *Science*, 255:583, 1992.

[13] J. Osing and I.V. Shvets. *Surf. Sci.*, 1998.

[14] J.A.C. Bland, C. Daboo, G.A. Gehring, B. Kaplan, A.J.R. Ives, R.J. Hicken, and A.D. Johnson. *J. Phys.: Condens. Matter*, 7:6467–6476, 1995.

[15] R. Wiesendanger. *Scanning probe microscopy and spectroscopy.* Cambridge University Press, Cambridge, 1994.

[16] C. Julian Chen. *Introduction to scanning tunneling microscopy.* Oxford University Press, New York, 1993.

[17] J. Bardeen. *Phys. Rev. Lett.*, 6:57, 1961.

[18] S. Maekawa and U. Gafvert. *IEEE Trans. Magn.*, 18:707, 1982.

[19] J.C. Slonczewski. *J. Physique C*, 8:1629, 1988.

[20] J.C. Slonczewski. *Phys. Rev. B*, 39(10):6995, 1989.

[21] A.A. Minakov and I.V. Shvets. *Surf. Sci. Let.*, 236:L377, 1990.

[22] R. Wiesendanger, D. Bürgler, G. Tarrach, A. Wadas, D. Brodbeck, H.-J. Güntherodt, G. Güntherodt, R.J. Gambino, and R. Ruf. *J. Vac. Sci. Technol. B*, 9(2):519, 1991.

[23] M. Johnson and J. Clarke. *J. Appl. Phys.*, 67:6141, 1990.

[24] M. Bode, M. Getzlaff, and R. Wiesendanger. *Phys. Rev. Lett.*, 81(19):4256, 1998.

[25] W. Wulfhekel and J. Kirschner. *Appl. Phys. Lett.*, 75(13):1944, 1999.

[26] I.V. Shvets, R. Wiesendanger, D. Burgler, G. Tarrach, H.J. Guntherodt, J.M.D. Coey, and S. Graser. *J. Appl. Phys.*, 71:5489, 1992.

[27] Aidan Quinn. Development of an ultra-high vacuum scanning tunneling microscope. *PhD-thesis*, Trinity College Dublin, 1996.

[28] Omicron Vakuumphysik. *Idsteiner Str.78, D–65232 Taunusstein, Germany.*

[29] G. Mariotto, M.D. D'Angelo, Y. Kresnin, and I.V. Shvets. *accepted by Appl. Surf. Sci.*, 1999.

[30] Vakuum Schmelze. *Hanau, Germany.*

[31] Molecular Devices and Tools for NanoTechnology. *103460 Moscow, State Research Institute of Physical Problems, Russia.*

[32] L.F. Cohen and E.L. Wolf. *Meas. Sci. Technol.*, 2:83, 1991.

[33] B. Michel, W. Mizutani, R. Schierle, A. Jarosch, W. Knop, H. Benedickter, W. Bachtold, and H. Rohrer. *Rev. Sci. Instrum.*, 63(9):4080, 1992.

[34] W. Seifert, E. Gerner, M. Stachel, and K. Dransfeld. *Ultramicroscopy*, 42-44:379, 1992.

[35] D. Rugar, C.S. Yannoni, and J.A. Sidles. *Nature*, 360:563, 1992.

[36] Y. Manassen, R.J. Hamers, J.E. Demuth, and A.J. Castellano. *Phys. Rev. Lett.*, 62:2531, 1989.

[37] Bywell Springs and Pressings Ltd. *Millsborough House, Ipsley St., Redditch B98 7AL, UK.*

[38] California Fine Wire Company. *Grove City, CA 93433, USA.*

[39] Caburn MDC Ltd. *The Old Dairy, The Street, Glynde, East Sussex BN8 6SJ, UK.*

[40] Staveley Sensors. *91 Prestige Park Circle, East Hartford, CT 06108, USA.*

[41] Vacuum Generators. *Maunsell Road, Castleham Industrial Estate, Hastings, East Sussex TN389NN, UK.*

[42] G. Tarrach, D. Bürgler, T. Schaub, R. Wiesendanger, and H.J. Güntherodt. *Surf. Sci.*, 285:1, 1993.

[43] E.J.W. Verwey and P.W. Haayman. *Physica*, 8:979, 1941.

[44] R. Aragon, D.J. Buttrey, J.P. Shepherd, and J.M. Honig. *Phys. Rev. B*, 31(1):430, 1985.

[45] Prof. Honig. *Purdue University, Indiana, USA.*

[46] RTI GmbH. *Technologiepark 12, D-33100 Paderborn, Germany.*

[47] R.G. Musket, W. McLean, C.A. Colmenares, D.M. Makowiecke, and W.J. Siekhaus. *Appl. Surf. Sci*, 10:143, 1982.

[48] T. Michely, K.H. Besocke, and G. Comsa. *Surf. Sci.*, 230:L135, 1990.

[49] T. Michely and G. Comsa. *Surf. Sci.*, 256(3):217, 1991.

[50] T. Michely and G. Comsa. *Phys. Rev. B*, 44(15):8411, 1991.

[51] J.C. Girard, Y. Samson, S. Gauthier, S. Rousset, and J. Klein. *Surf. Sci.*, 302:73, 1994.

[52] T. Michely and C. Teichert. *Phys. Rev. B*, 50(15):11156, 1994.

[53] C. Teichert, M. Hohage, T. Michely, and G. Comsa. *Phys. Rev. Lett.*, 72(11):1682, 1994.

[54] M. Aeschlimann, G.L. Bona, F. Meier, M. Stampanoni, and H.C. Siegmann. *Appl. Phys. Lett*, 49(13):824, 1986.

[55] M. Aeschlimann, G.L. Bona, F. Meier, M. Stampanoni, and G. Zampieri. *Fruhjahrstagung der SPG/SSP*, 60:794, 1987.

[56] R. Wiesendanger, I.V. Shvets, and J.M.D. Coey. *J. Vac. Sci. Technol. B*, 12(3):2118, 1994.

[57] J. Tershoff and D.R. Hamann. *Phys. Rev. Lett.*, 31:805, 1985.

[58] E. Stoll. *Surf. Sci.*, 143:L411, 1984.

[59] Y. kuk, P.J. Silverman, and H.Q. Nguyen. *J. Vac. Sci. Technol. A*, 6:524, 1988.

[60] G.W. Stupian and M.S. Leing. *Rev. Sci. Instrum*, 60:181, 1989.

[61] P.K. Hansma and J. Tersoff. *J. Appl. Phys.*, 61:R1, 1987.

[62] V.T. Binh. *J. Microsc.*, 152:355, 1988.

[63] H. Neddermeyer and M. Drechsler. *J. Microsoc.*, 152:459, 1988.

[64] J.A. Stroscio, R.M. Feenstra, and A.P. Fein. *Phys. Rev. Lett.*, 58:1668, 1987.

[65] D.K. Biegelsen, F.A. Ponce, J.C. Tramontana, and S.M. Koch. *Appl. Phys. Lett.*, 50:696, 1987.

[66] D.K. Biegelsen, F.A. Ponce, and J.C. Tramontana. *Appl. Phys. Lett.*, 54:1223, 1989.

[67] R. Guckenberger, C. Kosslinger, R. Gatz, H. Breu, N. Levai, and W. Baumeister. *Ultramicrsocopy*, 25:111, 1988.

[68] P.J. Bryant, H.S. Kim, Y.C. Zheng, and R. Lang. *Rev. Sci. Instrum.*, 58:1115, 1987.

[69] M.J. Heben, M.M. Dovek, N.S. Lewis, R.M. Penner, and C.F. Quate. *J. Microsoc*, 152:651, 1988.

[70] L.A. Nagahara, T. Thundat, and S.M. Lindsay. *Rev. Sci. Instrum.*, 60:3128, 1989.

[71] J.P. Ibe, P.P. Bey Jr., S.L. Brandow, R.A. Brizzolara, N.A. Burnham, D.P. DiLella, K.P. Lee, C.R.K. Marrian, and R.J. Colton. *J. Vac. Sci. Technol. A*, 8(4):3570, 1990.

[72] S.N. Molotkov. *Surf. Sci.*, 261:7, 1992.

[73] A.J. Melmed. *J. Vac. Sci. Technol. B*, 9:601, 1991.

[74] S. Murphy, J. Osing, and I.V. Shvets. *Appl. Surf. Sci.*, 144-145:497, 1999.

[75] J.A. Jacobs. *Geomagnetism.* Academic Press, 1989.

[76] R. Blakemore. 190:377, 1975.

[77] H.A. Lowenstam. *Geol. Soc. Am. Bul.*, 73:435, 1962.

[78] M.P. Sharrock and R.E. Bodner. *J. Appl. Phys.*, 57:3919, 1985.

[79] R.M. Cornell and U. Schwertmann. *The iron oxides.* Verlagsgellschaft mbH, Germany, 1996.

[80] D.J. Monsma, J.C. Lodder, Th.K.A. Popma, and B. Dieny. *Phys. Rev. Lett.*, 74:5260, 1995.

[81] V.Y. Irkhin and M.I. Katnelson. *Sov. Phys. - Uspekhi*, 164:705, 1994.

[82] A. Bratkovsky. *Phys. Rev. B*, 56(5):2344, 1997.

[83] R. Meservey and P.M. Tedrow. *Phys. Reports*, 238:173, 1994.

[84] J.M.D. Coey. Magnetic properties of iron in soil iron oxides and clay minerals. In J.W. Stucki, B.A. Goodman, and U.Schwertmann, editors, *Iron in soils and clay minerals*, page 397. D. Reidel Publ. Co., 1988.

[85] H. Soffel. *Paläomagnetismus und Archäomagnetismus.* Springer, Berlin, 1991.

[86] E. Murad. Properties and behaviour of iron oxides as determined by mössbauer spectroscopy. In J.W. Stucki, B.A. Goodman, and U.Schwertmann, editors, *Magnetic properties of iron in soil iron oxides and clay minerals*, page 309. D. Reidel Publ. Co., 1988.

[87] W.H. Bragg. *Nature*, 95:561, 1915.

[88] T.F.W. Barth and E. Posnjak. *Zeits. f. Krist.*, 82:325, 1932.

[89] C.G. Shull, E.O. Wollan, and W.C. Koehler. *Phys. Rev.*, 84:912, 1951.

[90] E.J.W. Verwey and E.L. Heilmann. *J. Chem. Phys.*, 15(4):174, 1947.

[91] R.W.G. Wyckoff. *Crystal structures.* John Wiley and Sons, 1964.

[92] E.J.W. Verwey, F. de Boer, and J.H. van Santen. *J. Chem. Phys.*, 16(12):1091, 1948.

[93] E.J.W. Verwey and J.H. de Boer. *Rec. Trav. Chim. Pays-Bas*, 55:531, 1936.

[94] J.H. de Boer and E.J.W. Verwey. *Proc. Phys. Soc.*, 59A:59, 1937.

[95] E.J.W. Verwey, P.W. Haayman, and R. Romeyn. *J. Chem. Phys.*, 15:181, 1947.

[96] E.J.W. Verwey. *Nature*, 144:327, 1939.

[97] P.A. Miles, W.B. Westphal, and A. von Hippel. *Rev. Mod. Phys.*, 29:279, 1957.

[98] P. Weiss and R. Forrer. *Ann. Phys*, 12(10):279, 1929.

[99] R.W. Millar. *J. Am. Chem. Soc.*, 51:215, 1929.

[100] L.R. Bickford. *Phys. Rev.*, 78:449, 1950.

[101] L.R. Bickford. *Revs. Modern Phys.*, 25:75, 1952.

[102] S.C. Abrahams and B.A. Calhoun. *Acta. Cryst.*, 6:105, 1953.

[103] C.H. Li. *Phys. Rev.*, 40:1002, 1932.

[104] Y. Fujii, G. Shirane, and Y. Yamada. *Phys. Rev. B*, 11:2036, 1975.

[105] M. Iizumi and G. Shirane. *Solid State Commun.*, 17:433, 1975.

[106] S. Iida, K. Mizushima, K. Yanai, N. Goto, and S. Yumoto. *J. Appl. Phys.*, 49:1456, 1978.

[107] H.A. Bethe. *Proc. Roy. Soc. A*, 150:552, 1932.

[108] L. Onsager. *Phys. Rev.*, 65:117, 1944.

[109] F. de Boer, J.H. Van Santen, and E.J.W. Verwey. *J. Chem. Phys.*, 18:1032, 1950.

[110] J.H. van Santen. *Phillips Res. Rep.*, 5:282, 1950.

[111] B.L. Waerden. *Z. Physik*, 118:473, 1941.

[112] P.W. Anderson. *Phys. Rev.*, 102:1008, 1956.

[113] S.M. Shapiro, M. Iizumi, and G. Shirane. *Phys. Rev. B*, 14:200, 1976.

[114] N.F. Mott. *Philos. Mag. B*, 42:327, 1980.

[115] J.H. Park, L.H. Tjeng, J.W. Allen, P. Metcalf, and C.T. Chen. *Phys. Rev. B*, 55(19):12813, 1991.

[116] J.M. Lavine. *Phys. Rev.*, 114:482, 1959.

[117] J.M. Honig. *J. Solid State Chem.*, 45:1, 1982.

[118] W.J. Siemons. *IBM J. Res. Develop.*, 14:245, 1970.

[119] I. Shiozaki. *J. Phys. C*, 14:4641, 1981.

[120] K. Siratori, S. Todo, and S. Kimura. *J. Phys. Soc. Jpn.*, 57:2093, 1988.

[121] W. Kundig and R.S. Hargrove. *Solid State Commun.*, 7:223, 1969.

[122] D. Ihle and B. Lorenz. *J. Phys. C*, 19:5239, 1986.

[123] L. Degiorigi, P. Wachter, and D. Ihle. *Phys. Rev. B*, 35:9259, 1987.

[124] A. Chainani, T. Yokoya, T. Morimoto, T. Takahashi, and S. Todo. *Phys. Rev. B*, 51(17):17976, 1995.

[125] B.A. Calhoun. *Phys. Rev.*, 94:1577, 1954.

[126] C. Constantin and M. Rosenberg. *Solid State Commun.*, 10:675, 1972.

[127] J.R. Cullen. *Phys. Rev. B*, 7(1):397, 1973.

[128] E.J. Samuelson, E.J. Bleeker, L. Dobrzynski, and T. Riste. *J. Appl. Phys.*, 39:1114, 1969.

[129] T. Yamada, K. suzuki, and S. Chikazumi. *Appl. Phys. Lett.*, 13:172, 1968.

[130] R.S. Hargrove and W. Kündig. *Solid State Commun.*, 8:303, 1970.

[131] J.R. Cullen and E.R. Callen. *Phys. Rev. Lett.*, 26:236, 1971.

[132] E. Wigner. *Trans. Faraday Soc.*, 34:678, 1938.

[133] J.M.D. Coey, I. V. Shvets, R. Wiesendanger, and H.-J. Güntherodt. *J. Appl. Phys.*, 73:6742, 1993.

[134] S. Iida, K. Mizushima, M. Mizuguchi, K. Kose, K. Kato, K. Yanai, N. Goto, and S. Yumoto. *J. Appl. Phys.*, 53(3):2164, 1982.

[135] S. Iida, M. Mizoguchi, N. Goto, and Y. Motomura. *J. Magn. Magn. Mat.*, 31-34:771, 1983.

[136] S. Iida. *Philos. Mag. B*, 42:349, 1980.

[137] A.J.M. Kuipers and V.A.M Brabers. *Phys. Rev. B*, 20:594, 1979.

[138] H.P. Weber and S.S. Hafner. *Z. Kristallogr.*, 133:327, 1971.

[139] V.A.M. Brabens, F. Walz, and H. Kronmuller. *Phys. Rev. B*, 58(21):14163, 1998.

[140] R. Aragon, R.J. Rasmussen, J.P. Shepherd, J.W. Koenitzer, and J.M. Honig. *J. Magn. Magn. Mat.*, 54-57:1335, 1986.

[141] M. O'Keefe. Volume i. In M. O'Keefe and A. Navrotsky, editors, *Structure and Bonding in Crystals*, page 299. Academic Press: New York, 1981.

[142] J.P. LaFemina. *Crit. Rev. in Surf. Chem.*, 3:297, 1994.

[143] F.M.F. de Groot, M. Grioni, J.C. Fuggle, J. Ghijsen, G.A. Sawatzky, and H. Petersen. *Phys. Rev. B*, 40(8):5715, 1989.

[144] M. Sancrotti, F. Ciccacci, M. Finazzi, E. Vescovo, and S.F. Alvarado. *Z. Phys. B. - Condensed Matter*, 84:243, 1991.

[145] D.J. Chadi. *J. Vac. Sci. Technol. A*, 5:834, 1987.

[146] H.H. Farrell, J.P. Garbison, and L.D. Peterson. *J. Vac. Sci. Technol. B*, 5:1482, 1987.

[147] M.D. Pashley. *Phys. Rev. B*, 40(15):10481, 1989.

[148] Y.J. Kim, Y. Gao, and S.A. Chambers. *Surf. Sci.*, 371:358, 1997.

[149] J.M. Gaines, P.J.H. Bloemen, J.T. Kohlhepp, C.W.T. Bulle-Lieuwma, R.M. Wolf, R.M. Reinders, R.M. Jungblut, P.A.A. van der Heijden, J.T.W.M. van Eemeren, J. aan de Stegge, and W.J.M. de Jonge. *Surf. Sci.*, 373:85, 1997.

[150] W.A. Harrison. *Electronic structure and the properties of solids*, Freeman, San Francisco, 1980.

[151] Gabor A. Somorjai. *Introduction to surface chemistry and catalysis.* Wiley Interscience, New York, 1994.

[152] J.C. Vickerman. *Surface Analysis.* Wiley & sons, Chichester, U.K., 1997.

[153] P.W. Tasker. *J. Phys. C: Solid state phys.*, 12:4977, 1979.

[154] F. Bertaut. *Compt. Rendu*, 246:3447, 1958.

[155] V.E. Henrich. *Surf. Sci.*, 57:385, 1976.

[156] F.C. Voogt. NO_2-assisted molecular beam epitaxy of iron oxide films. *PhD Thesis*, University of Groningen:65, 1998.

[157] N.W. Finnis. *Physica status solidi (a)*, 166:397, 1998.

[158] M.W. Finnis. *Collaborative computational project 3*, Newsletter:2, 1999.

[159] N.W. Finnis. Private communication.

[160] M. Seo, J.B. Lumsden, and R.w. Staehle. *Surf. Sci.*, 50:541, 1975.

[161] T. Fujii, M. Takano, R. Katano, Y. Bando, and Y. Isozumi. *J. Appl. Phys.*, 68(4):1735, 1990.

[162] F.C. Voogt, T. Hibma, G.L. Zhang, M. Hoefman, and L. Niesen. *Surf. Sci.*, 331-333:1508, 1995.

[163] Y. Gao, Y.J. Kim, S. Thevuthasan, S.A. Chambers, and P. Lubitz. *J. Appl. Phys.*, 81(7):3253, 1997.

[164] D.M. Lind, S.D. Berry, G. Chern., H. Mathias, and L.R. Testardi. *Phys. Rev. B*, 45(4):1838, 1992.

[165] J. Nerlov, S.V. Hoffmann, M. Shimomura, and P.J. Moller. *Surf. Sci.*, 401:56, 1998.

[166] W. Weiss, A. Barbieri, M.A. Van Hove, and G.A. Somorjai. *Phys. Rev. Lett.*, 71(12):1848, 1993.

[167] A. Barbieri, W. Weiss, M.A. Van Hove, and D.A. Somorjai. *Surf. Sci.*, 302:259, 1994.

[168] S.P. Sena, R.A. Lindley, H.J. Blythe, Ch. Sauer, M. Al-Kafarji, and G.A. Gehring. *J. Magn. Magn. Mat.*, 176, 1997.

[169] N.G. Condon, P.W. Murray, F.M. Leibsle, G. Thornton, A.R. Lennie, and D.J. Vaughan. *Surf. Sci.*, 310:L609, 1994.

[170] R. Jansen, B.J. Nelissen, D.L. Abraham, H. van Kempen, and V.A.M. Brabers. *IEEE Trans. Mag.*, 30(6):4506, 1994.

[171] R. Jansen, V.A.M. Brabers, and H. van Kempen. *Surf. Sci.*, 328:237, 1995.

[172] N.G. Condon, F.M. Leibsle, A.R. Lennie, P.W. Murray, D.J. Vaughan, and G. Thornton. *Phys. Rev. Lett.*, 75(10):1961, 1995.

[173] A.R. Lennie, N.G. Condon, F.M. Leibsle, P.W. Murray, G. Thornton, and D.J. Vaughan. *Phys. Rev. B*, 53(15):10244, 1996.

[174] R. Jansen, H. van Kempen, and R.M. Wolf. *J. Vac. Sci. Technol. B*, 14(2):1173, 1996.

[175] J.M. Gaines, J.T. Kohlhepp, P.J.H. Bloemen, R.M. Wolf, A. Reinders, and R.M. Jungblut. *J. Magn. Magn. Mat.*, 165:439, 1997.

[176] J.M. Gaines, J.T. Kohlhepp, J.T.W.M. van Eemeren, R.J.G. Elfrink, F. Roozeboom, and W.J.M. de Jonge. *Mat. Res. Soc. Symp. Proc.*, 474:191, 1997.

[177] N.G. Condon, F.M. Leibsle, T. Parker, A.R. Lennie, D.J. Vaughan, and G. Thornton. *Phys. Rev. B*, 55(23):15885, 1997.

[178] N.G. Condon, F.M. Leibsle, A.R. Lennie, P.W. Murray, T.M. Parker, D.J. Vaughan, and G. Thornton. *Surf. Sci.*, 397:278, 1998.

[179] S.A. Chambers and S.A. Joyce. *Surf. Sci.*, 420:111, 1999.

[180] R. Wiesendanger, I.V. Shvets, D. Bürgler, G. Tarrach, H.J. Güntherodt, and J.M.D. Coey. *Europhys. Lett.*, 19(2):141, 1992.

[181] A. Yanase and K. Siratori. *J. Phys. Soc. Jap.*, 53(1):31 2, 1984.

[182] M.L. Rudee, D.J. Smith, and D.T. Marguiles. *Phys. Rev. B*, 59(18):R11633, 1999.

[183] X.W. Li, A. Gupta, G. Xiao, and G.Q. Gong. *J. Appl. Phys.*, 83(11):7049, 1998.

[184] J.Y.T. Wei, N-C Yeh, R.P. Vasquez, and A. Gupta. *J. Appl. Phys.*, 83(11):7366, 1998.

[185] M. Shinkai, M. Yanase, M. Suzuki, H. Honda, T. Wakabaysashi, J. Yoshida, and T. Kobayashi. *J. Magn. Magn. Mat.*, 194(1-3):176, 1999.

[186] M. Babincova, P. Sourivong, D. Chorval, and P. Babinec. *J. Magn. Magn. Mat.*, 194(1-3):163, 1999.

[187] F.U. Ahmed, S.I. Bhuiyan, A.S. Mollah, M.R. Sarder, M.Q. Huda, M. Rahman, and M.A.W. Mondal.

[188] D.S. McKay, E.K. Gibson Jr., K.L Thomas-Keprta, H. Vali, C.S. Romanek, S.J. Clemett, X.D.F. Chiller, C.R. Maechling, and R.N. Zare. 273(5277):924, 1996.

[189] C. Seoighe and I.V. Shvets. *Surf. Sci.*, 440:116, 1999.

[190] Oxford Instruments. *Tubney Woods, Abingdon, Oxon, OX13 5QX, UK.*

[191] J. Naumann. *Diplomarbeit, Trinity College Dublin*, 1996.

[192] X.-S. Wang, J.L. Goldberg, N.C. Bartelt, T.L. Einstein, and E.D. Williams. *Phys. Rev. Lett.*, 65:2430, 1990.

[193] R. Maboudian, V. Bressler-Hill, K. Pond, X.-S. Wang, P.M Petroff, and W.H. Weinberg. *Surf. Sci.*, 302:L269, 1994.

[194] R. Kariotis and M.G. Lagally. *Surf. Sci.*, 1991:295, 248.

[195] E.J. Heller, Z.Y. Zhang, and M.G. Lagally. *Phys. Rev. Lett.*, 71:743, 1993.

[196] B.A.G. Kersten, H.J.W. Zandvliet, D.H.A. Blank, and A. van Silfhout. *Surf. Sci.*, 322:L7, 1995.

[197] K.W. Self, X.-S. Wang, K. Pond, V. Bressler-Hill, and W.H. Weinberg. *Surf. Sci.*, 398:1, 1998.

[198] J.F. Anderson, M. Kuhn, H. Diebold, K. Shaw, P. Stoyanov, and D. Lind.

[199] O. Albrektsen, H.W.M. Salemink, K.A. Morch, and A.R. Tholen. *J. Vac. Sci. Technol. B*, 12(6):3187, 1994.

[200] T. Mizoguchi and M. Inoue. *J. Phys. Soc. Jpn.*, 21:1310, 1966.

[201] T. Paxton. *Private communication*, 1999.

[202] E. Kita, Y. Tokuyama, A. Tasaki, and K. Siratori. *J. Magn. Magn. Mat.*, 31-34:787, 1983.

[203] C.J. Chen. *Phys. Rev. Lett.*, 69:1656, 1992.

[204] J. Shen, R. Skomski, M. Klaua, H. Jenniches, S. Sundar Manoharan, and J. Kirschner. *Phys. Rev. B*, 56(5):2340, 1997.

[205] Y. Obi, Y. Kawano, Y. Tange, and H. Fujimori. *J. Magn. Magn. Mat.*, 93:587, 1991.

[206] J. Malzbender, M. Przybylski, J. Giergiel, and J. Kirschner. *Surf. Sci.*, 414:187, 19998.

[207] H.J. Elmers, J. Hauschild, and U. Gradmann. *Phys. Rev. B*, 54(21):15224, 1996.

[208] D. Sander, A. Enders, C. Schmidthals, D. Reuter, and J. Kirschner. *Surf. Sci.*, 402-404:351, 1998.

[209] J. Osing. Studies towards spin sensitive scanning tunneling microscopy. *PhD Thesis*, University of Dublin, 1998.

[210] W. Pluschell and V.S. Sarma. *Archiv fuer das eisenhuttenwesen*, 44(3):161, 1973.

[211] M. Kerker, P. Scheiner, D.D. Cooke, and J.P. Kratohvil. *J. Colloid interface sci.*, 71:176, 1979.

[212] F. Hund. *Angew. chem. int. ed. eng.*, 20:723, 1981.

[213] Coda system Ltd. *Agricultural house, The Avenue, Braintree, Essex CM 6HY, UK.*

[214] R.M. Bozorth. *Ferromagnetism.* IEEE magnetics society, New York, 1993.